Imperial College London
Department of Materials

Chemically Functionalised Graphene Biosensor for the Label-free Sensing of Exosomes

Deana Kwong Hong Tsang

Supervisor: Professor Norbert Klein

Submitted for fulfillment of the requirements for the degree of
Doctor of Philosophy in Materials Science
at Imperial College London, March 2019

Declaration

Statement of Originality

I declare that the work presented in this thesis is my own and that all else is appropriately referenced and acknowledged.

Copyright Declaration

Acknowledgements

Firstly, I would like give huge thanks to my supervisor Professor Norbert Klein for encouraging me to pursue materials science after my undergraduate degree and taking me on as a student. I'd also like to thank the rest of the group, both past a present, who have provided continuous help and support. In particular, I would like to thank Dr Clare Watts who has offered constant motivation and advice both within and outside the PhD.

Thanks to my family: my mum, dad, brother, uncle Andy and all those in Mauritius for supporting me throughout my entire academic experience. They have helped immensely by having confidence in me and for always showing interest in what I do. Without their encouragement I'm sure I wouldn't have made it to where I am today. I would also like to add a special dedication of this thesis to my late grandmother, Mary-Ann, who was never able to see me graduate but I hope to have made her proud.

Deepest thanks extend to all materials department staff and technicians, without whom the work in this thesis certainly wouldn't have been possible. I must also thank them for making my whole undergraduate and postgraduate experience at Imperial so enjoyable and manageable. Additionally to all users of lab LG55a: thank you for keeping the lab in order and I am happy I was able to contribute as lab manager. Finally, I would like to thank all the friends that I've made along the way who have helped keep me social and sane: particular thanks to everyone in office 1.01, 'The Bois' and 'Key Players' who were not only a thorough source of entertainment but also a tremendous support.

Abstract

Exosomes are a subpopulation of vesicles that are expelled from all cells and are speculated to have some role in the development of cancerous tissue. The work in this thesis presents the sensitive and specific electrical detection of exosomes in solution using a graphene field-effect transistor (gFET) biosensor: non-covalently functionalised using an intermediate linker and conjugated with anti-CD63 antibodies. The intermediate linker chosen was a pyrene-based molecule, which π - stacks to the graphene surface without disruption, or introduction of high defect density, to the graphene sp^2 hybridised structure unlike covalent functionalisation. The gFET biosensor could act as an cheap, wafer-scalable alternative to more conventional labelling techniques and the current state-of-the-art optical techniques that use surface plasmon resonance (SPR) on functionalised gold substrates, which have so far detected down to 1000 exosomes/µL.

By exposing only part of the graphene surface to charged species using a microfluidic channel, regions of different doping levels arose in the same graphene film. This manifested as an additional minimum, which shifted to higher gate voltage (V_g) in the transfer characteristic and saturated over 30 minutes when graphene was exposed to exosomes. The saturation was attributed to an equilibrium between exosomes binding and unbinding to anti-CD63 antibodies. As exosomes exhibit negative charge when in phosphate buffered saline (PBS) at pH 7, the accumulation of positive charge in the exposed graphene as they come close to its surface causes a shift to higher V_g by the electrostatic field effect. Therefore the exposed graphene becomes p-doped relative to when exposed only to PBS. The value of the shift after 30 minutes was also concentration dependent with sensitivity down to a concentration of 0.1 µg/mL exosomes (5000 exosomes/µL). By using two negative controls: an isotype control antibody and a non-specific protein target, the gFET sensor was also shown to be specific to CD63 in exosome membranes. Both back-gated and electrolyte top-gated gFETs were used for exosome detection whereby capacitative effects as well as electrostatic effects contributed to the sensing mechanism for the electrolyte top-gated gFET.

Publications and Conferences

Journal Publications

- **D. K. H Tsang**, T. J. Lieberthal, C. Watts, I. E. Dunlop, S. Ramadan, A. E. Rio del Hernandez, N. Klein. "*Chemically functionalised graphene FET biosensor for the label-free detection of exosomes*" Scientific Reports, [In peer review], March 2019.

Conference Oral Presentations

- **D. K. H Tsang**, T. J. Lieberthal, A. E. Rio del Hernandez, N. Klein. "*Chemically functionalised graphene FET with double conductance minima for the label-free sensing of exosomes*" TMS2018, 11 – 15/02/18, Phoenix, Arizona, USA.
- **D. K. H Tsang**, T. J. Lieberthal, C. Watts, I. E. Dunlop, S. Ramadan, A. E. Rio del Hernandez, N. Klein. "*Chemically functionalised graphene FET biosensor for the label-free detection of exosomes*" Graphene Korea 2019, 27-29/03/19, Incheon, Korea.

Poster Presentations

- **D. K. H Tsang**, T. J. Lieberthal, A. E. Rio del Hernandez, N. Klein. "*Chemically functionalised graphene sensing of exosomes*" Graphene 2017, 28-31/03/17, Barcelona, Spain.
- **D. K. H Tsang**, T. J. Lieberthal, A. E. Rio del Hernandez, N. Klein. "*Chemically functionalised graphene for DC and microwave sensing of exosomes*" Postgraduate Research Day, 18/03/17, Imperial College London, London, UK.

Contents

List of Tables

List of Figures

Chapter 1

Introduction

The fabrication and discovery of new, innovative materials has proven pivotal in the development of the next generation of electronic devices. Since its discovery in 2004 by mechanical exfoliation from graphite, graphene has made a huge impact, not only in the scientific community but also in mainstream media, being described as a 'wonder material'. Since then, many advances in research have led to it being implicated in applications such as field effect transistors (FETs) for gas and biosensors, electrochemical sensors, photodetectors and wearable, flexible electronics. [1, 2, 3, 4].

A major challenge for this generation is the miniaturization of electronic device, whilst pushing high-performance metrics and keeping fabrication costs low. Graphene was seen to be a material that could potentially answer that demand: the 2-dimensional (2D) material has been implemented into many devices and the vision is for it to be commercially produced with high quality at affordable prices. Within the past decade, concerns regarding graphene's scalability have been also addressed and new fabrication techniques are being implemented such as roll-to-roll production of up to 30-inch films [5]. In this case, large-area graphene has been fabricated using chemical vapour deposition (CVD); which is one of the many processes developed for the fabrication of graphene as an alternative to mechanical exfoliation. From an electronic device perspective, this opens up opportunities for the creation of wafer-scalable graphene arrays.

Graphene itself, coupled with appropriate manufacturing and fabrication technology, hence gives it potential to replace existing, conventional materials for many applications [6, 7].

This thesis presents the use of CVD graphene for the fabrication of an FET-based biosensor. The creation of graphene FETs (gFETs) has been largely studied and its resulting current response with application of a gate voltage is well-known. The utilization of the working principles of a gFET is therefore important for understanding the response and mechanism of sensing as a result of the introduction of biomolecules to the graphene surface. Graphene's biocompatibility also makes it a promising candidate for biosensing applications and has been proven to be useful for the detection of disease biomarkers, most notably cancer [8, 9, 10]. These biomarkers, if sensed to clinically relevant concentrations, can be indicative of both the presence of a disease and its stage. Therefore, by thoroughly investigating a gFET response to specific biomarkers, there exists the potential for the development of clinical diagnostic devices for the sensitive detection of diseases.

1.1 Motivation and Objectives

Clinical diagnostic tools for the identification of disease state and stage often require time-consuming, complex techniques. The need for biosensor devices stems from the potential to replace these with fast, point-of-care, lab-on-chip electronics. The specific detection of biomolecules is possible through functionalisation of surfaces with appropriate probe molecules: by identifying a target antigen, the complementary antibody that will specifically bind to it can be attached to a gFET surface. As these bind, they will modulate graphene's electronic properties that can be detected by a designated read-out. Graphene's sensitivity to charge and its tunability can be used as an indication of the presence and concentration of specifically bonded species such as proteins and cells.

For the application of fast, portable biosensor devices, often conventional tissue biopsies are impractical and highly invasive to the patient. As an alternative, a 'liquid biopsy' is a sub

mL volume of biological fluid, such as blood serum, urine or saliva, that can be extracted in a non- or minimally invasive manner. These liquids contain blood-circulating biomarkers that can be isolated and used to give quantitative information of disease etiology, progression and response to disease treatment. A class of these blood circulating biomarkers is exosomes, which are extracellular vesicles expelled by all cells: both healthy and diseased. The explusion of an exosome containing genetic information and the transportation of its cargo to another cell has been shown to influence or cause the development of tumour related pathways such as angiogenesis and metastasis. As they are typically present in blood serum in high numbers (10^6 - 10^{11} per mL) [11, 12], their capture and isolation could be highly important for the detection of cancer.

Cancer itself was accountable for 28 % of deaths in the UK in 2016 and Cancer Research UK claims 1 in 2 people in the UK will be diagnosed with a form of the disease in their lifetime [13]. Current research focusing on early cancer diagnosis and effectiveness of treatment has seen the 5-year survival rate increasing from 50 % to 66 % between the years of 1975 - 2004 [14] and the further increase in this value could lie with further technological advances. Biosensors similar to gFETs have been developed to sense cancer biomarkers such as specific single proteins and circulating tumour cells that must be detected to very low (pM - fM) concentrations for clinical relevance. Therefore, by targeting exosomes expelled from tumour cells, the gFET could provide an opportunity for the diagnosis of cancer in early-stages that does not require such low detection limits whilst being simple in design and low on cost. The work presented in this thesis utilizes a functionalised CVD gFET for the detection of healthy exosomes and investigates its sensing mechanism for a proof-of-principle concept of a type of exosome sensor that, to the best of our knowledge, has not been seen before.

1.2 Thesis Outline

In this thesis, the development of the gFET biosensor for the specific detection of exosomes was performed step-by-step. This is presented in the following order:

- **Chapter 2**: This will be the introduction to graphene including the basic theory behind its band structure and highlighting the fundamental properties that result from its unique physical structure. The different methods for fabricating graphene will be discussed and implementation of these for biosensors briefly described.

- **Chapter 3**: This chapter will discuss the importance of the materials used in FET structures. It will contain a comparison between the various structures used to create gFETs and include design considerations for structures used for electrical measurements in liquid.

- **Chapter 4**: The principles of biosensing using graphene will be discussed here with a comprehensive review of gFETs used for sensing of biomolecules. Some commonly used routes for functionalisation will also be compared.

- **Chapter 5**: This chapter will be an introduction to exosomes, which will describe their clinical importance with regards to cancer and current methods of isolation and detection.

- **Chapter 6**: All experimental methods and materials used for this thesis will be presented here. The fabrication of the gFET sensor with functionalisation and making up of all biological solutions will be included. For materials characterisation techniques, their principles of operation will be described as well as how they are used specifically for graphene.

- **Chapter 7** This is the first of the results chapters and discusses the process of finding the best functionalisation route for the biosensor. Preliminary liquid measurements as well as more extensive back-gated FET measurements with exosomes will be presented.

- **Chapter 8** The second of the results chapters will focus on the implementation and optimisation of the electrolyte top-gated gFET, which builds upon results in chapter 7.

- **Chapter 9** This will summarise the work carried out, collate the conclusions from each chapter and go over proposed future work.

Chapter 2

Introduction to Graphene

Graphene is commonly known as a 2D crystalline sheet of carbon atoms i.e. one layer of graphite. The atoms are arranged in a hexagonal, planar structure and form one of the best-studied carbon allotropes. It was first prepared in 2004 by Novoselov and Geim [15] by mechanical exfoliation from graphite, which itself can be viewed as layered graphene crystals that are weakly coupled together [16] and has since been fabricated and used in a range of applications. Graphene exists and is stable under ambient conditions, contrary to previous belief that materials with 2D structures would lead to instability and impracticality. Properties that arise as a result of the 2D structure includes ballistic transport [17], which makes graphene a promising candidate for electronic devices.

Other allotropes of carbon have since been explored such as carbon nanotubes and fullerenes, as illustrated in figure 2.1, and all exhibit abnormalities in physical and chemical behaviour. In the case of graphene, single-walled carbon nanotubes (SWCNT) and fullerenes, the unique properties arise due to the reduced dimensionality and electronic band structures, such as zero band gap, high carrier mobility and high mechanical strength [19, 20, 21]. For electronic devices, the exceptional electronic transport properties of graphene have led to the potential for replacement of silicon in traditional FET technology.

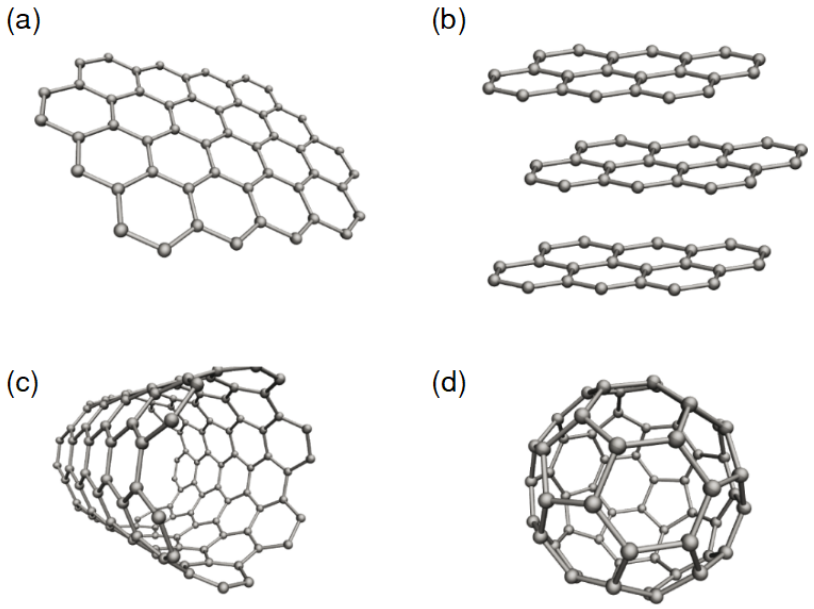

Figure 2.1: Schematic representation of the various carbon allotropes: (a) monolayer graphene, (b) graphite, (c) C_{60} fullerene and (d) single-walled carbon nanotube (SWCNT). Reproduced from [18].

2.1 Electronic Transport Properties

2.1.1 Carbon Hybridisation

The hybridisation between adjacent carbon atoms in graphene's structure is fundamental for our understanding of its electronic properties. In graphene, the carbon atoms are arranged in a planar three-coordination state as a result of sp^2 hybridisation, which leads to a C-C bond length of ≈ 1.42 Å and C-C-C bond angles of 120° [16]. The electronic configuration of carbon is $1s^2 2s^2 2p^2$. When carbon atoms bond, it is energetically favourable for an electron in the 2s orbital to fill a third 2p orbital. The electron is therefore in an excited state. New orbitals are then formed through the combination of the s and p orbitals, known as sp^x hybrid orbitals, where the order gives an indication of how electrons are involved in the bonding. For sp^2 hybridisation, 3 sp orbitals are formed, which leaves a remaining p-orbital. Single carbon bonding is hence a result of overlapping sp^2, known as a σ bond, and the overlap of

the p-orbitals are known as π bonds. It is these p-orbitals that are then responsible for the delocalised π system, which forms the basis of many conduction properties of graphene. The evolution of this bonding is described in figure 2.2.

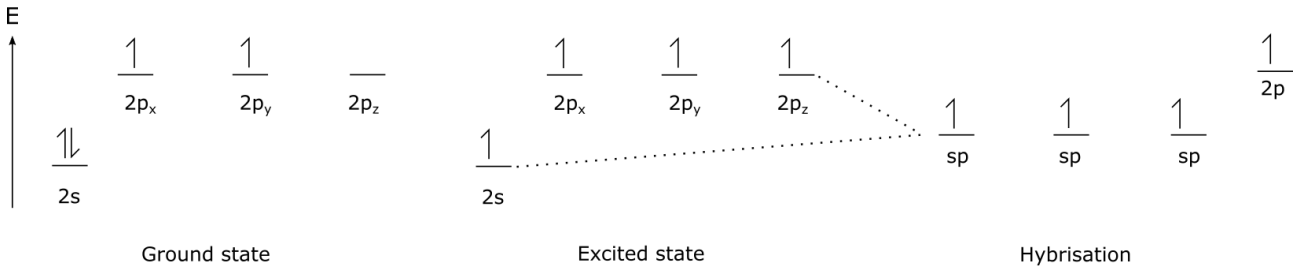

Figure 2.2: Schematic of the orbital evolution from a ground state to an excited state carbon atom to an sp^2 hybridisation.

Often the sp^2 hybridisation results in what is described as graphene's honeycomb structure as seen in figure 2.3(a). Upon chemical functionalisation, these can undergo sp^3 hybridisation, which is often the result of deliberate covalent bonding out of the graphene plane or associated with defects. These defects then effect the electrical properties as discussed in later sections.

2.1.2 Band Structure

The honeycomb structure of graphene can be presented by the Bravais lattice, from which the primitive unit cell is easily visualised. The Bravais lattice describes the equivalent atomic positions which can be related by two lattice vectors $\vec{a_1}$ and $\vec{a_2}$. This creates a repeating pattern of equivalent atomic positions where each has an identical surrounding environment with adjacent atomic positions related by either lattice vectors. The repetition of the unit cell hence creates the hexagonal, Bravais lattice as seen in figure 2.3. Hence, it is important to note that the honeycomb and Bravais lattice structure are not the same.

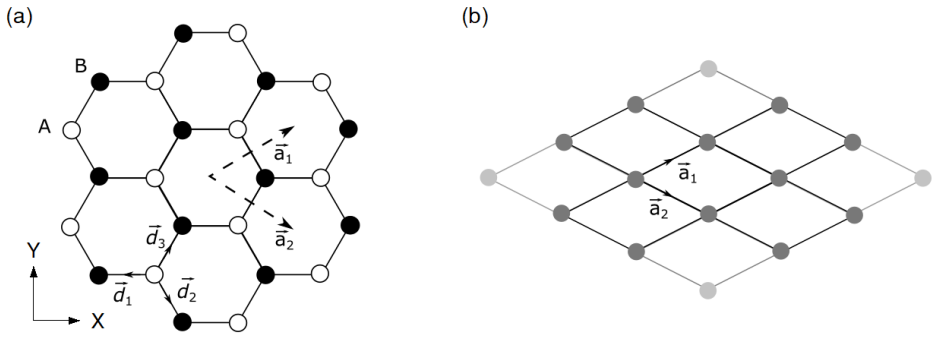

Figure 2.3: Schematic representation of graphene's (a) honeycomb structure where A and B atoms making up the respective sublattices, $\vec{d}_{1,2,3}$ depict vectors adjoining two atoms in the elementary cell and $\vec{a}_1$ and $\vec{a}_2$ are the unit cell lattice vectors. (b) Representation of the resulting Bravais lattice made up from the lattice vectors defined in (a).

From figure 2.3(a), the vectors $\vec{d}_{1,2,3}$ relate two bonded carbon atoms in real space. As mentioned, the C-C bond length, and therefore the distance between adjacent atoms, l, is ≈ 1.42 Å, which gives a unit cell lattice constant, a, of 2.46 Å. The respective vectors that describe adjacent atomic positions, $\vec{d}_{1,2,3}$ are hence related by the following equation where $\mathbf{x}$ and $\mathbf{y}$ describe the Cartesian coordinate system.

$$\vec{d_1} = -a.\mathbf{x}, \quad \vec{d_2} = \frac{a}{2}(\mathbf{x} - \sqrt{3}\mathbf{y}), \quad \vec{d_3} = \frac{a}{2}(\mathbf{x} + \sqrt{3}\mathbf{y}) \tag{2.1}$$

The real space unit cell lattice vectors are therefore:

$$\vec{a_1} = \frac{a}{2}(3\mathbf{x} + \sqrt{3}\mathbf{y}) \quad and \quad \vec{a_2} = \frac{a}{2}(3\mathbf{x} - \sqrt{3}\mathbf{y}) \tag{2.2}$$

The area of the unit cell is therefore ≈ 0.051 nm^2 and as there are two carbon atoms per unit cell, this gives a carbon density of 3.9×10^{15} cm^{-2}. This also corresponds to the density of delocalised electrons as there is one π electron present per carbon atom. This is not to be confused with the carrier density, which is a parameter for electronic transport properties, and depends on the density of states (DoS).

As for conventional materials, the band structure is usually described by reciprocal lattice points. Reciprocal space is defined in relation to real space by $a_i.b_j = 2\pi\delta_{ij}$ where δ_{ij} is the Kronecker delta. The electronic band structure can be more easily visualised using reciprocal lattice as points in this space define significant points of interest between graphene's conduction and valence bands seen in figures 2.4 and 2.5.

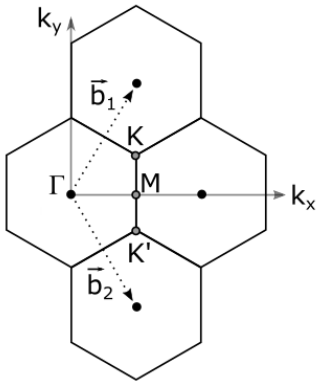

Figure 2.4: Schematic representation of the reciprocal lattice where black points indicate reciprocal lattice points and $\vec{b_1}$ and $\vec{b_2}$ represent reciprocal lattice vectors.

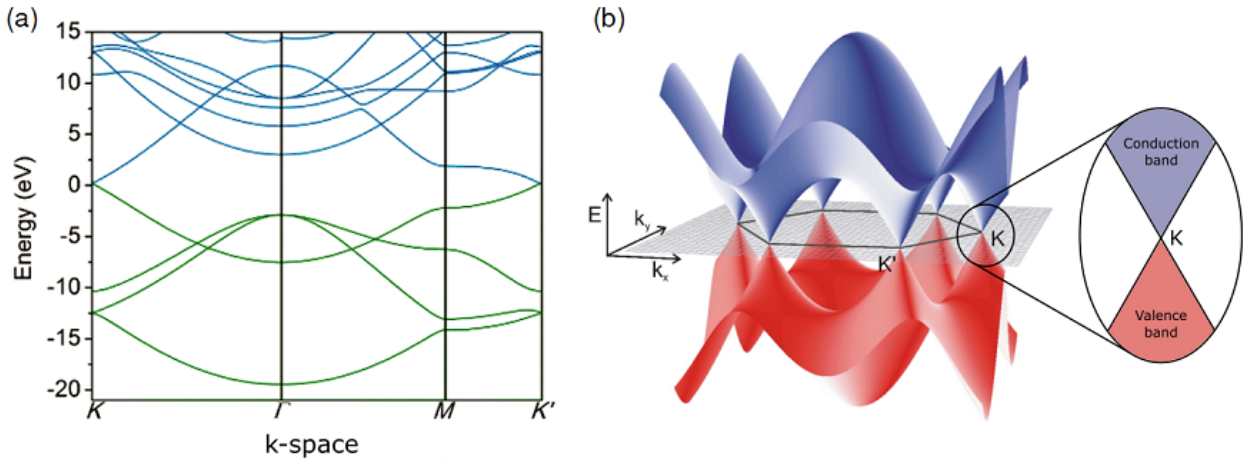

Figure 2.5: (a) Band structure of graphene in k-space with both σ and π bands. (b) Band structure of graphene showing only the π (red) and π* (blue) bands centred around the reciprocal lattice and resulting linear energy dispersion relation at the K point. Reproduced from [22] and [23].

The band structure is easily depicted using points in the reciprocal lattice. Figure 2.5(a) shows

the crossing of the π and π* bands at K and K' points, which result in graphene's famous linear conical energy dispersion, *E(k)*. The band structure reveals equivalent K and K' points due to the lattice symmetry, which results in crossing of the conduction band and valence bands cross at the Fermi energy (E_F) at which the DoS is zero. In contrast to typical semi-conductor materials used in electronic devices, graphene has zero band gap, which leads to interesting properties such as graphene's ambipolar effect: whereby conduction can be continuously altered between electrons and holes through the application of an electric field [24]. A positive gate voltage (V_g) increases E_F, which leads to and increase in the DoS and higher electron conductivity whereas a negative V_g would lead to increased hole conductivity. This is summarised in figure 2.6 where the resistivity of graphene is shown as a function of an applied electric field through an applied V_g. At 0 V, the maximum resistivity is a result of no states being occupied at that energy level (DoS of zero). This is commonly referred to as graphene's Dirac point (also known as the point of minimum conductivity) and is heavily affected by extrinsic doping, which forms the basis of most graphene-based electronic sensors.

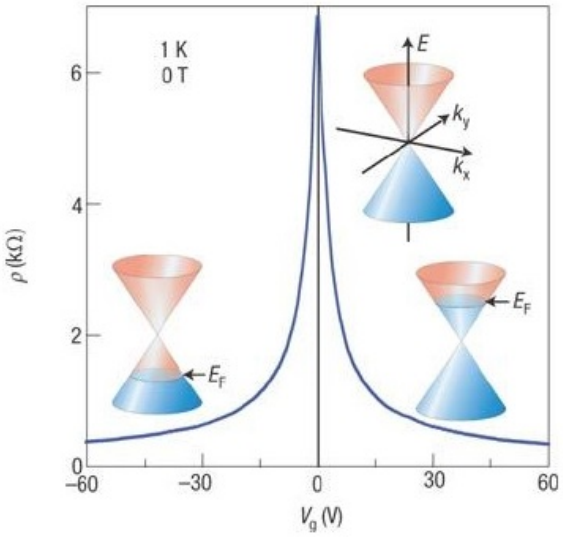

Figure 2.6: Ambipolar effect in graphene: the resulting resistivity upon application of gate voltage V_g for the generation of an electric field. The band structure E shows that for $E < E_F$, hole conduction is promoted and $E > E_F$ results in electron conduction. At 0 V, the zero density of states results in maximum resistivity in graphene. Reproduced from [25].

2.2 Growth and Fabrication

Graphene can be produced in several different ways. For large-area graphene applications, chemical vapour deposition (CVD) is frequently used where graphene is grown on a chosen substrate (most commonly metal) [26]. The scalability of this process allows the production of uniform, high-quality materials under the right conditions [27]. Of course, there are many alternatives to CVD graphene on metal substrates, including graphene obtained by mechanical exfoliation of highly oriented pyrolytic graphite (HOPG), reduction of graphite oxide and epitaxial graphene grown on SiC substrates. The method used, and the type of graphene obtained (monolayer, bilayer or multilayer) hence determines the material properties and suitability for the application.

2.2.1 Chemical Vapour Deposition

The ability to control growth conditions for graphene makes CVD a preferable choice. Pressure, temperature, substrate choice, heat rate and precursor flow rate are all tailorable parameters that can result in the control of properties such as the number of layers and domain size [28], which then influences electric properties. An added advantage is the capability to etch the underlying metal substrate using suitable etchants, allowing for the transfer of graphene to other substrates, such as silicon for potential electronic applications [28].

Often methane is used as the main precursor for graphene and introduced into the reaction chamber alongside a combination of hydrogen and argon at an elevated temperature. This can be performed in different furnace geometries: vertical or standard horizontal CVD, where vertical is sometimes employed for the growth of graphene on both sides of the substrate. Developments in the CVD process has resulted in a relatively well-established mechanism for graphene growth using methane. As the temperature of the reaction chamber increases, decomposition of the methane (or alternative hydrocarbon source) occurs on the substrate. Metals are often used as the substrate (as will be discussed in detail later) as they act to catalyse the

decomposition [29]. The resulting carbon (C) diffuses into the substrate hence, the solubility of carbon in the substrate must also be considered, for example if a metal like nickel (Ni) is used as the substrate, cooling causes the carbon solute to come to the surface in the form of a graphene sheet; a process commonly known as segregation. Otherwise, if the substrate has low carbon solubility, for example copper (Cu), carbon atoms will instead diffuse across the substrate surface and the graphene sheet will form by lateral nucleation of domains around an atom; this is known as self-limited surface deposition as the process is limited by the coverage of the substrate [30, 31]. Both these mechanisms, depicted in figure 2.7, result in the subsequent formation of the sp^2 hybridised structure by bonding of carbon atoms. They are predominantly substrate dependent and can be further adapted by changes in cooling rate, gas composition [31] and pressure [29].

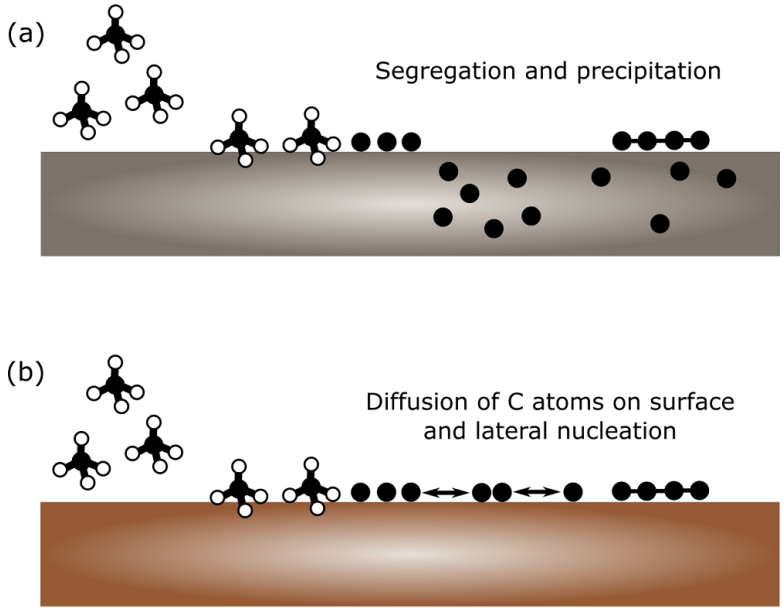

Figure 2.7: CVD mechanisms for methane showing adsorption on the surface and following process for substrates with a) high C solubility where C atoms diffuse into the substrate (segregation) and precipitate at the surface and b) low solubility carbon where C atoms remain at the surface of the substrate and diffuse to nucleation points that expand laterally to form graphene sheets. Reproduced from [32].

The size of the graphene sheet produced is also controlled by the size of the substrate used. For example, for Cu foil, large-area monolayer graphene has been obtained on the cm scale

and this allows for easy subsequent patterning and device fabrication from a single sheet after transfer to suitable substrates. Various metals have been used to catalyse the CVD process, all with different C solubility (at 1000 °C) such as Cu (0.04 %), Ni (2.03 %) and platinum (Pt) (1.76 %), the last of which has shown to have either segregation or surface diffusion and nucleation depending on other growth conditions [33, 34]. The choice of metal substrate and degree of crystallinity is also key in influencing the number of graphene layers: Cu being the most popular substrate for monolayer growth [5]. Due to the nature of the mechanism on high C solubility metals such as Ni, few layer or multilayer graphene is preferentially grown and this is mostly due to the presence of grain boundaries on the metal substrate. As carbon atoms adsorb onto the metal surface (figure 2.7(a)), grain boundaries of the metal act as low energy points for preferential segregation [35, 36] resulting in heterogeneous graphene with multilayer regions. In contrast, the combination of nucleation and lateral expansion of graphene on Cu substrates and the formation of transient bonds between the copper and carbon [35] makes producing multilayer graphene less likely and single layer growth is more easily controlled.

CVD graphene has been exploited for biosensors for sensing targets such as glucose, DNA and bacteria [37, 38, 39]. By using CVD, most of these examples take advantage of its ability to produce monolayer graphene under controlled conditions for integration into gFETs. Z. Xu et al. [40] created a solution-gated CVD gFET sensor for the real-time sensing of DNA. Their graphene was reported to have a single-crystal domain and was monolayer dominated, which was then patterned using oxygen-plasma etching to a defined size. By chemical modification of the graphene, the sensor was able to monitor DNA binding kinetics and sense down to 10 pM [40]. Similarly, J. Ping et al. [41] fabricated a CVD graphene back-gated sensor for DNA detection and reported a detection limit of 10 fM [41], several orders of magnitude lower than that by Z. Xu et al. despite very similar device fabrication. Their differences lie in the detail of the electrical measurement methods and set-up, which may explain how a lower limit of detection is obtained, which is discussed in detail in section 4.3. Despite this, both prove CVD graphene's ability to sense biological species to low limits of detection.

2.2.2 Other Graphene Fabrication Techniques

Developments in other graphene synthesis methods are abundant and various applications suit graphene fabricated in alternative ways to CVD where large-area graphene is not necessary or ideal. For example, mechanically exfoliated graphene remains a popular method since its early attempt with adhesive tape.

To achieve single layer graphene from mechanical exfoliation of graphite, van der Waals forces hold graphene sheets together and these can be overcome when sheets are peeled layer by layer from bulk graphite [42]; as in-plane σ bonds are stronger, individual graphene sheets can be obtained (figure 2.8). Mechanically exfoliated monolayer graphene has already proven useful for biosensor applications: Y. Ohno et al. [43] obtained high quality monolayer graphene flakes by mechanical exfoliation of graphite through micro-cleavage [43]. Graphene flakes obtained in this way can then be transferred onto a variety of substrates. In the case of Y. Ohno et al., graphene was transferred onto Si/SiO_2 for electrical detection of immunoglobulin E protein [43].

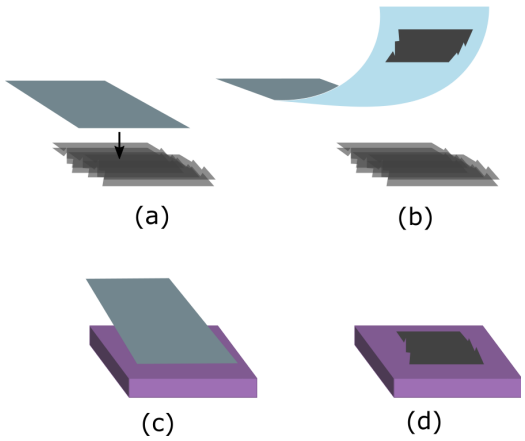

Figure 2.8: Schematics of the mechanical exfoliation of graphite using the adhesive tape method: a) tape is pressed onto the graphite b) then lifted off successive times until a monolayer sheet of graphene is obtained. c) The tape with graphene is then placed onto the desired substrate and d) lifted off.

In comparison to CVD graphene, mechanically exfoliated graphene displays many desirable

properties such as high mechanical strength, the highest carrier mobility at room temperature (in suspended graphene), lower asymmetry between electron and hole conduction and lower levels of disorder associated with CVD graphene growth (such as lattice defects and grain boundaries) [44, 45, 46]. However, the method itself is still limited by scalability as flake sizes and sheet thicknesses are highly variable.

Chemical methods of obtaining graphene have also been explored. This requires the exfoliation and oxidation of graphite (or exfoliation of graphite oxide) first to obtain sheets of graphene oxide (GO) [47]. The final result is reduced GO, the which has been utilised for electrochemical biosensor applications [48]. Graphite can be oxidised using $KMnO_4$ [49] (figure 2.9). This is often also coupled with ultrasonication to separate individual flakes therefore turning graphite oxide into graphene oxide however, the main drawback of this aggressive separation is the reduction of flake size.

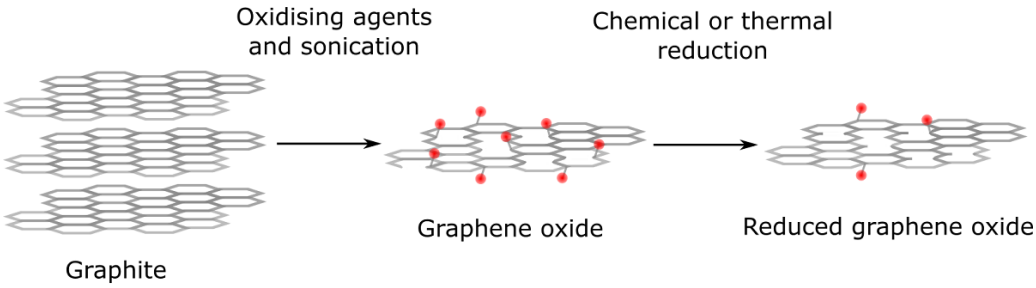

Figure 2.9: Preparation of reduced graphene oxide from graphite. Red dots represent oxygen containing groups such as -COOH or -OH.

Despite the reliability of this method, the interplanar spacing and oxidation to GO also severely limits the electrical properties due to the large disruption to the sp^2 hybridised structure. Hence, reduction is necessary to restore the conductivity to a value as close to pristine graphene as possible. The use of reduced GO in FET biosensors has been shown by S. Mao et al. [50] where the sensor surface was functionalised with gold nanoparticle-antibody conjugates for the specific detection of IgE protein [50]. This can be directly compared to Y. Ohno et al. who used mechanically exfoliated graphene for a similar FET structure [43]. However, Y. Ohno et al. reported a lower detection limit of approximately 0.55 ng/mL for IgE protein compared

to 2 ng/mL as reported by S. Mao. This gives reason to believe that the processing methods of chemically reduced GO may hinder the electronic sensitivity of their FET devices. Other drawbacks of this method include the limitation of graphene sheet size (as well as large size variation between sheets) and possible aggregation, hence the addition of stabilising agents is sometimes necessary.

As well as maintaining good structural integrity, epitaxially grown graphene holds the ability to create nanostructured graphene without the need for complex microfabrication [51]. It also does not require any additional transfer of the graphene to other substrates as it is directly grown on SiC. The direct growth ensures controlled interfaces between the graphene and substrate (6H-SiC (0001)) [52]. Substrates are initially hydrogen etched to obtain atomically smooth surfaces then heated to high temperatures ($\approx$ 1200 °C) [53]. These high temperatures cause the thermal sublimation of Si from the surface leaving behind C atoms [54] as seen in figure 2.10.

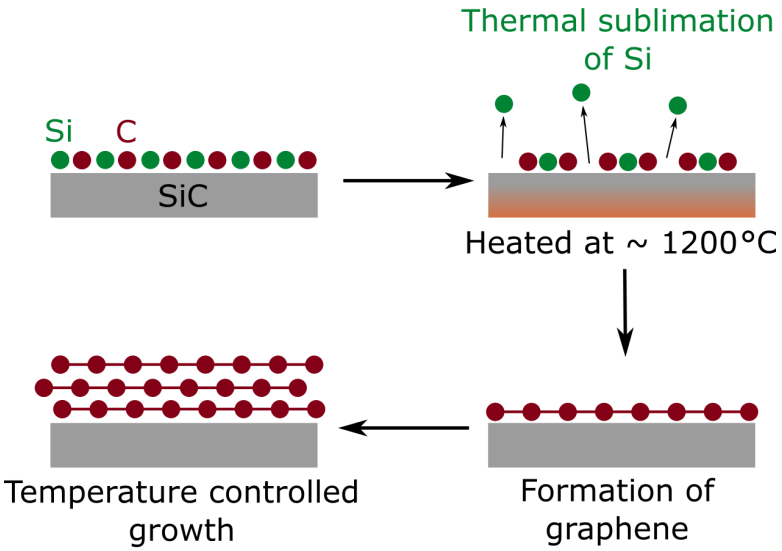

Figure 2.10: Schematic representation of the epitaxial growth of graphene on SiC.

Epitaxial graphene has also been used in biosensor applications: Z. Tehrani et al. [55] covalently functionalised multilayer graphene grown on SiC for the specific detection of an oxidative stress cancer biomarker. Covalent modification of epitaxially grown multilayer graphene with diazonium salts gave sensors with a detection limit of 0.1 ng/mL, comparable to values with

mechanically exfoliated and chemically reduced graphene [43, 48]. Of course, results can not only be attributed to the method of graphene fabrication as the subsequent chemical modification routes used are different in each case. However, this shows that despite the fabrication method used, with appropriate chemical modification, graphene is indeed suitable for the sensitive detection of biological species.

Chapter 3

Graphene Field Effect Transistors (gFETs)

3.1 GFET structures

The back-gated gFET was designed to take advantage of graphene's superior electronic transport properties as an alternative to conventional semiconductor-based FETs, namely those fabricated using silicon. Having established many different approaches to synthesizing graphene as discussed in section 2.2 and its transfer onto a large variety of materials, graphene is an alternative, atomically thin, FET material with exceptionally high conductivity. The combination of its properties, design of metal contact electrodes and appropriate gate dielectrics reveals many opportunities for gFETs in fields such as sensing, optoelelectronics and high-speed electronic devices [7, 6, 56]. The high sensitivity of graphene to chemical surface modification and the effect of electrostatic doping of graphene from charged species provides a huge potential for achieving enhanced sensing capabilities compared to conventional FET structures.

3.1.1 Comparison to Conventional Semiconductor FETs

The most commonly and well-known semiconductor FETs are based on silicon technology, from which the metal-oxide-silicon FET (MOSFET) is famously derived. Of MOSFETs, complementary-

MOSFETs (CMOS) designs are defined as mix of p-type and n-type MOSFET transistors that are still commonly used for a wide range of applications using integrated circuits including image sensors and microprocessors [57]. However, many believe that MOSFET technology and scalability is a major issue whilst the desire for smaller, faster integrated electronics continues to grow. For this reason, new materials for FET designs for a range of applications have been investigated with graphene being an obvious choice. This section focuses mostly on the comparison in the key principles of operation and device design between MOSFETs and back-gated FETs.

In general, a FET consists of source, drain and gate electrodes with a conductive channel that connects the source and drain [58]. For a typical silicon FET, the field-effect arises due to the electric field produced through a silicon dioxide (SiO_2) dielectric layer, which separates the silicon channel from the metal gate electrode, when a gate voltage is applied. The basic structure of a n-type MOSFET (nMOS) is shown in figure 3.1(a). Here, p-type silicon can be used and oxidised to form a layer of SiO_2 of desired thickness, which is then patterned accordingly to create the gate dielectric. Regions of n-type silicon are also created within the bulk silicon to act as the source and drain. A gate electrode is deposited on the gate dielectric to fabricate a gate electrode. When a voltage is applied between the drain and source (V_{ds}) and upon the application of a positive voltage between the gate and source (V_g), an electric field is generated within the dielectric such that a thin layer of negative charge collects in the silicon close to the dielectric/silicon interface, known as an inversion layer. This creates a path or channel through which electrons can travel.

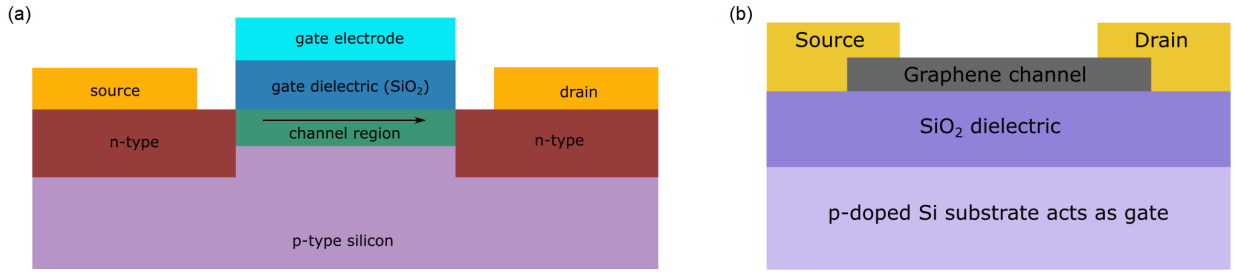

Figure 3.1: Schematic representation of (a) an nMOS showing the resulting channel region and (b) a back-gated gFET using a Si/SiO_2 substrate with positions of source, drain and gate electrodes.

Compared to MOSFETs, gFETs are designed with graphene as the conducting channel rather than silicon. Due to its electronic transport properties as introduced in chapter 2 and its 2D nature, it is an obvious choice for the fabrication of high performance FETs and was first reported by M. Lemme et al. in 2007 [59]. Figure 3.1(b) shows the basic design of a back-gated gFET. In comparison to the MOSFET seen in figure 3.1 (a), V_g is applied through the back of the device. The transfer of graphene onto a Si/SiO_2 substrate allows for the application of the back-gate voltage through the conductive silicon and field-effect through the SiO_2 dielectric without the need to fabricate additional electrodes. In such cases, silicon substrates p-doped with boron to give high doping concentrations (1×10^{15} cm^{-3}) are used as highly conductive gates [59]. As graphene is already conductive, the field generated through the dielectric (in the same way as in a parallel plate capacitor) then modulates the carriers in the graphene channel and results in a unique characteristic when the current between the drain and source (I_{ds}) is measured as a function of the applied V_g.

The advantage of the back-gated gFET structure, for bio- or chemical sensing applications in particular, is that the graphene channel region is exposed and is not obscured by gate dielectrics or gate electrodes. Graphene's electrical properties are also extremely sensitive to changes in its chemical environment [60, 7]. This allows for exposure of the graphene surface to liquids and gases that can electrically modulate the graphene surface to result in changes in its electrical characteristics and properties.

The main limiting factor for gFETs is the lack of band gap. For traditional MOSFETs, silicon has a band gap of ≈ 1.12 eV at room temperature [61]. This means that there is a well-defined 'off-state' for when the silicon channel does not conduct. Graphene's zero band gap implies that it has no true 'off-state' due to the constant conduction and as a result it is not suitable to replace silicon in logic applications without modification [62]. To overcome this, graphene can undergo band gap opening by mechanical strain, lateral confinement and chemical doping, reaching values in the range of 450 meV [63, 64, 65, 66]. An additional drawback to back-gated gFETs using Si/SiO_2 is the dramatic reduction of mobility after graphene transfer as a result of charge carrier scattering from trapped charges and impurities at the graphene/SiO_2 interface. To compensate, back-gated gFETs using suspended graphene has been reported to show mobilities as high as 200000 $cm^2\ V^{-1}\ s^{-1}$ by K. Bolotin et al. [44] but are obviously limited by the dielectric breakdown of air at low voltages.

In summary, gFETs as substitutes for the classic silicon-based MOSFET is promising. Back-gated devices have been made using conventional photolithography techniques similar to MOSFET fabrication [41, 59] and take advantage of the range of techniques available for graphene synthesis as discussed in the previous chapter. Although gFETs may not exhibit the desired properties for logic applications due to graphene's zero band gap, other applications, based on graphene's sensitivity to extrinsic charges and chemical modification, make gFETs an obvious choice for bio- or chemical sensors.

3.1.2 Designs and Applications

Back-gated gFETs offer an exposed graphene surface for chemical modification and are only one type of gFET design. Others include top-gated and dual-gated devices as shown in figure 3.2. As mentioned, although back-gate gFETs are easily fabricated, they often suffer from low mobility and the SiO_2 is also limited by its breakdown voltages, which can be overcome by thick oxide layers but increases overall device size. Suspended graphene FETs have also been reported but require complex fabrication methods with questionable device yield. As an alternative, top-

gate gFETs can be fabricated with high dielectric constant (high-κ) solid dielectrics as well as electrolyte solutions, polymer-based electrolytes and ionic gels [67, 68, 69, 70].

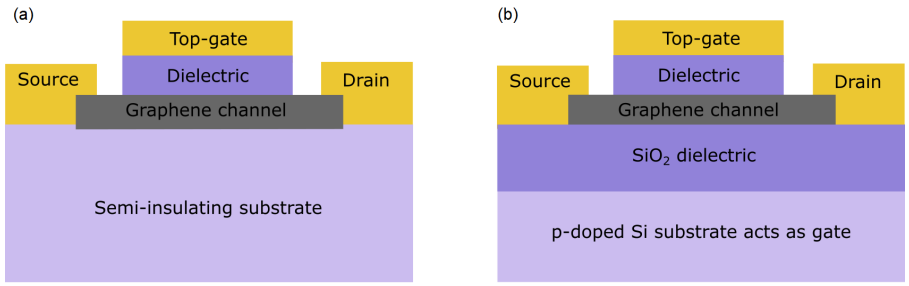

Figure 3.2: Schematic representation of a (a)top-gate gFET with a semi-insulating substrate instead of Si/SiO_2 and (b) dual-gate gFET with a top gate electrode and dielectric and Si/SiO_2 substrate.

By using a top-gated structure, new opportunities for the choice of substrate material become available as these are no longer limited to conductive semiconductors. In back-gated FETs the choice of a silicon substrate, whilst being a well-known and characterised material, produces an opaque, rigid FET structure. For many applications, the move to both flexible and transparent devices has huge implications in optoelectronics, biosensors, pressure sensors and wearable devices [71, 72, 73]. For example, Y. H. Kwak et al. [74] successfully demonstrated a sensitive gFET-based glucose sensor with detection limits of 3.3 – 10.9 mM, which correspond to clinically relevant glucose concentrations. By taking advantage of graphene's mechanical properties, the sensor still showed sensitive responses to glucose upon device bending, proving its potential for easy integration into wearable electronics to give real-time diagnostic information [74].

Both top-gated and back-gate gFETs have been proven to show excellent capabilities for a variety of applications and have been fabricated with a wide range of materials. However, despite similar fabrication methods and design, the dual-gated structure (figure 3.2(b)) has not been extensively studied. Most literature using this design shows the operation of a gFET with two independent gate electrodes to report the dual-operation of the gFET but rarely report the symmetric and simultaneous application of an electric field [75, 76]. It is believed that gFETs designed with this geometry could use the simultaneous field application to further enhance

capabilities such as channel transconductance [76].

Graphene's potential for electronic devices in place of conventional silicon-based MOSFETs is on the rise and different device geometries and smart material choices can be made for the dielectrics to improve performance. For biosensors, the choice of graphene for its electronic sensitivity has proven successful in many cases. Of course, each device has some drawbacks but by tailoring these for the specific needs of the sensor, the gFET becomes a remarkably diverse device. One also has the choice between different graphene fabrication methods, as discussed in section 2.2 and this, as well as the device geometry, will have some effect on the gFET capabilities. It is worth noting that when comparing literature concerning biosensing, in particular where sensitivities and limits of detection are often used to quantify device performance, the tailorability of these devices may make these figures-of-merit hard to compare. This is discussed in detail concerning biosensing using gFETs in chapter 4.

3.1.3 Solution Top-Gated gFETs

Top-gated gFETs have been designed using different materials for the solid top-gate dielectric, however, liquid or solution top-gates have also been implemented for gFET devices. Particularly in the field of biosensing, this is an efficient way of applying electrical gating whilst allowing the sensor to operate in an aqueous environment, which is necessary for the detection of biomolecules such as cells or single proteins. The use of a solution as the dielectric layer also allows for integration into flexible and transparent substrates, as mentioned in the previous section, and microfluidics for high-throughput lab-on-chip devices.

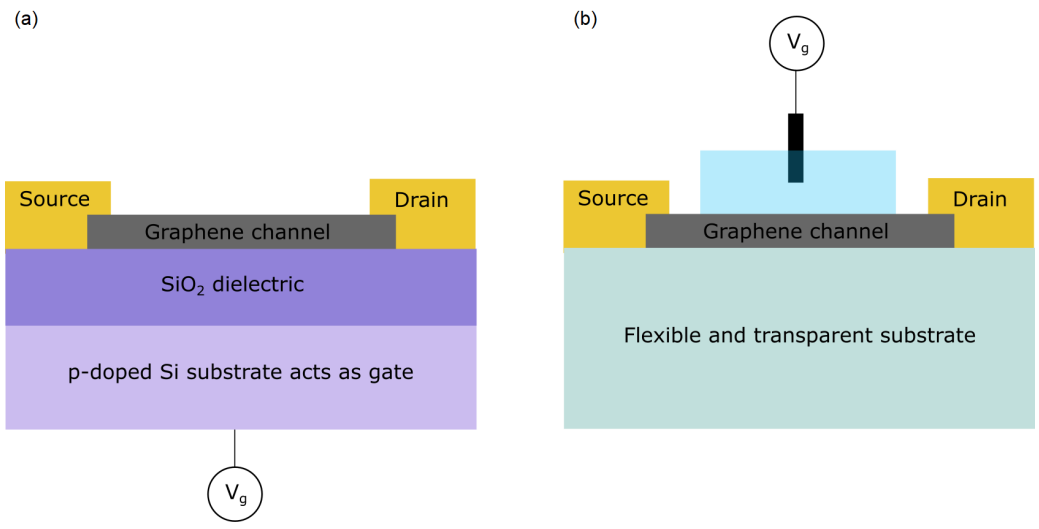

Figure 3.3: Schematic representation of (a) a typical back-gated gFET on a SiO_2/Si substrate with application of V_g through the conductive silicon and (b) an example of a solution top-gated gFET on a flexible and transparent substrate with application of V_g through an electrochemical electrode.

The main difference between the back-gated and solution top-gated gFET is illustrated in figure 3.3. In figure 3.3(a), V_g is often applied through the conductive silicon substrate or a metallised electrode, however in 3.3(b), this is done through a chemically stable reference electrode immersed in the solution, conventionally confined within a reservoir or microfluidic channel chamber [7]. The application of V_g results in the accumulation of ions at the solid/liquid interface, which creates a double ion layer known as an 'electrical double layer' (EDL) [77]. The distribution of ions is governed by the sign of V_g applied but in all cases results in a double-layer capacitance [7]. The thickness of the EDL (known as the Debye length, d) is determined by the ionic strength in the solution. For high ionic concentrations such as concentrated salt solutions, this is usually in the range of 1 nm, which essentially acts as an extremely thin dielectric layer. For back-gated gFETs, the EDL does indeed form as well and the Debye length must be considered for screening effects, however the liquid itself is not used to apply the gating. As the thickness of the dielectric layer is greatly reduced for solution-gated FETs (in comparison to $>$ 10 nm thicknesses in back-gated gFETs [78, 79]) to generate the same electric field, a much smaller V_g can be applied. Equation 3.1 describes the effect of the thickness of the

dielectric layer, t, on the electric field, E (when the gFET is modelled with uniform field). For a 300 nm SiO_2, a V_g of 100 V results in $E \approx 3 \times 10^8$ V m^{-1}, whereas for an electrolyte solution top-gate, assuming physiological conditions where $t \approx 1$ nm, the same field is generated for $V_g = 0.3$ V.

$$E = \frac{V_g}{t} \tag{3.1}$$

For solution top-gated sensors, in general, the Debye length is a key parameter in determining its operation and sensitivity. The EDL is formed as ions in a liquid arrange close to a charged material surface and hence causes a potential gradient. The charges are not uniformly distributed and as a result diffuse into the bulk liquid away from the charged material surface. Of course, this also forms at the gate electrode/electrolyte interface for top-gated electrolyte gFETs. The EDL itself and how the charges are distributed next to a charged surface can be described by the Gouy-Chapman Stern model, discussed in the following section.

3.2 The Electrical Double Layer (EDL)

3.2.1 Distribution of Ions in the EDL

If a material surface is exposed to an electrolyte solution, charge will accumulate at this surface. The way the charges distribute close to this interface is described by the EDL. A known model used to describe the charge distribution when a charged electrode is brought into contact with an electrolyte solution is the Gouy-Chapman Stern model and is depicted by figure 3.4(a). In this case, the electrode is negatively charged so positive charge in the electrolyte solution accumulates at the surface.

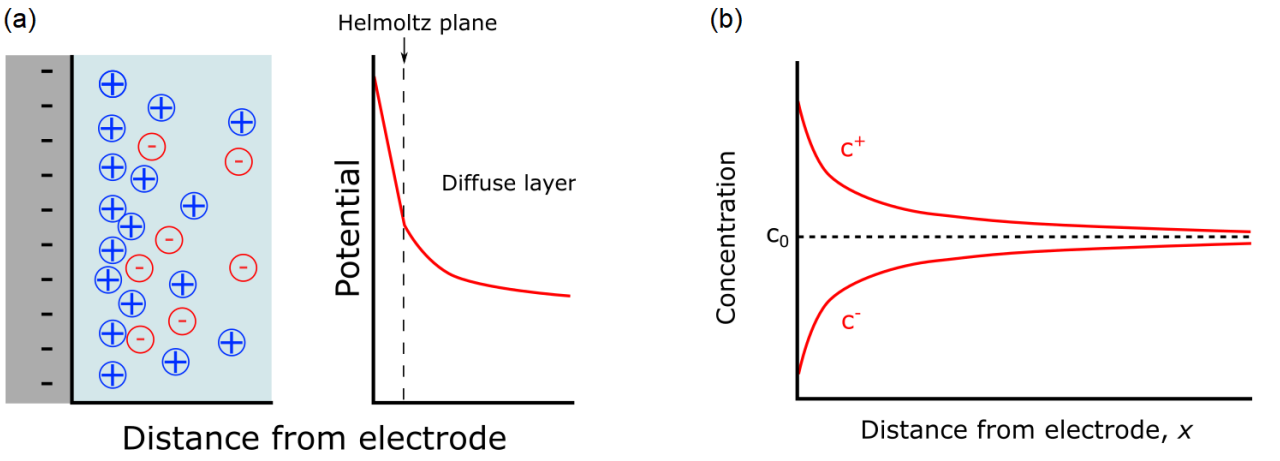

Figure 3.4: (a) A simplified schematic representation of the EDL above an electrode/electrolyte interface upon an applied bias and the resulting net charge as a function of distance away from the electrode surface as modelled by the Gouy-Chapman-Stern model. (b) The change in ionic concentration with distance away from the electrode surface, x, where c_0 is the bulk concentration and c^+ and c^- are the concentration of positive and negative ions, respectively.

If an electrode is under bias such that all accumulated charge resides at its surface, a layer of ions in the electrolyte solution occupy a plane, a distance d_H away from its surface. This layer of ions was first postulated Heltmoltz and can be modelled by a parallel plate capacitor, where the Helmholtz capacitance, C_H, is given by equation 3.2 and is dependent only on the electrolyte relative permittivity, ϵ_r, permittivity of free space, ϵ_0, d_H and area, A. In figure 3.4(a), a negatively charged electrode causes the accumulation of positive ions from the solution close to the surface. Negative ions are repelled and hence there is a lesser number of negative ions at the surface.

$$C_H = \frac{\epsilon_r \epsilon_0 A}{d_H} \tag{3.2}$$

As the distance from the electrode increases, a diffuse layer of ions is present due to the competing effects of molecular diffusion, which acts to evenly distribute positive and negative ions, and electrostatic forces, which act to separate them. This layer is therefore known as the diffuse layer. The distribution of charges from the electrode surface can be interpreted by

using Maxwell-Boltzmann statistics, which results in the dependence of the concentration of the ith ionic species, c^i, on the electrostatic potential difference, ϕ. The Poisson – Boltzmann equations state that the electrostatic potential difference, ϕ, decays exponentially from the electrode surface with respect to the potential of the bulk solution, ϕ^0. Instead of solving rigorously, the Debye – Huckel approximation provides a solution for this for small distances. The resulting relation of ϕ with distance from the electrode surface, x, for a binary electrolyte with positive ions with valency $+z$and negative ions with valency -z($+z$:-z) is given by equation 3.3. This then describes the exponential potential drop observed in figure 3.4(a) with x.

$$\phi = \phi^0.exp^{-\kappa x} \tag{3.3}$$

Here, κ has the dimension length^{-1}. $1/\kappa$ is the distance at which the potential has dropped to 0.36 of its value at the surface and is defined as the thickness of the diffuse layer of ions, or the Debye length, d. Equation 3.4 is derived from the differential of equation 3.3 in terms of x.

$$\kappa = \sqrt{\frac{2e^2z^2cN_A}{\epsilon_r\epsilon_0k_BT}} \tag{3.4}$$

The dependence of c^i on ϕ gives equation 3.5, where the concentration of the ith ionic species in the bulk solution is c_0^i, z_i is the valency of the charged species, e is the charge on an electron, k_B is Boltzmann's constant and T is the temperature.

$$c^i = c_0^i.exp^{(\frac{-z_ie\phi}{k_BT})} \tag{3.5}$$

Equations 3.3 and 3.5 therefore dictate that at an infinite distance away from the charged electrode surface, $\phi = 0$ and as a result, c^i is equal to that of the bulk solution. However, closer to the electrode surface, $\phi \neq 0$, hence c_i deviates from c_0^i. This dependence of concentration on x and ϕ is for the case of figure 3.4(a) and is illustrated in figure 3.4(b).

In the case where the electrolyte solution is asymmetric, the z^2c in equation 3.4 is replaced

with the expression for the ionic strength of the solution, I, which is a function of all ionic components of the solution [80].

$$I = 0.5 \sum_{i}^{N} c_i z_i^2 \tag{3.6}$$

3.2.2 Implications for Biosensors

Figure 3.5(a) shows the formation of the EDL close to the graphene surface and shows how the charge diffuses away from the interface. For biosensors, the EDL and corresponding Debye length is an important factor that determines the sensor's ability to detect target molecules. Most are based on planar designs where a flat surface is exposed to a liquid containing the target. If the target is present at a distance from the sensing material surface at a length greater than the Debye length, the target is electrically screened and its electronic effect on the sensing material is not detected [4, 81]. This is likely to occur in two possible scenarios as illustrated in figure 3.5(b): (i) by having a short Debye length from a high ionic buffer concentration or (ii) having long probe molecules (specific capture molecules) that extend outside of the Debye length, or of course a combination of the two. To overcome this, planar biosensors carefully consider the ionic concentration and/or the probe molecule length. For example, to shorten probe lengths, aptamers are often employed instead of larger antibodies to specifically capture the target [82]. H. So et al. [83] has employed this strategy to detect the protein, thrombin using anti-thrombin aptamers with 1 - 2 nm size. If the specific naturally occurring antibody was used, its large size of 10 nm would greatly exceed the Debye length of 3 nm (using a 10 mM buffer electrolyte) [83]. Hence by using a shorter aptamer, the recognition events between the anti-thrombin and thrombin target would occur within the Debye length and hence cause a change to the sensor's electrical properties.

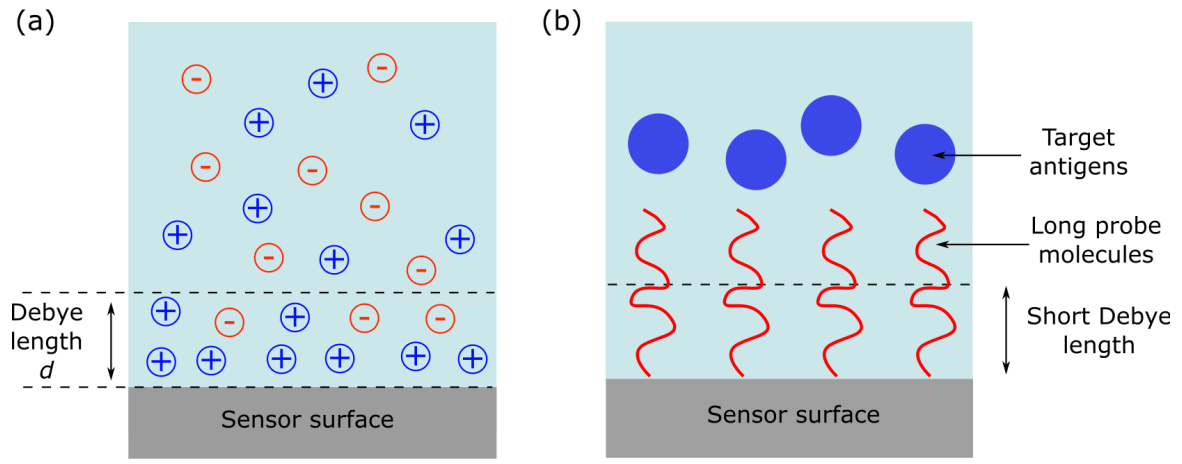

Figure 3.5: (a) A simplified schematic representation of the EDL and Debye length above the graphene/electrolyte interface upon an applied bias and accumulation of positive charge at the interface and (b) schematic representation of the screening of target molecules by a biosensor surface due to short Debye length and long probe molecules.

An interesting approach to minimising the molecular probe length was employed by J. Kim et al. [84] by using enzyme-cleaved antibody-binding fragments present at the very tips of the "Y"-shaped antibody. As it is only the antibody-binding fragments that are responsible for the binding to targets, this greatly shortens the length of the overall probe [84]. As antibody-target binding then occurs within the Debye length, J. Kim et al. were able to greatly increase the sensitivity of the device to immunoglobulin G from 1000 ng/mL to 1 pg/ml. Similar work has been done by S. Cheng et al. [85] whereby an antibody fragment lowered the detection limit of a tumour marker from 10 ng/mL to 100 pg/mL for a 3-aminopropyltriethixysilane FET biosensor due to lower charge screening effects. From both examples, a significant improvement on the limit detection was seen purely by choosing shorter probes, which only highlight the importance of being aware of the Debye length for the specific sensor system.

As mentioned, the alternative approach is to reduce the ionic concentration of the buffer solution to increase the Debye length. This therefore reduces the limitations on the probe molecules. E. Stern et al. [86] demonstrated a decreasing device sensitivity to streptavidin for a silicon nanowire FET with increasing concentration of phosphate buffered saline (PBS). As the PBS concentration was increased between 0.01 - 1× PBS, the Debye length increased from 0.7 to

7.3 nm, respectively. At the highest ionic concentration, and therefore shortest Debye length, most of the streptavidin charge is screened and the measured I_{ds} signal returns to the baseline value close to that of when no streptavidin is present [86].

Drawbacks to the approach of using low ionic concentrations obviously include the loss of stability of both the target molecules and binding antibody due to non-physiological conditions [87]. Similarly, the desire to not be limited by the probe molecules has led to advances in the structural design of the sensor such as changes to the surface topology to enhance device performance against screening effects or also using alternating - currents (AC) [4, 87]. In the former case, by using a nanoporous zinc oxide surface as the active region for sensing, R. Muje et al. [4] demonstrated the enhancement of the device sensitivity to the target protein due to the generation of a non-Faradaic capacitance at the EDL. The clever design of the nanoporous structure allows for physical confinement of the target molecule for a higher chance of capture probability and overall interaction with the sensor surface, which increases the likelihood of charge transfer. Additionally, by creating a structure such that the walls of the nanopores are at a length scale comparable to the Debye length, as illustrated in figure 3.6, a region of overlapping EDLs is formed, which can result in the enhancement of charge sensitivity of the sensor and help to overcome screening effects that arise from high ionic concentrations [88].

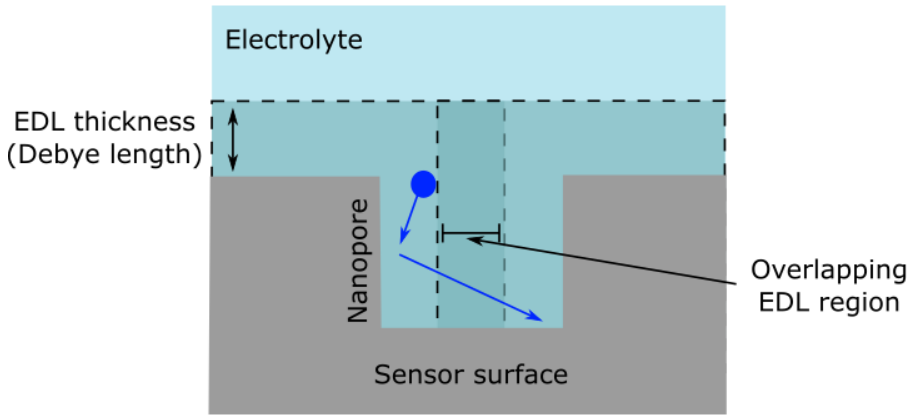

Figure 3.6: Schematic representation of a sensor's nanopore, as part of a nanotextured surface, and interface with an electrolyte with the resulting EDL and Debye length. The nanopore helps to confine the target particle (blue) and hence encourages its path to remain close to the sensor surface. Additionally, the length scale of the nanopore causes overlap of the EDL regions within the nanopore. Reproduced from [88].

Often the combination of the influence of the EDL and the gFET design must be considered alongside the graphene fabrication method. For example, both J. Ping et al. [41] and S. Xu et al. [40] used μm^2 size CVD graphene and subsequently use non-covalent functionalisation to permanently attach probe DNA to the graphene surface. J. Ping et al. detected DNA to 10 fM, several orders of magnitude lower than S. Xu et al. Other than the preparation methods, the difference in sensing mechanism can be found in the measurement geometry of the FET devices. For S. Xu et al., an electrolyte top gate was used with $0.01\times$ PBS to ensure minimal screening. This low concentration ensures a large enough Debye length such that the DNA bound to the probe DNA on the surface is detected. For J. Ping et al. a Si global back gate was used with 300 nm thermally grown SiO_2, which uses a much larger V_g measurement range. By using a global back gate, a larger V_g is applied through the substrate and an electrolyte (or ionic solution) is no longer needed, hence DNA was introduced to the sensor surface in DI water. As DI water is used, there is already a much lower concentration of ions present than in PBS, which would increase the Debye length. This would perhaps give higher device sensitivity as a larger Debye length means charges can be further from the sensor surface without being screened.

3.3 Summary

Graphene has been shown to be an effective alternative material for the replacement of traditional silicon-based FETs for certain applications. The key strength of the FET is the tailorability of every component, which enables a wide variety of options for device design in terms of gate geometry. For graphene, by taking advantage of its ability to be transferred onto a range of substrates and its optical and electronic properties, devices such as biosensors and optical sensors are easily fabricated and can result in flexible and transparent designs for applications in medical diagnostics and wearable technology. Features such as the gate material and substrate material have been explored to further optimize the gFET. This has led to significant advancements such as biosensors that can sense target molecules down to pg/mL concentrations

by implementing solution gates, which combine the need for biosensors to operate in solution and removes the need for conductive, rigid substrates by applying gate voltages through a gate dielectric formed by the EDL.

For the EDL, its formation is key to understanding the principle of operation of a biosensor and factors such as the ionic concentration gives an indication of its thickness above the sensing material/electrolyte interface. When the EDL forms a big problem associated with the design is the effect of charge screening, which limits device performance. This poses a significant issue for use in biosensing as the Debye length controls the maximum length away from the sensor surface within which it is able to detect charged species. Several different strategies can be employed to overcome this and their effectiveness and which is employed is ultimately governed by the nature of the system. For example, the Debye length cannot be trivially overcome by choosing a different probe for a specific target if few are available. Likewise, if a protein's stability is highly dependent on the buffer concentration, decreasing this may result in structural degradation or denaturing of the target. These features, as well as fabrication methods mentioned in chapter 2 must be taken into account when designing a gFET biosensor and one must be clever with their choices in order to optimize sensitivity without compromising any one of these key factors.

Chapter 4

Biosensing Using Graphene

This chapter will outline key literature concerning using graphene and gFETs for biosensing. GFETs have so far been used as biosensors for a range of disease biomarkers [89, 90, 8, 10], all of which use specific functionalisation and chemical modification methods to make the sensor surface suitable for target capture. Once a target molecule is successfully captured on the sensor surface, a change in electronic signal can indicate its presence; for gFETs this is seen in changes to the electrical characteristics that reflect certain changes to graphene's electrical properties such as the effect of chemical doping. In this chapter, some of these chemical modification routes will be discussed and compared as well as some of the governing mechanisms behind sensing.

4.1 Chemical Modification

As-fabricated graphene can't specifically detect target biomolecules. Indeed, biomolecules such as proteins will tend to non-specifically and spontaneously adsorb onto the graphene surface due to hydrophobic-hydrophobic interactions [91, 92]. However, in the case of liquid biopsies, often many different proteins are present and ensuring only one protein is responsible for a certain electronic read-out requires specific functionalisation. However, as specific probe molecules

are often biomolecules themselves with no available groups to directly bond to graphene, intermediate linker molecules are necessary to act as an anchor for these probe molecules to the graphene surface, which are often single organic molecules that can arrange on the graphene surface as a self-assembled monolayer (SAM).

4.1.1 Covalent and Non-Covalent Functionalisation

Chemical modification of graphene has been previously reported with a number of different molecules which fall into two categories: (i) non-covalent, which utilises the physisorption of molecules on graphene's basal plane and (ii) covalent modification, which sometimes takes advantage of the oxygen containing groups present at the graphene surface and/or edges [93]. Such methods induce chemical doping of graphene due to the introduction of either donor or acceptor levels, hence increasing the charge carrier concentration and changing the electronic transport properties.

A range of biomolecules have been analysed for the sensing capabilities of graphene each with their tailored method of functionalisation. Covalent modification lies mostly with the use of diazonium salts as linker molecules [94, 55] which covalently bind to sites on the surface and disrupt the sp^2 hybridisation. Again, such methods are largely based on work produced on SWCNT functionalisation using diazonium salts due to similarities in surface chemistry. For example, functionalisation with 4-nitrophenyl diazonium tetrafluoroborate (4-NPD) has been successful on both SWCNTs and graphene as shown by J. L. Bahr and G. L. C. Paulus et al., respectively [95, 96]. The general mechanism for grafting these types of molecules onto graphene involves a delocalised electron that is transferred from the graphene to the aryl diazonium cation, which becomes an aryl radical after releasing a molecule of N_2 [96]. The aryl radical then forms a covalent bond with a carbon atom in the graphene lattice as shown in figure 4.1.

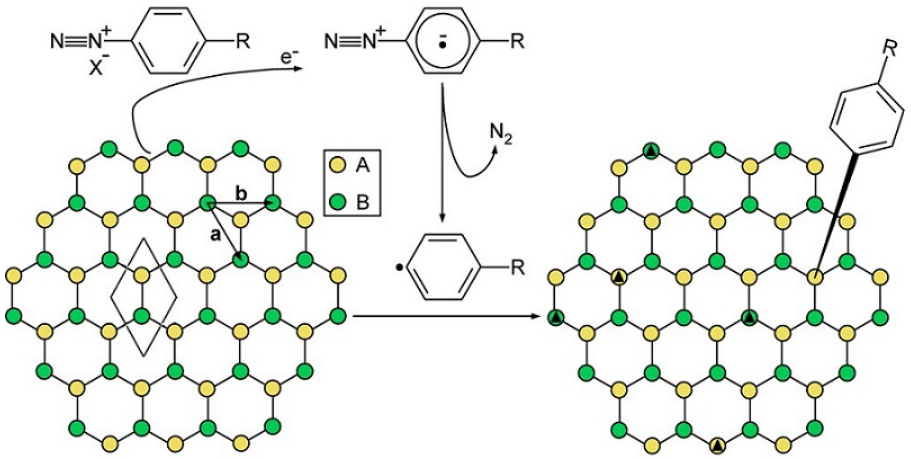

Figure 4.1: Schematic representation of the electrografting procedure between a diazonium salt onto graphene, where R is the functional group and X^- is the necessary counter ion. The graphene is made up of two carbon atoms (in the A and B sublattices) with unit cell outlined by the diamond and with lattice vectors **a** and **b**. Black triangles show the thermodynamically favourable locations for further aryl grafting. From [96].

The majority of work performed using covalent methods base their sensing capability on the charge transfer between the graphene and linker molecule from which conductivity changes can be measured. In the majority of cases, as the covalent bond formation requires the transition between sp^2 to sp^3-hybridisation in the graphene, electrochemical methods are employed to attach the linker molecule to the graphene surface. Z. Tehrani et al. [55] and S. Eissa et al. [94] both used covalent functionalisation to investigate the viability of a cancer-risk biomarker and investigate a graphene-based sensor for ovalbumin, respectively. Their general schemes follow the same principle: a graphene-based device is prepared, functionalised with diazonium salt, further functionalised with specific antibodies and finally assessed by introducing the target molecule and investigating conductivity changes. In both cases, the diazonium salt is electrochemically reduced to produce an aromatic radical that is free to bond to the graphene [97]. As a result of the bond formation, the graphene becomes increasingly p-doped with functionalisation [96].

The advantage of this functionalisation technique is the stability of the bond. As the groups are strongly attached, they are not easily removed even by vigorous ultrasonic rinsing [98]. Ad-

ditionally, the electrochemical reduction and electrografting of the diazonium salt to graphene electrodes is commonly performed under an electrochemical 3-electrode cell whereby the process is monitored using cyclic voltammetry (CV). A reduction peak in the resulting cyclic voltammogram indicates the reduction process and the depletion of this peak typically signifies the termination of the reaction, which can be interpreted as full coverage of the graphene with aryl groups or the reaching of an equilibrium for the reaction [97]. Covalent bonding is sometimes also preferred because it disrupts the original graphene structure: as well as being more robust, the covalent bonding leads to stronger changes in the electrical properties due to the formation of defects in the lattice, which are clearly observed through use of Raman spectroscopy and X-ray photoelectron spectroscopy (XPS) [99, 100, 39].

Despite these benefits of covalent functionalisation, with applications for gFET sensors, many tend to take a non-covalent functionalisation approach. Biosensors based on covalent functionalisation for the specific capture of target biomolecules tend to use electrochemical detection techniques such as CV or electrochemical impedance spectroscopy (EIS), the latter of which is widely used for the monitoring of the interfacial properties of electrode surfaces upon chemical modification [94, 101]. As these molecules affect the graphene's electrical and structural properties so strongly, non-covalent functionalisation is sometimes preferred.

Non-covalent approaches mostly consist of the physical interaction between a pyrene-based molecule and graphene sheet. The bonding consists of the π-stacking between aromatic rings and graphene, similar to the interactions between graphene sheets in bi- and multilayer graphene. For biosensing applications, the most prominent non-covalent interaction used is π - π stacking between the graphene and aromatic linker molecules and these will be predominantly discussed.

For π - π interactions to exist, two prevalent requirements must be met: the first is the existence of π systems, and the second relates to the geometry of the systems involved. Due to nature of these interactions, they are mostly favoured when both systems are highly planar [102]. Pristine monolayer graphene has a rich extended aromatic system with almost planar geometry, hence, when brought into contact with small aromatic molecules, is likely to result in strong π - π interactions. As the free surface available on pristine monolayer graphene is high for the

aromatic molecules, strong non-covalent bonds are expected as a result [102]. Similar to covalent methods, non-covalent functionalisation will also contribute to the modulation of the graphene's properties such as the charge carrier mobility and density [103]. The specifics lie with the molecule itself, for example when an electron-rich system interacts with one which is electron-deficient, negative charge is transferred. Figure 4.2 shows just a few aromatic compounds that have been employed thus far for non-covalent functionalisation on graphene.

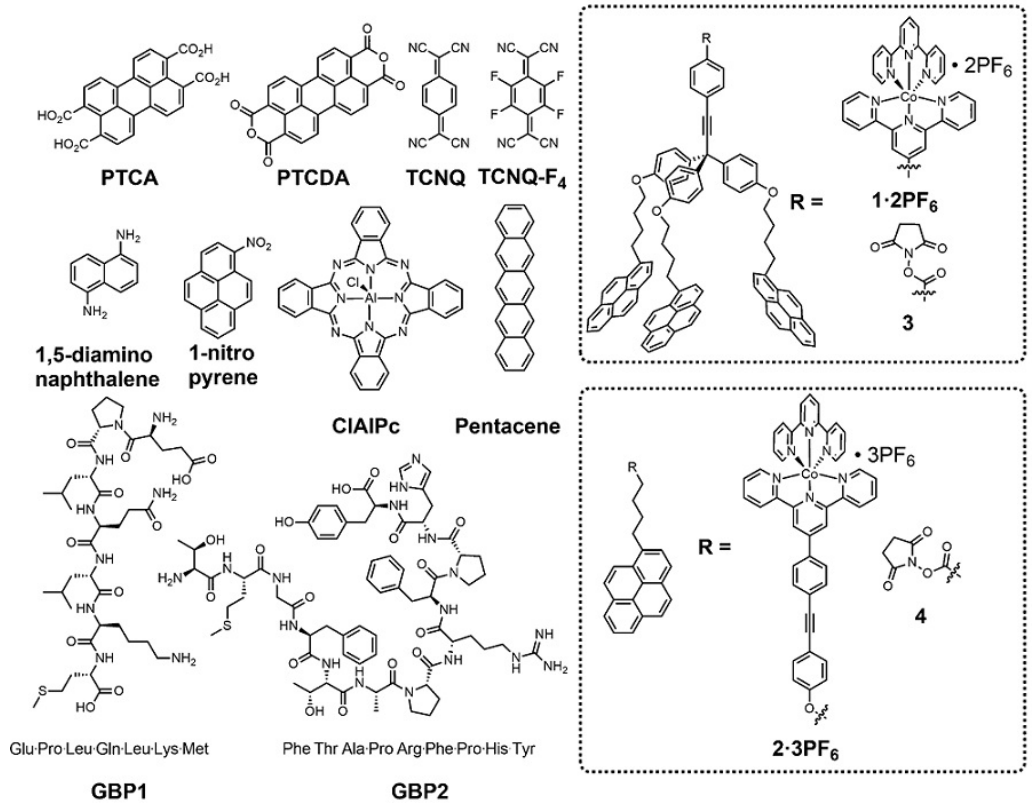

Figure 4.2: Aromatic molecular adsorbates that have been used to demonstrate non-covalent functionalisation on graphene. From [103].

The electrical effect of molecular adsorbates based on aromatic structures on graphene has been demonstrated both theoretically and experimentally [104, 105, 106]. H. Cheng et al. [106] used two aromatic molecules: 1,5-diaminonaphthalene (an n-type dopant) and 1-nitropyrene (a p-type dopant) and deposited these on selective regions of a single monolayer graphene device. By monotiring the I_{ds} - V_g transfer characteristic, it was shown that the n-doping by 1,5-diaminonaphthalene and p-doping by 1-nitropyrene resulted in a left-shift and right-shift of

the Dirac point, respectively.

Non-covalent methods of surface modification have been successful but for biosensing the choice of molecule must be more specific. The linker molecule must have dual-functionality in order to π-stack onto the graphene but also offer functional groups that can conjugate to biological probe molecules such as antibodies or aptamers. As a result, the options for biosensing must be carefully chosen. J. Mann et al. [107] presented a tripod-like linker derived from a pyrene structure. The pyrene itself consists of 4 aromatic rings that are able to spontaneously π stack to graphene; having 3 to form the base of the tripod linker ensures that the bond to graphene, although non-covalent, remains strong. The other end of the linker offers an N-hydroxysuccinimide (NHS), which is a functional group often used for the conjugation of antibodies [108]. These structures resulted in the formation of a monolayer linker layer that subsequently caused the successful conjugation of anti-E. coli antibody and the detection of E. coli to a detection limit of 7.8×10^5 cells cm^{-2}. However, one must also consider the limitation of the Debye length as discussed in section 3.2 for biosensors. If used for application in gFET biosensors, the choice of the linker molecule (whether covalent or non-covalent) is limited by its length. If the sensor works under high ionic concentration and the length of the linker exceeds the Debye length, the sensitivity of the sensor to the target molecules is lost. Additionally, the linker must be controlled and terminated as a monolayer for the same reason.

4.1.2 PBASE Properties

The most prevalent molecule that takes these factors into account for use in gFET biosensor applications is 1-pyrenebutyric acid N-hydroxy succinimide ester (PBASE) illustrated in figure 4.3. PBASE itself is an example of a small, pyrene-based aromatic molecule that can be used for non-covalent functionalisation onto graphene surfaces. A benefit to its use is its self-limiting nature, meaning only SAMs should form. Multilayer formation from the SAM is suppressed as the pyrene group is only able to stack parallel to the graphene plane and is blocked by doing so by the NHS functional group. Again, the presence of the NHS also allows for antibody

conjugation.

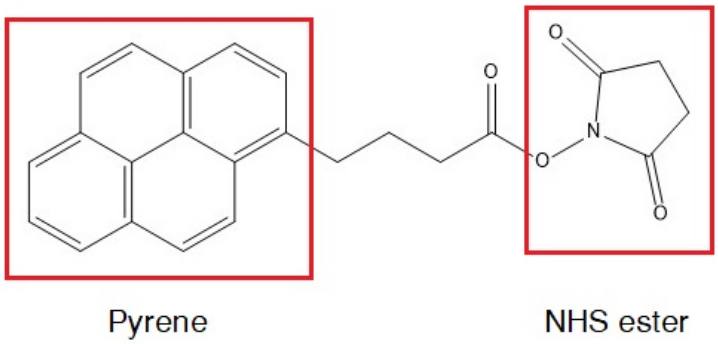

Figure 4.3: Molecular structure of a PBASE molecules. The red boxes highlight the pyrene group and NHS ester.

The pyrene group, being highly aromatic in nature is known to interact strongly with the basal plane of graphite via π - π stacking and was first used for the non-covalent functionalisation of SWCNTs for electrical biosensing [109, 110]. The other side of the molecule contains the NHS ester, which reacts by nucleophilic substitution to primary and secondary amines that exist in abundance on the surface of antibodies. By using PBASE, antibodies retain functionality and conformation when conjugated as opposed to when they non-specifically adsorb on the surface without a linker.

A noticeable lack of literature revolves around the surface coverage of PBASE molecules on carbon-based materials. Although it is relatively easy to determine PBASE's presence through techniques such as electrical measurements, XPS or AFM [41, 111], such methods are difficult to use to get a visual idea of the homogeneity of the adsorbants. PBASE molecules can be used to conjugate antibodies with fluorescent labels for imaging, however for this it is assumed that each PBASE molecule binds an antibody. In reality, complex situations occur for imaging the labelled antibodies: if not many antibodies fluoresce, there may either not be much PBASE present on the surface or there may be many unreacted PBASE molecules present, in which case extensive surface passivation is necessary. Hence, surface coverage is an important parameter which effects the overall device sensitivity but is difficult to quantify. Only recently

X. Zhen et al. [112] recorded the surface coverage of pyrene derived compounds on graphene using surface contact angle measurements. Here, it was shown that decreasing contact angles indicated increasing surface coverage for a range of molecules and the expected that by using a concentration of 0.30–3.6 mM, 90 % surface coverage is already achieved for the majority of these molecules [112]. This surface coverage as well as the effect of PBASE on graphene's electrical properties are further discussed in this thesis in section 7.2.1.2.

4.2 Specific Biofunctionalisation

To capture specific biological molecules such as proteins or cells, it is important to know the exact marker that must be targeted. For cells and vesicles, this is more often a transmembrane protein present in the phospholipid bilayer membrane, which is known as a surface marker. So far, gFETs have been implemented for detection of DNA, cells and viruses, some of which have already been discussed over this chapter [37, 113, 114, 89]. The aim of these devices is often a functional, medical device to be used in point-of-care diagnostics. For this to be achieved, specificity of the device is a key factor as liquid biopsies will contain a number of undesired species that will be physisorbed onto the sensor surface. To remove these either constant fluid flow is used or some form of rinsing must be employed where afterwards the target must still be present, which is possible through the use of specific probe molecules like antibodies or aptamers.

Antibodies are excellent biorecognition components that can be used for biosensors due to their exceptional specificity and high affinity for their cognate antigen [115]. Polyclonal antibodies are known as non-homogeneous antibodies with different specificity and affinity towards the same target. This is non-ideal for biosensors as each antibody conjugated to the sensor surface must have high specificity and affinity for maximum sensor sensitivity; as a result, for such applications, monoclonal antibodies have been developed. Antibodies in general are "Y"-shaped proteins that can be divided into two distinct blocks: the antigen-binding fragment (Fab) and the constant fragment (Fc) as illustrated in figure 4.4. The Fab section contains the fragment

variable (Fv) region, where the complementary-determining regions (CDRs) are found [116]. Theses CDRs are the regions that are responsible for the antibody's specificity and determine exactly what it is specific to [115].

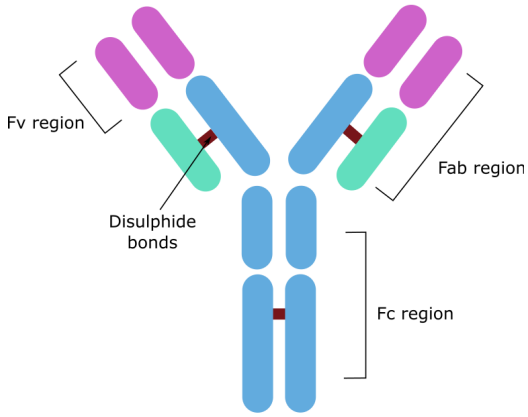

Figure 4.4: Schematic representation of the structure of an antibody with its Fab, Fc and Fv regions.

The surface of the antibody molecule formed by the conformation of the CDRs in the Fv region of antibodies creates the site to which a target binds [117]. The CDRs themselves are made up of amino acids and since these are different depending on the type of antibody, so is the shape of their surfaces. As the target molecules often varies in size from a small peptide to a protein of comparable shape to the antibody itself, the way in which it binds to the CDRs is dependent on its size and shape. The bond between the antibody and target itself is non-covalent and made up of a number of types of forces: electrostatic, hydrogen bonds, van der Waals and hydrophobic forces. The amount that each force contributes to the overall interaction also depends on the particular antibody and antigen involved. Hence, the shape, size and forces involved all contribute to the specificity of the antibody - target reaction.

Antibodies are necessary for the specificity in graphene-based biosensors and have been successfully implemented whether conjugated to covalent or non-covalent linkers [8, 118]. For example, Y. Ohno et al. [43] used a PBASE-functionalised gFET with conjugated IgE aptamer (cleaved from an IgE antibody to ensure a working length within the Debye length) to specifically capture IgE target proteins. Not only did the gFET sensor show response to the IgE protein

down to 0.29 nM but also displayed specificity as the introduction of two non-specific proteins, bovine serum albumin (BSA) and streptavidin, did not cause a significant electrical response [43]. This shows that although proving the positive result of sensing the target molecule using a conjugated antibody, to truly be viable for clinical application, the sensor must prove to be highly specific. This often requires negative controls such as using a non-binding antibody or non-specific target.

4.3 Sensing Mechanism

The working principle of gFET biosensors is not often clear as this depends on the gFET geometry and target species. When a charged biomolecule binds or comes close to a gFET sensor surface, the changes to graphene's electrical properties can be mostly described by 4 electrical effects. These are: (i) electrostatic gating, (ii) charge transfer, (iii) capacitative effects and (iv) charge impurity scattering. However, it is often very difficult to class a sensor's electrical response into only one of these groups and sometimes it is more realistic for the response to be a combination of these effects.

4.3.1 Electrostatic Gating Effect

The electrostatic gating effect by adsorbed charged species is a mechanism adopted to explain the shift in I_{ds} - V_g transfer characteristic of some gFET sensors. This theory involves the notion that the charged species adsorbed on an FET channel will induce an opposite charge within the graphene itself, thus doping via the electric field effect. The mechanism works much like gating a typical transistor and charged species act like a 'molecular gate' hence, the charged species must be separated from the channel surface to some degree.

Due to graphene's ambipolar nature, the gating effect allows it to experience both p-type and n-type doping as a result, which is observed through the shift in Dirac point. For example, when a positively charged species is present on the graphene surface, but separated by some

physical distance, the net positive charge causes negative charge to accumulate in graphene. This abundance of electrons is explained as the graphene channel being n-doped, thus causing a shift of the Dirac point to a more negative V_g. The opposite occurs for a net negative charge: graphene accumulates positive charge (holes) and the Dirac point shifts to more positive V_g. Figure 4.5 demonstrates the electrostatic gating effect where gFETs were doped using two different polyelectrolytes. Polyallylamine hydrochloride (PAH) and sodium polystyrene sulfonate (PSS) are positively and negatively charged, respectively and hence this induces the accumulation of the opposite charge in the graphene, which translates as a shift in the Dirac point on the I_{ds} - V_g transfer characteristic.

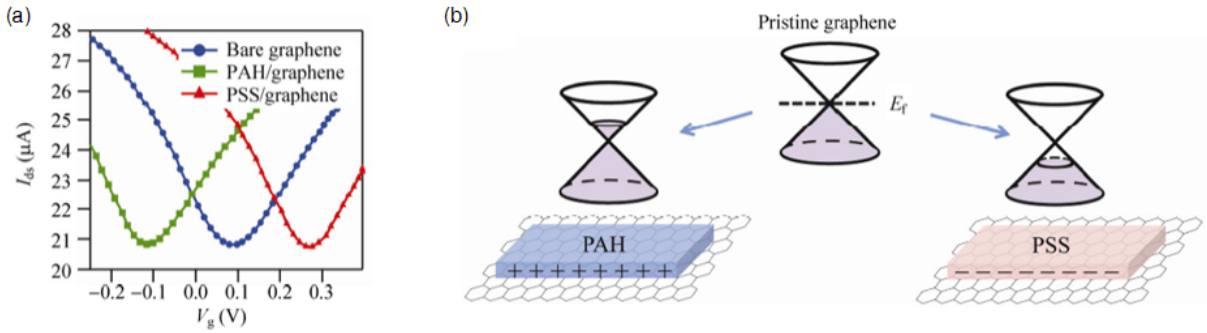

Figure 4.5: (a) I_{ds} - V_g transfer characteristics for a bare graphene gFET and with deposited polyallylamine hydrochloride (PAH) and sodium polystyrene sulfonate (PSS). (b) Schematic representation of the the resulting Fermi energy shift with the deposition of PAH and PSS on the graphene surface. Reproduced from [119].

The electrostatic gating mechanism has also been shown for the detection of negatively charged DNA using a gFET whereby the Dirac point shifted to higher V_g due to the accumulation of positive charge in the graphene [41]. However, there are results that seem to contradict this theory. For example, D. Kim et al. [120] changed the charge on a prostate specific antigen, by changing the pH of the buffer solution. By changing the pH to below the protein's isoelectric point (IEP), an excess of H^+ results in a positively charged protein. This would have an expected consequence of n-doping the graphene, however results showed a shift in the Dirac point to higher V_g (p-doping). It is for this reason that other mechanisms are considered.

4.3.2 Charge Transfer

The second mechanism for sensing is charge transfer between the target molecule and sensor material. This is contradictory to the previous theory as electrostatic gating relies on charge separation. If a species is adsorbed directly onto the graphene surface, this theory states that it is possible that the species either donates or accepts charge. For example, if a negatively charged species is adsorbed it is able to transfer excess negative charge to the graphene, thus causing the graphene to become n-doped, shifting the Dirac point to more negative V_g.

Previously, charge transfer has been shown to be the mechanism behind shifts in the charge neutrality point for a carbon nanotube (CNT) FET where proteins were adsorbed directly on the surface without linkers or specific probes [121]. Z. Hao et al. [122] have demonstrated a sensor based on charge transfer for the specific detection of insulin using a CVD graphene FET. Here, despite the physical separation of negatively charged insulin and the graphene surface by PBASE molecules and specific aptamer, an increase in insulin concentration lead to increasingly n-doped graphene. This suggests that the transfer of electrons between the insulin and graphene leads to graphene's n-doping, however by electrostatic field-gating, p-doping would occur. As there is speculated charge transfer between target molecules and graphene, efforts have also been made to determine the quantity of charge transferred [121]. For J. Lin et al. [123], the charge transfer between graphene and nucleobases on DNA were modelled using density functional theory (DFT). Here, the p-doping of graphene was proposed to be due to charge transfer from graphene to these nucleobases. However, the resulting charge was deemed too small to contribute to the experimental shift in Dirac point and to cause such a shift, an unrealistic areal density of analytes would be required. The contradicting results may suggest that the sensing mechanism is in fact dependent on the nature of the target molecule and is difficult to predict.

4.3.3 Capacitor Effects

Capacitor effects have also been investigated for electrolyte-gated FET biosensors. Sometimes charge transfer or electrostatic gating by charged biomolecules, which causes doping of the graphene, contradict each other in terms of the Dirac point shift and cannot explain features such as broadening of the I_{ds} - V_g about the Dirac point. To explain these, other effects must be considered such as the change in capacitance between the gate electrode and graphene, which can occur when biomolecules bind to the graphene surface due to the effect of their different dielectric properties relative to the electrolyte solution. This was shown by K. Besteman et al. [124] on a SWCNT FET whereby the near-full coverage of glucose oxidase from immobilization on the surface was achieved. This inhibits the ions in the electrolyte from coming close to the SWCNT surface and hence changes the dielectric constant and gate capacitance. Of course, this relies on the near-full coverage of biomolecules to inhibit permeation of ions to the sensor surface.

4.3.4 Charged - Impurity Scattering

Finally, charged-impurity scattering is another alternative mechanism but is usually coupled with effects from either charge transfer or electrostatic gating [41]. This is associated with the long-range nature of Coulomb impurities introduced with analytes on graphene. Charged impurities either in the substrate or in the vicinity of graphene create a spatially inhomogeneous potential distribution in the graphene plane which act as scattering centers. In most cases, the effect of charged impurities manifests as changes to the graphene mobility due to increased scattering, which is obvious from the shape changes to the I_{ds} - V_g transfer characteristic. This effect is typically predominant at low carrier density (therefore at the Dirac point). The spatially inhomogeneous potential results in the breaking up of the system up into puddles of electrons and holes [125] and hence determines the minimum conductivity. Therefore, this effects the conductivity and I_{ds} at the Dirac point.

The effect of charge-impurities has been widely studied regarding the effect of the dielectric

environment on graphene's electrical characteristics. The mobility-limiting factor in gFETs is known to be the Coulomb scattering of charged impurities that are present on graphene or in the underlying substrate. Hence, by placing the graphene in an environment with high dielectric constant, this screens the electric field due to the impurities and causes improvements to mobility. A likely source of impurities that contribute to scattering can be fabrication residues. By placing the graphene in different liquid environments with varying dielectric constant, the mobility of the graphene has been observed to change due to screening of these residues [126]. This has implications in biosensing since the graphene is often surrounded by polar solvents such as water or PBS. As the dielectric properties close to the graphene surface changes from the binding of target species [127], the dielectric constant is different to that in the bulk solvent, which ultimately results in mobility changes in graphene.

4.4 Summary

Biosensing using graphene has been explored for a range of different molecules. Functionalisation is used to make the graphene surface suitable for the specific detection of biomolecules using a combination of linker molecules and probe molecules such as antibodies and aptamers. For the linker molecules, either covalent or non-covalent approaches are used, the choice is often dependent on the application as this chemical modification itself causes changes to graphene's electrical properties. Of the non-covalent approaches, the most prominent molecules used in graphene biosensing literature is PBASE, which is capable of π-stacking with graphene on one end and bond to antibodies or aptamers using the NHS ester on the other. The probe molecule is the main component in the tailorability of the graphene sensor as these are used to specifically bind target molecules. For antibodies, CDR regions are responsible for specific binding. The overall, typical structure necessary for graphene biosensors is illustrated in figure 4.6. In all cases, the total length of functionalisation above the graphene surface must be considered because of the effects of the Debye length.

Furthermore, the actual sensing mechanism of gFET biosensors is largely debated. The changes

to the I_{ds} - V_g transfer characteristic are often explained through not just one mechanism but a combination. As target biomolecules bind to the sensor, the electrical properties of graphene are modified and can manifest as several changes to the I_{ds} - V_g transfer characteristic such as shifts in the Dirac point or broadening of the curve. Often, it is easier to isolate one feature of the I_{ds} - V_g transfer characteristic that consistently changes with target molecules rather than evaluate all effects as these are often also influenced by sample - to - sample variation.

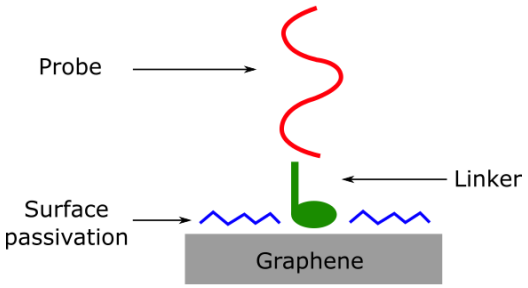

Figure 4.6: Schematic representation of the typical graphene with necessary surface functionalisation for the specific detection of target molecules.

Chapter 5

Introduction to Exosomes

5.1 Structure, Properties and Biological Role

Recently, there has been great interest in using gFETs for early diagnosis and improved prognosis of disease biomarkers. Blood circulating biomarkers, such as proteins, circulating tumour cells (CTCs) and nucleic acids, can provide valuable insight into the disease stage and progression and can be identified using a 'liquid biopsy'. Such biopsies can be taken in sub-millilitre volumes and eradicate the need for invasive surgeries that are typically undergone for tissue biopsies. Of these biomarkers, extracellular vesicles (ECVs) are gaining attention as they carry a wide variety of information derived from the cells from which they are excreted [128, 129]. As ECVs are secreted by both healthy and tumour cells [130], effective isolation and detection could lead to early-stage cancer diagnosis without the need to extract the cells themselves [131, 132]. Of these ECVs, exosomes are membrane-bound phospholipid nanoscale vesicles (of size 40 - 150 nm). They circulate in blood and other eukaryotic fluids in high numbers (10^6 – 10^{11} per mL) [11, 12], unlike other circulating biomarkers such as CTCs, which are typically found in order of 1 - 10 per mL of blood [133].

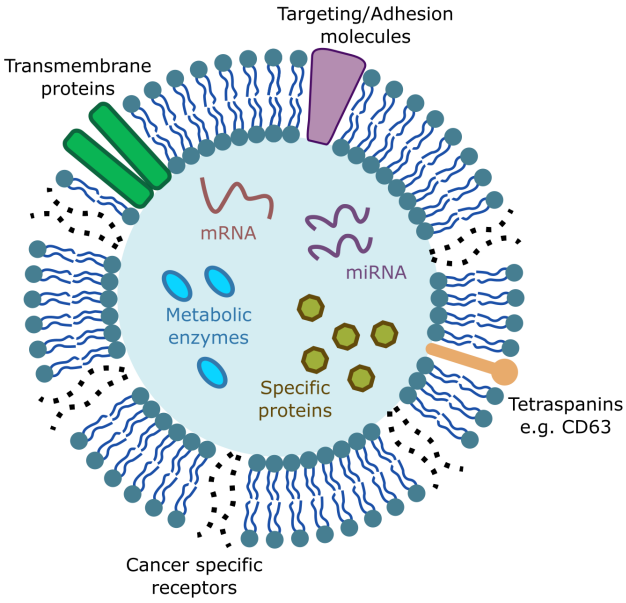

Figure 5.1: Schematic representation of the structure of an exosome showing the phospholipid bilayer, various transmembrane proteins and enclosed genetic information.

The typical structure of an exosome is shown in figure 5.1; they are released from cells during the fusion of multivesicular endosomes with the plasma membrane. As vesicles are released from a variety of eukaryotic and prokaryotic cells, most would be expected to have specialised functions depending on the cell and surrounding environment. The size and shape of cell-derived exosomes are consistent in literature with most reporting $\approx$ 100 nm diameter and cup-like shape by imaging using transmission electron microscopy and atomic force microscopy [134]. However, using only size and shape to characterise these vesicles is often non-trivial due to the adhesion of exosomes to surfaces usually causing some morphological changes, sometimes resulting in a spherical to hemispherical shape change [134].

All exosomes have a phospholipid bilayer membrane, which encapsulates the exosome's contents. One common feature that exosomes share with their parent cell is that the membrane proteins are typically in the same orientation [134]. Often these proteins are also examined to characterise exosomes and those specific to membrane transport and fusion are often identified. A common transmembrane protein to identify on exosomes is CD63, which has been used as

a target throughout this thesis: this is a protein with 4 hydrophobic, transmembrane domains and 2 extra cellular domains. These are specifically enriched in exosome membranes [135] and hence a good choice for targeting as their high density increases the likehood of binding and capture on the gFET surface.

Analogous to colloidal nanoparticles, exosomes have been characterised in terms of their surface charge by the Zeta potential [136, 137]. When present in a polar medium, exosomes will acquire a surface charge due to the arrangement of charges around the particle. In such buffers such as PBS at pH 7, this results in a negatively charged exosome [138]. In this case, by reconstitution of exosomes in an appropriate buffer medium, the negative charge exhibited could lead to the charge modulation in a graphene film when exosomes are introduced to the surface.

5.2 Importance in Cancer

Exosomes are known to aid processes such as cell-cell communication and through the distribution of molecules such as proteins and mRNA, can lead to the transmission of disease from one cell to another, hence allowing for participation in disease progression [139]. They also include surface markers and genetic information that are representative of the cells from which they originate [129]. Hence, exosome-mediated transport of cargos between cells can promote the progression and spread of cancer [140], for example by metastasis, whereby cells travel from a primary tumour site to another area of the body for cancer cell proliferation. By capturing exosomes released from tumour cells in blood, proteins and genetic information that they contain, which relate to the cell from which they are derived, can be analysed. In addition, exosomes are reported to be remarkably stable in circulation and have been located in blood, urine, saliva, breast milk and amniotic fluid [11]. So far, tumour-derived exosomes have been extracted from lung pleural effusions, ascites, and bladder cancer urine [141, 142, 129], which are all viable non-invasive accessible sources.

The isolation of exosomes for early-stage cancer diagnosis proves useful as their protein cargo is

often a positive indicator of the disease. For example, mass spectrometry has been successfully used to identify the protein cargo of pancreatic cancer exosomes and identified glypican-1 (GPC1) as a cell surface marker which is highly expressed by tumour exosomes [132]. Hence, it is agreed that being able to purify exosomes from human serum to high efficiency and with high throughput has emerged as a promising area for investigation.

By examining the exosome cargo, microRNAs (miRNA) have been identified to be enveloped within exosomes, which can be taken up by neighbouring and distant cells, and as a result, modify the recipient cells [143]. For example, K. Shimbo et al. [144] showed that exosomes released with miR-143 that were taken up by osteosarcoma cells reduced the cell migration [144]. Specific miRNAs from exosome populations have also been reported to show a correlation between their expression and tumour presence and aggression [140]. For example, S. Pfeffer et al. [145] reported higher exosomal miRNA from the plasma of patients with melanoma than control subjects. Similarly, X.Hao et al. [143] reported higher levels of miR-141 in the serum derived exosomes for patients with prostate cancer than healthy patients. In terms of the spread of cancer through the body, exosomes containing miR-23a from lung cancer cells have been shown to have a direct effect on the conditions that promote tumour angiogenesis (the formation of blood vessels). The increased level of miR-23a, was reported to cause the accumulation of hypoxia-inducible factor-1 α (HIF-1 α) in endothelial cells, where hypoxia causes favourable conditions for tumour angiogenesis [146]. Hence, an obvious benefit for the quick and efficient isolation of exosomes from liquid biopsies would be the opportunity for the analysis of cargo such as miRNA.

In addition to the internal content of exosomes, general population statistics such as exosome concentration in cancer patients has also been studied. Both J. Baran and G. Poste et al. have shown that the number of exosomes in the plasma of gastric and lung cancer patients, respectively, was higher than that of healthy patients [147, 148]. In addition, the number of exosomes released also correlated to the aggressiveness of the associated tumour. Other cancer significance of exosomes includes roles played in the transfer of chemoresitance between tumour cells and the upregulation of the programmed death-ligand 1 (which is associated with the

surpression of the immune system) for chronic lymphocytic leukemia [149, 150]. The accurate sensing of the concentration of tumour derived exosomes can hence serve as a tool for the diagnostic assessment of cancer and its stage. If this quantification is coupled with the ability to isolate and capture exosomes for further analysis of their internal cargo, exosomes prove to be a key player in the field of cancer biomarkers.

5.3 Isolation and Sensing of Exosomes

5.3.1 Exosome Isolation

A current technique for exosomes isolation from plasma and other biological fluids is ultracentrifugation. When a heterogeneous suspension is subjected to centrifugation, sedimentation of particles in the suspension according to their density, size, and shape will occur with denser and larger particulates settling out first [151]. By using ultracentifugation, suspensions can be subjected to centrifugal forces of up to 1000000 $\times$ g. The use of ultracentrifugation for exosome isolation is considered to be the gold standard of separation and is the most commonly used method to date [151]. For exosomes, the speeds used are increased in steps reaching maximum centrifugal forces of 100000 to 120000 $\times$ g [144, 152], a process that can take several hours: a limiting factor in clinical applications and an impracticality for point-of-care diagnostics. To avoid the use of time consuming methods with loss of yield, innovative isolation methods using microfluidics have been employed to sort based on size [131].

Compared to ultracentrifugation and filtration, microfluidic technology can offer fast isolation speed, high yield and efficiency of exosome isolation. Specific exosome surface markers can be taken advantage of for isolation by immunoaffinity. For example, microfluidic channels have previously been functionalised with anti-CD63 antibodies for specific capture from human serum [153]. This produced a high yield of pure exosomes from 100 – 400 µL volumes, which is more realistic for consideration in liquid biopsy implementation. This is the principle behind enzyme-linked immunosorbent assay (ELISA) methods, which have also been employed in exo-

some isolation by conjugating exosomes to primary and secondary antibodies [154], where the secondary antibody is enzyme-linked. A chemical substrate, which specifically reacts with the linked enzyme, is then added and when this reaction occurs, a colour change is observed. This colour change is hence the indication of the exosome presence. By combining this technique with microfluidics, exosomes can be rapidly isolated from small volumes without the need for labelling.

The use of microfluidic technology for the size-based sorting of exosomes was pioneered by the H. Lee et al. [131] whereby acoustic forces were combined with straight channel microfluidic chips to isolate exosomes up to a certain size cut-off. A high recovery rate (80 %) with the benefit of requiring small volumes over 10-minute run times makes it a significant improvement on ultracentrifugation in terms of clinical practicality. This technique then results in a high-throughput and rapid isolation method, which excludes the need for surface markers, specific antibodies or labelling. The interaction between a standing surface acoustic wave with the exosomes travelling through the microfluidic channel causes the lateral separation of particles such that larger particles are forced to the outer edges of the channel and smaller particles under the size cut-off are streamlined in the center as seen in figure 5.2.

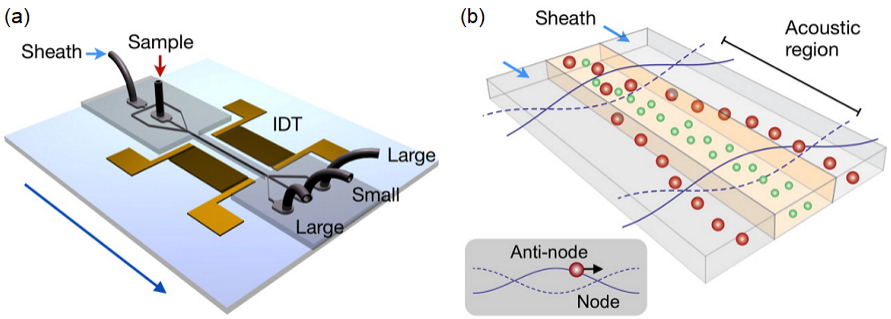

Figure 5.2: (a) Microfluidic chip with acoustic standing surface wave integration with interdigitated transducer (IDT) gold electrodes. (b) The direction of exosome and sheath flow through the microfluidic channel and interaction of the acoustic wave with particles that results in size sorting. Reproduced from [131].

Although size-based sorting seems promising, the isolation of exosomes suffers from the considerable overlap in both biochemical and physical properties between them and other types of

extracellular vesicles. For example, although the size of exosomes and apoptotic vesicles may be similar, their protein cargo would differ drastically [134]. Hence one must be extremely careful when isolating exosomes and quantifying their numbers to ensure that the type of vesicle is also specified. This implies that although size-based sorting provides many benefits, the use of labelling or specific surface markers may still be necessary for the best results in clinical applications.

5.3.2 Sensing

The challenge of exosome capture is not only limited to their isolation but also their quantification and method of detection. Conventional analysis often employs techniques such as western blot analysis or flow cytometry [155], however these again have drawbacks such as larger sample volume requirements and complex biochemical preparation. The move towards lab-on-chip devices like that of K. Lee et al. [131] has also allowed for the development of on-chip sensing systems for the sensitive detection of exosomes, such as those based on surface plasmon resonance (SPR), whereby exosomes are detected through a change in the refractive index of a medium on which they are covalently bound. This is the most prominent sensing non-labelling sensing technique for exosomes and has so far shown sensitivity down to 1000 particles/µL [156], which is reported to be orders of magnitude mores sensitive than ELISA and Western blotting techniques.

L. Zhu et al. [157] used this strategy and reported an exosome detection limit of 5 µg/mL by printing a variety of antibodies, which correspond to multiple exosome surface markers, onto a gold-coated chip over which exosomes were flowed over using a microfluidic channel. When a surface plasmon is excited through the chip using a light source, the resulting change in refractive index of the medium by bound exosomes causes a change in the excited surface plasmon and hence a change in the surface plasmon resonance angle in the reflected light. Multiple exosome surface markers were used as targets, and this further increased the capture probability as exosomes were flowed over a functionalised gold surface. By using microfluidics

and specific targeting techniques, SPR combines the benefits of small sample volumes (in this case 30 µL) and sensitive biochemical detection using multiple specific antibodies. Similarly, H. Im et al. [158] was able to reach a limit of detection of 3000 exosomes (corresponding to approximately 0.05 µg/mL) under constant flow of µL sample volumes through a microfluidic channel. By using a periodic array of nanoholes as the sensor chip, matching the size of the holes to the size of exosomes improved detection sensitivity and the measurement of the transmitted signal from SPR rather than a reflected signal like traditional SPR devices was measured. The nanoholes amplified the transmitted light which led to higher detection sensitivity. SPR for exosome sensing devices with integrated microfluidics and specific surface marker targeting is the most common method for sensitive and quantitative evaluation of exosome concentration, which could be an important diagnostic factor [159].

SPR methods for exosome detection overcome many limitations of more conventional benchtop methods. For example they utilize low sample volumes, do not require fluorescent labelling and can give results within short time-frames. In addition, they allow for multiplex sensing whereby multiple exosome markers can be targeted to increase capture probability or allow for the simultaneous capture of exosomes with different surface markers. Similarly to the development of gFET arrays, sensor chips that use SPR for exosome sensing may have the potential for wafer-scale processing. Table 5.1 summarises recent sensing devices implemented for exosomes. A major limitation for SPR methods lies with the need for gold-coated surfaces, which does not allow for the development of flexible, transparent devices. From table 5.1 the lowest reported detection limit utilises a transparent ELISA-based GO sensor, which relies on a fluorescent signal from the fluorescein produced during the enzyme-mediated process [160]. Although this no longer relies on rigid, gold surfaces, this method is still dependent on labelling and the scalability of the device for clinical application is highly questionable. In terms of exosome sensing based on surface marker capture and detection, there still lacks a device that combines a non-optic, non-labelling lab-on-chip device that takes advantage of sub-milliliter sample volumes.

Table 5.1: Table comparing current exosome sensing technologies

Device	Detection sensitivity	Detection method	Markers	Reference
SPR imaging array	5 µg/mL	SPR imaging	CD9, CD63, CD81, CD82, CD41b	[157]
nPLEX chip	1000 particles/µL	SPR on a multiplexed nanohole arrays	CD24, CA125,CA19-9, HER2, MUC18,EGFR, CLDN3, CD45,CD41, D2-40	[158]
SPR chip	7 µg/mL	SPR response over time	CD63	[159]
ExoSearch chip	750 particles/µL	Multiplexed detection using immunomagnetic beads and fluorescence imaging	CA125, EpCAM, and CD24	[161]
GO/PDA nano-IMEX	50 particles/µL	Sandwich ELISA capture	D9, CD63, CD81, EpCAM	[160]

As mentioned, the internal cargo of exosomes can give key information relating to the nature of a disease. By using the SPR methods by H. Im and L. Zhu et al. [158, 157] it would be possible to analyse the captured and quantified exosomes for cargo such as specific messenger RNA (mRNA). However, this uses two separated methods of analysis: capture and quantification then followed by mRNA isolation. H. Shao et al. [162] have developed a novel microfluidic, immunomagnetic exosomal RNA (iMER) platform for the combination of exosome enrichment and their RNA isolation on one device. Here, immunomagnetic microbeads were specifically

modified with antibodies that specifically bind to surface markers on exosomes. Once exosomes were bound to the beads, magnetic separation gave > 93 % capture efficiency. This step involves the use of the first chamber of the microfluidic chip as seen in figure 5.3. Next, the captured exosomes undergo lysis, which is the disintegration of the phospholipid bilayer membrane such that the mRNA cargo is released [163]. This is performed using a combination of lysis buffer and physical shearing of the membrane by micro-size glass beads. Finally, the isolated mRNA is reverse transcribed onto its complementary DNA (cDNA) with an attached fluorophore in a process called quantitative polymerase chain reaction (qPCR). The resulting cDNA polymerises and hence the intensity of the fluorophore increases as the reaction progresses with increased presence of cDNA.

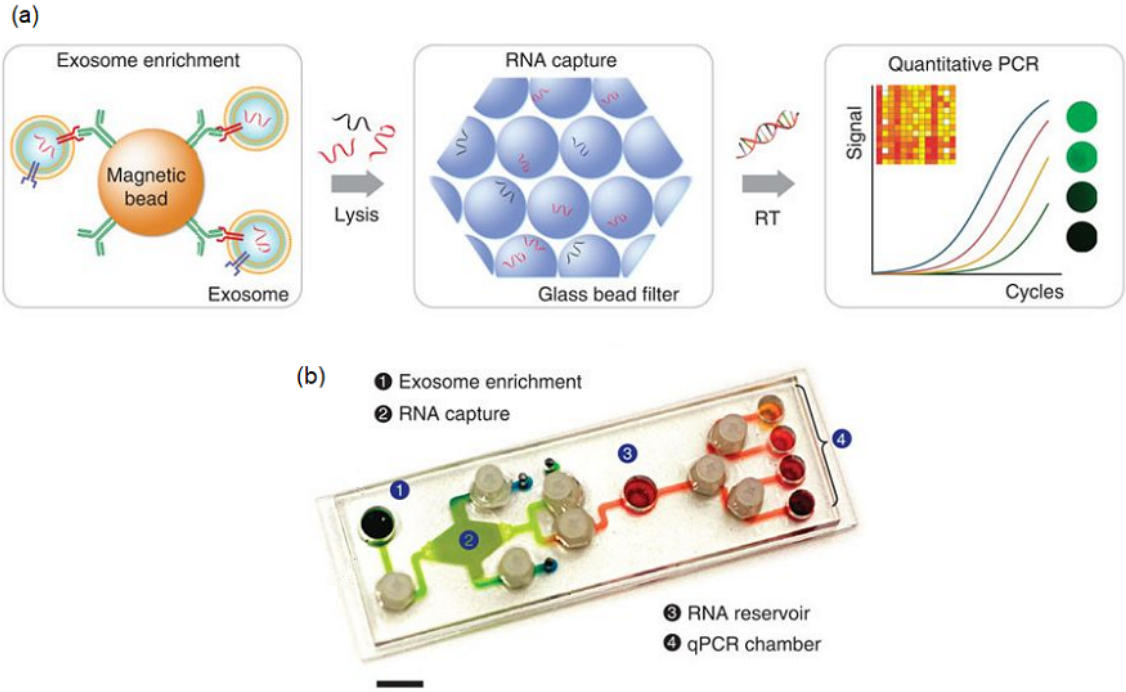

Figure 5.3: (a) Schematic representation of the main stages in the iMER exosome and mRNA platform whereby exosomes are first targeted using magnetic beads based on surface markers. They then undergo lysis where mRNA is isolated by physical shearing by glass beads and chemically lysed by a lysis buffer. Finally, qPCR is implemented to quantify mRNA. (b) Image of the iMER with specific chambers in the microfluidic design for 1. Exosome enrichment, 2. RNA capture, 3. RNA reservoir and 4. qPCR analysis (scale bar = 1 cm). Reproduced from [162].

5.4 Summary

Novel approaches to exosome capture/isolation and sensing have been implemented using both conventional methods such as ultracentriguation and novel lab-on-chip devices. Overall, exosomes are no doubt of interest for use as cancer biomarkers due to their physical and biochemical characteristics, of which much detail has not been fully explored. Nonetheless, effective techniques have been designed to investigate fully their diagnostic potential. However, it is apparent that many do not take advantage of the charged nature of exosomes, which may be an area of opportunity. gFET biosensors have been implemented for single molecule sensing such as specific protein biomarkers, virus and cell detection as discussed in section 4.4 but as of yet not been implemented for exosome sensing. gFETs are also extensively employed for chemical functionalisation for the specific detection of biomolecular targets and have also been shown to integrate well with microfluidics, potentially allowing for a lab-on-chip style device for sensitive and specific exosome isolation and quantitative detection.

Chapter 6

Materials and Methods

6.1 Graphene Transfer

CVD monolayer graphene grown on (111) copper was purchased from GrollTex, Graphenea and Graphene Supermarket. To remove the graphene from the copper substrates and transfer them onto suitable substrates for further characterisation, a wet chemical transfer procedure was employed for all samples. This is outlined in figure 6.1.

Graphene was cut to size and spin coated using a vacuum spin coater with 6 % poly (methyl methacrylate) (PMMA) in anisole (obtained from MicroChem Corp.) to ensure the delicate monolayer graphene was stabilised and protected from damage due to water surface tension during wet chemical transfer. By spin coating at 7700 RPM the resulting thickness of the PMMA was typically 300 nm [164] after overnight curing at room temperature.

The PMMA/graphene/copper stack was then cleaned using 10 % nitric acid to remove back-side graphene and any PMMA that might have got onto the copper side, which would otherwise prevent complete removal of the copper. Ammonium persulphate (APS), purchased from Sigma-Alrich, was made-up in de-ionised (DI) water to a concentration of 0.01 g/mL and distributed between beakers to create individual etchant baths for each sample. This etched away the copper foil, leaving the graphene unaffected, over the course of a day. The etchant

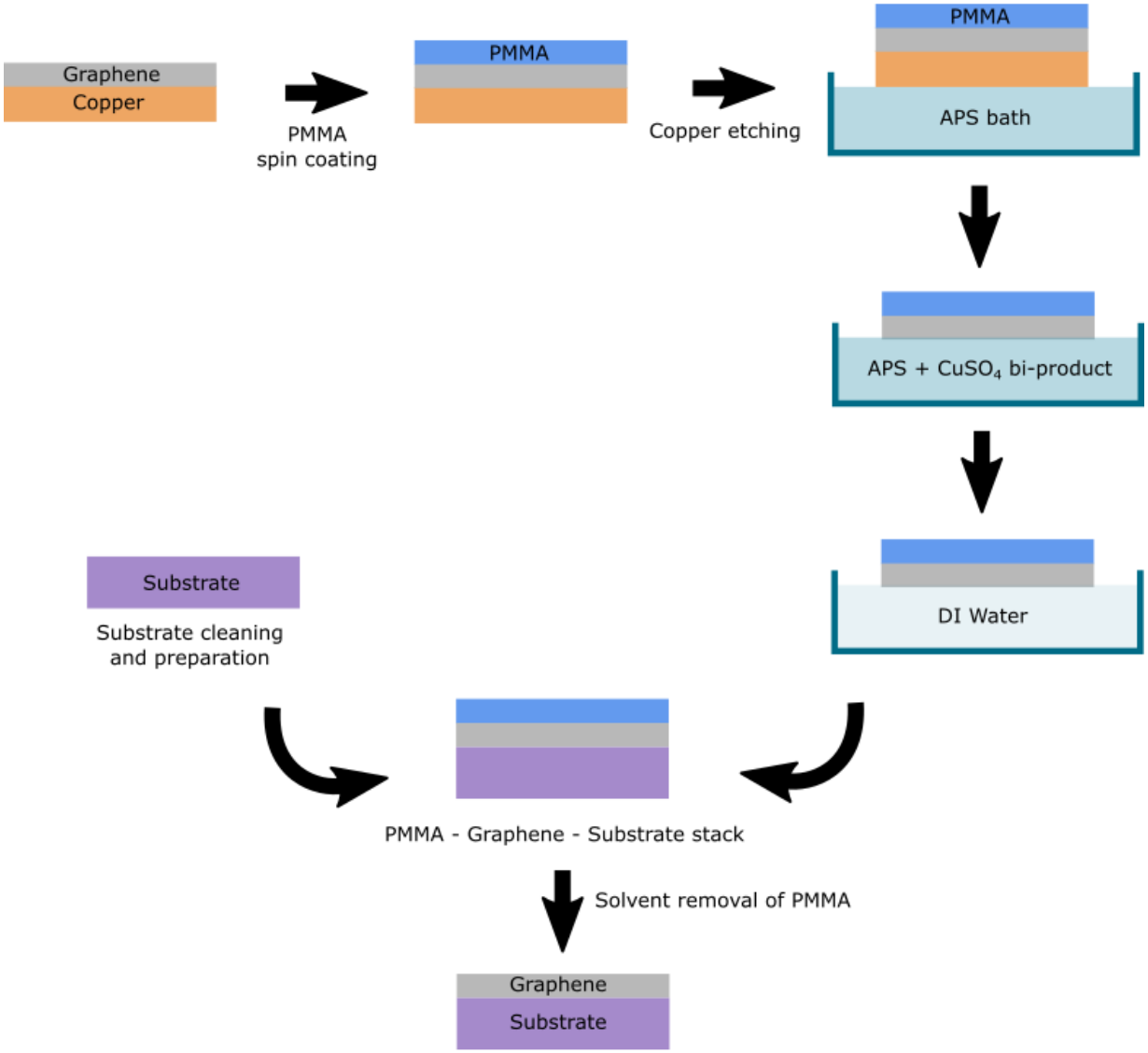

Figure 6.1: Schematic representation of the wet chemical graphene transfer method.

was then replaced with a fresh APS solution to remove any remaining microscopic copper to leave a clean PMMA/graphene stack. Transfer was done using a small scoop used to collect the floating sample to gently pour it in to the second bath, without damaging it.

The floating PMMA/graphene stack was then rinsed in in at least 3 consecutive water baths for a minimum of 15 minutes each in order to remove any residual APS ions from the underside of the graphene. Either precut 1×1 cm^2 SiO_2/Si substrates purchased from Crystec GmbH or uncut wafers, which were cut to size using a diamond pen were used before being cleaned while the

samples were rinsing. It is worth noting that all substrates were cleaned in the following manner: sonication for 30 seconds in acetone, sonication for 30 seconds in isopropanol and sonication for 2 minutes in DI water, before being dried with N_2. The PMMA/graphene stack was then manually deposited onto the substrates by submerging the substrate underneath the floating graphene and bringing it up and into contact so that the graphene, with water underneath, stuck to the surface. The PMMA/graphene/substrate stack was then left overnight to dry at room temperature. The PMMA/graphene/substrate stack was then placed on a hot plate for 1 hour at 180 °C to complete the drying process and ensure the removal of water between the graphene/substrate interface.

After being left to cool for at least 30 minutes back to room temperature, the PMMA was washed away using dichloromethane (DCM), obtained from VWR International, at room temperature over 24 hours under gentle and constant stirring. Upon removal of the DCM from the surface using N_2, this then leaves the graphene film fully transferred onto the substrate, which can then be used for further device fabrication as described in section 6.3.

6.2 Characterisation Methods

In addition to electrical characterisation, the following materials characterisation methods were employed to investigate the graphene quality and properties both before and after functionalisation and measurements with exosomes.

6.2.1 Optical Microscopy

Optical microscopy is a simple, rapid and effective method for qualitatively assessing the structural properties of graphene after transfer onto SiO_2/Si substrates. The technique provides a non-destructive way to visually determine the number of layers, and identify macro and microscopic tears and scratches in the film which may hinder electrical conduction.

By transferring the graphene onto SiO_2/Si substrates with thermally grown SiO_2 (90 or 300 nm), this provides good optical contrast, which makes for easy identification of the graphene film and substrate. Optical micrographs were taken using an Olympus BX51 compound optical microscope in bright-field illumination with a range of objectives from 1.25 to 100× magnification. Figure 6.2 shows the basic set-up and main components of an optical microscope.

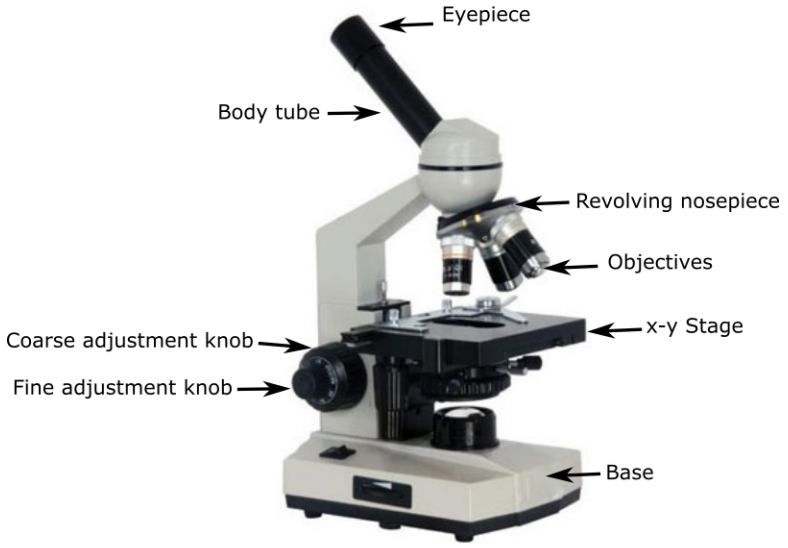

Figure 6.2: A compound optical microscope and its main components. Reproduced from [165].

For typical optical microscopes, the resolution obtained is in the order of 1 wavelength (λ) (in this case, $\sim$ 700 nm), which allows for easy identification of important features on the graphene film such as wrinkles and tears.

6.2.2 Raman Spectroscopy

Raman spectroscopy is a powerful and widely used graphene characterisation technique due to the well-studied peaks in the Raman spectra of graphene and gives both qualitative and quantitative chemical and structural information. Raman spectroscopy is a fast, non-destructive technique that can give spectra or Raman peak intensity mapping images over an area of a sample. By using a monochromatic light source, in this case a 532 nm laser, incident photons interact with the sample and results in the excitement of low-frequency modes such as

vibrational and rotational modes (this is the excitement of electrons to virtual energy states by photons). The resulting interaction between photons and phonons cause Stokes or anti-Stokes scattering if the light is inelastically scattered and Rayleigh scattering if elastically scattered as shown in figure 6.3. In the inelastic case, the scattering is defined as a Stokes or anti-Stokes mechanism if light decreases or increases in frequency upon interaction, respectively. Raman spectroscopy only utilises the inelastic photon scattering properties of a material. Therefore in the case of Rayleigh scattering, where the incident and scattered photons are the same frequency, the resulting signal is filtered as not to interfere with the signal arising from inelastic scattering.

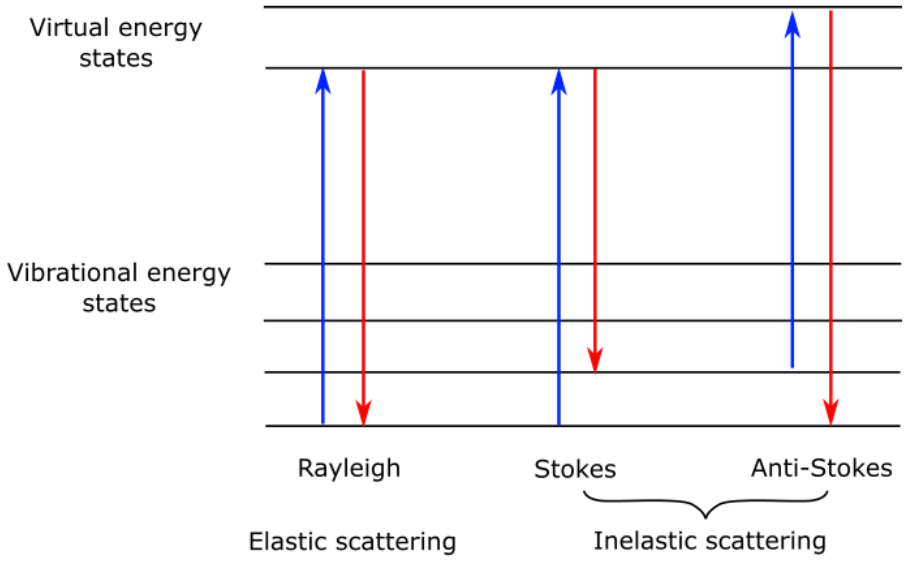

Figure 6.3: Elastic and inelastic scattering mechanisms that occur in Raman spectroscopy.

The energy difference between the incident and scattered photon is dependent on the phonon from which it is scattered. Raman spectroscopy measures the shift in frequency of inelastically scattered photons away from the frequency of the incident photons. A Raman spectrum is a plot of intensity as a function of this frequency shift, often quoted as 'wavenumber' $(1/\lambda)$. The resulting peaks in the spectrum are characteristic of the material and correspond to specific scattering mechanisms. For graphene these peaks are well understood and give information about the structural and chemical integrity of the film. Changes in the shape, position or

relative intensity of peaks give valuable information about the defect density, doping level and number of graphene layers [166, 167, 168].

The Raman spectrum that arises from graphene transferred onto SiO_2/Si contains peaks that are associated with both materials due to the depth resolution of Raman spectroscopy, which is typically in the range of 1 µm [169] and more than enough to penetrate through the graphene film. The spatial resolution depends on many factors such as the diffraction grating density and laser wavelength. Primarily, a rough estimate of the spatial resolution can be obtained using equation 6.1, which takes into account the laser wavelength, λ, and numerical aperture, NA, for focusing the laser on the sample.

$$Spatial\ Resolution = \frac{0.61\lambda}{\mathrm{NA}} \tag{6.1}$$

For a 532 nm laser and 0.90/100× objective, the resulting spatial resolution is $\sim$ 400 nm. However, this is often complicated further by the scattering processes and interaction of photons with material interfaces which causes this value to decrease to values closer to 1 µm [169].

To understand the Raman scattering processes in graphene, the reciprocal space unit cell of graphene and its energy dispersion relation at the Dirac point must be visualised. As described in section 2.1, the reciprocal lattice allows for the graphic representation of the Brillouin zone with centre point Γ and adjacent K and K' points on its corners. In Raman spectroscopy, the various scattering mechanisms that correspond to specific peaks in graphene's spectrum can be visualised using these reciprocal space points. For graphene, the main peaks observed (and which change according to doping level and number of layers present) are the 2D, G and D peak at wavenumbers of $\sim$ 2700, 1580 and 1350 cm^{-1}, respectively [168]. As an incident photon interacts with graphene, it causes the production of an electron-hole pair as the electron is excited to a virtual energy state. The creation of this virtual energy state causes the production of a phonon and the excited energy state is converted into an intermediate state. After some time, the electron-hole pair of the intermediate state decays radiatively and a photon is emitted and detected.

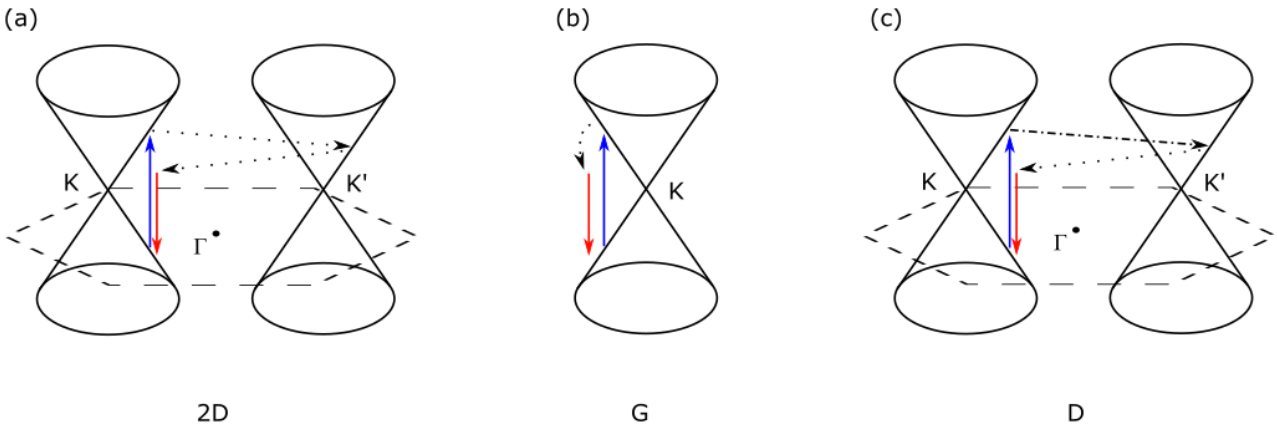

Figure 6.4: The electron dispersion relation around the K, K' and Γ in graphene's Brillouin zone (outlined by the dashed lines) in reciprocal space. The Raman scattering mechanism associated with (a) the 2D peak, (b) G peak and (c) defect induced D peak where the blue line depicts the excitation of the electron to a higher energy state as a result of photon interaction, the red line depicts the drop in energy of the hole during recombination, the dotted lines depict the path of the generated phonon and the dashed-dot line depicts the intraband transitions upon activation by a defect.

Figure 6.4 shows the Raman scattering mechanisms that occur for the 2D, G and D peak. Other scattering mechanisms are of course present and appear as distinct peaks on graphene's Raman spectrum such as the intraband double resonance process arising from a defect known as the D' peak, however those shown in figure 6.4 are those that are most typically identified and quantified. As seen by figure 6.4(a), the 2D peak arises due to a double resonance intraband process whereby an electron-hole pair is created and the scattering mechanism results in activation by two phonons before recombination. For graphene, a single resonance process is defined as an excitation that results in the creation of a phonon with very small momentum $\mathbf{q} \approx 0$ and a double resonance process is that used to define either the excitation resulting in the generation of a phonon with $\mathbf{q} \neq 0$ followed by the scattering by a defect or the generation of two phonons with opposite momenta $\mathbf{q}$ and $\mathbf{-q}$ [170]. As the 2D peak arises from the processes occurring between two adjacent K and K' points, all processes in this case are strongly resonant due to the linear energy dispersion relation [167]. For bi- and multilayer graphene, the dispersion relation changes and hence, processes associated with this peak weaken. The 2D peak in particular and its intensity ratio in the spectrum relative to other peaks can determine

the number of graphene layers.

Figure 6.4(b) shows the intraband scattering process attributed to the G peak, which is a single resonance process activated by one phonon. This is often used as a reference to the 2D peak to determine the overall quality of the graphene film and the I(2D)/I(G) peak intensity ratio is commonly used to identify the number of graphene layers. For good quality, monolayer graphene this ratio is expected to be ≥ 2 [171]. The associated D peak process is depicted in figure 6.4(c) where the second scattering event is activated by a defect instead of phonon. For this reason, the presence of the D peak and its intensity relative to the G and 2D peak act as a good indication of the defect density in the graphene film, which may be the result of doping or poor sample quality and fabrication.

The intensity of the different characteristic graphene peaks can be well visualised using Raman mapping, in which spectra are taken at discrete points (pixels) over a defined area of the sample (either 10×10 or 25×25 µm was used in this thesis) and the relevant peaks are identified and fitted with Lorentzian functions. The intensity of each fitted peak can then be plotted as a colour scale at each pixel to produce a map of intensity, or important metrics such as the I(2D)/I(G) ratio. For the gFET sensors, Raman spectroscopy was performed both by obtaining single spectra and Raman maps to compare the structural and chemical characteristics of graphene before and after functionalisation. Raman measurements were performed both in air under ambient conditions and in solution at room temperature. The power of the laser was also controlled at < 1 mW to avoid sample heating.

6.2.3 Atomic Force Microscopy

As monolayer graphene is estimated to be < 1 nm thick [172], visualisation of the surface topography of graphene after transfer requires atomic level resolution. Atomic force microscopy (AFM) is a powerful tool for imaging on the nanoscale and is used to obtain information such as surface roughness, topology changes from functionalisation and presence of residues and contaminants (from transfer methods) on the surface. It is not only non-destructive for

graphene (when used in tapping or non-contact mode) but also does not require the sample to be conductive as in other imaging methods such as scanning electron microscopy (SEM).

For all measurements an Innova AFM (Bruker Corporation) was used in tapping mode to map the surface topography graphene on SiO_2/Si and measure height profiles. A schematic of the instrumentation is shown in figure 6.5, where the main components of an AFM are highlighted. The tip is positioned at the end of a cantilever, whose motion is controlled by a shake piezo for tapping mode measurements. A laser is focused onto the cantilever and deflected to the photodetector. As the angle of the cantilever is changed as the tip moves over the surface of the sample, the change in the position of the deflected laser on the photodetector is then used to reconstruct an image of that surface. A silicon nitride tip was used for all measurements and all AFM measurements were performed under ambient conditions.

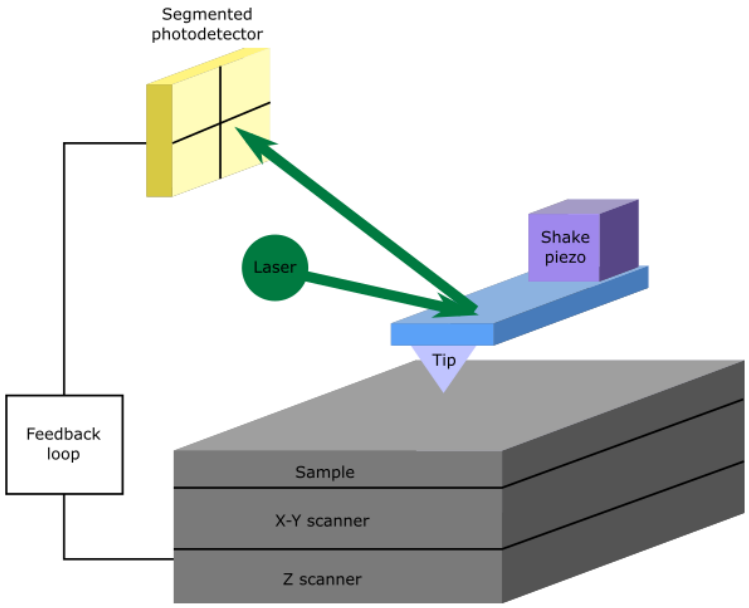

Figure 6.5: Schematic representation of the main components used in tapping mode AFM.

6.2.4 X-ray Photoelectron Spectroscopy

To investigate the chemical properties of graphene, X-ray photoelectron spectroscopy (XPS) was performed using a Thermo Fisher K-Alpha$^+$ spectrometer. To probe the chemical prop-

erties of graphene before and after functionalisation, Raman spectroscopy is a good technique for observing chemical changes, however, a powerful tool for chemical analysis that is complementary to Raman data is XPS. XPS gives both qualitative and quantitative information of the chemical and electronic state of the surface of a material (top 1-10 nm of the material). Hence, for characterising the functionalisation of graphene, this is particularly useful as it can indicate the presence of specific functional groups.

XPS gives the resulting energy spectrum by measuring the binding energy (in eV) of emitted electrons when they are photoemitted by excitation by X-rays. X-rays are created by bombarding a metallic anode (in this case, a micro-focused aluminium (Al) K-alpha source) with high-energy electrons, as seen in figure 6.6, and used to irradiate the sample surface. The anode material hence determines the energy of the emitted X-rays and the resulting beam intensity is dependent on the energy of the electron that bombards the metallic anode. The generated X-rays are monochromatic and focused onto the sample surface to a specific spot size (figure 6.6). As XPS relies on the accurate measurement of electrons emitted from the sample so the interference from surrounding gas must be minimised, hence the whole measurement is typically performed under high vacuum at pressures of 5×10^{-8} mbar.

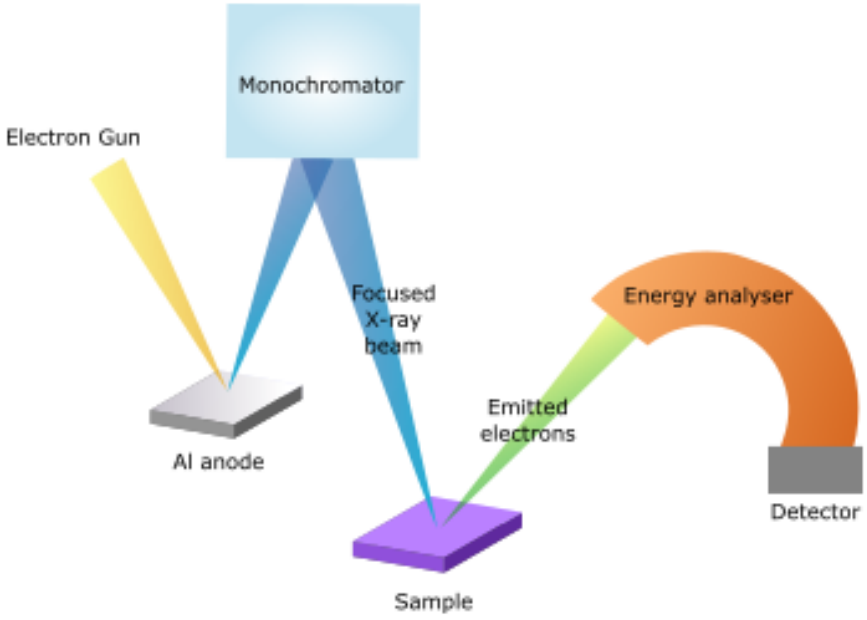

Figure 6.6: Schematic representation of an XPS instrument showing the generation of X-rays from the metallic anode and their irradiation onto the sample to produce photoemitted electrons. The electrons are emitted and analysed according to their energy by a hemispherical energy analyser before being counted by a detector.

If an atom at the surface of the sample absorbs an incident X-ray this causes ionisation via the emission of an electron from a core shell. An electron energy analyser is then used to detect the number of emitted electrons and their kinetic energy. The resulting spectrum plots the number of electrons (counts) against binding energy (BE), which relates to the kinetic energy (KE) through the following relations, where $E(A)$ is the energy of the atom, $E(A^+)$ is the energy of the ion and $E(e^-)$ is the energy of the electron.

$$E(A) + h\nu = E(A^+) + E(e^-) \tag{6.2}$$

As $E(e^-)$ is equivalent to the electron's KE, equation 6.2 can be rearranged to:

$$KE = h\nu - (E(A^+) - E(A)) \tag{6.3}$$

BE is the energy taken to remove the electron from the core shell and is defined as the difference in energy between the atom and ion after X-ray irradiation. Hence, equation 6.3 becomes:

$$KE = h\nu - BE \tag{6.4}$$

The energy of the X-rays generated from an Al K-alpha source is known, hence $h\nu$ in this case is 1486.6 eV.

The BE of electrons emitted from an atom's core shell is characteristic for every element and core atomic orbital. Therefore, the spectrum obtained will contain characteristic peaks for each element present in the sample and each element may give rise to multiple peaks due to emitted electrons from multiple core shells. For example, silicon emits electrons from both 2s and 2p orbitals upon irradiation with Al X-rays, as a result two peaks associated with the element are observed in the spectrum. In addition, chemical states can be determined because emitted electrons will have slightly different BE depending on the surrounding chemical environment. For example, an electron from a carbon atom in a C=O group will have slightly different BE than that in a C-C bond, thus resulting in slight shifts in the carbon peak in the spectrum.

Graphene samples were transferred onto SiO_2/Si substrates and functionalised as detailed in section 6.4 before being fixed onto a sample plate holder with carbon tape. The sample holder was inserted into the analysis chamber where the pressure was maintained at 5×10^{-8} mbar. For each scan, a 400 µm spot size was used to analyse each point on each sample with a pass energy of 20 eV for each individual element scan.

6.2.5 Ultraviolet - Visible (UV - Vis) Spectroscopy

Ultraviolet (UV) and visible (vis) spectroscopy is based on the principle of excitation of electrons via the absorption of light (the associated wavelengths are 10 - 400 nm and 400 - 800 nm for UV and vis light, respectively). As energy levels are quantized, electrons are excited only when light of a specific wavelength (and hence energy) corresponds to the energy difference between levels

[173]. These transitions are dependent on the molecular structure and consist of an electron from a full orbital being excited to an anti-bonding orbital, which are usually empty states, as depicted by figure 6.7(a). Consequently, the larger the difference in energy between these energy states, the shorter the wavelength of light absorbed.

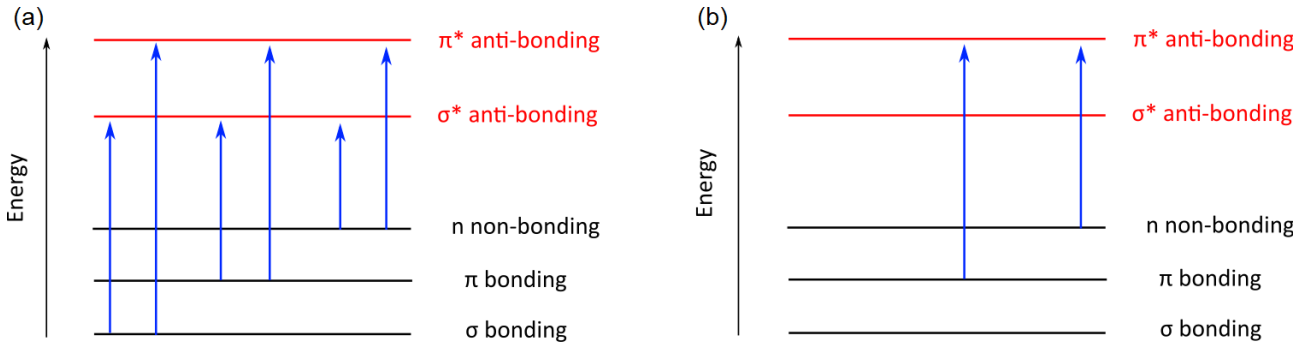

Figure 6.7: Schematic representation of (a) all possible electron transitions that may occur upon the adsorption of light and (b) the most relevant transitions for the 200 - 800 nm region of light.

Typical spectrometers operate between 200 - 800 nm, which allows only for the transitions shown in figure 6.7(b). Other transitions require high energy radiation using $<$ 200 nm and are not recorded in typical UV-Vis spectrometers. Hence, to be UV-Vis appropriate, the molecule-of-interest must contain either π bonds or atoms with non-bonding orbitals [173]. Graphene and PBASE are suitable for analysis using UV - Vis due to the presence of a conjugated system of alternating single and double carbon bonds, which results in the delocalisation of electrons. For systems such as these, a higher amount of delocalisation results in a decrease in the energy gap between π and π^* orbitals, which causes absorbance of longer wavelengths of light. When light interacts with the sample, a plot of absorbance and wavelength range will show a peak at a specific wavelength of light absorbed.

A Cary 5000 UV-Vis-Near-infrared spectrometer with deuterium arc lamp light source (λ = 200 - 800 nm) was used to measure the absorbance of graphene after transfer onto sapphire substrates. In all cases, reference spectra for the blank sapphire substrate and 100 % absorption were collected to give baseline and zero references before sample analysis.

6.2.6 Fourier-transform Infrared Spectroscopy

Fourier transform infrared spectroscopy (FTIR) involves qualitative molecular analysis of a material by obtaining a transmittance or absorbance spectrum. Infrared radiation is absorbed by molecular bonds and triggers their vibration in the form of stretching, asymmetric stretching or deformation vibrations. Different molecular bonds will vibrate from specific energies of light absorbed and hence these appear as peaks (or troughs) in the resulting absorption (or transmission) spectrum. This gives a chemical fingerprint and can hence be used to probe specific functional groups present on the surface of graphene.

For FTIR measurements, CVD graphene was analysed on copper foil in attenuated total reflectance mode using a FTIR spectrometer from Thermo Scientific. For each measurement, a background spectrum was collected before sample measurement.

6.3 Device Fabrication

The FET structure is created by transferring the graphene onto a SiO_2/Si with various oxide thicknesses, which act as the gate dielectric for back-gated measurements. Top-gate measurements were also performed using graphene on SiO_2/Si. Complete device fabrication requires the deposition of Ohmic, metal contacts for electrical measurements with sizes tailored to the device: slight variation in the graphene sizes was caused by manual graphene transfer onto the substrates.

6.3.1 Sputter Deposition of Metal Contacts

To create devices for applications such as the graphene FET, physical vapour deposition in the form of direct current (DC) magnetron sputtering using a Korvus Hex system, was employed to fabricate metal source and drain electrodes. Sputtering is a common physical vapour deposition technique where material from a target is ejected by the bombardment of high-energy ions. The

sputtered material, present in a gaseous state, then condenses on the substrate to form thin film layers where the film thicknesses are governed by the growth rates and sputtering times. Figure 6.8 outlines this process.

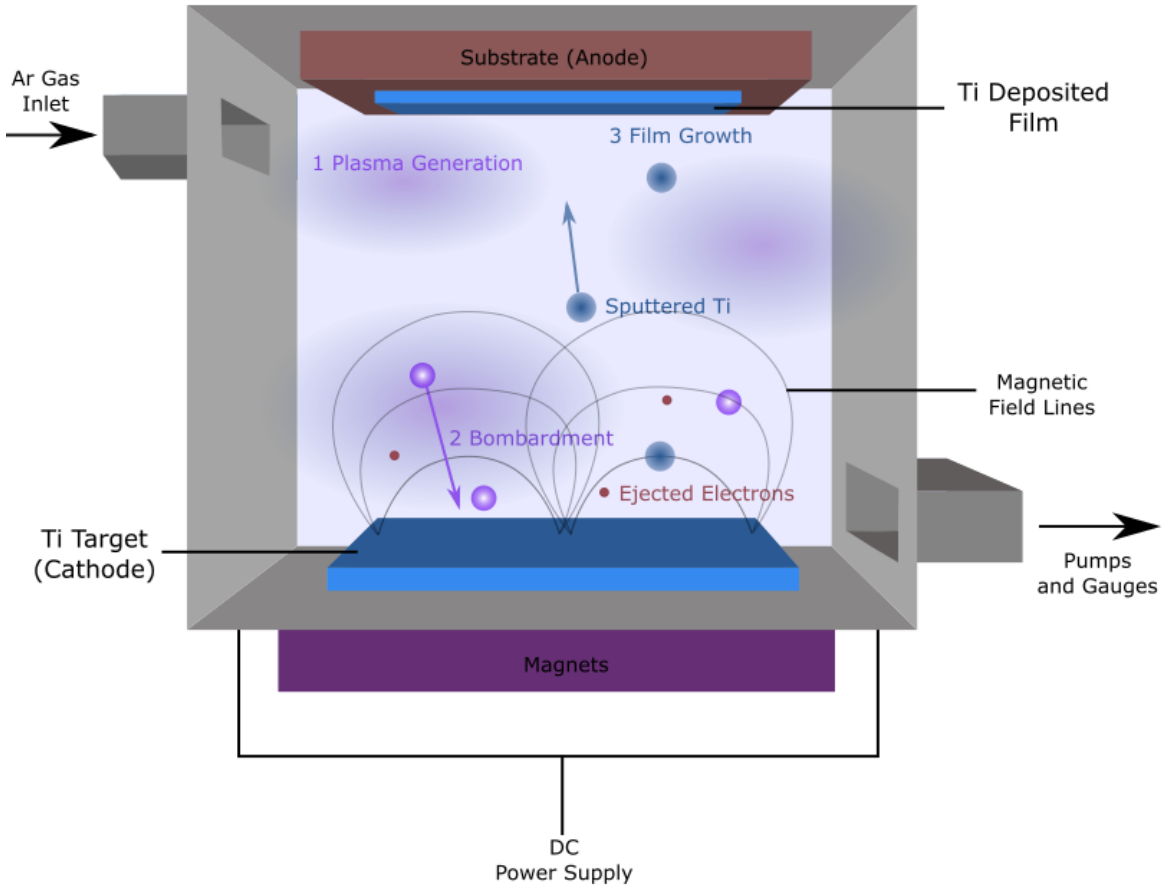

Figure 6.8: Schematic representation of the DC magnetron sputtering processes occurring inside the chamber where the target material in this case is titanium. The figure shows 1. Initial plasma generation by application of a DC source, 2. The bombardment of ions from the plasma on the target material resulting in ejected material and electrons and 3. Film growth at the substrate after material transportation.

The film deposition process mainly involves three key steps: formation of gaseous target material (flux), transportation of this material to the substrate and processes at the substrate surface. Generally, argon (Ar) gas is introduced to the chamber and ionised to Ar^+ to create plasma by a DC power supply as shown by step 1 in figure 6.8. The Ar gas flow for all metal contact deposition was set to 10 sccm and deposition was performed at a pressure of 5×10^{-3} mbar. This determines the overall growth rate as the flow rate governs the number of ions

generated for the plasma and hence, how many bombard the target. The Ar^+ ions are accelerated towards the cathode target and bombard its surface causing the ejection of material if the energy transferred is enough to overcome the material binding energy and it is this process that is known as sputtering. As well as target material, additional products of sputtering such as electrons, photons and re-sputtered primary ions are also ejected. As electrons are produced from the target, they can also go on to ionise the Ar gas, enhancing the production of plasma and increasing the sputtering yield. The sputtered titanium, as is the case in figure 6.8, is then transported as atoms to the substrate, where film growth occurs.

To prepare the samples for sputter deposition, the graphene on SiO_2/Si samples were secured to the sample stage at the top of the chamber and covered with shadow masks as shown in figure 6.9. Windows of size $\sim 1{\times}2$ mm^2 were cut from the foil which is then aligned to the graphene on the sample and positioned on the sample holder before being placed in the chamber. Once sputter deposition was complete, the shadow mask was removed, leaving sputtered material only on the uncovered areas to produce two contacts on either side of the graphene film.

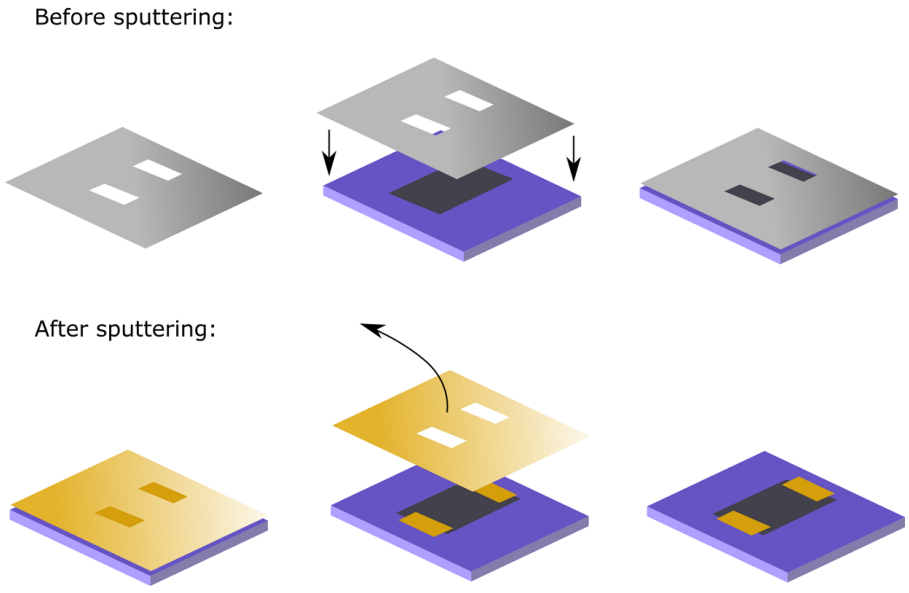

Figure 6.9: Schematic representation of the preparation of shadow masks (grey) and samples of $\sim 2{\times}5$ mm^2 graphene (dark grey) on $1{\times}1$ cm^2 SiO_2/Si for sputter coating metal contacts of specific desired sizes.

Table 6.1 outlines the parameters used, resulting deposition rates and times used for two sputtering materials: titanium (Ti) and gold (Au). Deposition rates were calculated by a combination of the flow rate, DC current source, pressure and target/substrate separation.

Table 6.1: Parameters used for the fabrication of Ti/Au metal contacts.

	Ti	Au
DC current source (mA)	100	50
Growth rate (nm/min)	3.3	10
Sputtering time (min)	5	5
Resulting film thickness (nm)	15	50

6.3.2 Microfluidic Channel Fabrication and Integration

To perform electrical measurements with liquid, a custom microfluidic channel was fabricated in-house to act as a reservoir for introduction and containment of liquids on the gFET sensor surface. It was also important to design the microfluidic channel such that the Ti/Au metal contacts would be isolated from the liquid to prevent leakage currents, hence the channel was designed to run perpendicular to a graphene strip such that the source and drain electrodes are not in contact with liquid.

The microfluidic channels were made using RTV 615 A + B polydimethylsiloxane (PDMS), which was supplied by Circuit Specialists Europe Ltd. The supplied PDMS is mostly made up by long chain vinyl-containing polydimethylsiloxane, vinyl-containing silicone resin, methyl hydrogen-siloxane, small amounts of solvent (benzene/toluene) and chloroplatinic acid, which acts as a catalyst. In order to cure the PDMS, the two parts, A and B, were mixed with a ratio of 12:1, where A is the vinyl-containing resin and B is the hydrosiloxane copolymer curing agent. This gave a soft and elastic PDMS that would adhere to the gFET surface. The process of moulding the microfluidic channels to the desired shape is shown in figure 6.10 whereby negative moulds were used to give a well-defined channel shape. Channels used during measurements

were cast using a 3D-printed negative mould (with dimensions detailed in figure 6.10). The negative mould was secured to the bottom of a clean container which was sprayed with mould release spray before the RTVA:RTVB mix was poured in such that it completely covered the mould. This was left to cure for a minimum of 18 hours at room temperature. Once cured, the PDMS was removed from the container and trimmed to an appropriate size to fit the gFET sensor. The negative mould was detached from the cured PDMS leaving the inverse shape, which gives a 3-walled open microfluidic channel. Inlet and outlet holes for the introduction and removal of liquid to the channel were created using a 1 mm diameter biopsy punch. Finally, the finished PDMS microfluidic channel was rinsed using acetone, isopropanol and DI water and aligned to the sensor surface such that the PDMS covers and isolates the Ti/Au source and drain electrodes. The channel design allows the liquid to contact the graphene only.

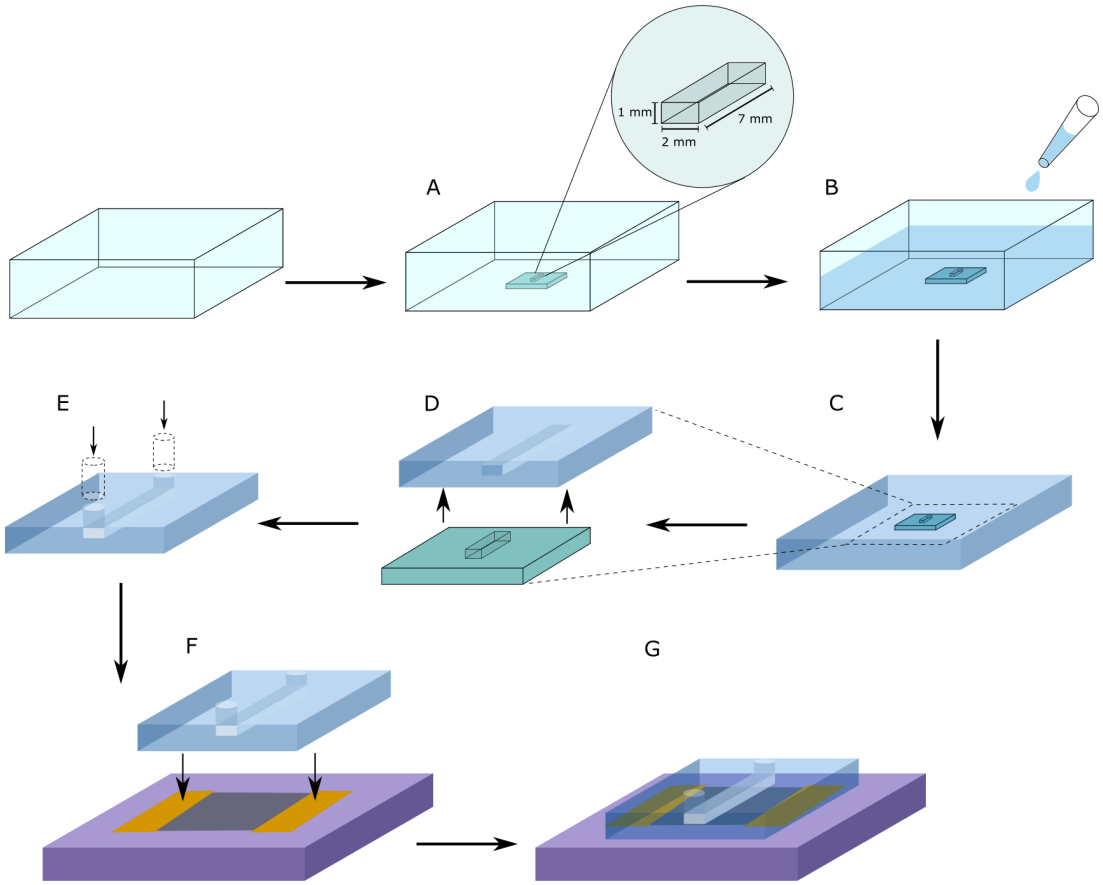

Figure 6.10: Schematic showing the step-by-step fabrication of PDMS microfluidic channels. A negative mould is 3D printed with the desired channel size and placed in a clean container (A). RTVA and RTVB are mixed together with the desired ratio and poured into the container, which is then left to cure overnight (B). The cured PDMS is then removed from the container and trimmed to a size appropriate for the gFET sensor such that excess PDMS is removed (C). The negative mould is then detached from the cured PDMS, which is left with the inverse shape of the negative mould (D). Inlet and outlets of the channel were created using a biopsy punch (E). The PDMS microfluidic channel is finally cleaned and aligned (F) and placed on the surface of the gFET sensor (G).

Upon initial testing of the microfluidic channel on the gFET sensor, flowing liquids resulted in leaks due to inefficient sealing of the PDMS to the sensor surface. The capillary effect would cause liquid to seep between the PDMS/sensor interface, causing the microfluidic channel to lift from the surface and become detached. An acrylic clamp was designed to overcome this and secure the microfluidic channel in place such that the slight pressure applied to the clamp would ensure no channel leaks. This is shown in figure 6.11 where the clamp consists of a

bottom and top plate that sandwiches the sensor and microfluidic channel.

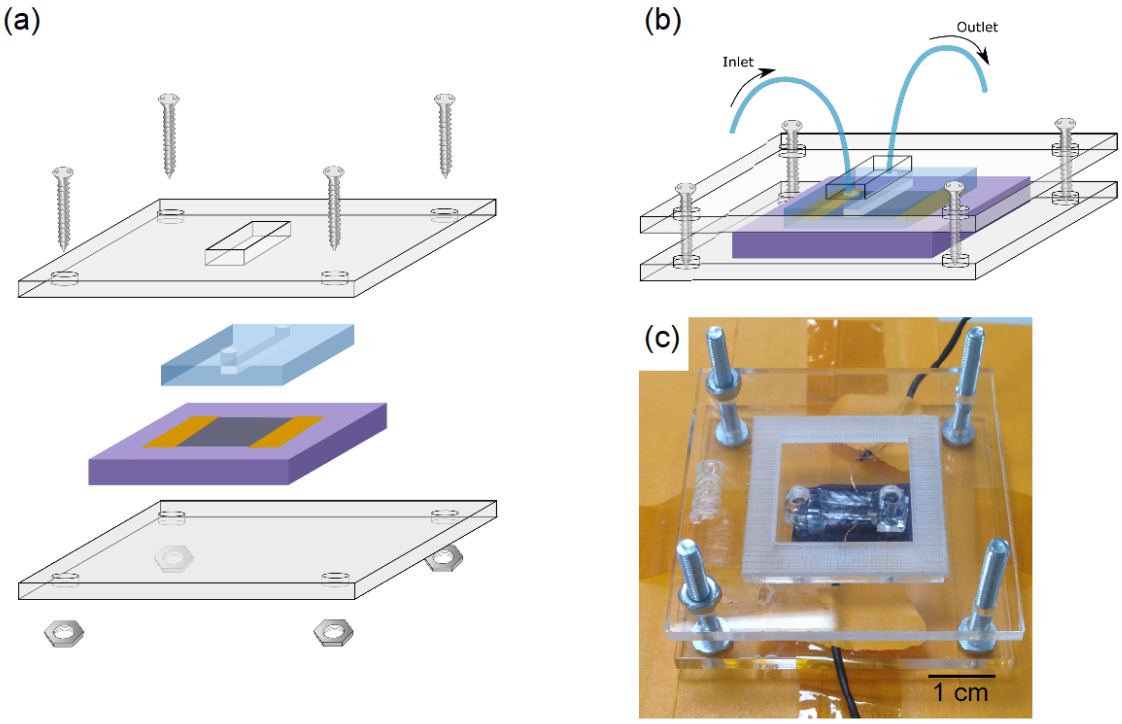

Figure 6.11: Schematic representation detailing the integration of microfluidics with (a) the individual components that make up the gFET sensor set-up and (b) the complete assembly showing the use of tubing that connects to the channel inlet and outlet to allow for fluid flow. (c) Image of the acrylic clamp with sample and microfluidic channel.

6.4 Functionalisation

The following section details all surface modification techniques employed.

6.4.1 4 - Nitrophenyl Diazonium Tetrafluoroborate

The samples were first covalently functionalised using a wet chemical method using this functionalisation approach. A 5 – 20 mM solution of 4 – ntirophenyl diazonium tetrafluoroborate (NPD) with 0.1 M tetrabutylammonium tetrafluoroborate (n-Bu_4NBF_4), both purchased from Sigma-Aldrich, was made up in acetonitrile following Z. Tehrani et al. [55].

GFET sensors, following the graphene transfer onto 525 µm thick SiO_2/Si substrates with 90 nm thermally grown oxide (0.001 - 0.005 Ω cm), were immersed in these solutions in the absence of light for 15 hours with continuous stirring at room temperature. After functionalisation, the samples were then sonicated in acetonitrile for 1 minute to remove any excess diazonium salt. They were finally dried with N_2.

6.4.2 1-Pyrene butyric acid N-hydroxysuccinimide ester (PBASE) Functionalisation

The non-covalent functionalisation of gFET sensors was also employed. This was done using a wet chemical method with a heterobifunctional linker, known as PBASE, which is known to non-covalently bond to graphene [112]. Concentrations of 5 – 30 mM PBASE solutions were made up by dissolving PBASE, purchased from Sigma Aldrich, in dimethylformamide (DMF) purchased from VWR International.

GFET sensors were fabricated by graphene transfer onto 525 µm thick SiO_2/Si substrates with both 90 nm thermally grown oxide from Graphene Supermarket (0.001 - 0.005 Ω cm) and 300 nm thermally grown oxide from CrysTec GmbH (0.01 – 0.02 Ω cm). Ti/Au contacts were then fabricated before functionalisation for samples that were used for electrical measurements. One droplet of the PBASE solution per sample was placed on the gFET surface such that the whole of the graphene to be tested in the channel was covered, and left for 2 hours at room temperature for spontaneous non-covalent functionalisation. Afterwards, the samples were rinsed in DMF, DI water and dried under a flow of N_2. These functionalised samples were found to be stable under dry conditions.

6.4.3 Antibody Conjugation

To specifically capture exosomes, the gFET surfaces were incubated with monoclonal purified mouse anti-human CD63 antibody (Ab) purchased from BD Biosciences US. Exosomes supplied

by HansaBioMed Life Sciences Ltd. were confirmed to express CD63, hence anti-CD63 Abs were chosen as the preferred antibody for graphene functionalisation.

The purchased stock solution of 0.5 mg/mL Ab in an aqueous buffered solution (containing $\leq$ 0.09 % sodium azide) was diluted to 100 µg/mL using 1× phosphate buffered saline (PBS) at pH 8.4 (the preparation of these solutions is detailed in section 6.5.1.1 and the specific chemical make-up of 1× PBS is detailed in section 7.3.3), which is the concentration used throughout all samples and measurements concerning antibodies. GFET sensors were incubated by placing a 25 µL droplet of the antibody solution onto the surface and left overnight in a humidified environment at 4 °C. he sensors were then rinsed in 1× PBS at pH 8.4, followed by DI water and dried in air or under N_2 flow.

This protocol was also employed for bare graphene sensors, which resulted in adsorbed antibodies on to the graphene surface. The sensors fabricated on silicon substrates with both 90 and 300 nm thermally grown oxide if first functionalised with PBASE, were referred to as anti-CD63 Ab conjugated samples due to the covalent bond formed between the PBASE and antibody. Anti-CD63 Ab conjugated sensors were named so to distinguish them from bare graphene sensors with only adsorbed antibodies.

In addition to both bare and PBASE-conjugated anti-CD63 antibody functionalisation, equivalent gFETs were incubated with purified mouse IgG1κ isotype control antibodies, purchased from BD Biosciences US, for specificity tests. These antibodies are not specific to exosomes but match the class and type of the anti-CD63 Abs and hence act as negative controls. In the same way as the anti-CD63 Abs, the stock solution of 0.5 mg/mL in an aqueous buffered solution (containing $\leq$ 0.09 % sodium azide) was diluted to 100 µg/mL using 1× PBS at pH 8.4. In order to conjugate these to PBASE functionalised surfaces, gFET sensors were incubated by placing a 25 µL droplet of the antibody solution onto the surface and left overnight in a humidified environment at 4 °C. The sensors were then sequentially rinsed in 1× PBS at pH 8.4, DI water and dried in air or under N_2 flow.

6.4.4 Glycine Treatment

Glycine is the simplest possible amino acid, consisting of only a hydrogen atom as its side chain. For the gFET biosensor, it is used after functionalisation steps as a terminator for excess PBASE functional groups.

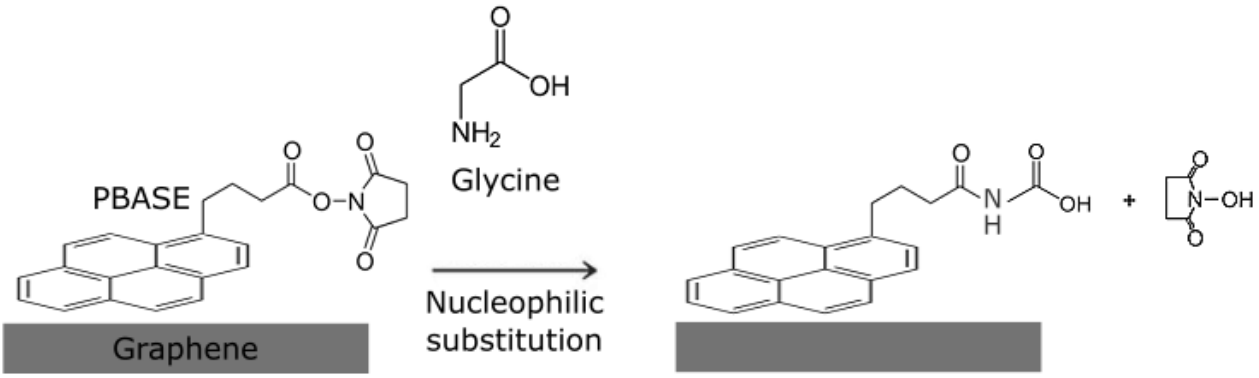

Figure 6.12: Schematic representation of the reaction of glycine with non-covalently functionalised PBASE molecules on graphene.

Glycine was used to terminate any excess PBASE molecules after the antibody conjugation step described in section 6.4.3 to ensure that exosomes bound only to antibodies and did not form non-specific covalent bonds to PBASE. The amine group present on the glycine reacts with non-terminated NHS esters as seen in figure 6.12 to form a non-reactive end group with respect to target biomolecules. This is a form of passivation; if additional biomolecules are introduced to the sensor surface alongside exosomes, this acts to block them from bonding to the PBASE layer and further facilitates the capture of exosomes only. Hence, any electrical signal detected from the introduction of exosomes to the sensor surface is more likely due to the exosomes themselves rather than other biological species.

Glycine solutions were made up to 100 mM by dissolving glycine (in powder form), purchased from Sigma Alrich, in 1× PBS pH 7. GFET sensors were immersed in this solution for 30 minutes to allow for termination of the excess PBASE and subsequently rinsed twice with DI water and dried under a flow of N_2. In the following sections of the thesis, a 'fully functionalised'

gFET sensor refers to the gFET sensor after PBASE functionalisation, antibody conjugation and glycine treatment.

6.5 Preparation of Biological Solutions

6.5.1 Phosphate Buffered Saline (PBS) Solutions

PBS was prepared using tablets purchased from Sigma Aldrich. PBS acts as a solution that imitates the osmolarity and ion concentrations of that of plasma. When dissolved in 200 mL DI water at room temperature, this yields a 1× PBS solution (0.0027 M potassium chloride and 0.137 M sodium chloride), commonly also referred to as 10 mM PBS with pH 7.4.

6.5.1.1 PBS for Antibody Conjugation

For the antibody conjugation procedure described in section 6.4.3, higher pH PBS solutions are recommended to improve coupling efficiency. Hence, all 1× PBS solutions used for this process were made up to pH 8.4. A stock 1× PBS solution at pH 7.4 was used and drops of diluted sodium hydroxide (NaOH) in DI water were added sequentially until the pH remained at a stable 8.4. This was monitored by a bench top Orion Star pH meter (from ThermoFisher Scientific) under constant stirring.

6.5.1.2 Other PBS solutions

All other PBS solutions were made up within the range of 0.0001 – 1× PBS and used both alone and for the making up of protein and exosome solutions. For diluted PBS solutions, DI water was always used. Further details on the composition of the PBS solutions and resulting Debye lengths are discussed in section 7.3.3.1.

6.5.2 Bovine Serum Albumin (BSA)

Bovine serum albumin (BSA) is a type of globular protein present in blood serum that is chemically similar to human serum albumin. BSA was purchased from Sigma Aldrich as a lyophilized powder. 1 % BSA was made up in 0.001× PBS at pH 7.4 and stored at 4 °C.

6.5.3 Exosomes

Lyophilized exosomes from plasma of healthy donors were purchased from HansaBioMed Life Sciences Ltd and stored at 4 °C. Per purchased vial, it was expected that this provides 30 µg exosomes, which is approximately equivalent to $> 1 \times 10^8$ particles. From the supplier specifications, the exosomes expressed CD63 before and after reconstitution, hence CD63 was used as the target receptor. Exosomes were isolated through a combination of ultracentrifugation and microfiltration carried out by the supplier.

A stock solution of 1 mg/mL exosomes was made up by adding 30 µL 1× PBS to the lyophilized standard. To properly reconstitute the exosomes, the exosomes were resuspended by pipetting the solution up and down 10 - 15 times, whilst avoiding bubbles before being vortexed for 60 seconds. The standard was briefly centrifuged at 3000 RPM for 5 seconds to ensure the solution is collected at the bottom of the Eppendorf tube. Finally, the solution was once again pipetted up and down 10 times to resuspend any particle aggregates.

For electrical measurements, exosomes were diluted with the desired PBS solution concentration to give exosome solutions between 0.1 µg/mL - 10 µg/mL. Nanoparticle tracking analysis (NTA) was performed by a collaborator to determine a population mode for the exosome diameters of the exosome standard of 117 nm, the results of which are shown in figure 6.13.

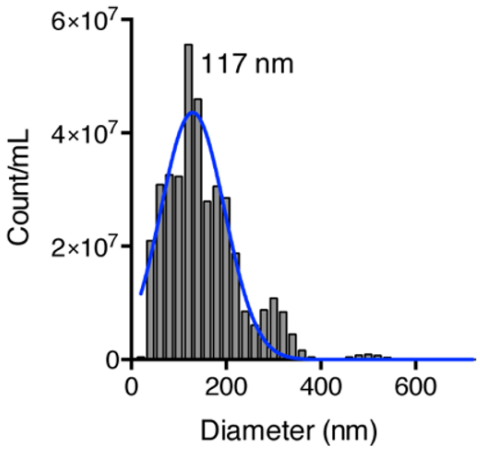

Figure 6.13: NTA analysis showing the distribution and population mode of the exosome standard.

6.6 Electrical Measurements

6.6.1 Direct Current (DC) Measurement Set-up

All direct current (DC) measurements were performed using a two - channel Keithley 2636B sourcemeter with capability of supplying up to 200 V for a single channel. By assigning channel A responsible for application and measurement of the source – drain voltage and current and channel B responsible for the gate, both channels were grounded to ensure the same electrical reference point. The setup is shown in figure 6.14 and all experiments were conducted at room temperature. For those involving the microfluidic channel, solutions were introduced into the microfluidic channel using gentle pipetting and were cleared from the channel using air between introduction of different solutions.

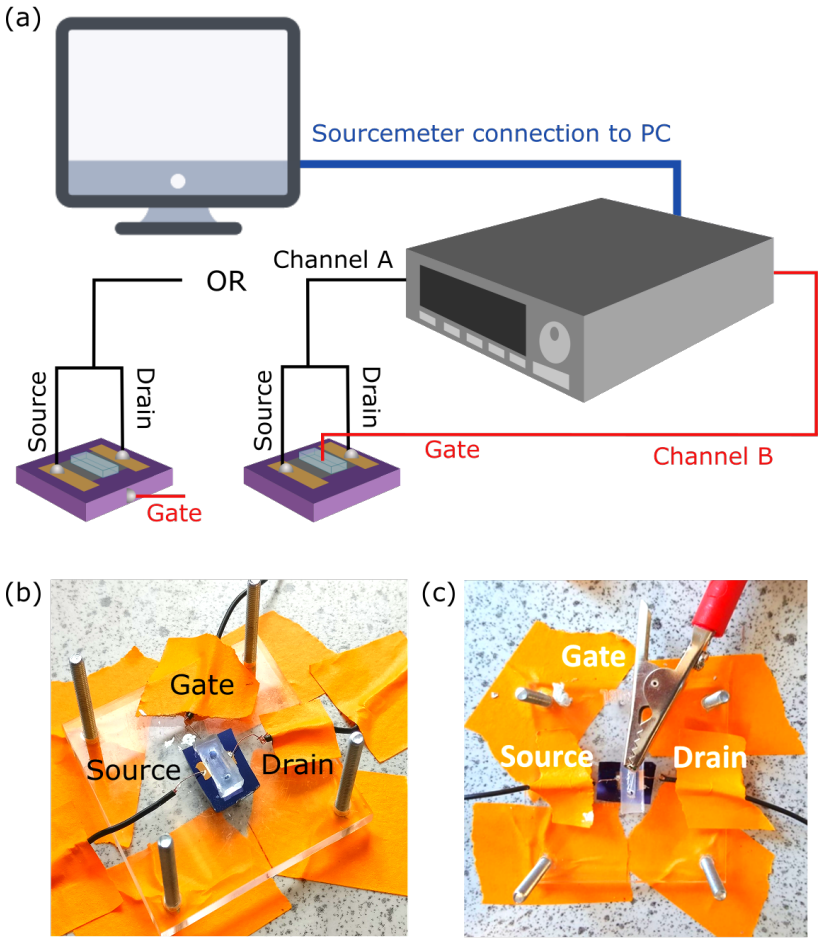

Figure 6.14: (a) Schematic representation of the DC measurement set up showing the relevant connections and channel allocations for the gFET sensor for the back and top-gate setup and photos showing the (b) back-gated and (c) top-gated set up.

6.6.1.1 Back-gate

For back-gated measurements, the source and drain electrodes were fabricated using sputter deposition as described in section 6.3.1. The gate is connected to the side of the SiO_2/Si substrate such that a global back-gate is generated (as seen in figure 6.14(b)), which back-gates the entire graphene film. This is done using silver conductive paint purchased from RS Electronics. Microfluidic integration was implemented, as by section 6.3.2, after contacting and solutions passed through the microfluidic channel. Like the metal electrodes, the placement of the silver paint was carefully done to ensure no liquid contact.

The approximate measurement range for the different SiO_2/Si substrates used is detailed in table 6.2. The variation in back-gate voltage applied here is due to the thickness of the oxide layer which ultimately governs the maximum voltage that can be applied before oxide breakdown. If oxide breakdown occurs, current can pass through the oxide layer resulting in a source-gate current known as a leakage current. For $I_{ds} - V_g$ transfer characteristic measurements, a constant V_{ds} of 200 mV was used and measurements were taken over 100 points with a time of 300 ms per point as shown in figure 6.15.

Table 6.2: Table showing the various substrates used with different oxide thicknesses and corresponding back-gated voltage range used during measurements.

SiO_2/Si substrate oxide thickness (nm)	Back-gate voltage range (V)
90	-20 to 70
300	-20 to 120

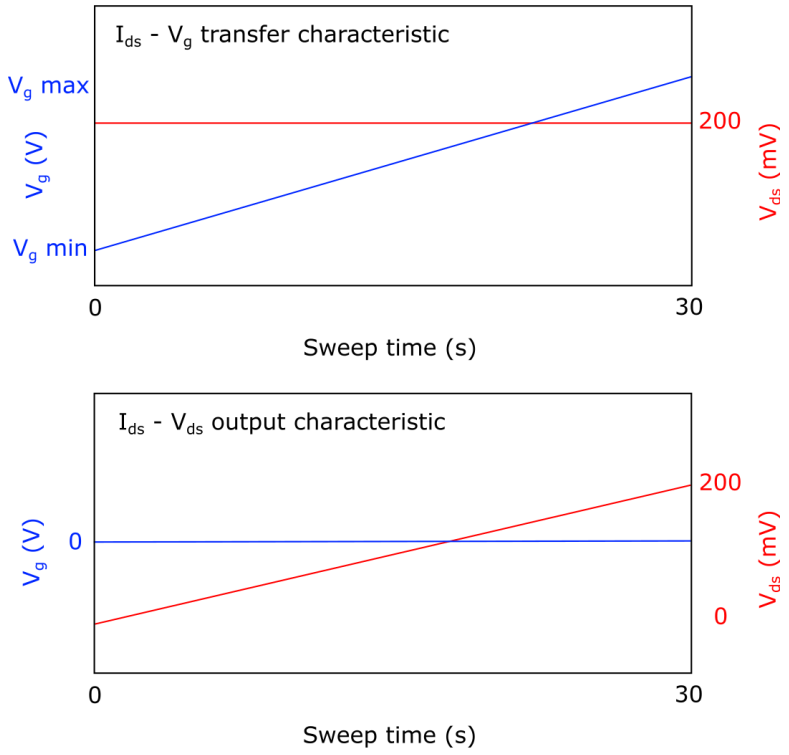

Figure 6.15: Most commonly used sweep settings used for back-gated measurements for the transfer and output characteristics.

The chosen sweep settings gave a total measurement time of 30 seconds per sweep. The same number of points and time per point were used for I_{ds} – V_{ds} output characteristics where the V_{ds} range would vary from 0 to the V_{ds} to be used in subsequent transfer characteristic measurements (usually 200 mV), while V_g was held constant.

6.6.1.2 Top-gate

The top-gate measurements were performed by using a 0.25 mm diameter platinum (Pt) wire purchased from Fisher Scientific as the gate electrode as represented in figure 6.14(c) where the red gate line is directly inserted into the microfluidic channel. The electrode was used in different geometries to optimise measurements and repeatability as shown in detail in section 7.3.4. The graphene films were transferred, and metal electrodes sputtered in the same way for back-gated measurements. However, in this case, only the graphene exposed to the solution is gated.

In this case, an electrical double layer is formed within the gate solution and, hence the applied V_g is no longer dependent on the SiO_2 layer thickness as it is in the back-gated set-up. As a result the V_g range for top-gate measurements is much lower, with the largest range used being -1 to 3 V. To optimise the DC measurements, different sweep times were investigated to give the most reproducible results and discussed further in section 7.3.4. All top-gated I_{ds} – V_g measurements were performed with a constant V_{ds} of 200 mV, as in back-gated measurements.

Chapter 7

Results and Discussion

7.1 Initial gFET Characterisation

The quality of the graphene after the graphene transfer onto SiO_2/Si substrates must be determined prior to any functionalisation or treatment as it is important to use this as a reference for any electrical and structural changes that might occur upon chemical modification. This section describes initial material and electrical characterisation performed to examine the properties of the graphene after transfer and the same techniques were used throughout the rest of the biosensor fabrication to analyse the effect of each modification step.

7.1.1 Graphene Properties After Transfer

Following the wet chemical transfer as outlined in section 6.1, optical microscopy was used as a quick and effective method of examining the quality of the graphene. Defects and imperfections on this microscopic scale can highly influence the electrical and chemical properties.

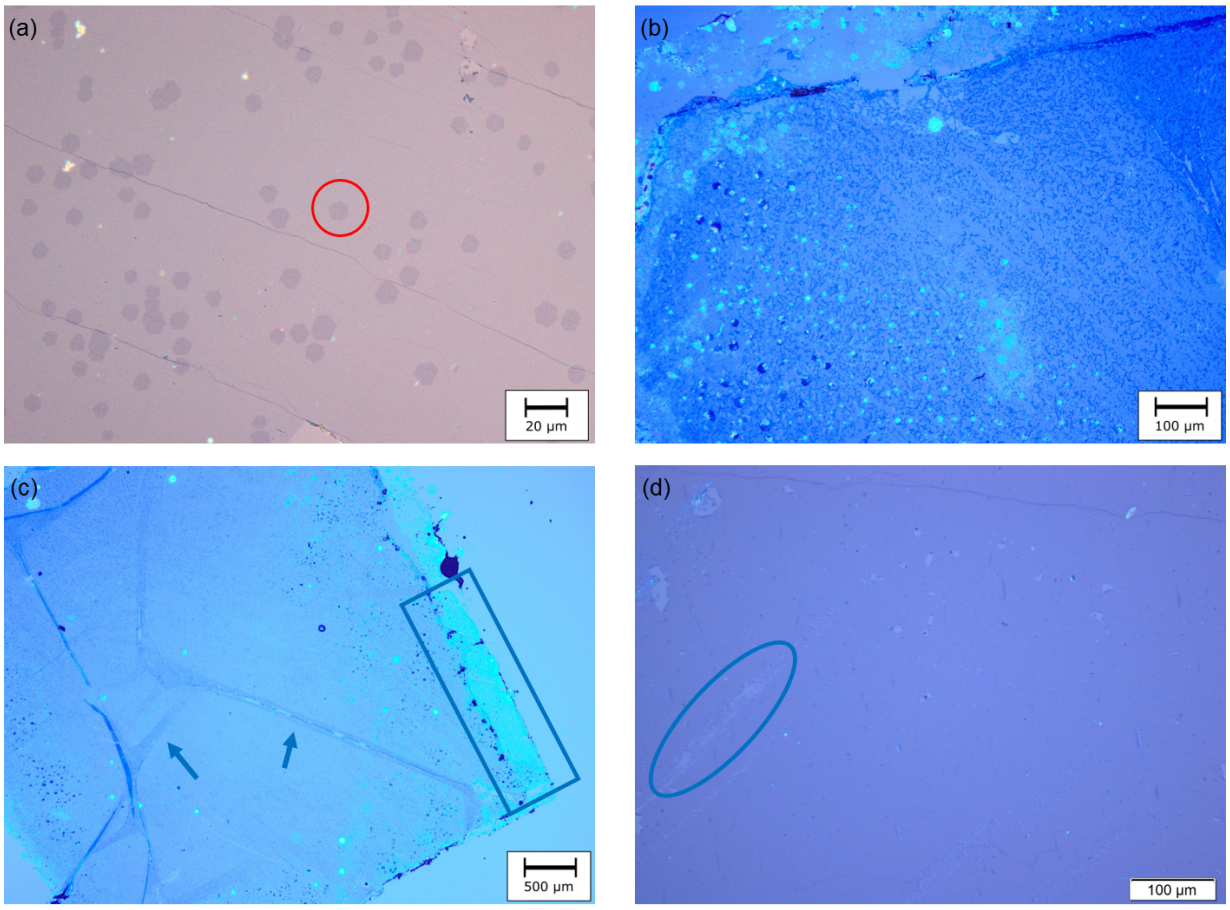

Figure 7.1: Optical micrographs of different graphene films transferred onto a) 90 nm SiO_2/Si taken at 50× magnification where the red circle highlights an area of bilayer graphene, b) 300 nm SiO_2/Si taken at 20× magnification, c) 300 nm SiO_2/Si taken at 2.5× magnification where the arrows indicate folds in the film and the blue rectangle shows residual PMMA and d) 90 nm SiO_2/Si taken at 10× magnification where the blue circle indicates tears in the film.

A number of features can be identified by using optical microscopy. Figure 7.1 shows several CVD graphene films transferred using the same method onto 90 and 300 nm SiO_2/Si substrates. The difference in contrast between these is ultimately governed by the thickness of the oxide layer as light penetrates through the oxide layer is reflected by the underlying silicon. As the light is reflected, constructive interference causes enhancement of specific wavelengths.

Figure 7.1(a) shows the first important feature that is observed on the micrograph; this is the presence of bi- or multilayer graphene. Often the presence of multilayer graphene is obvious as areas appear as geometric islands or flakes on top of the expected monolayer graphene as

highlighted by the red circle. In this case, the shape of the islands indicates Volmer - Weber type growth, which is characterised by well-faceted flakes [174]. The growth of these islands is relatively well documented in literature [174, 166, 175] and the colour and shape of the flakes in figure 7.1(a) are easily identified as bilayer graphene islands; multilayer islands are identified by changes in contrast (i.e. darker colour islands) within the islands themselves corresponding to changes in the number of graphene layers [174].

The coverage of the bilayer islands from figure 7.1(a) is estimated as 6.8 % as determined by ImageJ analysis (full analysis is outlined in the appendix). The presence of bilayer graphene is often unavoidable when using commercially bought graphene and its removal after transfer to the SiO_2/Si substrate is not trivial. The effect of having a high coverage of bilayer graphene on monolayer sensors may cause the electrical properties to vary within the graphene film. W. Zhang et al. [176] have previously shown that molecular adsorbates that result in the doping of bilayer graphene can cause an opening of a band gap due to the on-site energy asymmetry between the top and bottom layers [176] of AB stacked (Bernal) graphene. Functionalisation of the graphene is required to make a sensitive and specific biosensor and the chemical modification is expected to cause doping effects within the monolayer film. In bilayer areas, the molecular dopants would only adsorb on the top layer and could cause band gap opening. This may make it difficult to distinguish the effects of the molecular dopants on the monolayer graphene and bilayer graphene upon electrical characterisation of the gFET devices.

Another important feature to identify is shown in figure 7.1(b). Here small lines are scattered throughout the graphene film, which are likely rolled-up back-side graphene. Depending on the supplier of the commercial graphene, back-side graphene is often present on the underside of the copper foil substrate due to the nature of vertical CVD. The transfer process in section 6.1 describes using nitric acid to remove back-side graphene, however it is possible for it persist. Typically, this rolled-up graphene is found closer to the edges of the transferred graphene film as it is physically more difficult to clean the corners. The ineffective removal of the back-side graphene causes areas of stacked monolayer-on-monolayer areas of graphene, which not only exhibits different electronic properties to both monolayer and bilayer graphene [171] but can

cause problems with the adhesion between the graphene film and SiO_2/Si substrate [32], making the graphene more likely to lift off or be damaged during liquid measurements.

The presence of PMMA residues from the transfer process is also noticeable as seen on figure 7.1(c), highlighted by the blue box. Here, areas of brighter, lighter blue correspond to leftover PMMA that was not removed even after cleaning for 24 hours in DCM. Given that this high level of cleaning is not sufficient to remove this, it is possible that the PMMA left was a combination of PMMA above the graphene and also PMMA trapped at the graphene/substrate interface. The effect of these residues on the electrical properties of gFETs has been well studied [177, 178]. It has been shown that the presence of PMMA leads to a high density of charge traps at the graphene/SiO_2 interface, which results in graphene p-doping. With reference to the I_{ds} - V_g transfer characteristics of the gFET, this results in a shift of the Dirac point to more positive V_g such that the Dirac point becomes unobservable if outside the suitable V_g range. Additionally, if the coverage of PMMA on top of the graphene is high, it is possible that this blocks functional layers from adsorbing or bonding the surface of the graphene, which would lead to an inhomogeneous functionalisation and an overall decrease in the sensitivity of the sensor to target molecules. To remove these polymer residues, annealing is often employed after solvent cleaning.

Figure 7.1(c) also shows large wrinkles or folds in the graphene film as indicated by blue arrows. This can be caused by the way graphene dries on the substrate after transfer. During the transfer process, water trapped between the hydrophobic substrate and graphene/PMMA stack causes the stack to form a convex, pillow-like shape. As the graphene dries, this becomes flat, resulting in folds of graphene after the PMMA is removed. These also create areas of monolayer-on-monolayer stacked graphene unknown, uncontrollable orientations with respect to each other [179]. Upon functionalisation, the result would be a doped top layer and an undoped bottom layer, which would cause two regions with different Dirac point on top of each other. In terms of the I_{ds} - V_g transfer characteristic, it is difficult to tell what effect this would have, but it would certainly cause regions of different electronic properties where folded graphene is present.

Figure 7.1(d) shows transferred graphene with close to none of the features outlines in figure 7.1(a), (b) and (c). This is the ideal situation for the gFET biosensors so that the additional electrical effects these features give rise to are minimised. Tears and holes in the film as indicated on figure 7.1(d) are often difficult to avoid completely but should also be minimised as much as possible. These likely arise due to the graphene's improper adhesion to the substrate due to the reasons previously discussed on page 91. Figure 7.2 shows a typical AFM image of monolayer graphene after transfer, where microscale cracks and wrinkles can be seen that are otherwise difficult to see with optical microscopy alone. Again, these arise from the drying and stretching of the graphene film onto the substrate surface and result in areas where PMMA residues and contaminants can become trapped, leading to raised areas of up to 4 - 10 nm in height (figure 7.2(b)). Theses residues present on the surface could result in areas of the film that would be blocked from functionalisation.

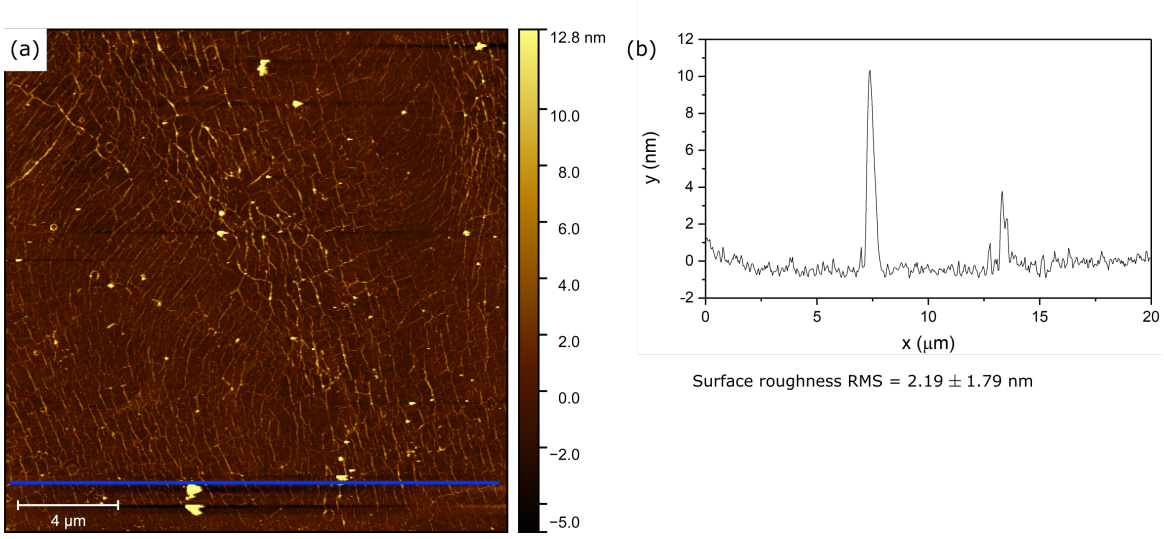

Figure 7.2: (a) AFM image of bare graphene transferred onto a 90 nm SiO_2/Si substrate and (b) height profile across the blue line.

Raman spectroscopy is a commonly used technique that can give qualitative and quantitative information regarding the graphene film's structural and chemical quality. Graphene gives an easily identified Raman signal and the presence of specific peaks, as well as their intensity ratio, gives information such as the number of graphene layers and the defect density. In figure 7.3, Raman spectra were taken over two different areas of the same sample, which optically clearly

show different number of layers. By comparing the intensity ratio between the characteristic 2D and G peaks, I(2D)/I(G), the number of layers can be inferred, as a ratio of 2 or above typically corresponds to monolayer graphene with a 2D full width half maximum (FWHM) of 24 cm^{-1} [167]. Figure 7.3(a) shows position 1 in red which appears to correspond with monolayer graphene from an I(2D)/I(G) of 1.94 and 2D FWHM of 29 cm^{-1} as determined from the spectrum in figure 7.3(b). Position 2 (blue) shows an area of the sample where the I(2D)/I(G) has decreased to 1.12 and the 2D FWHM is 34 cm^{-1}, which is typical of bilayer graphene [180].

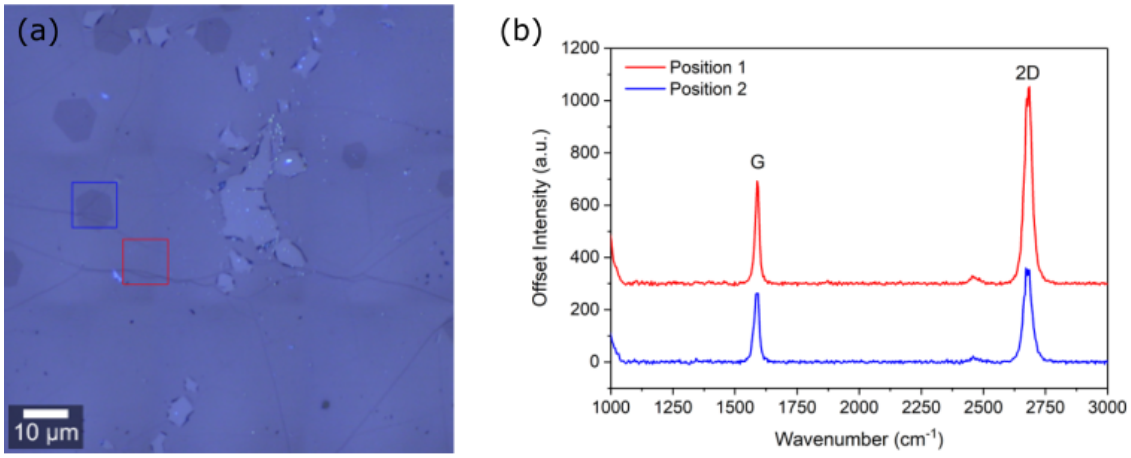

Figure 7.3: Optical micrograph of graphene transferred onto 90 nm SiO_2/Si showing position 1 (red) and position 2 (blue) from which spectra of monolayer and bilayer graphene were obtained respectively and (b) the resulting Raman spectra.

In all cases of transferred graphene, the underlying substrate will give rise to its own characteristic peaks in the spectrum if the material is Raman active as a 532 nm laser will typically penetrate up to 1 µm depth. Figure 7.4(a) shows the area of the sample analysed outlined in red. Here, the presence of the SiO_2/Si substrate is easily identified by the strong peak at 520 cm^{-1} (as well as a broad band between 930 – 1000 cm^{-1}), which appears alongside the characteristic monolayer graphene 2D and G peaks at 2676 cm^{-1} and 1583 cm^{-1} respectively in figure 7.4(b) with I(2D)/I(G) of 2.01 and 2D FWHM of 25 cm^{-1}. Specific peaks of a Raman spectrum measured over a given scanning area can be analysed separately. By fitting a specific

peak for each spectrum taken in the scanned area to a Lorentzian function, a Raman intensity map is produced by displaying the intensity of that function at each pixel in the area. In this case, the scanned area is outlined by the red box on figure 7.4(a). Figure 7.4(c) is resulting Raman intensity map for the silicon peak at 520 cm^{-1} and shows that Si/SiO_2 is present in all of the scanned area with the highest intensity observed on the right-hand side, suggesting that there is no graphene covering this area. Doing the same with the 2D and G peaks results in figures 7.4(d) and (e), which show that graphene is only present on the left-hand side of the area, in agreement with conclusions drawn from 7.4(a).

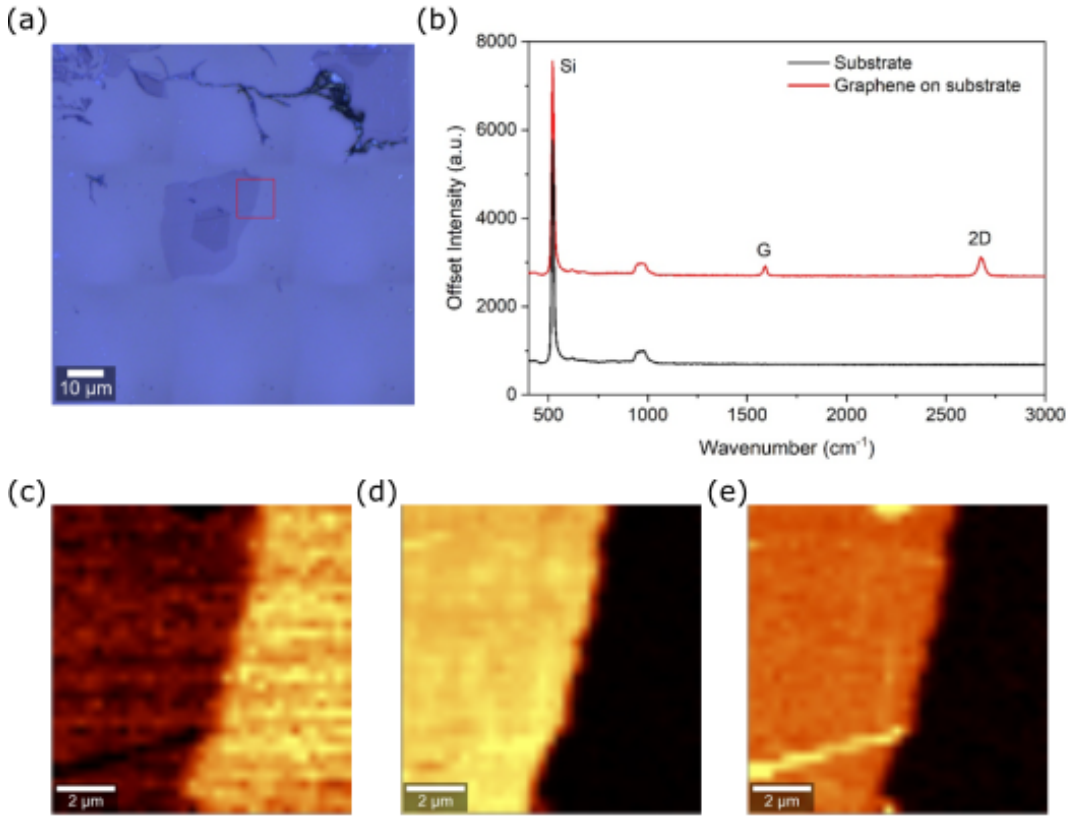

Figure 7.4: Optical micrograph of graphene transferred onto 90 nm SiO_2/Si and the scanned area (red). (b) The resulting spectra obtained from the scanned area from the left and right-hand sides of the scanned area and Raman intensity maps using the (c) 520 cm^{-1} (d) 2D and (e) G peak.

7.1.2 Preliminary Back-Gated DC Measurements

Initial electrical characterisation was performed using the back-gated gFET geometry as detailed in section 6.6.1.1. A typical monolayer gFET I_{ds} - V_g transfer characteristic is seen in figure 7.5(a), where there is a clear Dirac point at 38.9 V indicating p-doping of the graphene, which is commonly associated with polymer residues left after the transfer process and trapped charges at the graphene/SiO_2 interface. The transfer characteristic also displays the expected electron and hole conduction regimes on either side of the Dirac point, which are governed by the applied V_g.

7.1.2.1 I_{ds} - V_g Asymmetry

For all DC gFET measurements, an asymmetry in the gFET I_{ds} - V_g transfer characteristic is observed. Typically, the observed hole current and mobility (when extracted from the transfer characteristic using the gradient of the linear regions of the I_{ds} - V_g transfer characteristic) is higher than that in the electron regime. This contradicts the electron and hole mobilities associated with semiconductors: where the electron mobility is higher than hole mobility. This is usually attributed to the effect of the metal contacts when fabricating a gFET structure and is difficult to avoid. As metals get directly deposited on the graphene, the interaction causes the pinning of the work function of the graphene under the metal and results in a change in graphene Fermi level in this region. The graphene hence become more p-doped under the metal contacts compared to the bulk. Because of this slight p-doping effect, the graphene gives an asymmetric response to the electric field that arises from the bias voltage.

The asymmetry can be explained by dividing the I_{ds} - V_g transfer characteristic into 3 regimes as marked on figure 7.5(a), where V_g is the applied gate voltage and V_D is the Dirac point voltage:

1. $V_g < V_D$
2. $V_g = V_D$
3. $V_g > V_D$

Figure 7.5(b) shows the effect of the deposited metal on the graphene film and describes the graphene charge modulation as V_g is swept through the different regimes. In the first regime, where the bias applied is negative with respect to V_D, the pinned Fermi level of the graphene under the contacts remains p-doped and the conduction in the bulk graphene channel is mainly due to hole conduction according to the field effect as the bias augments the density of states. This results in a p-p$^+$-p graphene channel and the negative bias only adds to the p-type conductance. As V_g increases and approaches V_D, the Fermi level of the bulk graphene channel shifts such that the charge carriers start to neutralise. As there is charge neutrality in the channel and neither electron or hole conduction dominates, a conductance minimum is reached.

Upon increasing V_g, the bias becomes positive with respect to V_D and I_{ds} also increases due to the increase in electron density. This causes p-n-p graphene as the graphene under contacts is still pinned despite the bulk channel becoming n-type. Contact resistance then increases as charge carriers find it difficult to transport through the p-n-p 'junction' and as a result, the conductance suffers. Therefore, channel conductance in this regime competes with increasing contact resistance and causes lower overall I_{ds} compared to $V_g < V_D$.

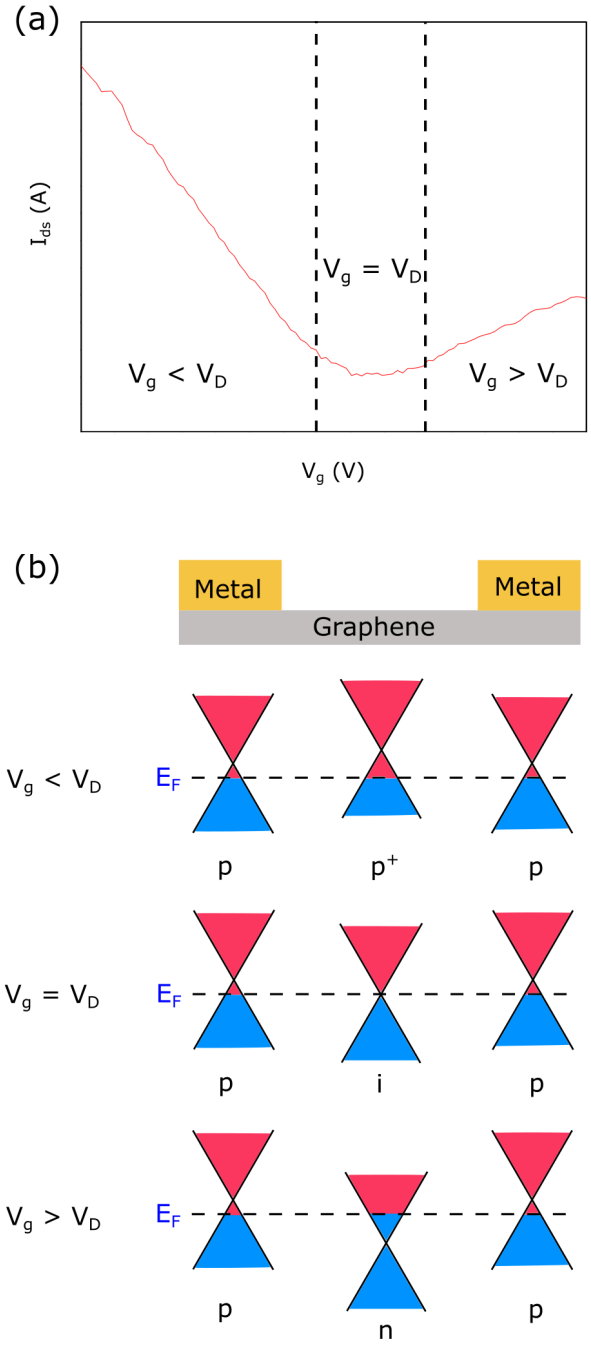

Figure 7.5: I_{ds} - V_g transfer characteristic with regimes based on the relation between V_g and the measured Dirac point and (b) schematic representation of the energy dispersion relation for graphene around the Dirac point and doping levels for graphene under metal contacts and uncovered graphene for regimes described in (a).

The effect described above would mean that all gFETs with metal contacts would exhibit I_{ds} - V_g asymmetry. This is true to some extent but this effect appears to be worse for the back-gated

FET geometry and not as pronounced for solution top-gated gFETs. The more symmetrical I_{ds} - V_g transfer characteristics for solution top-gate gFETs is further discussed in section 7.3.4.1.

7.1.2.2 Effect of V_g and V_{ds}

Several parameters will affect the gFET response, in terms of both the output and transfer characteristic as seen in figure 7.6. The I_{ds} measured across the source and drain is linearly (ohmically) dependent on the V_{ds} applied through the graphene film up to a critical V_{ds}. Figure 7.6(a) shows this observed Ohmic relationship in the I_{ds} - V_{ds} output characteristic for V_{ds} between 0 and 200 mV and multiple different back-gate voltages. As the V_g is increased, the output characteristic shows a decrease in maximum I_{ds} and an increase in resistance, which is extracted from the I_{ds} - V_{ds} gradient. This is because the maximum constant V_g used in this case is still below the observed Dirac point (seen in in figure 7.6(b)) and hence within the range for hole conduction. Therefore, as the V_g is increased, its value becomes closer to the Dirac point such that the graphene is being modulated closer to charge neutrality and its resistance increases.

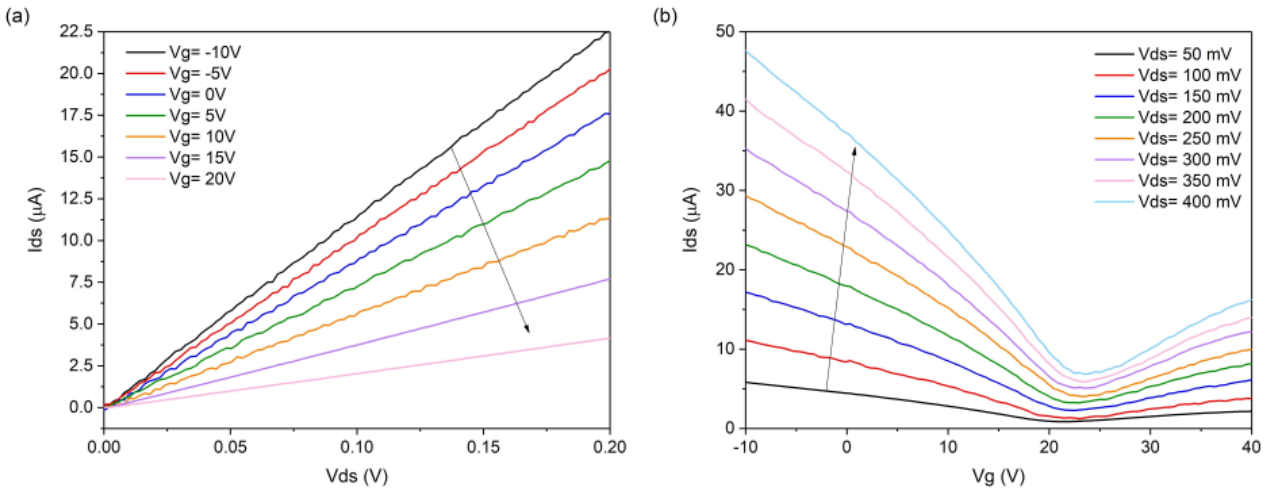

Figure 7.6: The resulting(a) I_{ds} - V_{ds} output characteristic measured at multiple constant V_g ranging from -10 to 20 V and (b) I_{ds} - V_g transfer characteristic measured at multiple constant V_{ds} ranging from 50 to 400 mV for one sample of graphene transferred onto 90 nm SiO_2/Si.

Figure 7.6(b) shows the resulting I_{ds} - V_g transfer characteristic for the same sample measured with multiple V_{ds}. As expected, due to the Ohmic relationship in figure 7.6(a), as V_{ds} is increased, the I_{ds} increases for all values of V_g, resulting in a shift of the plotted transfer characteristic upwards. Additionally, the Dirac point, originally observed at 38.9 V for V_{ds} = 200 mV, shifts to slightly higher V_g with increasing V_{ds}. This is due to a V_{ds} scaling effect that is reported for asymmetric I_{ds} - V_g characteristics for 2D materials and has been theoretically explained for CNTs [181]. For an undoped ambipolar transistor such as a gFET, the minimum current point is observed when a balance between the electron and hole current injected at the source and drain is reached. For an undoped gFET channel, this is equivalent to holding the Dirac point at 0 V by applying equal and opposite voltage to the source and drain. That is, the Dirac point is present at $V_g = 0$ V when the voltage at the source and drain are $+V_{ds}$ and $-V_{ds}$, respectively [182]. Hence, theoretically, as V_{ds} is increased, the voltage applied between the gate-source shifts by $\frac{1}{2}\,\Delta V_{ds}$ and therefore so does the Dirac point. For a doped gFET, the Dirac point will be present at $V_g \neq 0$ V and shift with $\frac{1}{2}\,\Delta V_{ds}$ from the non-zero value, as observed in figure 7.6(b).

The Dirac point shift seen in figure 7.6(b) highlights why it is important to keep V_{ds} the same for all sensor measurements otherwise it would be difficult to attribute these shifts to biomarker binding alone. Additionally, sample variation from factors related to the transfer process (as explained in 7.1.1) would also influence the electrical properties hence it is important to keep measurement parameters as consistent as possible.

7.2 Functionalisation

Bare graphene is not only sensitive to contaminants and impurities from its fabrication process but also to any charged species introduced to its surface: this includes charged biological species. This means that if bare graphene were to be exposed to exosomes, a change in its electrical properties would likely arise. However, this would also be the case for any additional biological molecules present in the same solution, serum for example contains an abundance of albumin,

glycoproteins and lipoproteins [183], all of which would contribute to an electrical change once adsorbed onto the graphene surface. The main challenge of the biosensor is therefore specificity: that is ensuring that exosomes and only exosomes are detected and therefore responsible for any electrical signals. To achieve this, the functionalisation of graphene is crucial, and this involves attaching linker molecules as well as exosome specific antibodies.

7.2.1 Covalent and Non-Covalent Functionalisation

7.2.1.1 Covalent Functionalisation Using 4 - Nitrophenyl Diazonium Tetrafluoroborate

Graphene used in biosensor applications can be functionalised in a variety of ways as discussed in section 4.2. To investigate the covalent functionalisation, 4- nitrophenyl diazonium (NPD) tetrafluoroborate was functionalised to the graphene surface using the methods in section 6.4.1. The principle of this functionalisation method is outlined in figure 7.7. The NPD is a diazonium salt that can undergo reduction under specific conditions, which allows it to react with the sp^2-hybridised structure of graphene to form a covalently bonded linker molecule. The nitro group still present on the end of this linker molecule can then be reduced to an amine group in order to bind to carboxyl groups present on specific antibodies.

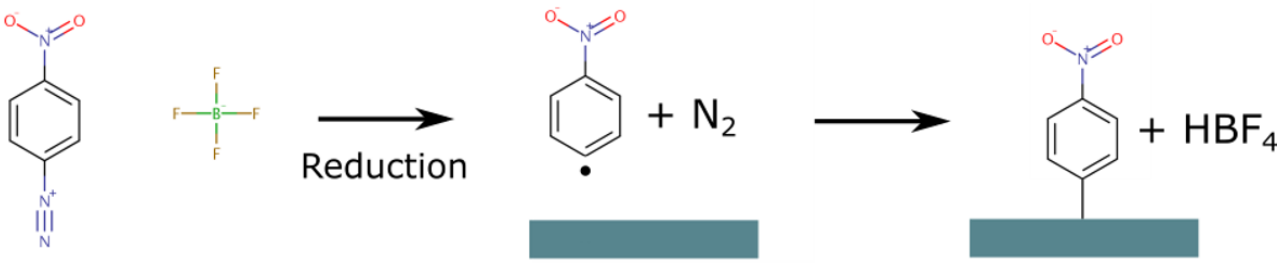

Figure 7.7: Schematic representation of the reduction of 4-nitrophenyl diazonium tetrafluoroborate and its functionalisation to a graphene surface.

Graphene was transferred onto a 90 nm SiO_2/Si substrate and functionalised with NPD and

analysed using AFM. As seen in figure 7.8(a), the bare graphene before functionalisation shows a slightly cracked film with topological features. From their large variation in size and soft features, the raised spots in figure 7.8(a) are likely PMMA residues that remain on the surface from the transfer process. Their presence mostly on the cracks and folds in the graphene film also suggests this as PMMA tends to accumulate during transfer due to the difficulty associated with removing it from these areas. In this case, the surface roughness was 3.40 ± 1.68 nm, higher than that in figure 7.2, which confirms the increased presence of residues and wrinkles. In figure 7.8(b), after functionalisation, sharper topological features are observed on the graphene film, which are consistent in size and shape. The surface roughness also increases to 6.46 ± 2.84 nm, which may suggest the presence of attached NPD diazonium molecules. It is assumed that single molecules would not be observed on this scale and the features observed here are in the range of 20 nm height and 200 nm width, which are again much larger than expected for a single molecule. It is possible that these are instead accumulations of the molecule that have coagulated on the surface when dried instead of forming a self-assembled monolayer. From AFM alone, it is difficult to determine whether the NPD molecules present on the surface are covalently bonded or not, let alone their surface coverage.

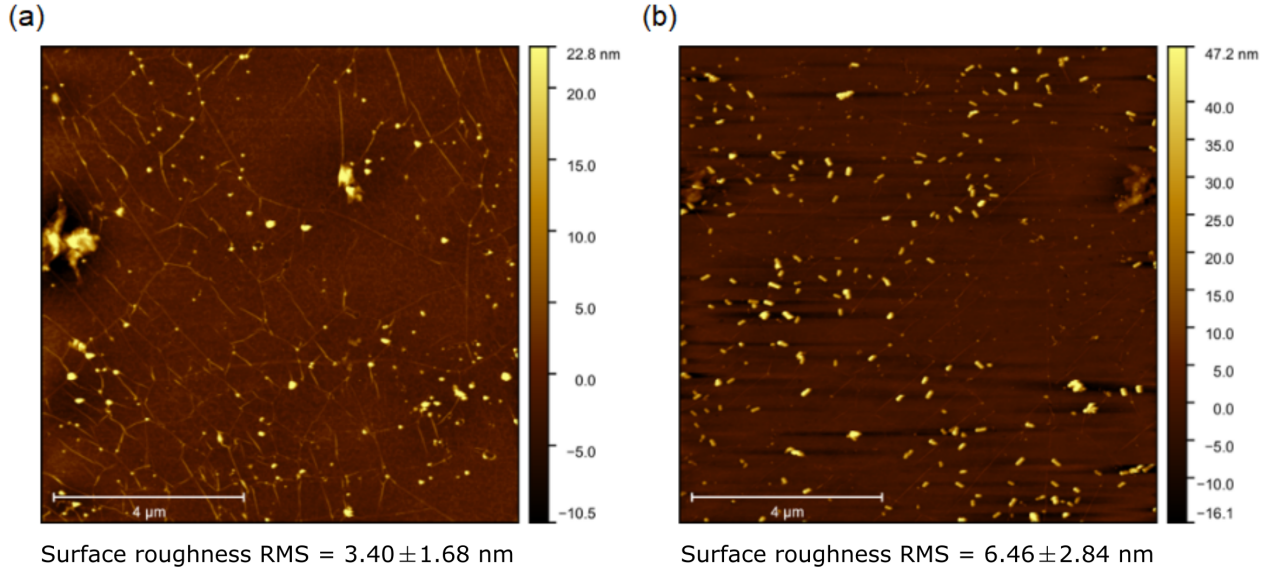

Figure 7.8: AFM images of (a) bare and (b) 10 mM 4-nitrophenyl diazonium tetrafluoroborate functionalised graphene on SiO_2/Si.

By conducting Raman spectroscopy on functionalised graphene samples, a pronounced effect was seen on the characteristic 2D and G peaks with increasing NPD concentration. Figure 7.9 shows the spectra for bare graphene where the 2D and G peak are clearly present with a reasonable I(2D)/I(G) intensity ratio of 1.81, suggesting a moderate quality monolayer graphene film. The D peak, which is commonly associated with disorder in the graphene sp^2- hybridised structure is also weak indicating minimal defects [184].

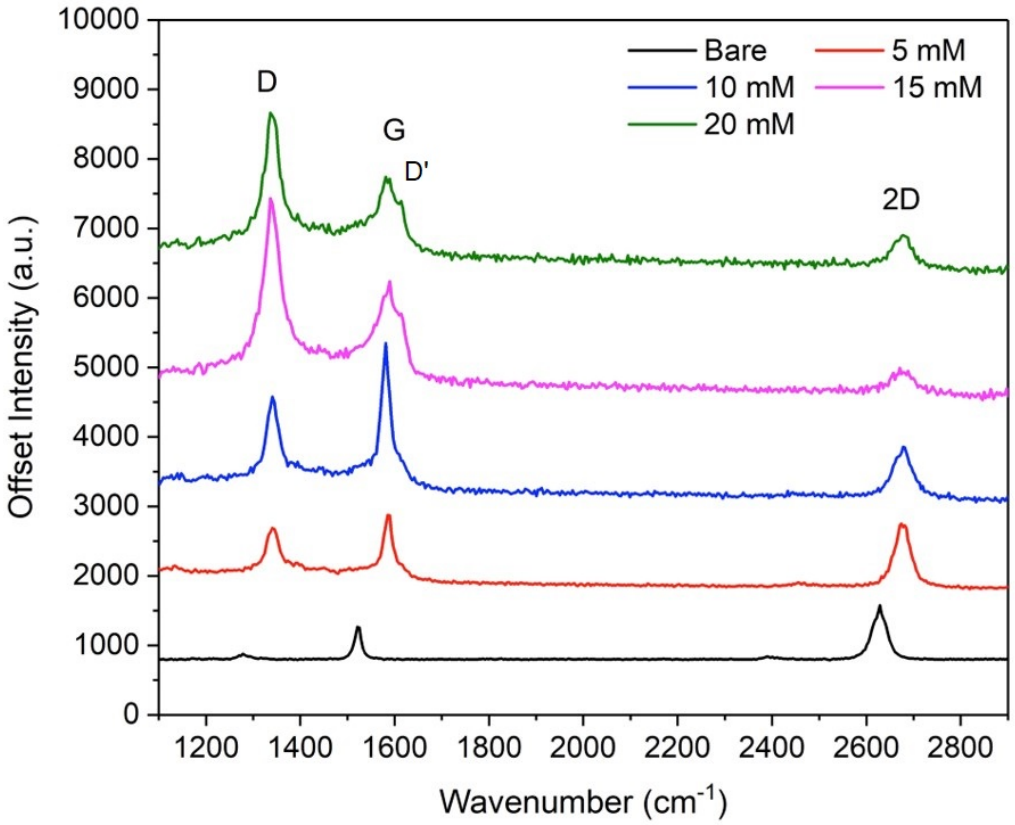

Figure 7.9: Raman spectra of CVD monolayer graphene functionalised with various concentrations of 4-nitrophenyl diazonium tetrafluoroborate.

When the lowest concentration of the diazonium salt (5 mM) was used to functionalise the graphene, a decrease in I(2D)/I(G) and presence of the D peak at 1540 cm^{-1} is immediately seen. As explained in section 6.2.2, the D peak arises from phonon scattering about a defect in the graphene structure. Defects are produced upon the change between sp^2 and sp^3-hybridisation in graphene upon the formation of a covalent bond. Hence, it is reasonable to assume that the prominent presence of the D peak in figure 7.9 is a result of NPD covalently bonding

to the graphene surface. With an increase in concentration, the D peak becomes even more pronounced and I(2D)/I(G) decreases with the exception of the highest concentration (table 7.1). This suggests that the increase in concentration indeed correlates to the increase in defects in the graphene structure, which indicates a higher density of covalent bonding to the graphene. For the highest concentration of 20 mM, the I(2D)/I(G) ratio increases due to the splitting of the G peak, which gives rise to the D' peak seen in figure 7.9. This is commonly associated with uniaxial strain in the graphene [185], which suggests that the high density of covalent bonding and disruption to the graphene structure also causes mechanical defects.

Figure 7.10 is reproduced from M. S. Dresselhaus et al. [185], which correlates the peak intensity ratio between the D and G peak with the length between defects present in graphene. The left-hand side of the peak is attributed to amorphous carbon and therefore, for analysis of crystalline samples, the right-hand side associated with spacing between defects > 4 nm, is used. From table 7.1, the I(D)/I(G) ratio is seen to increase with increasing NPD concentration, which suggests that the length between the introduced defects decreases. Therefore, the defect density increases as the graphene is functionalised using increasing concentrations, with 20 mM giving $L_D = 6$ nm.

Table 7.1: Table of the I(2D)/I(G) and I(D)/I(G) intensity ratio extracted from the Raman spectroscopy results for different NPD functionalisation concentrations.

Concentration (mM)	I(2D)/I(G)	I(D)/I(G)	L_D (nm)
0	1.81	0.17	> 20
5	0.96	0.71	13
10	0.36	0.63	14
15	0.24	1.78	7
20	0.41	2.30	6

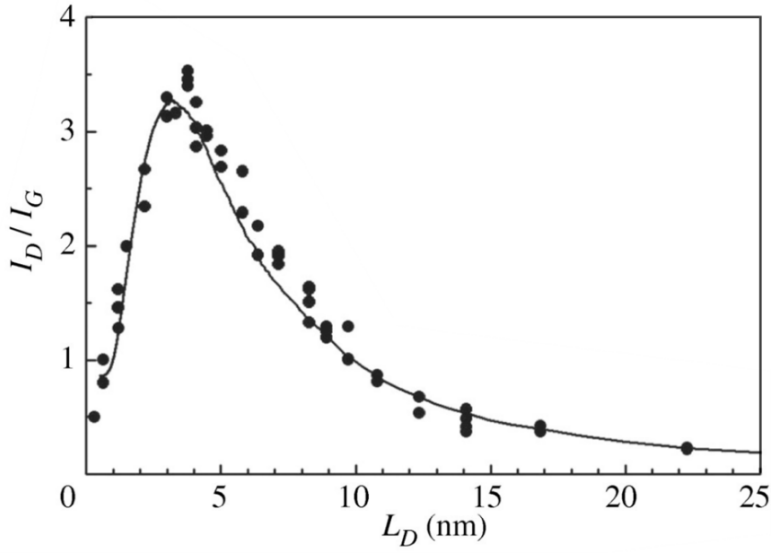

Figure 7.10: Correlation of I(D)/I(G) peak intensity ratio with the length between defects in graphene (L_D). Reproduced from [185].

With functionalisation at all concentrations, the covalent attachment of the NPD linker molecule also resulted in the upshift (blue shift) of the 2D and G peaks compared to bare graphene. Shifts in characteristic peaks can often be associated with strain but also doping effects within the material [186] and in graphene's case, an upshift can be interpreted to be a result of p-doping [187]. This is consistent with the mechanism of covalent bonding of the NPD molecule to the graphene: when the molecule is reduced, graphene donates an electron which results in an additional hole per molecule, hence leading to p-doping. This effect is more prominent between bare and 5 mM functionalised graphene whereas increasing the concentration does not cause significant subsequent upshift of the 2D or G peak. The lack of subsequent upshift may be attributed to the experimental method: different samples were functionalised at each concentration so some differences in their Raman spectra could be attributed to small intrinsic differences.

Despite the successful covalent functionalisation, there are drawbacks with using this method. By attaching these linker molecules, the appearance of the D peak in the Raman spectra in figure 7.9 and increasing defect density raises concerns about the amount of uncontrolled disruption to the sp^2 network that the functionalisation causes. In many cases, the increase in

defects may well positively contribute to the sensitivity of the device but also offer undesired sites for adsorption of non-target molecules and charges.

7.2.1.2 Non-Covalent Functionalisation Using PBASE

Having established potential problems with the covalent method of functionalisation, a non-covalent method was also explored. This involved the use of 1-pyrenebutyric acid N-succinimide ester (PBASE), which has dual functionality to allow for spontaneous binding to both graphene and antibodies as discussed in detail in section 4.1.2. The protocol in section 6.4.2 describes the making up of PBASE solution in dimethylformamide (DMF), which is a polar, aprotic solvent [188]. DMF is used because water would otherwise hydrolyse the NHS group. In order to investigate the effect of various chemical solvents on the electronic properties of graphene, graphene was transferred onto 90 nm SiO_2/Si and treated with DMF with and without PBASE.

The physisorption of chemical residues and molecular adsorbates are well known to affect the electronic properties of graphene [189]. Figure 7.11 shows the results of back-gated DC measurements of the same graphene sample whilst bare, after treatment with DMF, and functionalisation with PBASE in DMF.

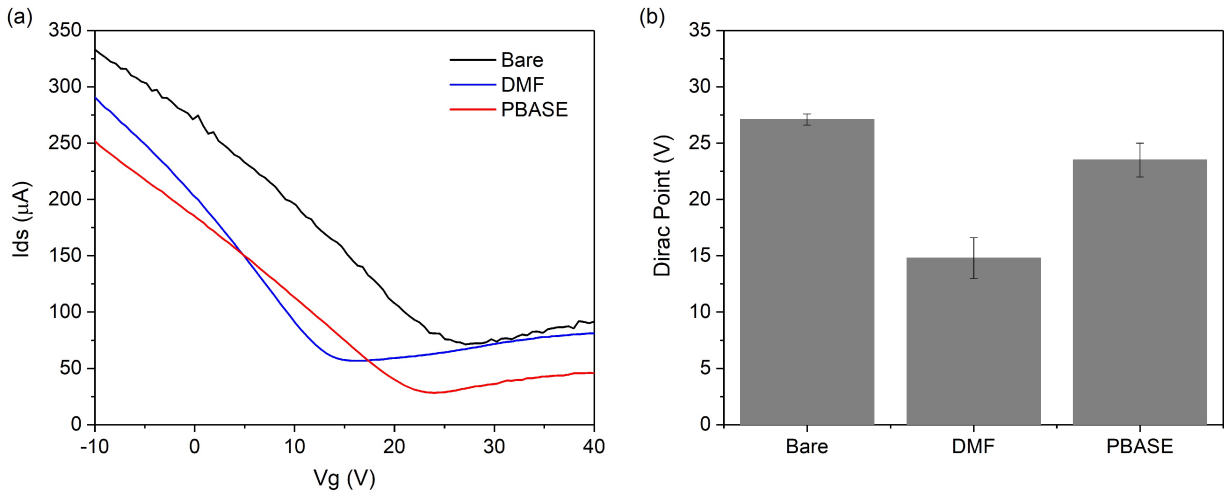

Figure 7.11: (a) I_{ds} - V_g transfer characteristics of monolayer graphene transferred onto 90 nm SiO_2/Si substrates for bare, treated with DMF and functionalised with 10 mM PBASE in DMF. (b) Corresponding Dirac points for each measurement. Error bars denote the standard deviation of the mean.

Upon measuring the bare sample, the Dirac point was visible at 27.1 V, seen in figure 7.11(a), indicating p-doping directly after the transfer process as seen with previous results in section 7.1.2. However, upon treatment with DMF, a lowering of the Dirac point, with respect to the bare graphene, is seen as the Dirac point shifts to 14.8 V. This suggests n-doping of the graphene and was also observed by G. Wu et al. [190], in which they attribute this to the electron donating nature of the DMF molecules when adsorbed on graphene. The temporary adsorption and n-doping by charge transfer may indeed occur due to adsorbed DMF molecules but because the sample is rinsed and dried afterwards, the DMF should completely evaporate. This would restore the graphene's electrical properties to that after the transfer, contradictory to the result in figure 7.11. As well as direct n-doping through charge transfer, it is likely that treatment with DMF helps to remove trapped water molecules at the graphene/SiO_2 interface, similar to treatment in acetone. As these trapped molecules commonly contribute to the p-doping of graphene after transfer, their removal therefore aids to restore the Dirac point to lower V_g.

Conversely, as the same sample is functionalised with PBASE in DMF, the Dirac point is seen

to shift to higher V_g to 23.5 V, which opposes the sole effect of DMF. Despite this positive shift, it is important to note that the Dirac point does not shift to higher V_g than that of bare graphene after functionalisation, hence the Dirac point is not restored to the V_g of bare graphene. Non-covalently bonded molecules modulate graphene depending on whether they are electron rich or deficient. PBASE itself is electronegative due to its NHS functional group so this p-doping effect, with respect to just DMF, is consistent with literature [40, 111]. However, as the Dirac point is neither restored, nor shifted to higher V_g above that of bare graphene, this suggests competing effects between the PBASE and DMF. Figure 7.11 indicates that some n-doping effect compared to bare graphene is still observed, as concluded by G. Wu et al. [190] and is not completely dominated by PBASE.

Shifts in the Dirac point can be attributed to the electron donating and withdrawing nature of the molecules, but also the displacement of ambient adsorbates introduced during the graphene transfer, such as water and oxygen. Therefore, as well as weak charge transfer effects associated with physisorption, the molecules also help to counterbalance p-doping effects of undesired residual charges introduced [105]. Overall, the study shows all solvents introduced to the graphene surface during functionalisation have effects on its electronic properties and cause measurable shifts in Dirac point.

Having established the effect on the electrical properties that PBASE has on graphene, its effect on the structural properties of graphene were also investigated and explored used Raman spectroscopy. The resulting spectra comparing bare and PBASE functionalised graphene is seen in figure 7.12(a). Originally (before functionalisation) the median I(2D)/I(G) intensity ratio of 2.37 shows reasonable quality after transfer. When functionalised with PBASE, figures 7.12(b), (c) and (d) show the decrease in the I(2D)/I(G) to 1.78 indicating some structural deformity, similar to what is observed for covalent functionalisation in figure 7.9(section 7.2.1.1).

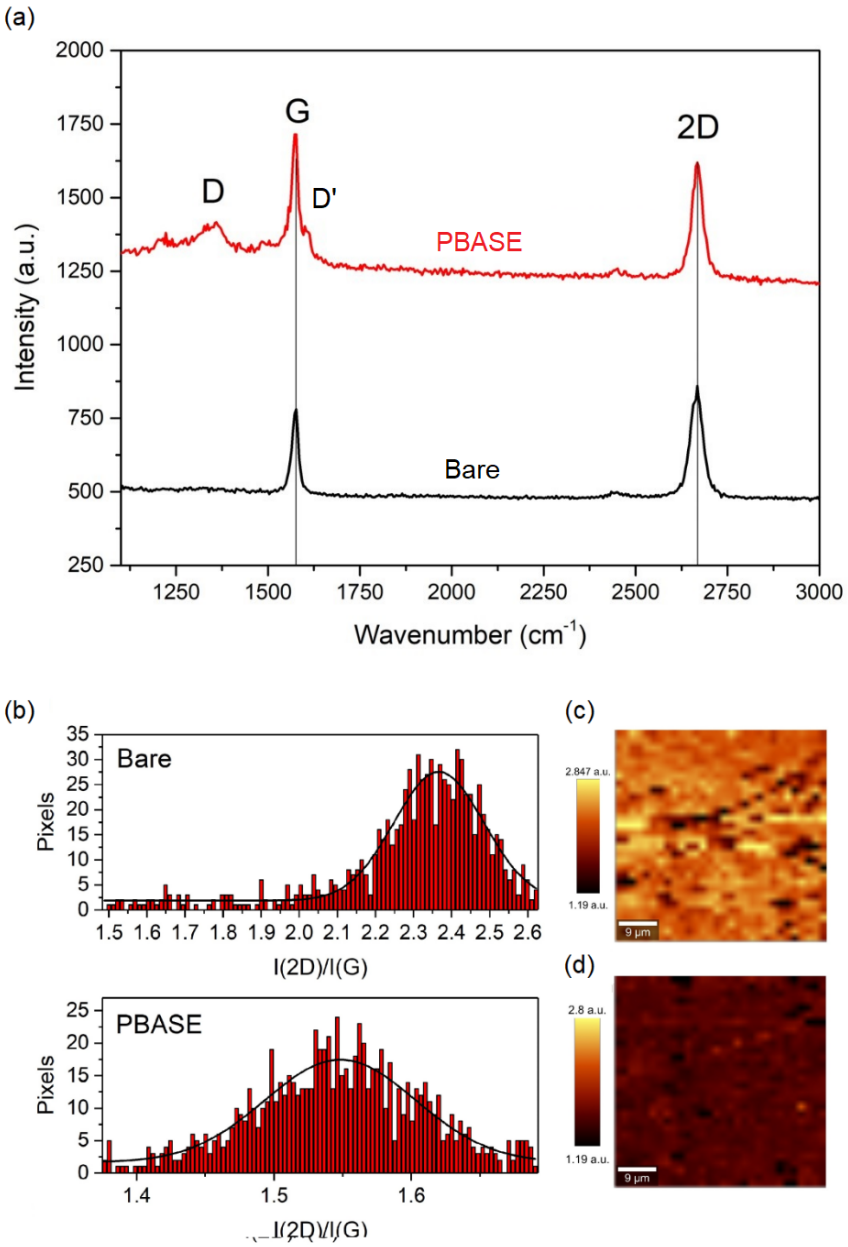

Figure 7.12: (a) Raman spectra of bare and 10 mM PBASE functionalised graphene with peak identifiers. The resulting spectra are averages of spectra taken from various points over the samples. (b) comparison of the I(2D)/I(G) intensity ratio between bare and PBASE graphene where histograms were fitted with Gaussian curves and the corresponding 2D/G Raman maps (c) before and (d) after functionalisation.

In addition to the reduction in I(2D)/I(G), functionalisation also causes a small D peak at 1350 cm^{-1}, again similar to the covalent case in figure 7.9. By comparing the result in figure 7.9 of graphene after covalent functionalisation with the NPD diazonium salt, the covalent functionalisation causes major disruption to the graphene structure. For the case of PBASE,

the mechanism of attachment to the graphene surface is different and hence, difficult to directly compare. However, figure 7.12 shows there is minimal disruption to the graphene structure from the low intensity of the D peak. In figure 7.9, the D peak that arises as a result of disruption to the sp^2-hybridised structure increases in intensity such that it surpasses that of the 2D peak and the I(2D)/I(G) ratio is significantly lowered at all concentrations compared to bare graphene. In comparison, the PBASE functionalised graphene, although the D peak appears, the spacing between defects is larger compared to covalent functionalisation and hence the defect density is expected to be smaller. The I(2D)/I(G) ratio is also not as largely affected and suggests that reasonable graphene quality is maintained.

Raman spectroscopy, although is useful for graphene characterisation, is unable to observe direct signals from the PBASE molecule itself. Hence, to support Raman spectroscopy and confirm that the observed structural changes to graphene are indeed from the PBASE functionalisation, UV - Vis and FTIR spectroscopy was performed.

The UV - Vis absorbance spectra in figure 7.13 shows that the peaks of interest mostly arise in the 200 - 400 nm range. Graphene was transferred onto sapphire substrates and analysed before and after PBASE functionalisation.

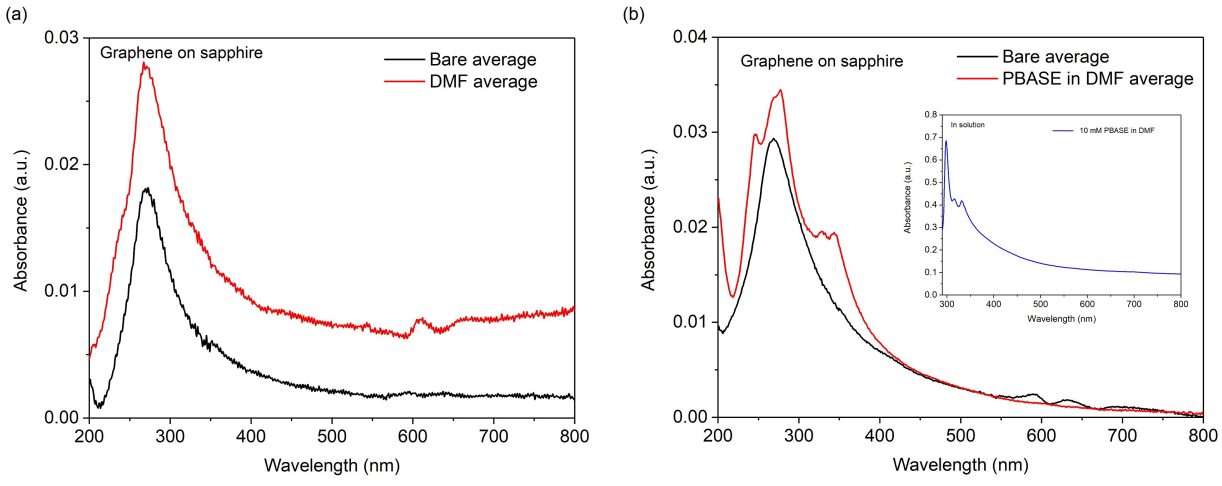

Figure 7.13: UV – Vis absorbance spectra for graphene transferred onto sapphire substrates (a) before (black trace) and after DMF treatment (red trace) and (b) before (black trace) and after functionalisation with 10 mM PBASE (red trace). Inset: UV - Vis absorbance spectrum for a solution of 10 mM PBASE in DMF.

The expected peak from graphene is observed at 272 nm, which present before and after functionalisation and consistent with literature [191, 192]. Figure 7.13(a) shows that DMF treatment does not affect the UV - Vis spectrum of graphene and hence peaks that arise in figure 7.13(b) must be due to PBASE only. The π - π stacking between PBASE and graphene is suggested to enhance electron delocalisation [180], which would cause absorbance at higher wavelengths as mentioned in section 6.2.5. The peaks at 326 and 340 nm should arise from enhanced delocalisation from PBASE functionalisation, which is consistent with results from X. Zhang et al. [193] and literature values of characteristic peaks of pyrene-based molecules [194]. This is also consistent with the control UV - Vis spectrum obtained for PBASE in DMF in solution as seen in the inset of 7.13(b). The additional peak at 245 nm may be from the NHS by-product, which is expected to absorb in this range [195], as a result of accidental NHS hydrolysis.

The FTIR spectra of copper foil, graphene on copper and graphene on copper with treatment with DMF and functionalisation with 10 mM PBASE are shown in figure 7.14.

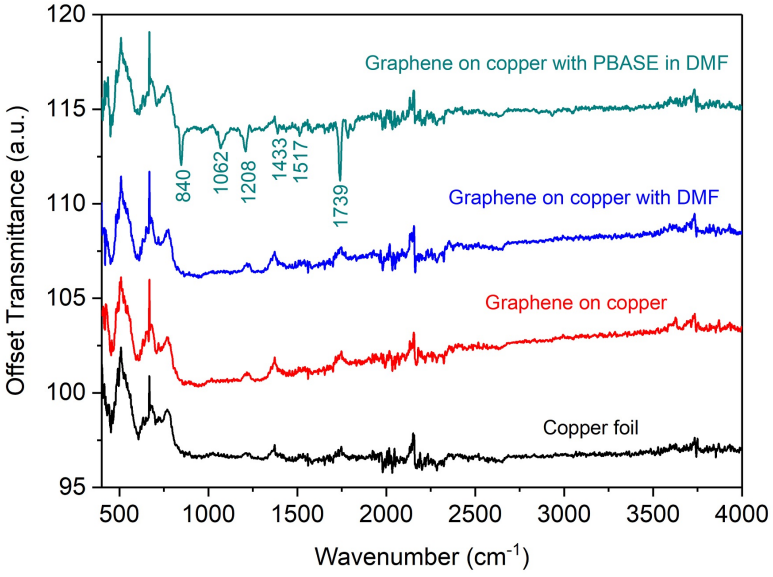

Figure 7.14: FTIR spectra of copper foil, CVD graphene on copper foil, CVD graphene on copper foil treated with DMF and CVD graphene on copper foil functionalised with 10 mM PBASE.

Figure 7.14 shows that there are no functional groups present on the surface of copper, graphene on copper or after treatment with DMF as expected. However, when functionalised with 10 mM

PBASE, multiple signals appear including those in the fingerprint region of the spectrum, which indicates the presence of chemical groups associated with PBASE. For example, signals present at 1062 and 1208 cm^{-1} are associated with C-O stretching. The weak signal at 1517 cm^{-1} could also correspond to N-O bond stretching, which is consistent with literature values [196]. More convincing is the strong signal at 1739 cm^{-1}, which is attributed to C=O stretching in the PBASE molecule that would otherwise not be present on bare graphene or graphene treated with DMF. Overall, the combination of electrical measurements, Raman, UV - Vis and FTIR spectroscopy spectroscopy provides a strong case to support the presence and non-covalent functionalisation of PBASE on graphene.

7.2.1.3 PBASE Concentration

As a result of the characterisation done in sections 7.2.1.1 and 7.2.1.2, PBASE was selected as the more appropriate linker molecule for making the graphene suitable for subsequent bio-functionalisation. Next, it was important to establish a suitable concentration for PBASE functionalisation and the effect of PBASE concentration on graphene's properties.

The structure of PBASE shows its one nitrogen atom present in the NHS ester group which, when the molecule is attached to the graphene surface, causes an increase in nitrogen signal when analysed using XPS. Figure 7.15 shows the N1s spectrum achieved as a result of functionalising various PBASE concentrations on separate graphene samples using the method described in section 6.4.2. As the PBASE concentration is increased, a proportional increase in the nitrogen peak is observed at $\approx$ 400 eV as more PBASE molecules non-covalently attach to the graphene surface.

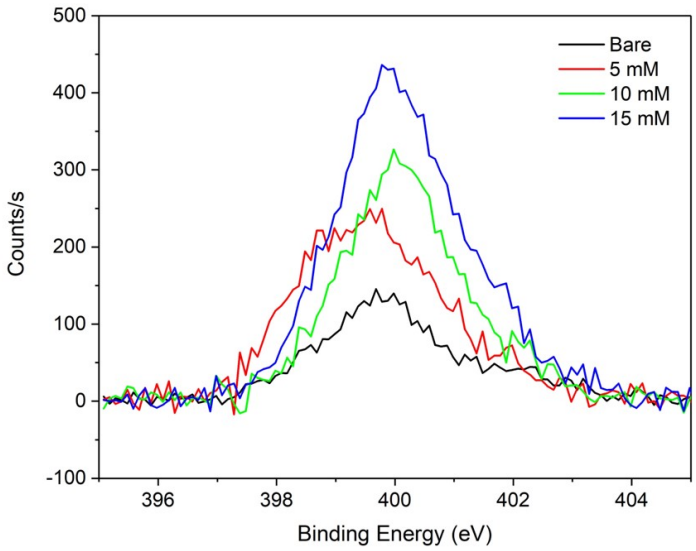

Figure 7.15: N1s XPS spectrum of CVD monolayer graphene functionalised with various concentrations of PBASE.

Due to its molecular structure, PBASE is expected to adhere to the surface as a self-terminating, self-assembled monolayer, however it is difficult to tell at which concentration the PBASE saturates as a homogeneous monolayer purely from XPS. It is expected that as the molecule π-π stacks with graphene hexagonal lattice, a reaction equilibrium is reached as the molecule saturates on the surface such that at higher concentrations, non-covalent bonding is terminated. Hence, as long as the N1s signal is significantly distinguishable from that of bare graphene, coupled with the expected change in the Raman spectrum (as seen in figure 7.12(a)), the non-covalent attachment of the PBASE linker molecule is guaranteed. However, figure 7.15 shows that even as the concentration is increased to 15 mM, the N1s peak still increases from 10 mM, indicating that the concentration increase may still have some effect after monolayer formation. This suggested the need for further investigation with electrical measurements.

As well as the influence of PBASE concentration on the surface properties of graphene, its effect on electrical properties was also investigated. As established previously in section 7.2.1.2, PBASE acts as an electron withdrawer whereby, as it non-covalently bonds to the graphene surface, it causes the shift of the Dirac point to higher V_g, with respect to DMF (although still lower V_g with respect to bare graphene). The I_{ds} - V_g transfer characteristic for a bare

graphene sample is seen in figure 7.16(a), whereby the typical p-doped characteristic arises as a result of the transfer process.

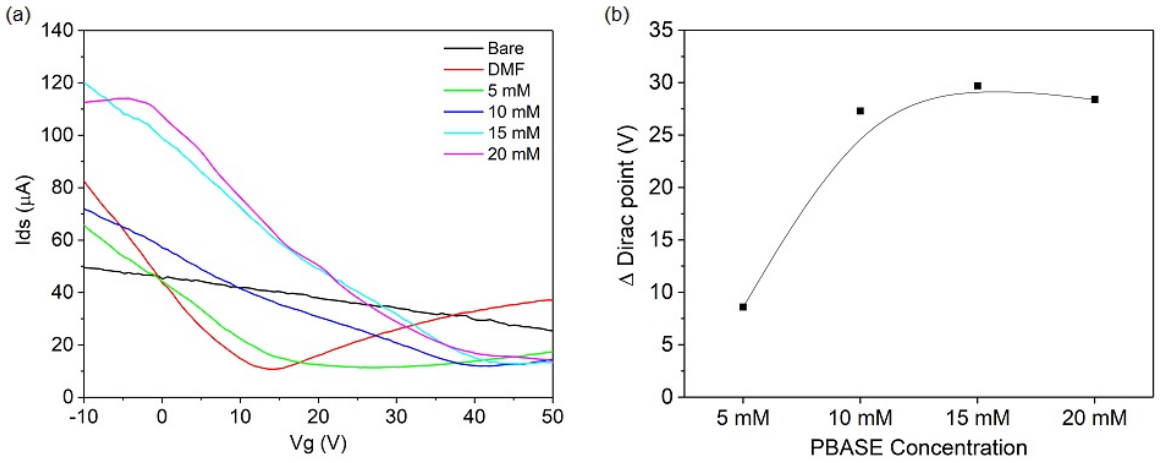

Figure 7.16: (a) I_{ds} - V_g transfer characteristics of bare graphene and graphene functionalised with 5, 10, 15 and 20 mM PBASE and (b) Dirac point shift with increasing PBASE concentration relative to that of graphene treated with DMF.

One bare gFET was treated first with DMF and functionalised with increasing PBASE concentrations between 5 – 20 mM and was back-gated to investigate the change in electrical properties. Figure shows the resulting I_{ds} - V_g transfer characteristics and confirms the result seen in figure 7.16 after DMF treatment. Similar to figure 7.11, the Dirac point shifts to higher V_g with the first functionalisation with 5 mM PBASE, which suggests p-doping of the graphene with respect to DMF. The coverage of non-covalently stacked pyrene-based molecules has not yet been extensively reported except only recently by X. V. Zhen et al. [112] where it was concluded that pyrene monolayer formation occurs and saturates by a concentration of 10 mM. Figure 7.16(b) supports this as the shift in Dirac point with respect to DMF appears to saturate at 10 mM, which may be associated with near-complete coverage of the graphene with PBASE molecules at this concentration. Additional PBASE molecules don't attach to the graphene surface after functionalisation with higher concentrations and hence no additional doping is observed.

In comparison to the XPS results seen in figure 7.15, the nitrogen signal does not appear to saturate after 10 mM. This discrepancy may be attributed to the fact that different samples,

which were fabricated independently were used for each PBASE concentration. As functionalisation relies on the π - π stacking, this is easily disrupted by possible residues left on the surface from the transfer process, which may vary between samples. This can lead to inhomogeneous PBASE coverage, which then affects the nitrogen detected by XPS.

7.2.2 Antibody Conjugation

After linker functionalisation whether covalent or non-covalent, to ensure the sensor is specifically sensitive to the target biomolecule and mitigate capture of unwanted species or impurities, specific antibodies must be attached. In this case, anti-CD63 antibodies are used, which specifically correspond to CD63 transmembrane proteins abundant within the exosome lipid bilayer [135]. By choosing non-covalent functionalisation by using PBASE, the antibodies bind to the PBASE by nucleophilic substitution that results in an amide bond as shown by figure 7.17.

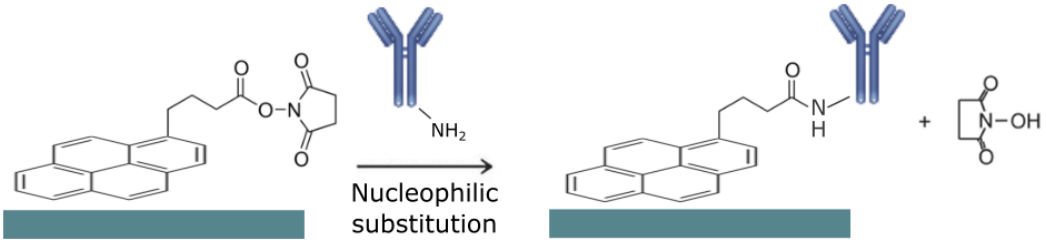

Figure 7.17: Schematic representation of the attachment of an antibody to a PBASE molecule by nucleophilic substitution.

Section 6.4.3 explains the method used for antibody conjugation whereby a high concentration of 100 µg/mL is used to guarantee a high surface density and maximise chances of exosome capture. XPS was used to determine the presence of antibodies on the surface by observing the C1s and N1s spectra as seen in figure 7.18(a) and (b) respectively. From the C1s spectrum in figure 7.18(a), the addition of antibodies on the graphene surface shows a difference in the typical asymmetric signal of graphene and similarly the N1s spectrum in figure 7.18(b) shows a significant increase in nitrogen signal due to the amines and amides in the proteins that make

up the antibody structure. This confirms that even without the PBASE molecule present on the surface, antibodies still adsorb onto the graphene surface due to its hydrophobic properties.

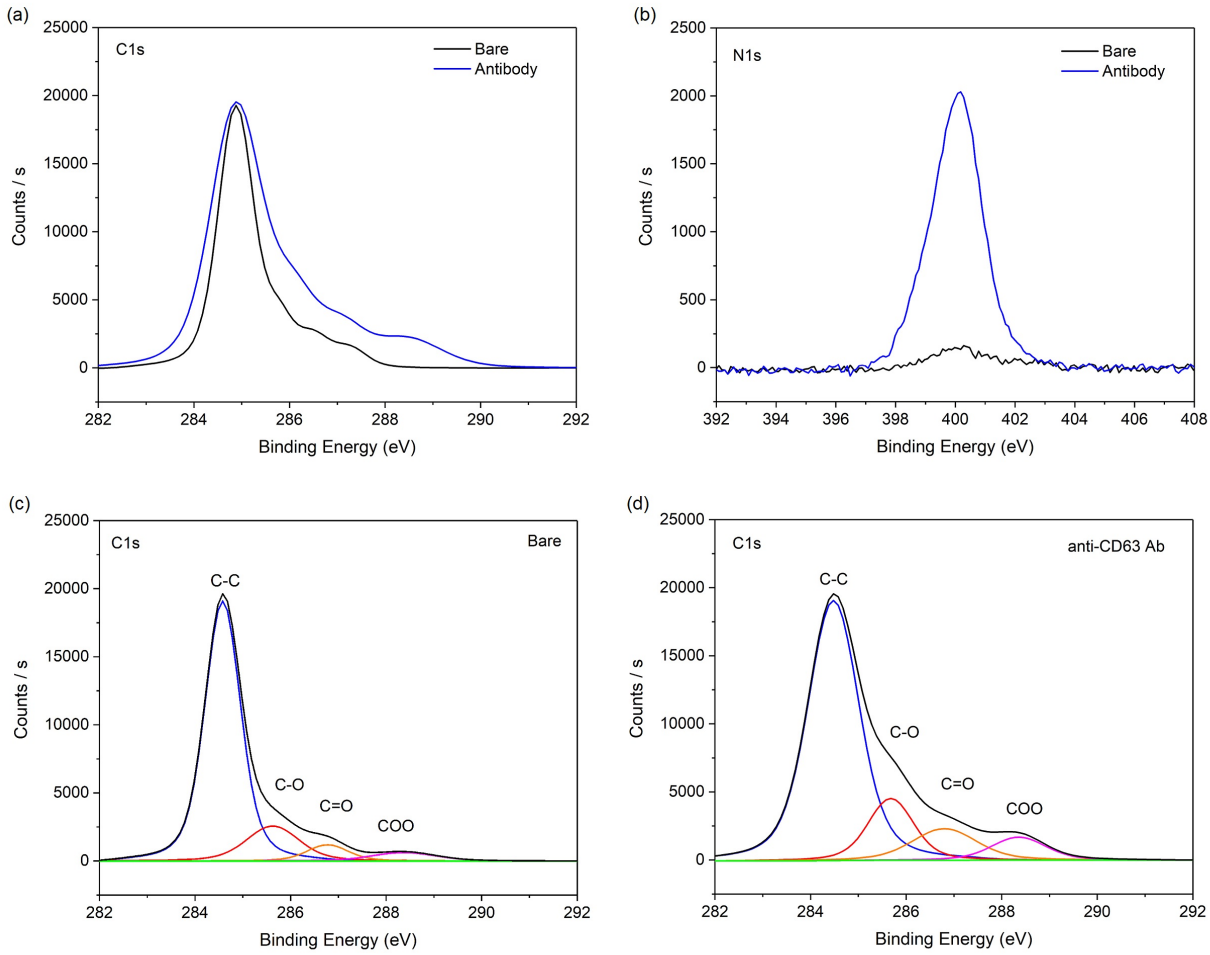

Figure 7.18: (a) C1s and (b) N1s spectrum of graphene when bare and functionalised with anti-CD63 antibody only. XPS analysis of the C1s spectra obtained from (c) bare and (d) anti-CD63 antibody functionalised graphene.

XPS analysis using peak deconvolution was employed for the C1s spectrum to investigate specifically which carbon groups are introduced by exosomes. From the C1s spectrum in figure 7.18(c), associated with bare graphene, the asymmetric tail at higher binding energies is typical of bare graphene with few organic contaminants, such as residual PMMA, which contributes C-O and C=O. When antibodies are adsorbed onto its surface, the numerous C-O, C=O and O-C=O groups associated with the protein structures that make up each antibody cause increases in their respective peaks at 285.8, 286.7 and 288.1 eV as seen in figure 7.18(d).

The Raman spectra of a sample functionalised with anti-CD63 antibodies only was compared to spectra of PBASE-anti-CD63 antibody functioned sample as seen in figure 7.19. In figure 7.19(a), it is difficult to observe fingerprint signals associated with antibodies, which are expected in the range of 1000 cm^{-1}, however, it is likely that this is largely due to the strong signal from the graphene that limits the detection of nucleic acid bands, which may require higher surface sensitivity to be observed [197]. In addition, the Raman spectra were obtained under dry conditions, which may further affect the resulting Raman signal intensity. Across the 5 scans taken at various points on the sample with only antibodies, there is relative uniformity in the results obtained suggesting that the use of 100 µg/mL results in the same effect on the graphene over the whole sample. The lack of the D peak shows that the antibodies do not introduce defects to the graphene structure or covalently bond. This suggests that their interaction is purely based on physisorption and no mechanical strain or deformation is imparted on the graphene itself.

When PBASE functionalisation is performed before the antibody conjugation, the resulting spectra averaged over 5 scans are seen in figure 7.19(a). This shows that there is a distinguishable difference between the Raman signals when PBASE is present between the graphene and antibodies. The splitting of the G peak and decrease in I(2D)/I(G) all support the previous results in section 7.2.1.2 and the averaged spectra recorded are representative of the samples as these are taken at multiple different locations. In figure 7.19(a), the spectra showing graphene with only antibodies (black trace) indeed shows weak Raman signal in the range of 1250 cm^{-1}, however when PBASE is present (blue trace), these signals are amplified meaning the PBASE may help to anchor the antibodies to the graphene surface after sample rinsing and drying as illustrated in figure 7.19(b).

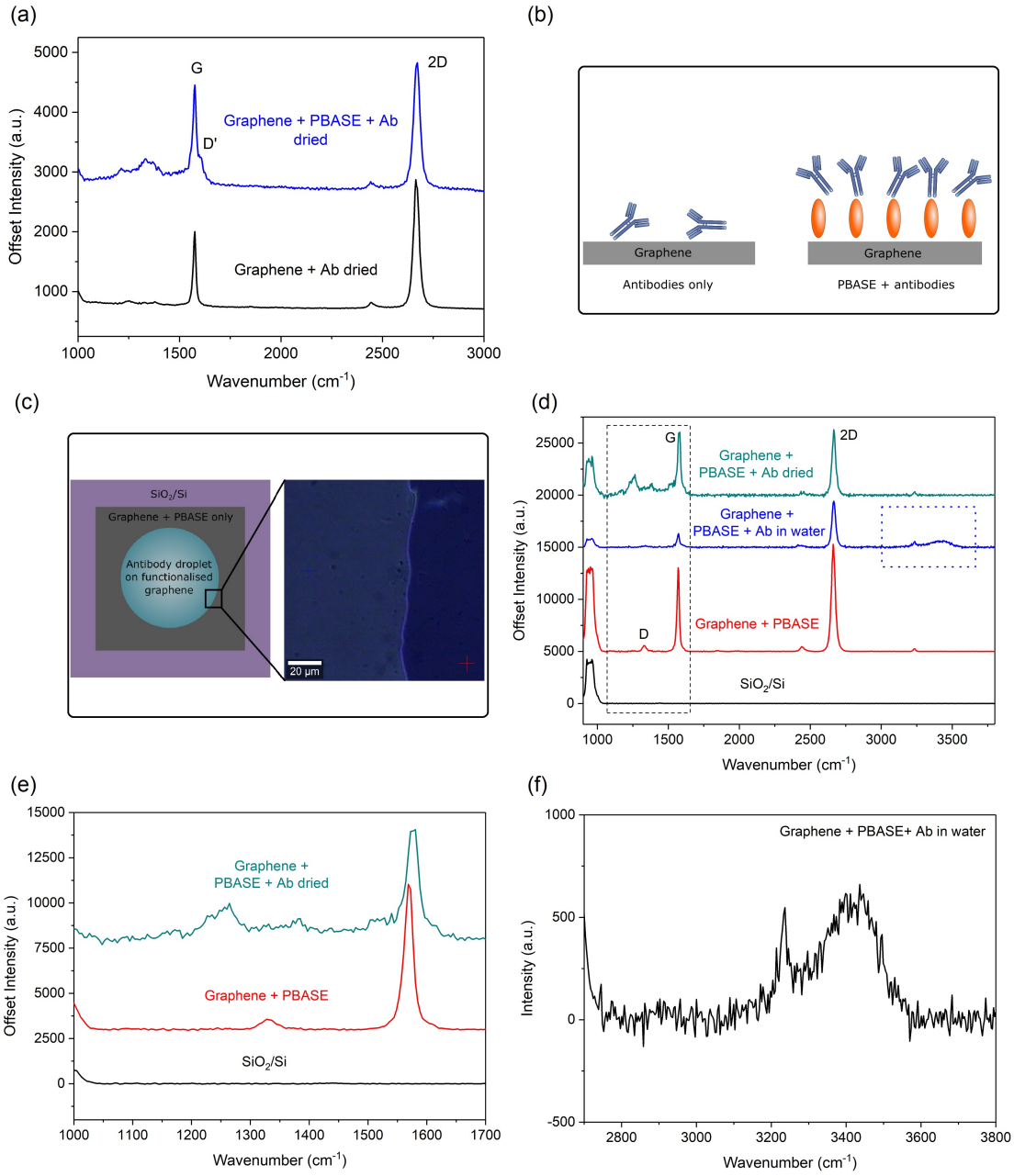

Figure 7.19: Raman spectra averaged over 5 separate spectra taken at different locations on the sample for (a) graphene with adsorbed anti-CD63 antibodies (black trace) and PBASE functionalised graphene with conjugated anti-CD63 antibodies (black trace). (b) Schematic representation of the distribution of antibodies on a graphene surface with and without prior PBASE functionalisation. (c) Shematic representation of the areas of a single functionalised sample analysed in Raman spectroscopy under wet and dry conditions and optical image of the boundary between the wet and dry conditions and locations of spectra taken. (d) Resulting Raman spectra of the Si/SiO_2 (black trace) with graphene functionalised with PBASE (red trace) and PBASE + anti-CD63 Ab functionalised graphene under wet (blue trace) and dry (teal trace) conditions. Zoomed in Raman spectra of the (e) dashed and (f) dotted region highlighted in (d).

By increasing the integration time and accumulations taken during Raman spectroscopy measurements, a more detailed study on antibody functionalised graphene surfaces was performed. One graphene sample transferred onto 90 nm SiO_2/Si was functionalised with PBASE and antibody conjugated according to the protocols in section 6.4.3. However, the sample was rinsed with PBS and DI water and not dried to maintain a droplet on the surface of the graphene for Raman measurements. The droplet in this case covered only part of the graphene sample, hence leaving some areas where there is graphene + PBASE only and the SiO_2/Si substrate only as shown in figure 7.19(c). After measurements in solution, the sample was subsequently dried for measurements of the antibody conjugated surface under dry conditions.

Figure 7.19(d) shows Raman spectra obtained over multiple areas of the same sample: SiO_2/Si substrate only, graphene + PBASE only and graphene functionalised with PBASE and antibodies under wet and dry conditions. In general, similar results are seen compared to those in figure 7.12 where the D, G and 2D peaks are observed for the areas of the sample containing graphene + PBASE only. For the spectrum of functionalised graphene in water, the D peak is more difficult to observe, and all other peaks are visibly less intense that those of the other spectra. This discrepancy is due to the presence of the water droplet on the surface as this makes it difficult to focus on the true sample surface.

From literature, Raman spectroscopy performed on antibodies in solution show a fingerprint region between $1000 - 1700$ cm^{-1} [198] associated with characteristic bands of the peptide group responsible for the structural make up of proteins, which are known as amide A, B, I, II ... VII in spectroscopic analysis. For the graphene sample, as mentioned before, the strong peaks associated with the graphene and SiO_2/Si substrate make it difficult to distinguish antibody signals from the noise. However, from initial observation of figure 7.19(d), the dried antibody conjugated area does display noticeable, additional bands in the expected range (as outlined by the black dashed box) that are not present in the spectra from graphene + PBASE and the substrate only. Figure 7.19(e) shows this wavenumber range more closely where prominent signals are observed at 1240 and 1270 cm^{-1}, which are associated in literature with amide III vibrations that correspond to the protein secondary structure [198].

Figure 7.19(e) shows multiple signals within the range where antibodies signals would be expected. It would be easy to dismiss these as noise, however if this was the case, this random noise would also be expected for the graphene + PBASE only and SiO_2/Si only spectra. In addition to the bands attributed to the protein secondary structure, bands can also be assigned to the 3D tertiary structure, for example, the signal present in figure 7.19(e) at 1540 cm^{-1} could refer to tryptophan, which is known as a marker for protein tertiary structure [199]. If this is the case, it is expected that this band may appear at a different wavenumber to that literature due to conformational changes upon drying of the protein on the graphene surface. In any case, it is apparent that the fingerprint region associated with antibodies, and therefore proteins, is detectable on graphene surfaces and there is a visible difference in spectrum compared to graphene + PBASE and substrate areas.

Alternatively, the higher wavenumber range can be used to detect the -OH stretching vibration peak of water. Figure 7.19(f) shows this peak present in a broad range between 3150 – 3600 cm^{-1}. Some focus on this peak due to the lack of overlap with other bands and is mostly used in spectroscopic analysis of cells to assess water content [200]. However, from graphene, the peak present at 3234 cm^{-1}, known as the second order 2D', obviously overlaps this region making it difficult to determine the exact wavenumber range of the -OH band. The use of Raman spectroscopy for exosomes in solution could provide information such as their water content, however, does not prove as useful for proteins. Overall, the combination of Raman spectroscopy and XPS is effective in supporting the presence of antibodies and functionalisation layers on the surface of graphene. In XPS, it is easier to distinguish the presence of antibodies from the PBASE layer from the obvious change in N1s signal, however by using Raman spectroscopy alongside this, measurements in solution are possible and distinct signals from the graphene, substrate and functional layers are easily separated.

7.2.3 Summary of Functionalisation

To summarise, functionalisation plays a key role in the operation and overall performance of the sensor. For the linker layer, two main functionalisation routes are available: covalent or non-covalent. By using 4-NPD as a covalent linker, Raman spectroscopy showed that major disruption to sp^2-hybridized structure of graphene occurs as suggested by the large increase in I(D)/I(G) intensity ratio with increasing 4-NPD concentration. Although covalent functionalisation may be more stable than non-covalent functionalisation, the high density of defects introduced to the graphene would degrade the electric properties and hinder sensitivity to target biomolecules. This defect density is also difficult to control and therefore this would further affect the reproducibility of the sensors.

Instead PBASE was chosen as a non-covalent alternative, which utilises the stable π - π stacking that occurs between graphene and the pyrene group of PBASE. Raman spectroscopy and XPS were both able to show the presence of the linker on the graphene surface. When investigating the effect of PBASE on graphene's electrical properties, literature suggests that the high electronegativity of PBASE's NHS group causes p-doping however back-gated DC measurements showed that there is a competing doping effect between PBASE and DMF (the solvent used to make the PBASE solution). Further electrical measurements showed a saturation in the electrical p-doping effect for PBASE concentrations above 10 mM. Therefore from this point, 10 mM PBASE was chosen as the concentration used for non-covalent functionalisation.

Anti-CD63 antibodies were then attached to bare and PBASE-functionalised graphene. Raman spectroscopy showed that without PBASE, weak Raman signals from the antibodies were detected in the range of 1000 cm^{-1}, however with the PBASE linker, these signals were much more pronounced. This indicated that without the PBASE linker, antibodies simply adsorbed onto the bare graphene surface and can easily denature, which would lead to weakened sensor performance. On the other hand, when conjugated to PBASE already present on the graphene surface, antibodies may retain their functionality as they are less likely to denature and more likely to retain their conformation. Therefore for the specific capture and detection of exo-

somes, the final functionalisation protocol chosen was functionalisation of PBASE followed by anti-CD63 antibody conjugation.

7.3 Liquid Measurements

To optimise sensor performance for liquid biopsies, the device must be suitable for measurements under physiological conditions and therefore in a variety of aqueous environments. To investigate the sensor response to liquids and its stability under these conditions, a PDMS microfluidic channel was fabricated as described in section 6.3.2 to contain liquids on the sensor surface in order to keep volumes consistent and prevent evaporation. Here, we describe the integration of microfluidics onto the gFET and the gFET response upon introducing different liquids through the channel. From here on, both bottom-gate and solution top-gated geometries of the gFET sensor were tested and compared. In each case, the geometry used for each measurement is specified.

7.3.1 Microfluidic Integration

Custom microfluidic channels were made from PDMS in-house. PDMS is a commonly used material for microfluidic applications and was easily applied to the sensor surface due to its elastic properties. As the sensor surface has some topology as a result of the metal deposited electrodes, PDMS was chosen over acrylic microfluidic channels to ensure the channels would be able to mould over any topological features to ensure a water-tight seal.

Originally, a microfluidic channel was simply placed on top of a gFET sensor. Upon introducing water into the microfluidic channel, leaks occurred occasionally from the channel sides and the channel itself was easily dislodged. Instead, an acrylic clamp was fabricated to hold the microfluidic channel in place above the gFET during liquid measurements (a detailed description of this set-up is shown in section 6.3.2).

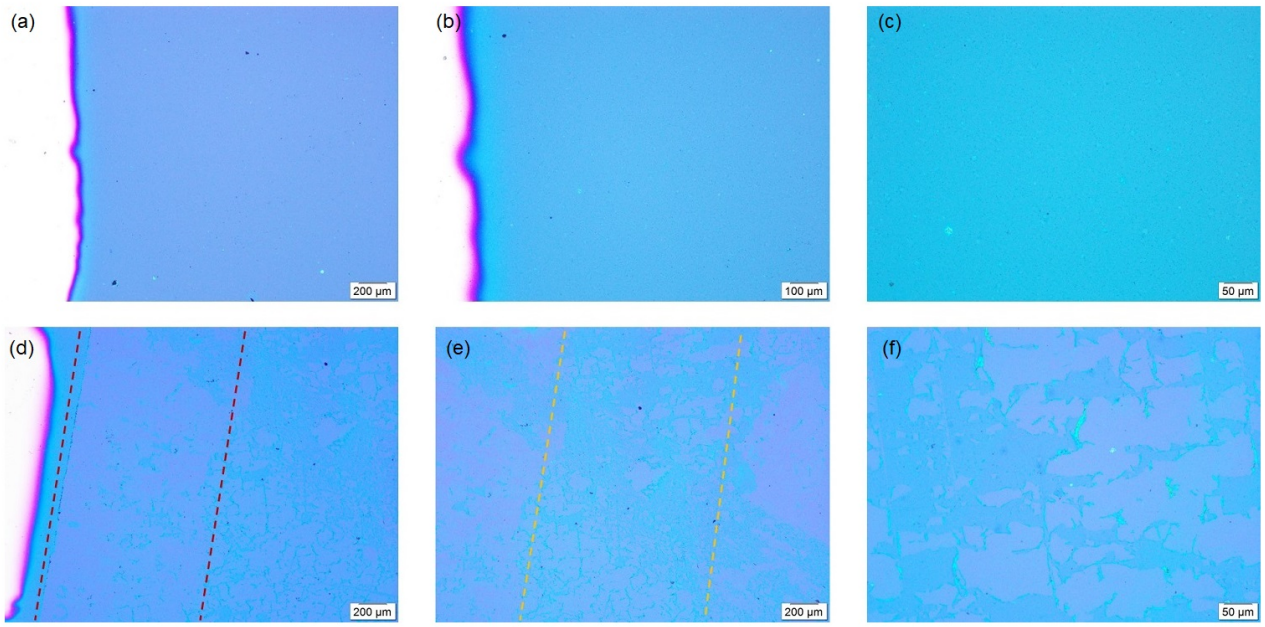

Figure 7.20: Optical images of bare graphene on 300 nm SiO_2/Si with metallised source and drain electrodes before microfluidic integration taken at (a) 5×, (b) 10× and (d) 20× magnification and after microfluidic integration taken at (d) 5×, (e) 5× and (f) 20× magnification. Red dashed lines indicate the area under the microfluidic channel walls and orange lines indicate the area of graphene exposed to liquid.

Initially the microfluidic channels and gFET sensors were thought to be reusable. To investigate the quality of the graphene before the channel and after the channel is removed, optical microscopy was performed on several samples. Figures 7.20(a), (b) and (c) show a sample at various magnifications before microfluidic integration and liquid measurements where the graphene quality is visually good. There are minimal tears and holes within the film, which led to good electrical characteristics as seen in figure 7.21. However, when the same sample was subjected to the microfluidic integration and liquids were subsequently introduced over the graphene surface and the optical images obtained are as seen in figures 7.20(d), (e) and (f). These show a heavily disrupted graphene film where holes and tears are present in all areas of the film. The PDMS in contact with the samples also peels off the graphene when the channel is removed. This means that if the surface of the graphene after electrical measurements in liquid were to be further analysed using Raman spectroscopy and/or XPS, the sample would no longer be useful for additional electrical measurements after removal of the PDMS channel.

As solutions are passed through the microfluidic channel, a small channel cross-sectional area and high flow rates can result in high pressure build ups, which correlate to high fluid velocities passing over the graphene surface. Effectively, the liquids shear off flakes of graphene resulting in the destroyed film seen in figures 7.20(d), (e) and (f), which completely inhibits electrical conduction between the source and drain. This is demonstrated in figure 7.21(a) where the conductivity of the graphene is not affected by the application of the microfluidic channel, however after flowing liquid through the channel, I_{ds} fluctuates near 0 A (attributed to noise) indicating a lack of electrical conduction through the graphene. The fact that the electronic properties do not degrade when the empty PDMS channel is simply placed on top suggests that microfluidic integration itself does not damage the graphene film.

The deterioration of the graphene due to the liquid flow through the channel therefore causes problems related to multiple passes of liquids through the microfluidic channel. In principle, one sensor would be subjected to PBS or a 'blank' liquid reference that does not contain the target molecule, which would serve as the reference measurement. A solution containing the target molecule would then be introduced through the channel and the resulting electrical characteristic compared to that of the reference. If the graphene film degrades after the first liquid, multiple measurements will not be possible or will be skewed by the reduction in electrical conduction. In order to mitigate this, lower flow rates were used to introduce liquids through the microfluidic channel and the resulting films are seen in figure 7.22 after PDMS channel removal. DC measurements in figure 7.21 (b) show that upon using lower flow rates (by gentle pipetting), the conductivity of the graphene is preserved.

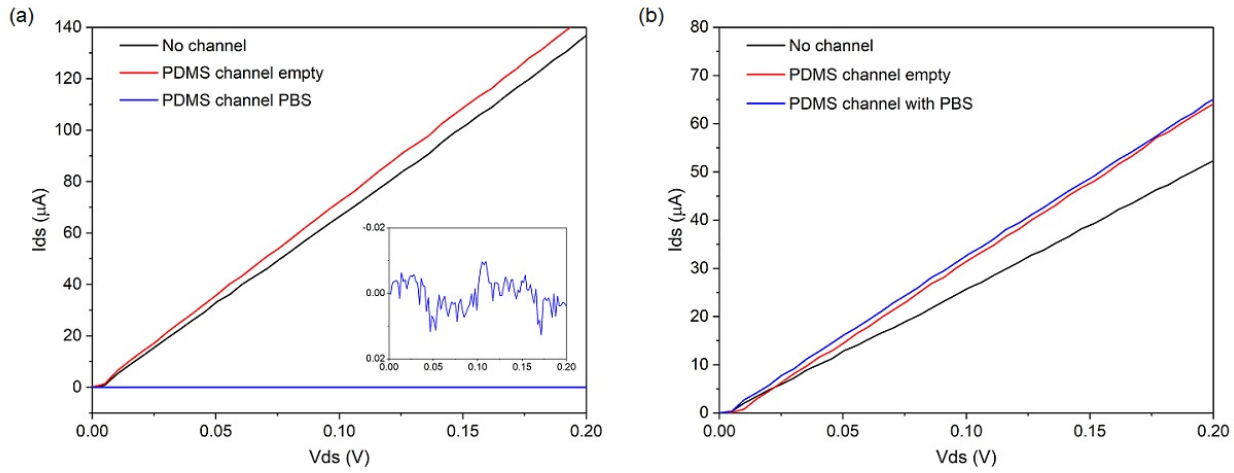

Figure 7.21: I_{ds} - V_{ds} output characteristics for 2 bare graphene samples before and after microfluidic integration with the PDMS channel. PBS was introduced to the channel with (a) high flow rate where the inset shows a scaled I_{ds} - V_{ds} output characteristic with PBS where I_{ds} hovers around 0 A and (b) lower flow rate where I_{ds} is maintained > 0 A.

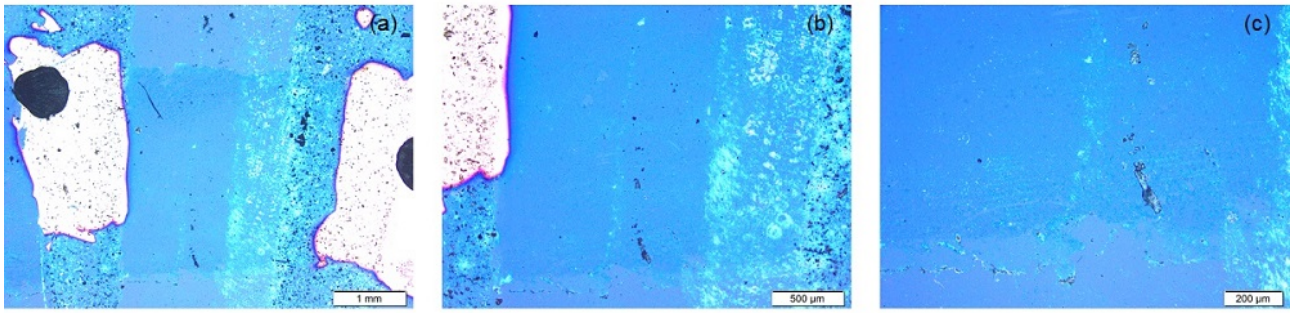

Figure 7.22: Optical images of bare graphene on 300 nm SiO_2/Si with metallised source and drain electrodes after microfluidic integration with lower flow rate taken at (a) 1.25×, (b) 2.5× and (c) 5× magnification.

7.3.2 Electrical Response to De-Ionised (DI) Water

Before understanding the sensor's response to more complex biological liquids, the simplest case of DI water was investigated first. Using DI water ensures that the majority of mineral ions (cations and anions) such as sodium, chloride, calcium and sulphate are removed leaving purified water [201]. As a result, the electrical conductivity is significantly lowered compared to tap water. As fewer charged species should be present, the graphene is expected to show

minimal response to DI water before and after functionalisation.

Figure 7.23 shows PBASE and anti-CD63 Ab functionalised gFET responses to both air and DI water. The response from air looks similar for every sample whereby the graphene has been highly p-doped from the device fabrication process and the only sample that gave a visible Dirac point was sensor 2. As DI water is passed through the microfluidic channel, the I_{ds} - V_g response tends to broaden indicating a decrease in hole mobility (the same is assumed for electron mobility, although this would require $V_g > 120$ V to be seen, which may cause a breakdown in the SiO_2 dielectric). This may be attributed to the adsorption of H^+ ions to graphene defect sites causing an increase charge scattering. This mechanism is discussed in section 4.3 and shows similar results to K. Besteman et al. [124] and A. Newaz et al. [126]. Air and water have different electric permittivities, hence this difference causes a slight change in the capacitance at the graphene surface. From equations 7.1 (where μ is mobility, C is the capacitance, L and W are the length and width of the graphene film, respectively) and 3.2, water has a higher electric permittivity than air, which leads to an increase in capacitance and decrease in mobility. This is a small effect at the capacitance that dictates the mobility is mostly governed by the SiO_2 layer but it may cause some slight broadening of the I_{ds} - V_g response. Additionally, since water is a polar solvent, A. Newaz et al. [126] have demonstrated a significant decrease in mobility for graphene surrounded by polar solvent compared to suspended graphene or graphene in non-polar environments. The dipole moment of water molecules means that there is a slight difference in charge density close to the graphene surface depending on the molecular orientation. The dipole moments are then suggested to result in Coulomb scattering, similar to the effect of charged residues on the graphene surface, which decreases mobility as observed in figure 7.23.

$$\mu = \frac{1}{C}\frac{L}{W}\frac{\Delta I_{ds}}{\Delta V_g}\frac{1}{Vds} \tag{7.1}$$

The removal of most charged species from water by de-ionisation would imply a minimal response of the gFET as charged ions that could normally result in doping effects are removed.

This is observed in the responses from sensors 1, 3, 4 and 5 where no significant changes are seen apart from the slight curve broadening. However, sensor 2 shows a 'w' shaped characteristic where a double minimum is seen, similar to the effect of regional doping of graphene [202].

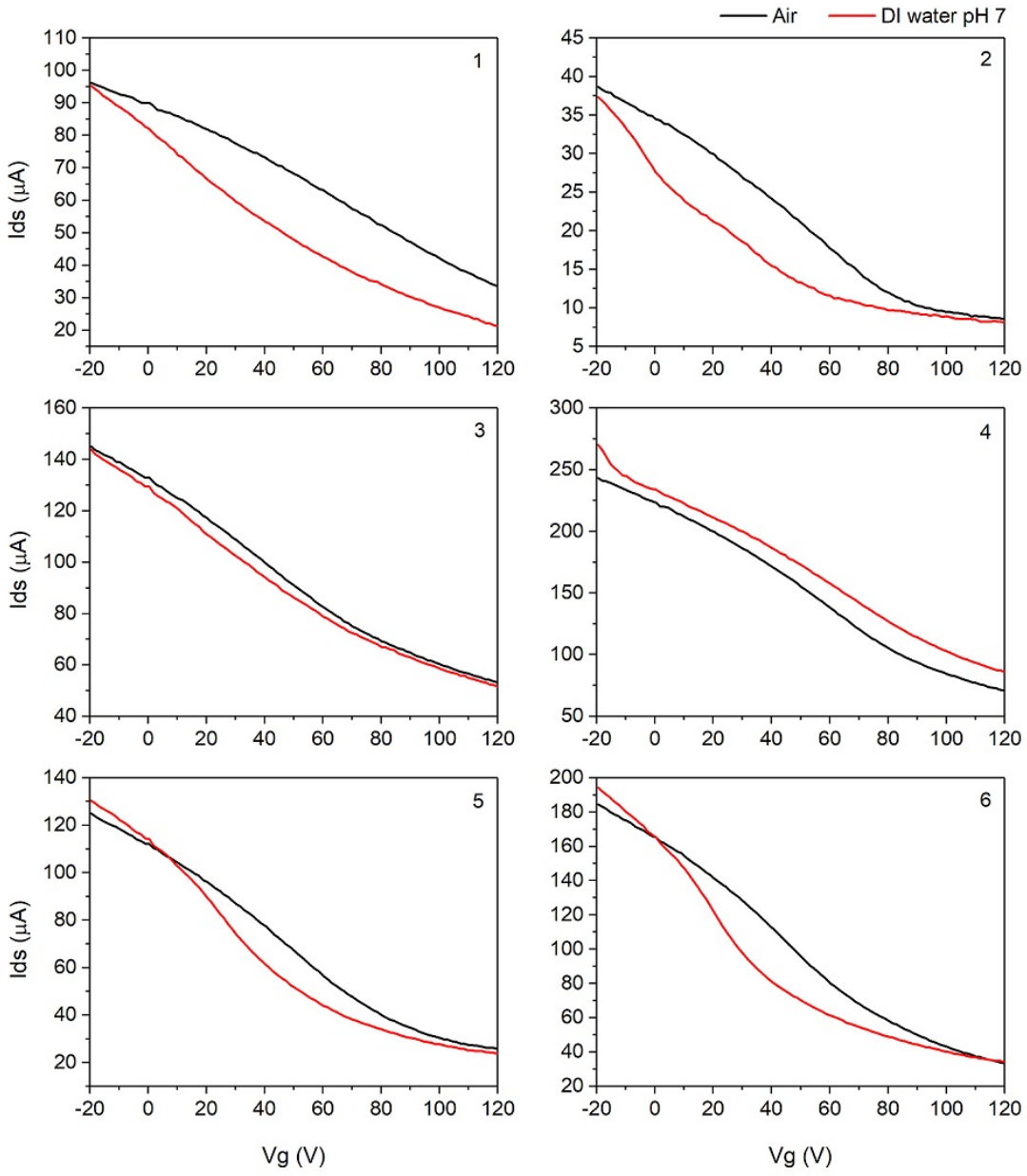

Figure 7.23: I_{ds} - V_g transfer characteristics from 6 different PBASE and anti-CD63 Ab functionalised gFET sensors and their responses to air and DI water pH 7 in the microfluidic channel.

Sensor 6 also displays a more significant change in I_{ds} - V_g curve shape. As each graphene sample was prepared independently, a higher number of defects and particularly surface roughness

would cause the graphene to be more sensitive to the adsorption of water as described by J. Moser et al. [203] and M. Luna et al. [204]. It is important to attempt to minimise this effect by careful sample preparation and avoid issues such as holes, tears and sample surface roughness (as described in section 7.1.1) as the effect of the liquid environment could disrupt the detection of the target biomolecules.

7.3.3 Back-Gated Response to PBS

7.3.3.1 PBS Concentration and Debye Screening

An important parameter for biosensing in aqueous environments is the Debye length; derived from κ as mentioned in section 3.2. After binding occurs, excess charges within the Debye length of a solution can further affect the graphene electronic properties and this can be seen as changes in the measured I_{ds} - V_g curve. However, if target molecules react to receptors outside the double layer, charge screening can occur by the ions in the buffer solution resulting in little changes and a less sensitive sensor.

By using PBS, the solution simulates the osmolarity and ion concentrations of that of human serum [205], hence exosome transmembrane proteins can maintain both their activity and conformation under these conditions. The ionic strength of PBS will therefore determine the EDL formed and the Debye length, calculated by equation 7.2, defined by parameters in section 3.2.1.

$$d = \left(\frac{\epsilon_r \epsilon_0 kT}{2e^2 N_A \sum_i z_i^2 c_i}\right) \tag{7.2}$$

To investigate the influence of PBS concentration on the device sensing ability, two devices were fabricated using monolayer graphene transferred onto 90 nm SiO_2/Si and functionalised with PBASE and anti-CD63 Ab. Two different PBS concentrations were chosen and 10 µg/mL exosomes were prepared using PBS at 0.1× and 0.0001× PBS. For each device, a 10 µL droplet

of PBS was placed on the surface for electrical measurements. Due to the preliminary nature of these measurements, there were not performed using the PDMS microfluidic channel and instead were made using droplets of known volume deposited directly on the graphene surface.

Table 7.2: A table showing the most common composition of 1× PBS, concentrations and ion valences.

Salt	Concentration (mol/m^3)	z_i
NaCl	137	1
KCl	2.7	1
Na_2HPO_4	10	2
KH_2PO_4	1.8	1

The standard composition of PBS is shown in table 7.2 where NaCl is the most prominent component and hence contributes the most to the ionic strength of the solution. By calculating the ionic strength of both PBS concentrations, d can be calculated for each using equation 7.2. Table 7.3 shows the resulting composition and ionic strength of 0.1× and 0.0001× PBS both diluted in DI water from a 1× stock solution. Hence, a value of d is obtained as 2.42 nm and 76.5 nm for 0.1× and 0.0001× PBS respectively.

Table 7.3: A table showing the composition of 0.1× and 0.0001× PBS, concentrations, valences and parameters for calculations for ionic strength.

	0.1× PBS		0.0001× PBS	
Salt	Concentration (mol/m^3)	$z_i^2 c_2$	Concentration (mol/m^3)	$z_i^2 c_2$
NaCl	13.7	13.7	0.0137	0.0137
KCl	0.27	0.27	2.4×10^{-4}	2.4×10^{-4}
Na_2HPO_4	1	2	1×10^{-3}	2×10^{-3}
KH_2PO_4	0.18	0.18	1.8×10^{-4}	1.8×10^{-4}
		$\sum = 16.15$		$\sum = 0.01615$

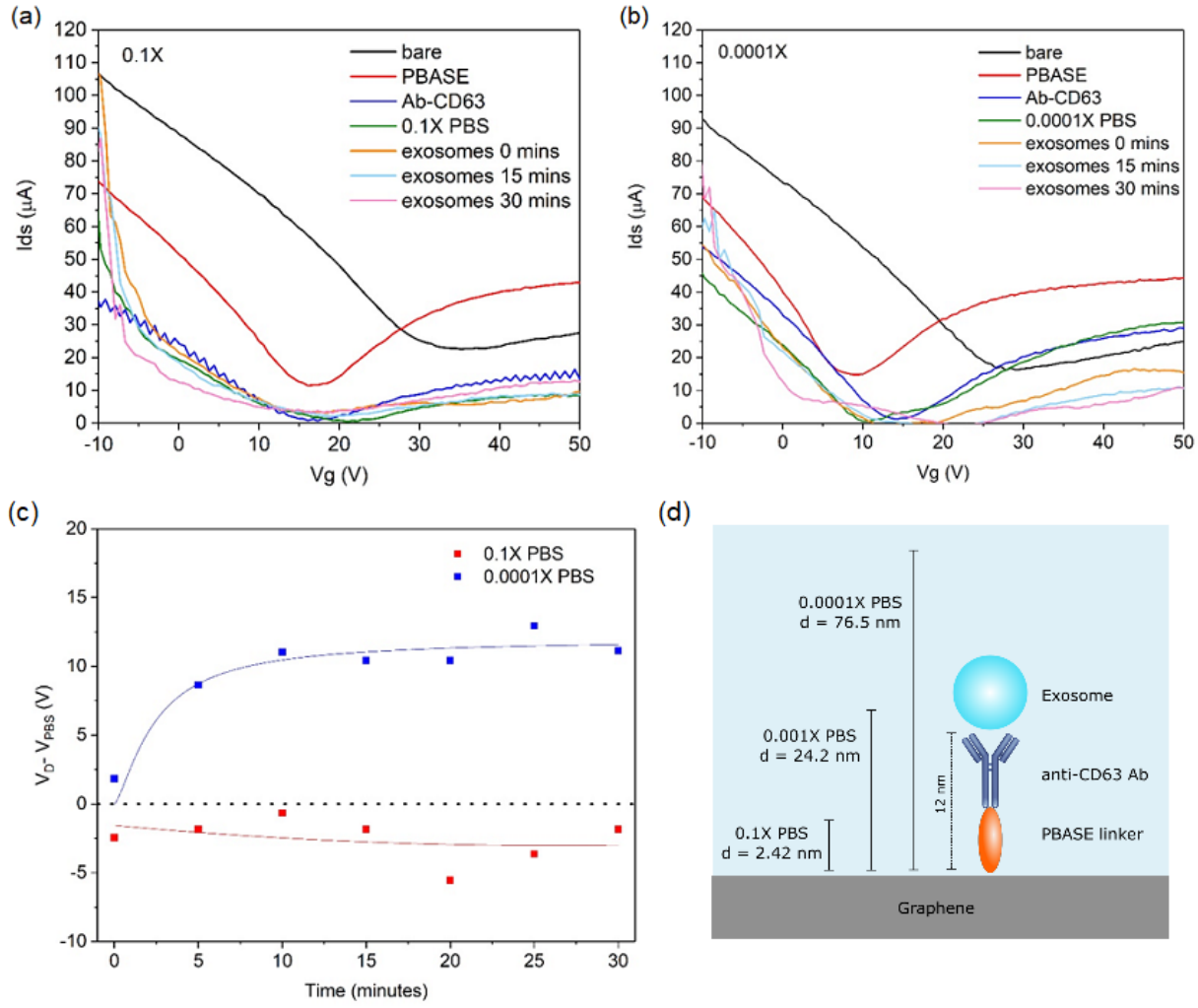

Figure 7.24: I_{ds} - V_g transfer characteristics of 2 PBASE and anti-CD63 Ab functionalised gFET sensors showing their responses to exosomes using a) 0.1× PBS and b) 0.0001× PBS. c) Shift in Dirac point with exosomes in respect to the Dirac point with PBS with time. (d) Schematic representation of the calculated Debye length, d, for 0.0001, 0.001 and 0.1× PBS with respect to the length of the functionalisation layers above the graphene surface.

Figure 7.24(a) shows the response of the device using 0.1× PBS where a clear Dirac point is observed at 34.2 V suggesting p-doping for the dry sample. After functionalisation and introduction of the PBS as a droplet, the Dirac point shifts and the curve dramatically broadens. The lowering of the overall current upon binding of the antibodies implies increased resistance of the graphene for all values of V_g. As antibodies conjugate to the graphene + PBASE surface, morphological effects such as introduction of stresses, strains and physical deformation could result in charge scattering, therefore increasing resistance across the film. This effect is observed

for both samples as seen in figures 7.24(a) and (b). As exosomes are introduced in 0.1× PBS, there is little variation in the Dirac point due to the screening of the exosome charges by the abundance of ions in solution (figure 7.24(c)) [206]. At such high ionic concentrations, the EDL forms at only 2.42 nm from the surface. As exosomes are expected to be $\sim$ 12 nm from the graphene surface due to total length of the PBASE - anti-CD63 Ab conjugate (figure 7.24(d)), this Debye length is too small for the graphene to detect any electrical contribution even after 30 minutes.

Figure 7.24(b) shows the response of the second sensor to exosomes in 0.0001× PBS. In this case there is a shift in the Dirac point with exosomes with respect to the PBS position, which does not occur for 0.1× PBS. The difference in response of the two sensors is shown in figure 7.24(c). This is attributed to the lower effect of screening as the Debye length has been increased to 76.5 nm because of lower ionic strength. This allows the receptor-ligand reaction to occur within the Debye length and hence a change in graphene's electronic properties is observed. In figure 7.24(c) an increase in the Dirac point occurs which eventually saturates due to the presence of exosomes, which is attributed to the achievement of an equilibrium of exosomes binding to the conjugated antibodies. This results in an overall p-doping effect on the graphene. As exosomes are expected to be negatively charged at pH 7, the overall p-doping effect suggests the electrostatic effect is dominant whereby the negatively charged exosomes cause an increase in positive charge graphene. As well as p-doping of the graphene, the decrease in current with exosomes suggest charge scattering and lowering in charge carrier mobility and conductivity.

In conclusion, this study showed the effect of the PBS concentration on the response of the gFET sensor, with the ionic concentration (and Debye length) being the determining factor. For the sensor to detect exosomes, it must be ensured that the ligand-receptor reaction occurs within the Debye length. Hence, the Debye length must be able to include the length of functional groups, antibodies and the site of exosome-antibody binding [43]. The extreme case of 0.0001× PBS allows for this to happen, however it has been shown that exosomes in environments dissimilar to physiological conditions may result in disruption of protein structure, loss of protein activity and/or loss of binding affinity [87]. As a compromise between the positive effects on sensitivity

of using a low PBS concentration and the negative effect this has on exosome viability, a less dilute PBS concentration of 0.001× was chosen for further measurements to minimalise disturbance to the exosomes and their phospholipid bilayer membranes.

By using equation 7.2 under room temperature and $\epsilon_r = 80$ (the relative permittivity is approximated at that value as the 0.001× dilution factor in DI water results in the dielectric properties being mostly represented by that of water). This gives $d = 24.2$ nm, which is a distance large enough to include all functional groups ($\sim$ 12 nm) and allow for graphene to detect exosome binding as shown in figure 7.24(d).

7.3.3.2 Double Conductance Minimum

Having established an appropriate PBS concentration such that the graphene doesn't screen target biomolecules, integration using the PDMS microfluidic channel was then employed. As the back-gated gFET is set up such that measurements are all relative to a reference solution, the sensor's response in air becomes less relevant. Instead, the sensor's response to PBS is what's used as the reference (or 'blank' measurement) as all biological species investigated were made up in the chosen PBS concentration.

Initially, a bare graphene sensor's response to PBS was investigated as seen in figure 7.25. Here, there is a clear difference between the sensor with air in the microfluidic channel compared to when PBS is present. The effect of the conductance minimum from introducing PBS into the microfluidic channel is discussed in greater detail in the next paragraph. The response to PBS also shows no variation in time. This is expected as there should be no change in the interaction between PBS and the graphene surface over time.

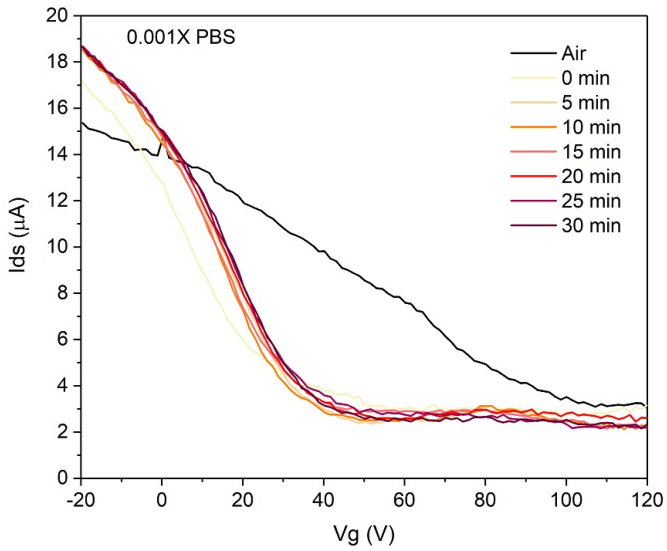

Figure 7.25: I_{ds} – V_g transfer characteristic of a bare graphene sensor showing its response to air and 0.001× PBS when left in the microfluidic channel when left over 30 minutes.

4 different sensors were fabricated and fully biofunctionalised before having 0.001× PBS passed through the channel where the resulting I_{ds} – V_g transfer characteristics are shown in figure 7.26. In each case, the original Dirac point, with the graphene exposed to just air was not observed, again due to high p-doping. However, when PBS was introduced through the channel, all gFET sensors showed a significant change in I_{ds} – V_g response. For all 4 sensors, a new and additional conductance minimum appeared at roughly the same V_g value. This is a result of charge modulation in only the area of the graphene film exposed to solution. The area exposed to PBS becomes regionally doped and hence has a different Dirac point than that of the unexposed graphene. In principle, the I_{ds} – V_g transfer characteristic would show a double dip due to the superposition of the two Dirac points if the original could be seen with these samples, but because of the intrinsic p-doping of the graphene it is not possible without voltage breakdown of the substrate. The double minima have been previously reported with both metal electrodes [202] and spatially controlled self-assembled monolayers on graphene [207, 208].

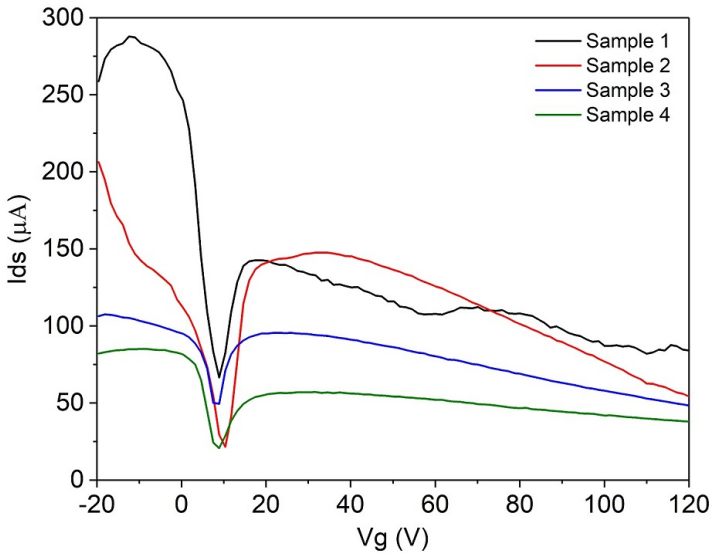

Figure 7.26: I_{ds} – V_g transfer characteristics for 4 different gFETs all identically biofunctionalised showing their response to 0.001× PBS when introduced through a microfluidic channel.

Essentially, two different regions with different doping levels are created within the same graphene film: the p-doped region not exposed to PBS and the less p-doped region exposed to PBS. For the purpose of explanation, the less p-doped region from here on is referred to as the n-doped region as it is n-doped in respect to the highly p-doped region. This causes a localised region of the graphene to have different electronic properties to the bulk of the film and a higher density of electrons is induced in the graphene film under the channel as a result of the PBS. Figure 7.27(a) shows the superposition of the n-doped and p-doped Dirac points on the same I_{ds} – V_g transfer characteristic where the n-doped area is associated with the graphene under the PDMS microfluidic channel in figure 7.27(b) and hence results in a difference resistance. The additional minimum for each sensor appears at similar V_g value with average position of 9.3 ± 0.7 V. This indicates that independently fabricated sensors show similar response 0.001× PBS. For future measurements with exosomes, this then becomes the reference point from which shifts are determined as the same graphene area exposed to PBS is subsequently exposed to exosomes.

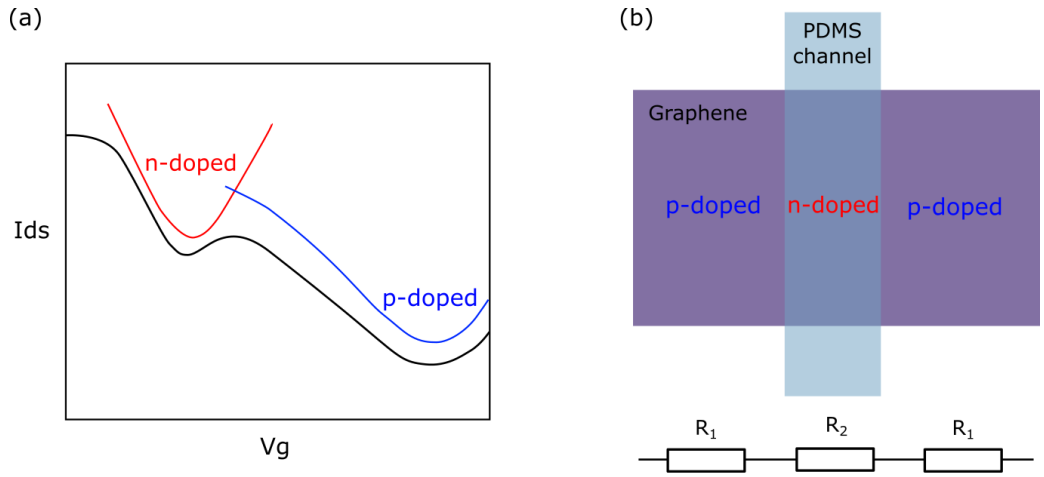

Figure 7.27: (a) Schematic of the I_{ds} – V_g transfer characteristic with double conductance minima showing the superposition of 2 graphene Dirac points and (b) schematic of the equivalent doping regions in the graphene as a result of PBS in the PDMS microfluidic channel where R_1 is the resistance of the p-doped graphene not exposed to PBS and R_2 is the resistance of the n-doped graphene exposed to PBS.

Compared to the bare sensor response in figure 7.25, the response of the functionalised sensor to PBS gives a sharp additional conductance minimum at lower V_g . The appearance of the additional minimum with presence of PBS is attributed to region doping as discussed previously, and this is believed to be due to the counteracting of charged impurities in the graphene/SiO_2 interface that result in its p-doping during fabrication. The main cause of p-doping is reported to be due to trapped water molecules, however, it is possible that the ions in PBS helps to mitigate this effect, therefore resulting in the strong n-doping of the graphene exposed to solution. This happens in both the functionalised and bare graphene case, however the additional functionalisation layer may cause some variation to this effect; therefore, resulting in a different additional conductance minimum position. It is important to note that this is a feature of the back-gated gFET sensor only and arises due to the silicon global back-gate that applies a gate voltage to the entire graphene film whether exposed to solution or not.

7.3.4 Optimisation of the Solution Top-Gated gFET

A top-gated FET is an alternative to the back-gated gFET geometry, as introduced in section 3.1.3. This can further increase the sensitivity of the biosensor and negate the effect of the area of graphene exposed to the solution versus that unexposed because only that exposed to solution is gated. As all measurements using this geometry are performed under a liquid environment, it must consider: the concentration of the ionic solution and top-gate electrode design.

For the global back-gated gFET measurements in section 7.3.3.2, the whole graphene surface experiences the field generated by V_g, even that not exposed to the solution. There are two regions of different doping levels on the same graphene film that result: that doped by charged species inside the microfluidic channel and that outside the microfluidic channel, therefore unexposed to the solution. The sensing mechanism is then reliant on the separation of these two regions and their individual electronic properties as will be discussed in further sections. Typically, back-gated gFETs work with V_g at 10 – 100 V [41, 209], and whilst this gives the advantage of measuring large changes in Dirac point, for low shifts when very low concentrations of the target molecule are detected in sensing applications, this wide range makes sensing shifts < 1 V difficult. As the V_g shift for solution top-gated gFETs can be in the range of 0.1 V, the transconductance (ratio between I_{ds} change over change in V_g) is often > 100 times larger compared to back-gated FETs [210].

7.3.4.1 Platinum Gate Electrode Design

For preliminary measurements using the solution top-gated gFET, a 0.25 mm diameter platinum (Pt) wire was used as the gate electrode and inserted into an arbitrary position in the PDMS channel, which contained 0.001× PBS.

Pt is known to be inert in many chemical reactions and therefore not expected to affect electrical measurements under aqueous environments [211]. The ionic conductivity of the solution should

provide a homogeneous field however due to the difference in surface area between the Pt wire and the graphene surface under the channel, the positioning of the wire with respect to the graphene could slightly affect electrical measurements. The position of the Pt electrode, if used as a point wire, will change as the electrode is continuously removed and re-inserted as solutions change during measurements. If the I_{ds} - V_g response is sensitive to this positioning, uncertainties are introduced when determining electrical changes from target molecules. To investigate this, the Pt wire was moved to various positions in the channel as shown in figure 7.28 and measurements were taken at each point.

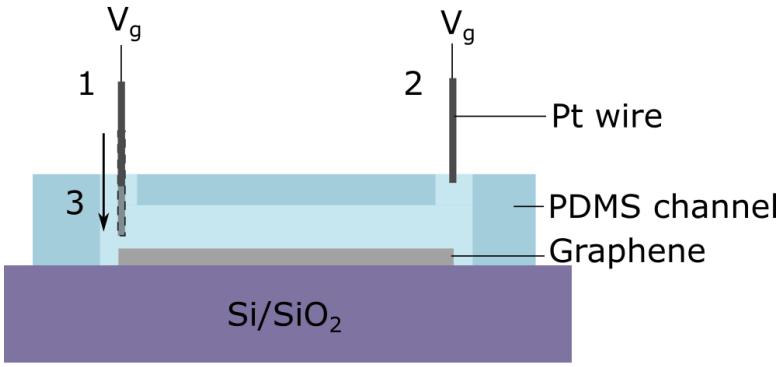

Figure 7.28: A schematic representation of the 3 positions of the Pt wire within the PDMS microfluidic channel where position 1 is at the inlet of the channel, position 2 is at the outlet and position 1 is at the inlet but closer to the graphene surface.

Figure 7.29 shows the effect of changing the position of the Pt electrode in the channel where a Dirac point shift is seen for all positions. Position 1 and 2 resemble each other as the wire was inserted at a similar height and moved only laterally in the set-up however, a narrowing of the response is seen when the Pt electrode is brought closer to the graphene surface (position 3).

It is worth noting that compared to back-gate results in section 7.3, solution top-gate measurements generally gave less asymmetric I_{ds} - V_g transfer characteristics. In section 7.1 some asymmetry can be attributed to the effects of the metal contacts. However, metal contacts are also used in solution top-gate measurements hence the asymmetry with back-gated measurements was most likely due to the contribution of leakage currents through the SiO_2. This

leakage current (between the source and gate, I_{sg}) is typically small compared to I_{ds} but can cause increased resistance in the dielectric layer as V_g is increased to high positive values. This resistance causes the V_g to be less than that applied and as a result, I_{ds} is lowered on the right-hand-side of the transfer characteristic. As seen in figure 7.29(b) for the solution top-gate measurements, this leakage current is extremely small and doesn't contribute such an effect to V_g, hence the transfer characteristics appear more symmetric.

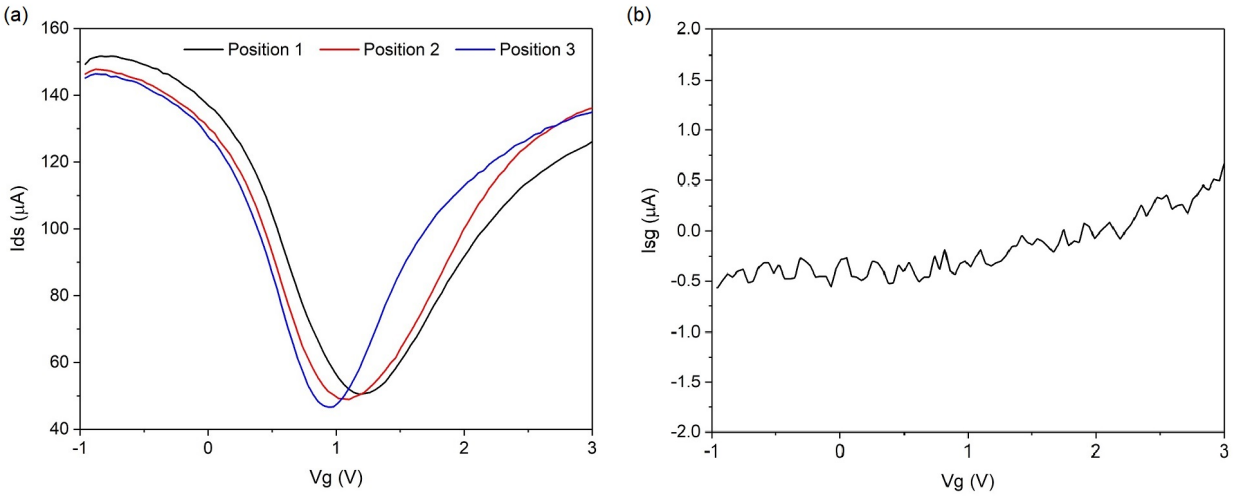

Figure 7.29: (a) I_{ds} - V_g transfer characteristic of the bare graphene device to 3 different positions of the Pt gate electrode. (b) I_{sg} - V_g showing the measured leakage current for the solution top-gate geometry for the Pt wire at position 1.

The Pt wire position is expected to change the resulting I_{ds} - V_g response because the capacitance changes depending on the geometry. For the back-gated gFET, a parallel plate capacitor can be used to model the capacitance between the Si back gate and graphene. However, the use of the point wire means that the electric field between the electrode and graphene may no longer be as uniform.

As a result of a slight non-uniform capacitance, C, the change in charge upon binding of target molecules, Δq, is no longer homogeneous within the graphene sheet and neither is the shift in Dirac point, ΔV_D, according to equation 7.3. To accurately monitor ΔV_D upon charge modulation by biomolecules, the design of the Pt wire must ensure that a uniform field is generated along the graphene film.

$$\Delta V_D = \frac{\Delta q}{C} \tag{7.3}$$

The I_{ds} - V_g response showed variation with the position of the wire. To avoid this in future measurements, the electrode was designed as a loop to ensure more reproducibility between measurements. The loop was designed such that it would span the whole lateral dimension of the microfluidic channel (figure 7.30) therefore ensuring a more uniform field applied to the graphene.

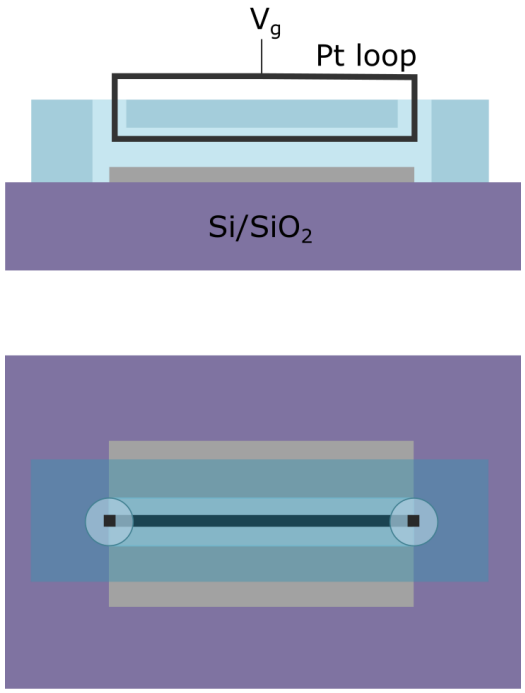

Figure 7.30: Cross-sectional and top-down schematic representation of the Pt wire loop placed in the microfluidic channel on top of the graphene surface.

Using the Pt wire loop design, an initial I_{ds} - V_{ds} response was measured as shown in figure 7.31(a) to ensure an Ohmic relationship with 0 V gate bias for this Pt wire design with and without PBS. This indicates that the typical non-rectifying output characteristic is obtained with Ti/Au contacts and that they are properly isolated. The same sweep parameters that were used in section 7.1 for the back-gated measurements, 30 second sweeps (300 µs per point

and 100 points), were used to obtain figure 7.31(b). Here, a typical solution top-gate I_{ds} - V_g transfer characteristic for graphene was observed using the Pt loop design.

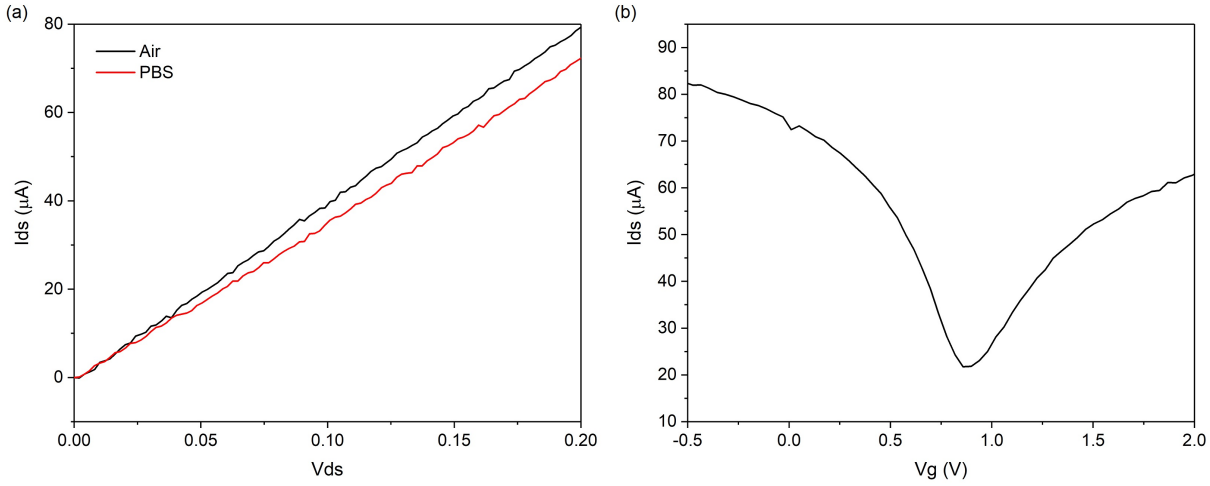

Figure 7.31: (a) I_{ds} - V_{ds} output characteristic of the bare graphene sensor with the looped Pt wire electrode and (b) I_{ds} - V_g transfer characteristic of the same sensor with a 30 second sweep.

7.3.4.2 Sweep Optimisation

Having designed the electrode to give better field uniformity upon application of the top-gate bias through the solution, the I_{ds} - V_g transfer characteristics were investigated in terms of stability with repeat measurements on the same graphene sample by measuring 10 successive sweeps. The different sweep settings used are given in table 7.4 (the number of points for each sweep were kept consistent at 100 points). As subsequent measurements are often used to monitor the response of the gFET between PBS and exosomes in PBS immediately after they are introduced to the microfluidic channel, any drift in V_D must be minimised to ensure any change in Dirac point is due to exosomes only.

Table 7.4: Top-gate measurement sweep settings investigated with the looped Pt wire in PBS. For each case, every individual sweep was made up 100 points.

Total sweep time (s)	Time per point (ms)
10	100
20	200
30	300
40	400

Figure 7.32(a) shows the response of a solution top-gated gFET with sweep times of 10 seconds. Despite improved field uniformity using the Pt loop, a drift in V_D to higher V_g was observed. The positive ΔV_D suggested p-doping of the graphene upon successive sweeps. This effect was previously reported by J. M. Park et al. [212, 210] and H. Wang et al. [213] whereby hysteresis and drain current drift was attributed to trapping of charges at interfaces upon repeat measurements. The sweeps are carried out from -0.5 to 2 V, hence electrons accumulated in the graphene at the end of the sweep can become trapped in the underlying SiO_2. The graphene then progressively gets p-doped upon subsequent sweeps due to the loss of electrons in these traps and V_D shifts positively as a result. The density of charge traps relates to the shift in Dirac point by equation 7.4, where C_g is the capacitance of the underlying SiO_2.

$$N = \frac{C_g \Delta V_D}{2e} \tag{7.4}$$

A faster sweep rate should reduce the effect of charge trapping [214], hence increasing the sweep time to 20 seconds was expected to increase ΔV_D. However, figure 7.32(b) instead shows a reduction in the charge trapping effect. As well as charge trapping, an additional effect must be considered due to the solution top-gating. Ions accumulated at the graphene surface during the first sweep are "remembered" and a delay in the movement of mobile ions causes a different ionic concentration than expected upon the following sweep [213]. This only affects the solution top-gated measurements and might be why back-gated measurements give more

stable I_{ds} - V_g transfer characteristics as seen in figure 7.33. As it takes some time for the potential to distribute within the solution, the accumulation of positive ions at the graphene surface from the previous sweep still remain at the start of the following sweep and the applied V_g is not as negative as expected. This would cause the whole characteristic, and V_D, to shift to the left, which opposes the effect of charge trapping. The effect of the delay in distribution of ions opposes the effect of charge trapping and is stronger as the sweep time is increased from 10 to 40 seconds.

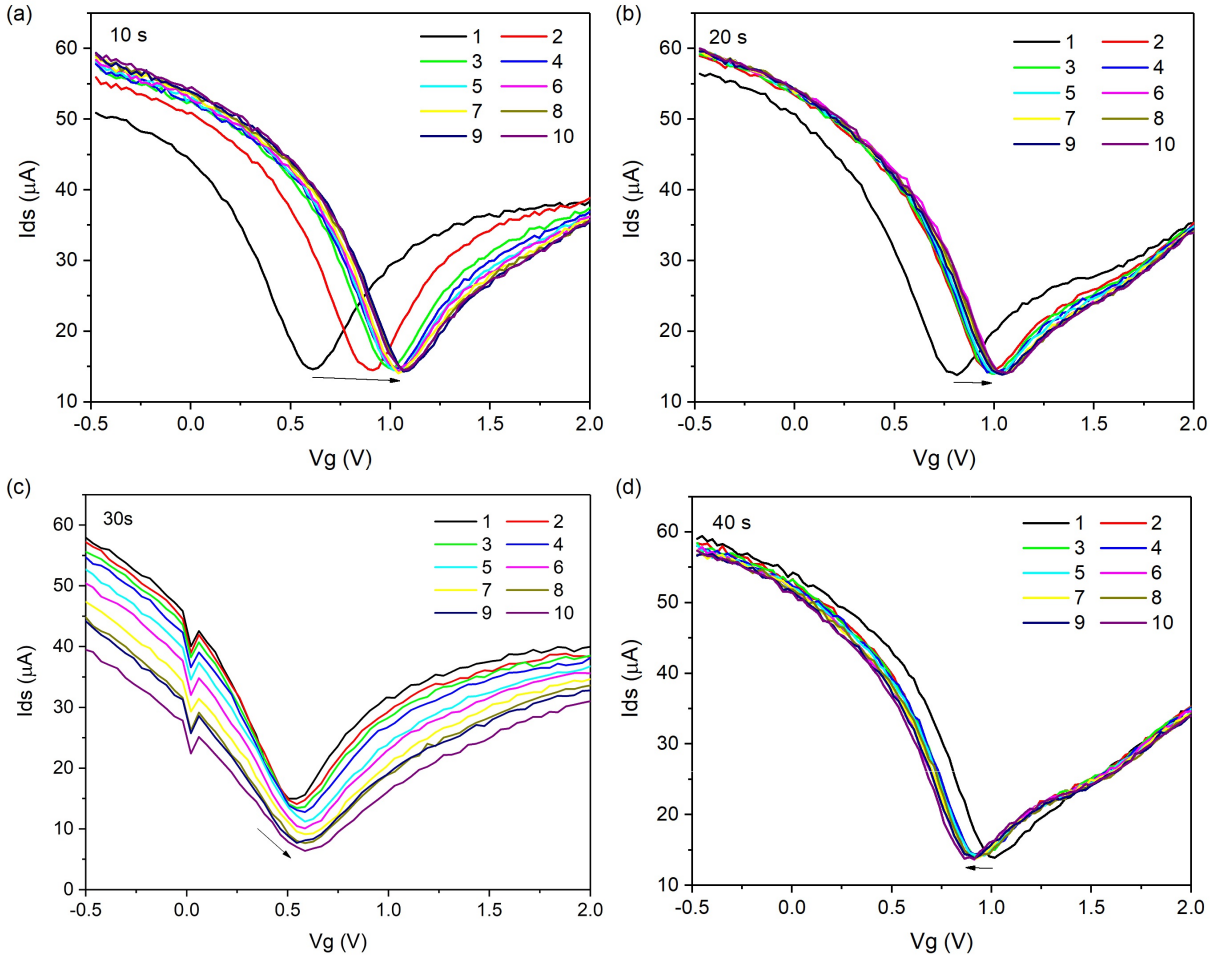

Figure 7.32: I_{ds} - V_g transfer characteristic of the same bare graphene sensor for different sweep times: (a) 10 seconds (100 µs per point), (b) 20 seconds (200 µs per point) and (c) 40 seconds (400 µs per point). For each case, 10 sweeps successive sweeps were recorded.

The Dirac point drift for all sweeps is summarised in figure 7.34. For the 40 second sweep, the charge trapping effects and ion distribution effects oppose each other such that subsequent

measurements remain the most stable, hence future measurements were conducted at this sweep length.

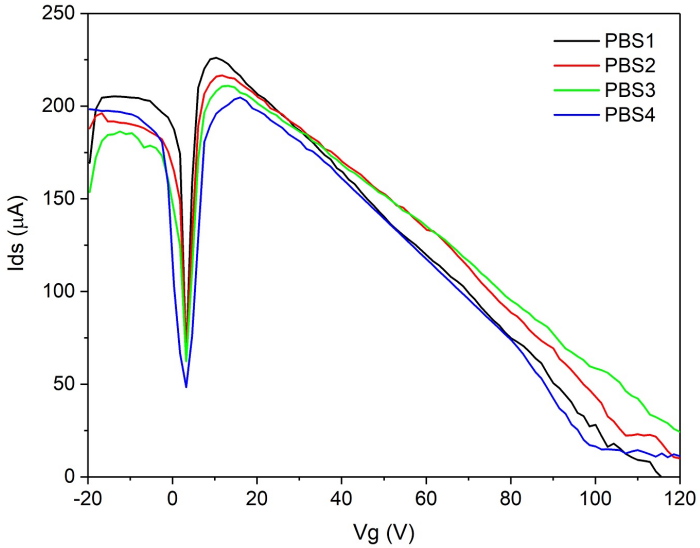

Figure 7.33: 4 subsequent measurements of the I_{ds} - V_g transfer characteristic for a back-gated gFET sensor with PBS in the microfluidic channel.

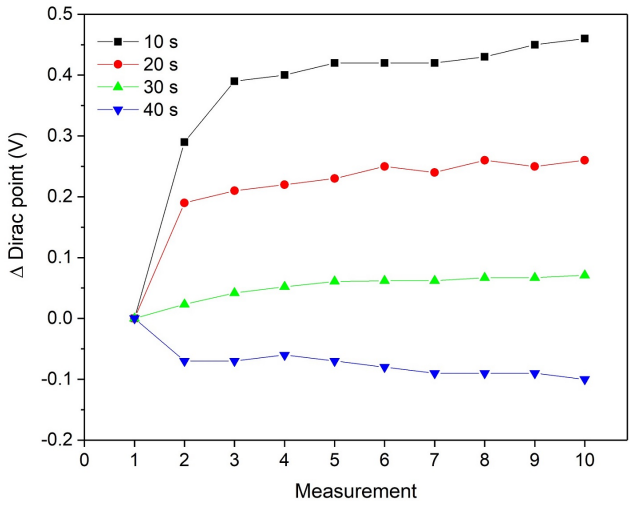

Figure 7.34: (a) Dirac point and (b) Dirac point shift from measurement 1 for each sweep length time.

For continued sweep optimisation for future biosensor measurements, the time between sweeps was also investigated. For biosensor measurements it is more realistic to record data every 5 minutes as shown in subsequent sections, for a total allocated time, to allow for binding of a

target molecule. Hence the experiment was repeated using a 40 second sweep with 5 minutes left between each measurement and the results shown in figure 7.35.

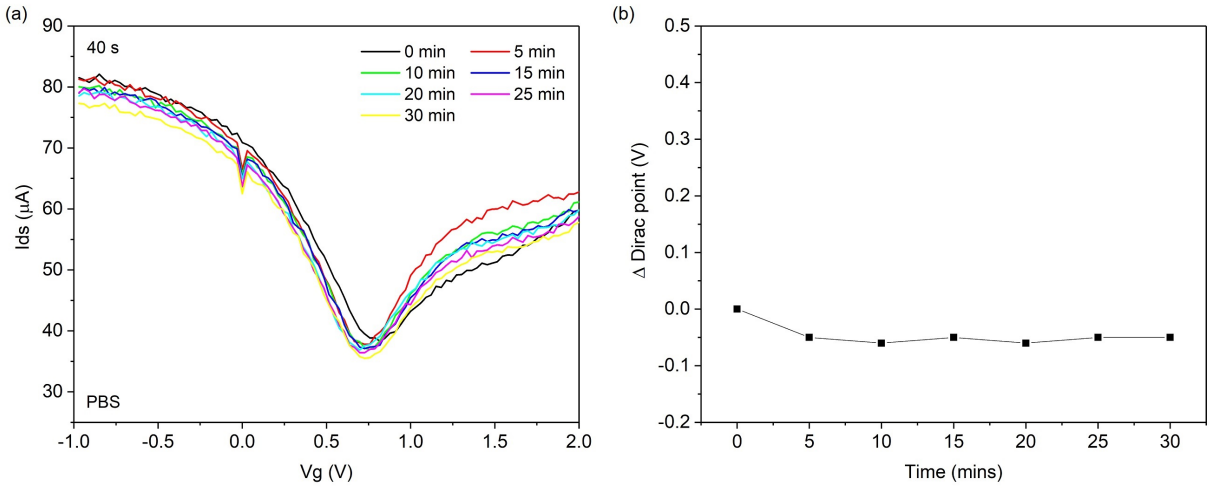

Figure 7.35: (a) I_{ds} - V_g transfer characteristic of a bare graphene sensor with a 40 second sweep recorded every 5 minutes for 30 minutes and (b) resulting Dirac point and Dirac point shift with time.

By performing static measurements over 30 minutes this allows for maximised binding of the target antigen to conjugated antibodies. Therefore, it is vital that I_{ds} - V_g measurements taken every 5 minutes should be representative of the electrical characteristics and any changes due to the target biomolecule. For bare graphene, the Dirac point was measured to ensure that it remained stable and unaffected by charge trapping over 30 minutes with the presence of PBS only. Figure 7.35(a) shows the result obtained by sweeping V_g under these parameters, whereby the Dirac point does not seem to show large variation in position compared to figure 7.34. The Dirac point was again tracked and figure 7.35(b) shows this under the same scale as figure 7.32 for reference. The average Dirac point was 0.734 $\pm$ 0.021 V. Therefore, as long as measurements are carried out using these sweep parameters and the shift in Dirac point is $>$ 0.02 V upon target molecule binding, it is likely that any detected shift is due to electrical alterations from the target molecule rather charge trapping or ion distribution effects.

7.3.5 Electrical Response to BSA

Biological solutions are often referred to as any liquids consisting of organic constituents that are able to play some role in biological and bodily functions. Having studied the response of the graphene FET sensor more simple liquids such as DI water and salt solutions, it is important to review its response to various, more complex biological media. An effective biosensor must be able to specifically sense the presence of the target biomolecule in a medium consisting of other biological, organic solutes. To ultimately capture exosomes from a liquid biopsy, the other constituents of the solution must either have negligable effect or must be able to be removed from the sensor. In a sample of blood, the serum is defined as the component that is neither a blood cell, nor contains any proteins or factors that contribute to blood clotting. However serum does contain all non-blood clotting proteins. These charged non-targeted proteins will inevitably have some effect on the biosensor, hence it is important to investigate and distinguish these signals. Blood serum and plasma are a common source of biomarkers, including exosomes, and have been found to contain many of those associated with cancer.

Serum albumins are globular proteins present in blood serum and human serum albumin in particular, is the most abundant protein found in human blood plasma. Bovine serum albumin (BSA) is a type of serum albumin that derived from cows and is chemically similar to human serum albumin. It is often used as a laboratory standard for protein solutions due to its stability, lack of effect in biological reactions and low cost [215]. Herein, 1 % BSA was used as a benchmark for exosome studies in the following sections and used to give an initial idea of the response of the graphene biosensor to biological solutions. For many experimental methods using a biological standard, it is necessary to keep proteins suspended in a stable medium that is non-toxic to biological species. For this reason, the effect of PBS was investigated in the previous section and used to make all protein solutions and exosome suspensions used in this thesis. In the following subsections, both back-gated and solution top-gated gFET geometries were investigated and compared with various levels of functionalisation: bare, PBASE only-functionalised and PBASE + anti-CD63 Ab functionalised, as illustrated in figure 7.36.

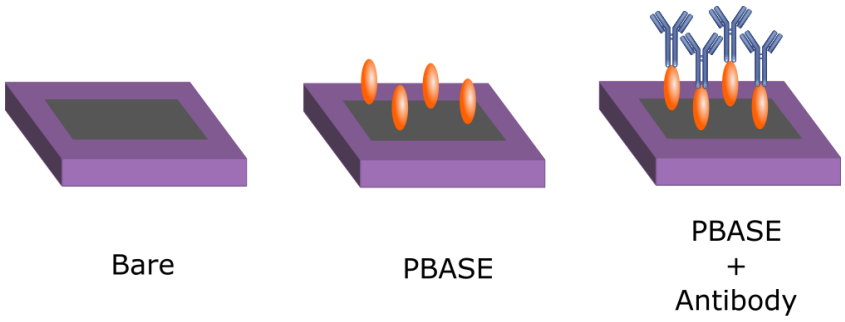

Figure 7.36: Schematic representation of graphene sensors functionalised to different extents for measurement using both the back-gated and solution top-gated geometry.

7.3.5.1 Back-Gated BSA Measurements on Bare Graphene

1 % BSA solutions in 0.001× PBS pH 7 were introduced into the microfluidic channel and left for 30 minutes and the resulting I_{ds} - V_g curves are shown in figure 7.37(a). As before there is the development of an additional minimum at 15.5 V when PBS is flowed over the sensor. Upon introduction of BSA in 0.001× PBS solution, the double conductance minimum is also observed in the I_{ds} - V_g curve. In figure 7.37(a) the Dirac points of the unaffected graphene outside the microfluidic channel and the additional minimum caused by the adsorption of BSA on the exposed graphene area are seen at 34.5 and 11.7 V respectively.

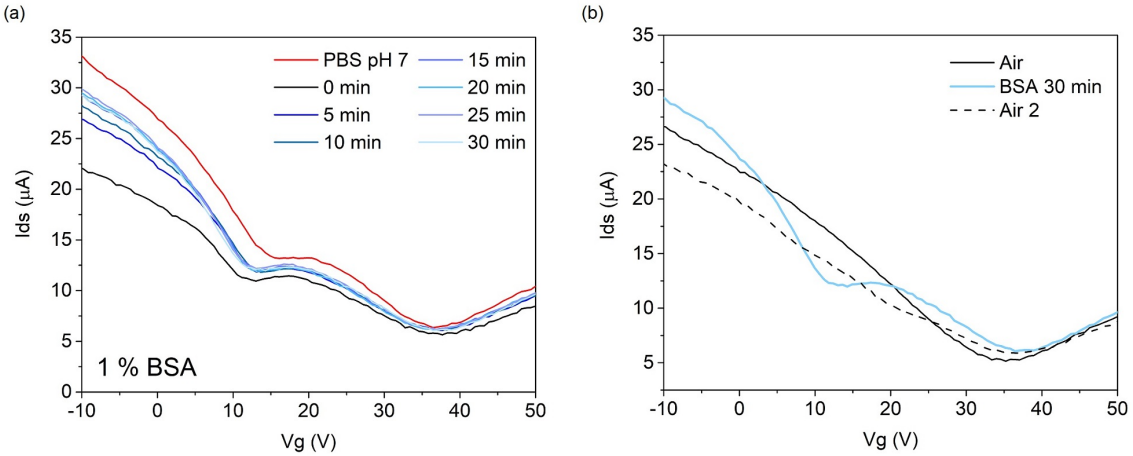

Figure 7.37: (a) I_{ds} - V_g transfer characteristic comparing bare graphene's response to air, PBS and BSA for 30 minutes after graphene transfer onto 90 nm SiO_2/Si and (b) I_{ds} - V_g transfer characteristic showing the effect of clearing the microfluidic channel with air after 30 minutes of BSA.

The surface charge of proteins depend on the pH of the surrounding medium because of their isoelectric points (IEP) and in this case, the shift in the additional minimum from the PBS position to a lower V_g when BSA is present is likely due to the negative charge on the BSA molecules at pH 7. The IEP is the pH at which the protein presents no net charge, also known as the protein's pI. This stems from the various functional groups present on the protein structure, which is dependent on their fundamental amino acid make up. These become protonated and deprotonated (this is the or gain and loss of H^+) depending on the solution pH, hence there is a specific pH where the protonated and deprotonated groups combine to give overall net zero charge on the molecule. BSA has pI 5.4, hence at pH 7, we expect an overall negative charge due to the depletion of H^+.

As there is no spatial separation between the BSA and the sensor surface, the n-doping of the graphene respective to the PBS position must be due to some charge transfer between the BSA and the graphene. The change in the I_{ds} - V_g curve with BSA over 30 minutes, confirms the overall n-doping even after time. Here, the greatest change in the position of the additional minimum with time occurs between 0 and 5 minutes. As adsorption of BSA on graphene is expected to take place quickly, this change in response may be attributed to a maximum in

the coverage of adsorbed BSA, which occurs within the first 5 minutes. After this time, the position of the additional minimum does not appear to significantly change.

Figure 7.37(b) suggests that by clearing the channel with DI water and air, the adsorbed BSA is somehow removed as the original I_{ds} - V_g curve is restored. It may be that this is enough to overcome the weak forces between the BSA and graphene, however literature suggests DI water alone is not sufficient [216]. There appears only to be a slight residual effect where the I_{ds} at $V_g < V_D$ is slightly lower than that of the original air measurement. However, it is also possible that forcing air through the microfluidic channel causes the physical shearing of the BSA from the surface as well as denaturing those still stuck. A more useful test would be to flow PBS through the channel to observe if the original reference position is restored. In the case of specific binding, we would expect that the sensor response would not change upon cleaning the microfluidic channel with DI water or PBS.

7.3.5.2 Back-Gated BSA Measurements on Functionalised Graphene

PBASE is used to act as an intermediate linker between graphene and the conjugated antibodies. The linker serves as a physical separation (of length $\sim$ 2 nm) between the biomolecules in solution and the sensor surface. This causes the charged biomoelcules to act as a 'molecular top-gate'. Monolayer graphene was again transferred onto a 90 nm SiO_2/Si substrate and functionalised with 10 mM PBASE following the protocol outlined in section 6.4.2. The surface was then treated with glycine to ensure no reaction between the NHS esters and amines present on BSA.

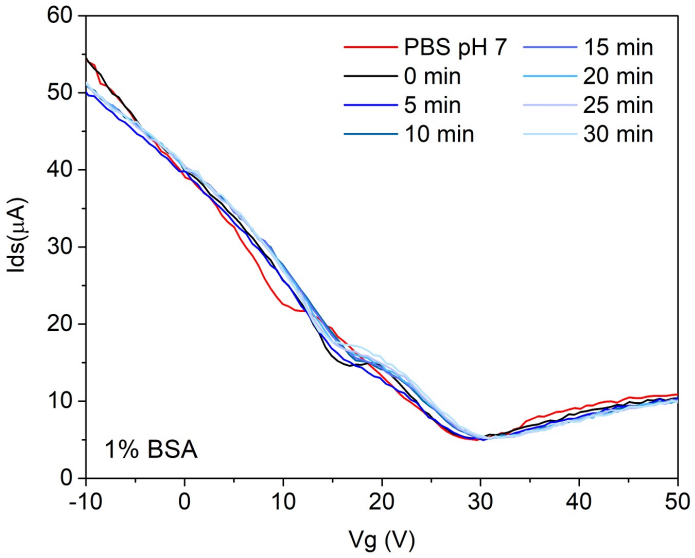

Figure 7.38: I_{ds} - V_g curve showing the response of a 10 mM PBASE functionalised and glycine treated gFET sensor to 1 % BSA in PBS pH 7.

Figure 7.38 shows a shift of the additional minimum to higher V_g from V_{PBS} when BSA is introduced to the surface of the PBASE functionalised sensor. Here, the shift to higher V_g represents p-doping of the graphene under the channel from BSA with respect to PBS. Even though the relative p-doping occurs due to BSA, the presence of the original Dirac point of the uncovered graphene (due to fabrication methods and trapped charges) on the I_{ds} - V_g curve suggests the unexposed graphene is still more p-doped. Nonetheless, the relative p-doping from BSA differs from the result in figure 7.25, where the BSA results in n-doping with respect to PBS, despite solutions being made at pH 7. We expect the BSA molecules to have negative surface charges at this pH hence the different doping effects are attributed to the surface of the sensor. The PBASE monolayer that physically separates the BSA from the graphene surface acts as a dielectric layer. The effect that this has on the interaction between graphene and negatively charged BSA is shown in figure 7.39.

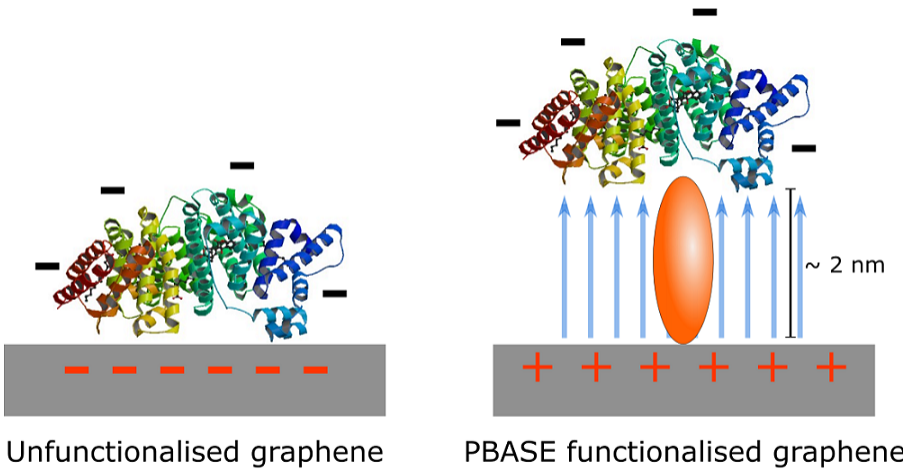

Figure 7.39: Schematic representation of the difference between unfunctionalised and PBASE functionalised graphene when negatively charged BSA is present, and the effect this functionalisation has on the electrical properties of the graphene.

The proteins exist in the solution as like-charged particles that are homogeneously distributed in solution due to mutual repulsion. As BSA is introduced into the microfluidic channel, the immediate presence of charged proteins close to the graphene surface results in the modulation of the exposed graphene's electronic properties. Therefore, even though BSA is not expected to bind to the surface, it is possible that the presence of negative charge at a certain distance away from the sensor surface is enough to induce positive charge accumulation in the graphene.

Having established the effect of functionalisation on the sensor response with respect to BSA adsorption, the antibody conjugated surface must be studied. In order to specifically capture exosomes anti-CD63 Ab is conjugated to the surface, which is able to specifically bind to CD63 transmembrane proteins.

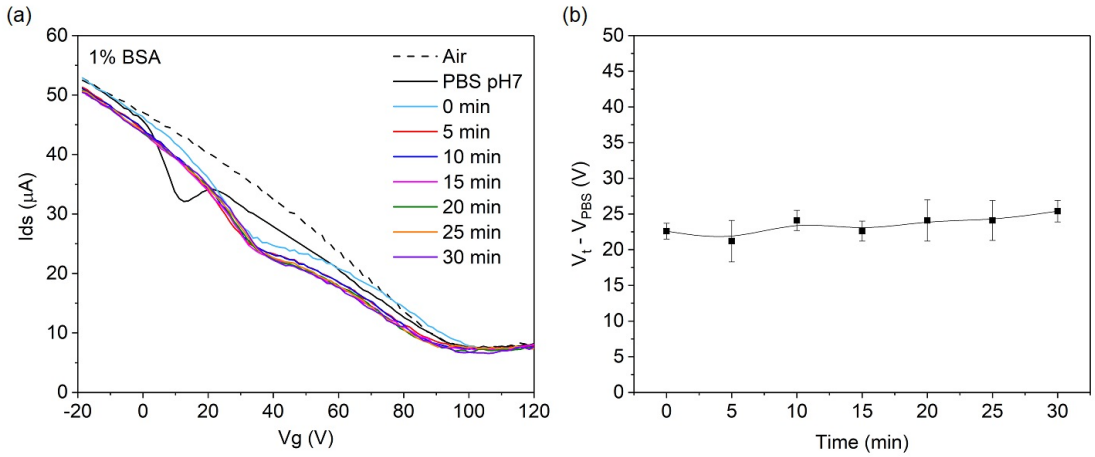

Figure 7.40: (a) I_{ds} - V_g transfer characteristic of a PBASE and anti-CD63 Ab conjugated sensor showing its response when 1 % BSA is passed through the channel and left for 30 minutes. (b) The additional minimum shift with time with respect to V_{PBS} where the error bars denote the confidence intervals of extracting the minimum value from the I_{ds} - V_g curve.

Figure 7.40 shows the response of the PBASE and anti-CD63 Ab conjugated sensor to BSA. Here, the shift of the additional minimum to higher V_g with BSA is once again due to the physical separation between the graphene and the negatively charged BSA molecules, which is consistent to the result in figure 7.38. In this case, the antibodies add an additional $\sim$ 10 nm to the separation distance but the concentration of PBS ensures the biomolecules are within the Debye length as discussed in section 7.3.3.1. As expected, the original Dirac point of the uncovered graphene remains consistent with time at 101.6 V. The functionalisation is exosome specific so BSA doesn't bind to the antibodies and hence, the additional minimum is solely due to the immediate presence of randomly distributed negative charge close to the graphene surface. Figure 7.40(b) supports this where there was some initial shift from V_{PBS} but no significant change with time was seen.

The end goal of the sensor is to be able to specifically detect exosomes in a liquid biopsy with various other proteins present, such as serum albumin. Ideally, a sensor would have the ability to specifically capture exosomes before having unwanted proteins and charged species flushed from the channel. It is therefore important to establish the sensor's ability to restore its response to that before BSA after BSA is left in the channel for 30 minutes to determine

whether non-specifically adsorbed molecules could be removed. Herein, the channel was first filled with PBS and the position of the additional minimum recorded before BSA. After BSA was left in the channel for 30 minutes, assuming no specific binding had taken place, flushing the channel with PBS was expected to restore the additional minimum to the original PBS position.

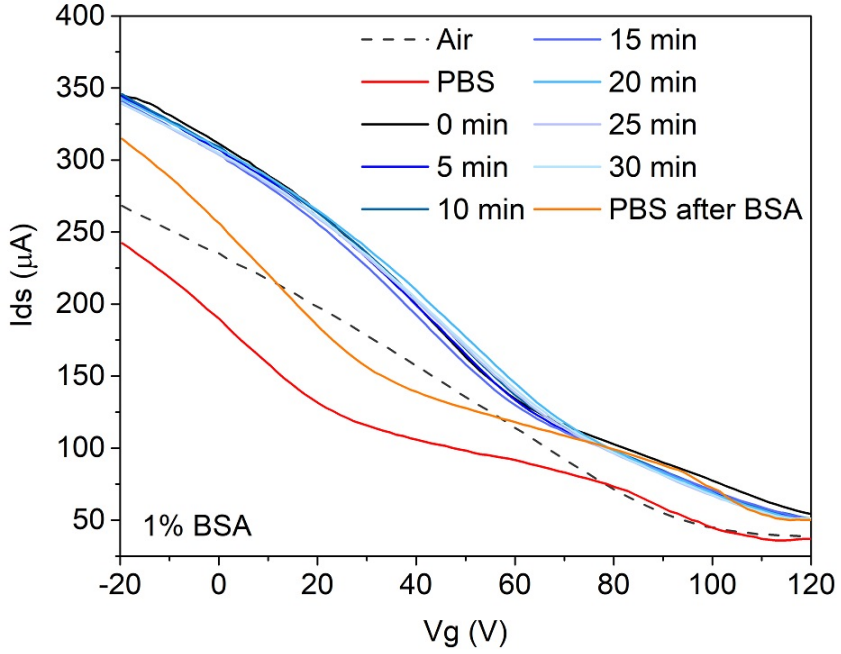

Figure 7.41: I_{ds} - V_g transfer characteristic of a PBASE and anti-CD63 Ab conjugated sensor showing its response when the channel is filled with PBS, 1% BSA, left for 30 minutes and flushing using PBS.

Figure 7.41 shows a large shift from V_{PBS} with BSA and p-doping due to the negative surface charge of the BSA molecules as consistent with figure 7.40. Similarly, there was negligible shift from V_{PBS} over the 30 minutes as the BSA does not specifically bind to the surface and instead non-specifically adsorbs or settles on the sensor instead. The first reference PBS solution gives V_{PBS} = 31.9 V, from which the additional minimum shifts $\sim$ 30 V with BSA. After the 30 minutes, PBS was used to flush the microfluidic channel, which resulted in the restoration of an additional conductance minimum at a lower V_g value close to the original V_{PBS}. This suggests that upon PBS flushing, the adsorbed BSA was somewhat removed from the sensor surface such that the electrical response changes back to resemble the original PBS curve. Despite the

similar V_{PBS} values initially and after flushing, the biggest difference in the I_{ds} - V_g transfer characteristic was the overall increase in I_{ds}; I_{ds} at all V_g was higher after flushing the channel with PBS compared to the original PBS curve before BSA. This may be due to the residual effect of some BSA that has not been washed away from the surface, which suggests flushing with only PBS may not be entirely effective for BSA removal.

7.3.5.3 Solution Top-Gated BSA Measurements on Bare and Functionalised Graphene

For back-gated measurements with BSA in section 7.3.5, the sensing mechanism used is based on the presence of the additional conductance minimum and distinguishing its shift from the original PBS reference position. This sensing mechanism works when the additional minimum and original Dirac point do not overlap, however this is not always guaranteed and it may not always be possible to separate these two regions In this case, the solution top-gated geometry was also investigated. As with back-gated measurements, the solution top-gated measurement setup was initially investigated by the gFET's response to 1 % BSA in 0.001× PBS. The sweep settings and set-up used for the following measurements were as optimised in section 7.3.4. Figure 7.36 shows the 3 gFET sensors each with different levels of functionalisation: bare, PBASE functionalised, and PBASE + anti-CD63 Ab conjugated graphene.

For bare graphene, results shown in 7.3.5.1 suggest that as BSA adsorbs onto bare graphene, the dominant mechanism responsible for the shift in the additional minimum on the I_{ds} - V_g transfer characteristic was charge transfer between the negatively charged BSA and graphene due to their direct contact. Figure 7.42(a) also supports this mechanism due to the shift in Dirac point to less positive V_g with BSA in the microfluidic channel over time. As discussed at the beginning of this chapter, only the area of graphene exposed to solution under the microfluidic channel is gated hence, instead of displaying an additional minimum alongside the Dirac point (as in back-gated measurements), the actual Dirac point is affected by the presence of charged species. The magnitude of this shift is also much larger than that which is attributed to drift, as obtained in 7.3.4.2. Therefore, it is reasonable to assume that this shift is in fact due to the

graphene's response to BSA.

For PBASE functionalised graphene, figure 7.42(b) again shows a shift to lower V_g from BSA with time. In section 7.3.5.2, the presence of PBASE showed that the dominating mechanism for the response of graphene was the electrostatic field-effect because of the physical separation between the BSA and graphene. In this case, the shift to lower V_g suggests that charge transfer occurs like that of bare graphene in figure 7.42(a). This occurred because the PBASE surface was not passivated to terminate the NHS esters. Like antibodies, BSA itself has many amine groups that allow it to covalently bond to the PBASE. The shift in Dirac point suggests that the BSA bonded to the PBASE and this facilitates some transfer of negative charge to the graphene surface. Figure 7.42(c) finally shows the result for a gFET sensor functionalised with anti-CD63 Abs, which are not specific to BSA. Compared to the cases of bare and PBASE only functionalised graphene, the shift in the Dirac point from the PBS reference was much smaller. This is expected because BSA should not bind. Similarly to the back-gated result in figure 7.40(b), the Dirac point shift in figure 7.42(d) shows a negligable shift with time as BSA is not expected to show time-dependent binding to the surface. However, V_D shifts to slightly less V_g instead of more positive values, which would be expected from the electrostatic gating mechanism. Again, this sample was not passivated to terminate unreacted PBASE hence, BSA could bond to these unreacted linkers causing some charge transfer that dominates over electrostatic gating.

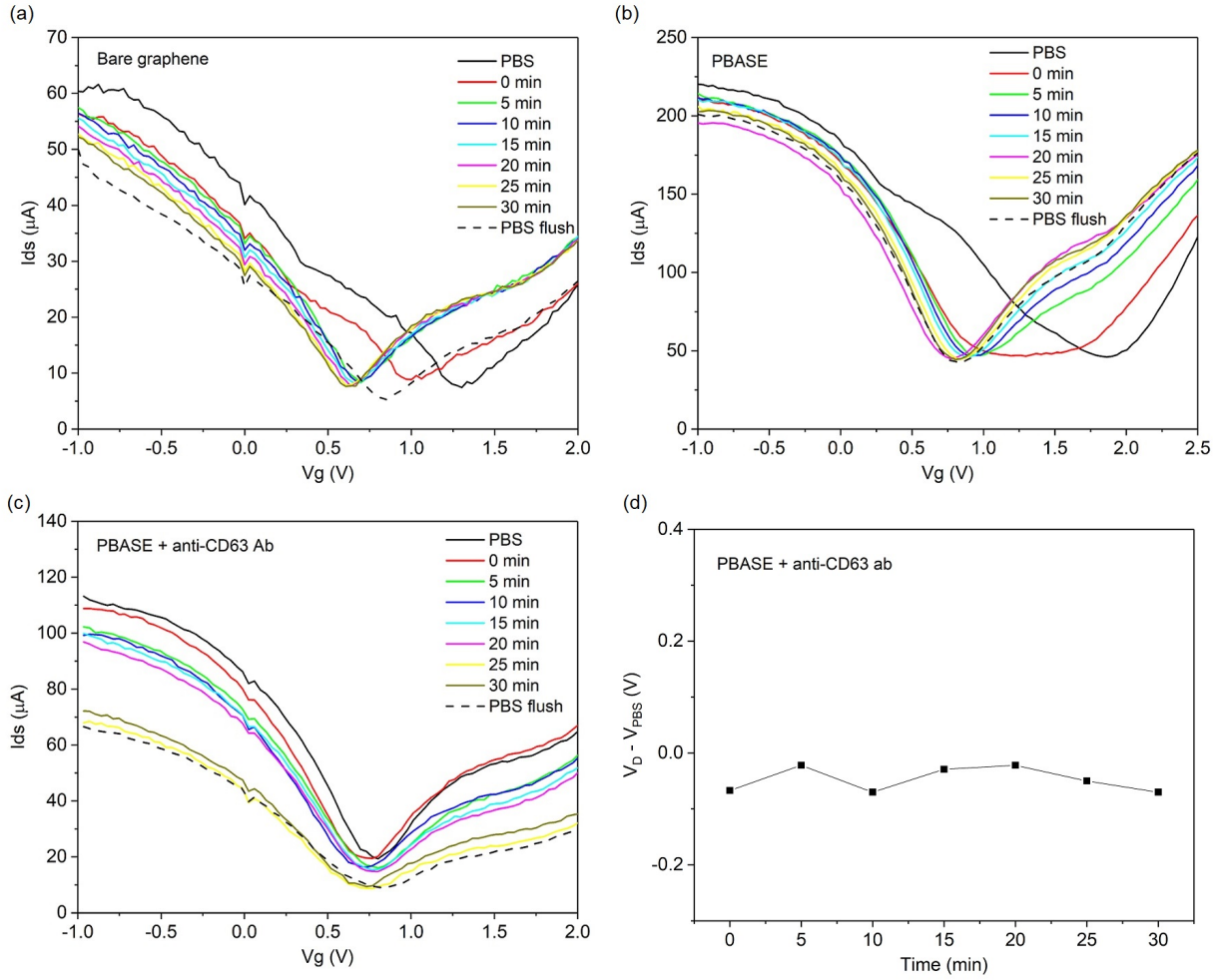

Figure 7.42: I_{ds} - V_g transfer characteristics for 3 solution top-gated gFET sensors and their response to 1 % BSA in 0.001× PBS over 30 minutes. (a) Bare (b) 10 mM PBASE functionalised and (c) PBASE and anti-CD63 Ab conjugated graphene. (d) Shift in V_D from the PBS reference point with time when 1 % BSA in 0.001× PBS is introduced to sensor surface for the PBASE and anti-CD63 Ab conjugated graphene.

For each sample, the microfluidic channel was flushed with PBS after 30 minutes. Figure 7.43 shows shift of the Dirac point, V_D, from V_{PBS} (V_D - V_{PBS}) for all 3 samples. It was expected that the Dirac point would not fully recover after flushing with PBS on the bare graphene sample because adsorbed BSA is difficult to remove with DI water or PBS solutions alone. The fact that the Dirac point did not restore after flushing with PBS on PBASE supports the formation of a covalent bond between the NHS ester and BSA and the facilitation of charge transfer. For PBASE + anti-CD63 functionalised samples, there was negligible shift in Dirac

point as expected. Upon flushing with PBS, the Dirac point restored close to the original PBS position, which suggests the BSA simply exists as negative charge in solution and does not permanently affect the graphene properties (similar to back-gate results in 7.3.5.2).

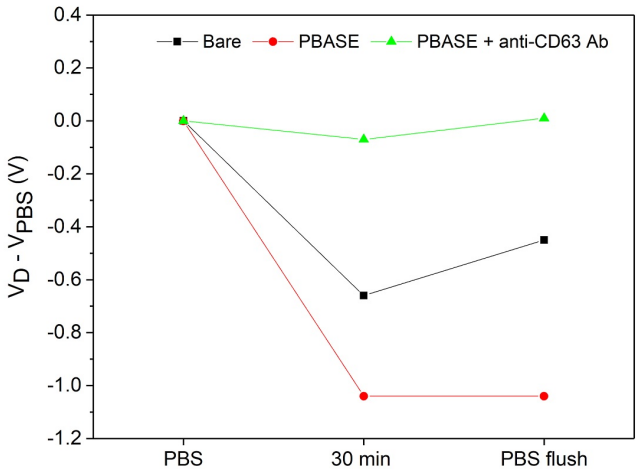

Figure 7.43: Shift in the Dirac point away from the PBS reference value (V_D - V_{PBS} with the initial PBS measurement, after 30 minutes with BSA and after flushing with PBS for bare, PBASE functionalised and PBASE and anti-CD63 Ab conjugated graphene.

7.3.6 Summary of Liquid Measurements

In this section the gFET sensor, in both the back-gated and solution top-gated set-ups, was tested under different conditions to investigate its response to both neutral and charged species with different levels of functionalisation. A microfluidic channel was secured to the sensor to allow for the introduction of different liquids to the surface. DI water showed small changes to the I_{ds} - V_g transfer characteristics in the form of small mobility changes due the different in ϵ_r between water and air. Instead of water, PBS was used to make up all subsequent biological solutions and its ionic concentration and its effect on the Debye length had to be controlled. A higher ionic concentration is more suitable for replicating physiological conditions, however this results in a shorter Debye length and increased screening of target biomolecules during sensing. As a compromise, 0.001× PBS was chosen for subsequent sensing measurements, which gives a Debye length of 24.2 nm.

When PBS was introduced to the microfluidic channel during back-gated measurements an additional minimum appeared in the I_{ds} - V_g transfer characteristic. This was due to the different levels of doping that occur within the same graphene film when part of it is exposed to solution and part is unexposed, which manifests as the superposition of two Dirac points on the same I_{ds} - V_g curve. The PBS acted to reduce the p-doping in the graphene film and increase mobility as a sharp additional minimum appeared at lower V_g than the original Dirac point. To further investigate this, solutions of 1 % BSA in 0.001× PBS were introduced to the graphene surface, which again resulted in the presence of an additional minimum, which shifted slightly to more positive V_g compared to that of the PBS reference position. This is because BSA exhibits negative charge at pH 7 and hence slightly p-dopes the graphene by electrostatic gating. This mechanism of sensing was confirmed by investigating devices with different levels of functionalisation. As bare graphene exhibits not physical separation between its surface the BSA protein, direct charge transfer occurs. However, when a layer of PBASE (or PBASE + antibodies) is present, the physical separation causes the electrostatic gating effect where the presence of negative charge imparts the accumulation of positive charge in graphene. Similarly, the solution top-gated set-up showed similar results and confirmed that for both set-ups, BSA does not specifically bind to conjugated anti-CD63 antibodies and therefore the gFET sensor did not show any time-dependent binding response.

7.4 GFET Response to Exosomes

Back-gated DC measurements on 300 nm SiO_2/Si of fully functionalised gFETs with exosomes were performed using the set-up depicted in figure 6.14(b) in section 6.6. For all measurements, exosomes in PBS pH 7 were prepared as described in section 6.5.3. The response of the bio-functionalised gFET to different concentrations of exosomes was investigated with respect to the I_{ds} - V_g transfer and I_{ds} - V_{ds} output characteristics. For solution top-gated measurements, samples and solutions were similarly prepared and the set-up used is shown in figure 6.14(c) in section 6.6.

7.4.1 Preliminary Measurements with Exosomes

The gFET sensor was first exposed to PBS, which acted as a reference solution against which all electrical changes were compared. 0.001× PBS was chosen due to the reasons discussed in section 7.3.3. PBS can therefore be considered the 'blank', which then can be spiked with various biological species to imitate more complex liquid biopsies.

Initial results were obtained with the highest concentration of exosomes prepared: 10^{-2} µg/µL (10 µg/mL). This gives approximately 1×10^5 exosomes/µL, which was a reasonable starting concentration for detection considering this is within typical, clinically relevant concentrations of exosomes in blood serum ($\approx 1 \times 10^3 - 1 \times 10^8$ exosomes/µL). Figure 7.44 shows the response of a bare graphene sensor to this concentration of exosomes. The additional conductance minimum was observed when PBS is present in the microfluidic channel and appears at a lower V_g (41.9 V) compared to the original Dirac point of the graphene under dry conditions (109.0 V).

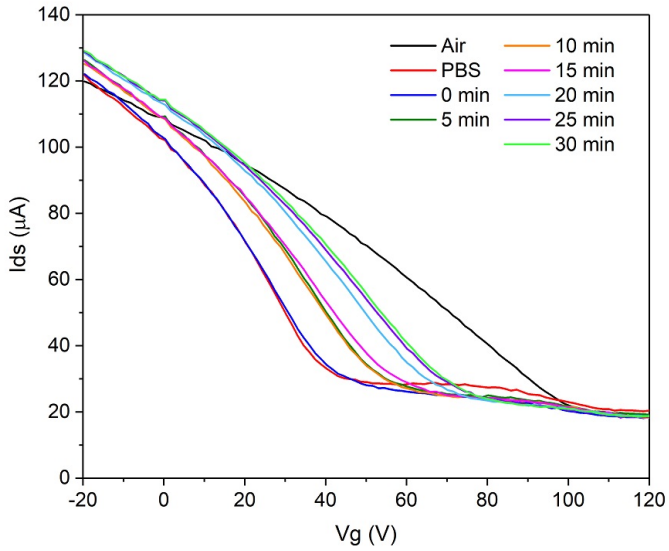

Figure 7.44: I_{ds} - V_g transfer characteristic for the back-gated unfunctionalised gFET with response to PBS and 10 µg/mL exosome in 0.001× PBS over 30 minutes.

In contrast to results in section 7.3.3.1 where only PBS is present in the channel, despite the lack of functionalisation, it appears that the bare graphene sensor is sensitive to exosomes to

a degree. With time, the I_{ds} - V_g response corresponding to exosomes in the microfluidic shift to higher V_g compared to that of PBS, which is attributed to the non-specific adsorption of exosomes on the graphene surface. In contrast to the result of bare graphene with BSA in figure 7.37, the additional minimum instead shifts to higher V_g with exosomes. Both should exist as negatively charged particles in solution so it was expected that bare graphene would show similar responses to both biomolecules. From these two results, the adsorption of exosomes on the graphene surface and how this affects the electronic properties is not entirely clear and has not been studied in literature. When globular proteins like BSA adsorb on hydrophobic surfaces, they expose their hydrophobic core to facilitate adsorption by a hydrophobic - hydrophobic interaction. Compared to BSA, exosomes are far more complex due to the phospholipid bilayer and various transmembrane proteins. This may be the cause of some discrepancy as the exosome structure could also be affected by adsorption onto a hydrophobic surface. The result shows that further study into exosomes on bare graphene is required and supports the need for a surface with specific functionalisation to prevent these problems.

For PBS, there should be no time dependent interaction between graphene and the ions in solution. The change in electrical response to BSA and exosomes with respect to PBS measurements indicates that graphene is sensitive to charged biomolecules. However, without any specific functionalisation by antibodies, it would be extremely difficult to distinguish between a signal arising from exosomes and proteins or other biomolecules that would be present in a liquid biopsy. Hence specific functionalisation is also necessary to specifically target exosomes in solutions with multiple charged species.

The time dependency observed for BSA and exosomes suggests that non-specific adsorption is the reason for the shift in additional minimum from V_{PBS} for bare graphene. For exosomes, the shift of the additional minimum is gradual over 30 minutes whereas for BSA, the largest shift occurs over the first 5 minutes and is also significantly smaller. 1% BSA corresponds to 0.01 g/mL; this is 1000× higher than the concentration of exosomes used to compare the bare graphene response. If the concentration of BSA is high, it is possible that the maximum surface coverage of adsorbed protein occurs after 5 minutes. For the lower concentration of

exosomes, this may take longer due to their random motion in solution. The difference in the magnitude of the shift in additional minimum between exosomes and BSA may be attributed to the difference in charge per molecule. The result would suggest that the charge per exosome is larger than the charge per BSA protein. Although, again this is difficult to interpret given the way in which exosomes adsorb onto the bare graphene surface is still unclear.

Following on from the result in figure 7.44, the sensitivity of the sensor's response to exosomes is believed to be increased by the presence of specific functionalisation. The use of PBASE and antibodies would allow for specific binding of exosomes and their permanent capture. Figure 7.45(a) shows the I_{ds} - V_g response of 3 identical gFET sensors to PBS and exosome suspensions, where the additional conductivity minimum is observed for all aqueous measurements. Under dry conditions, the Dirac point of the functionalised graphene was not observed under V_g of 120 V due to extreme p-doping from the device fabrication methods. It was not recommended to exceed a back-gate of 120 V as the breakdown voltage for 300 nm SiO_2 is in the range of 150 V, hence this was done to avoid possible leakage currents.

It was estimated that ligand-receptor binding for the exosomes and anti-CD63 Ab conjugated surface is maximised over 30 minutes; hence sweeps were measured every 5 minutes to track changes in the I_{ds} - V_g transfer characteristics as shown in figures 7.45(a) - (c). The additional minimum, arising from exosomes, appears to shift to higher V_g with time for all 3 sensors suggesting p-doping of the graphene with respect to the PBS. However, the additional minimum still remains at a V_g lower than the Dirac point of the unexposed graphene because of the screening effect of PBS mentioned in section 7.3.3.2. From immediate observation, the exosomes cause a higher response on a functionalised graphene surface compared to when the surface is bare in figure 7.44.

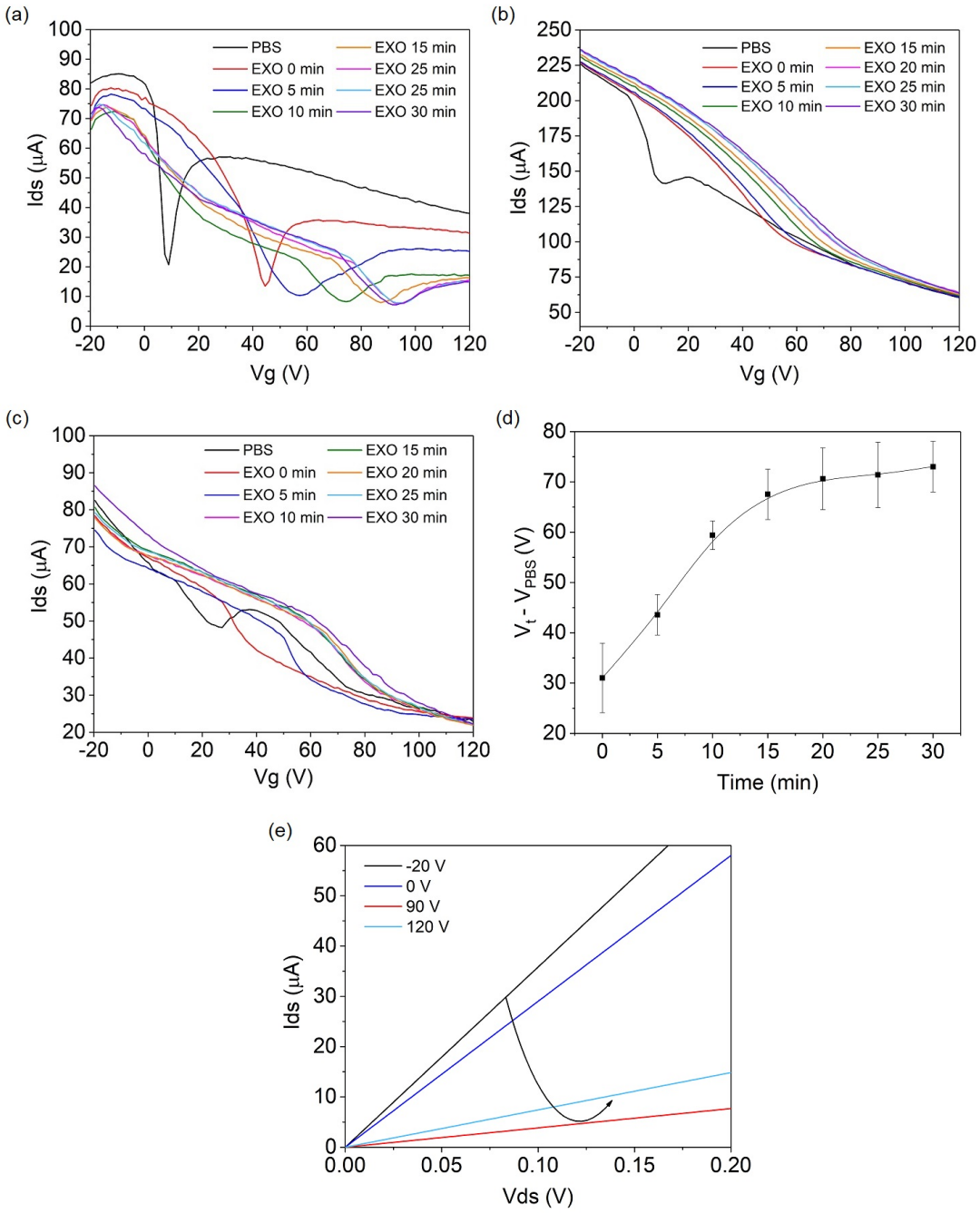

Figure 7.45: I_{ds} - V_g transfer characteristic of 3 fully functionalised gFET sensors: sample (a) 1, (b) 2 and (c) 3 each with 10 µg/mL exosomes in 0.001× PBS measured at room temperature over 30 minutes. (d) Shift in the additional conductance minimum V_t from the V_{PBS} reference position with time averaged over the 3 samples. Error bars denote the standard deviation on the mean of V_t values obtained for the 3 samples. (e) I_{ds} - V_{ds} output characteristic for the preliminary 10 µg/mL measurement on sample 1 at various constant V_g after 30 minutes of exosome binding.

The shift due to exosomes with respect to PBS is depicted in figure 7.45(d) where V_t is the

additional minimum at each time point and V_{PBS} is its position for PBS only (8.90 V). These were extracted from the original I_{ds} - V_g transfer characteristics by fitting the minimum regions to parabolas where possible (the detailed method for which is described in the appendix). As exosomes bind to the sensor surface over 30 minutes, a 'saturation' in the additional minimum position is seen, which we associate with the binding of all, or at least most, exosomes to the surface after which an equilibrium is reached.

As exosomes are believed to exhibit negative charge at pH 7 [136, 137], the positive shift in V_t is believed to be dominated by electrostatic contributions via the field effect as the functionalised layers act as a molecular dielectric. The bound exosomes act as a 'molecular top-gate' whereby their negative charge induces an accumulation of positive charge within the graphene causing a p-doping effect (or less n-doping with respect to the PBS-only condition). Of course, there may also be charge transfer, which is usual for ligand-receptor binding, but the obvious positive shift suggests the dominance of the field-effect in this case. This is similar to the effect seen for BSA in figure 7.40 as exosomes also exist as homogeneously distributed negative charge in solution above the sensor surface. When they are first introduced into the channel, there is an immediate shift in the additional minimum from the PBS reference as seen at 0 minutes. This is attributed to the immediate presence of negative charge close to the graphene surface. However, as they bind to the anti-CD63 Abs, they begin to exist as a non-homogeneous distribution of charge as more exosomes accumulate close to the sensor surface with time. This suggests that the time-dependency seen is an indication of exosome binding that otherwise does not occur for non-specific targets like BSA.

From the response of the sensor to PBS and exosomes, the graphene exposed to charged species is doped with respect to the unexposed graphene by the solutions introduced through the microfluidic channel. This implies that there are different doping regions within the same graphene film. Figure 7.45(e) shows the I_{ds} - V_{ds} output characteristic of the same sensor with exosomes after the 30 minutes binding time. The linear relationship is maintained between I_{ds} and V_{ds} even with different doping levels present in the graphene film, which shows that the Klein tunnelling effect in graphene is able to overcome these doping boundaries to give an

ohmic relationship between the source and drain contacts. This occurs because electrons are able to tunnel through the potential barriers. I_{ds} is also lowest when the sensor is held at a constant $V_g = 90$ V, which is consistent with the result in figure 7.45(a).

The sensor surface was also investigated using XPS and SEM at each stage of functionalisation and after exosome binding. Figure 7.46(a) shows the N1s XPS spectrum of the bare graphene and the first layer of functionalisation. PBASE molecules result in a small increase in nitrogen signal due to the presence of one nitrogen atom per molecule. The PBASE molecules are subsequently conjugated to the anti-CD63 Abs, which are abundant in amines and amides that result in a significant increase in nitrogen as described in detail in section 7.2.2. Similarly, exosomes contain similar groups to an even larger extent in their lipid bilayer membrane, hence resulting in a further increase in nitrogen.

Figure 7.46(b) shows the SEM image of bare graphene and graphene after identical functionalisation to that used in XPS and for DC measurements. Here, exosomes were introduced to the graphene surface using the same stock solution and can be clearly seen on the graphene. From the SEM analysis, exosomes found on the graphene surface, as shown by the arrow markers, were estimated to be 94.1 $\pm$ 31.4 nm, which is consistent with literature values and that provided by the supplier.

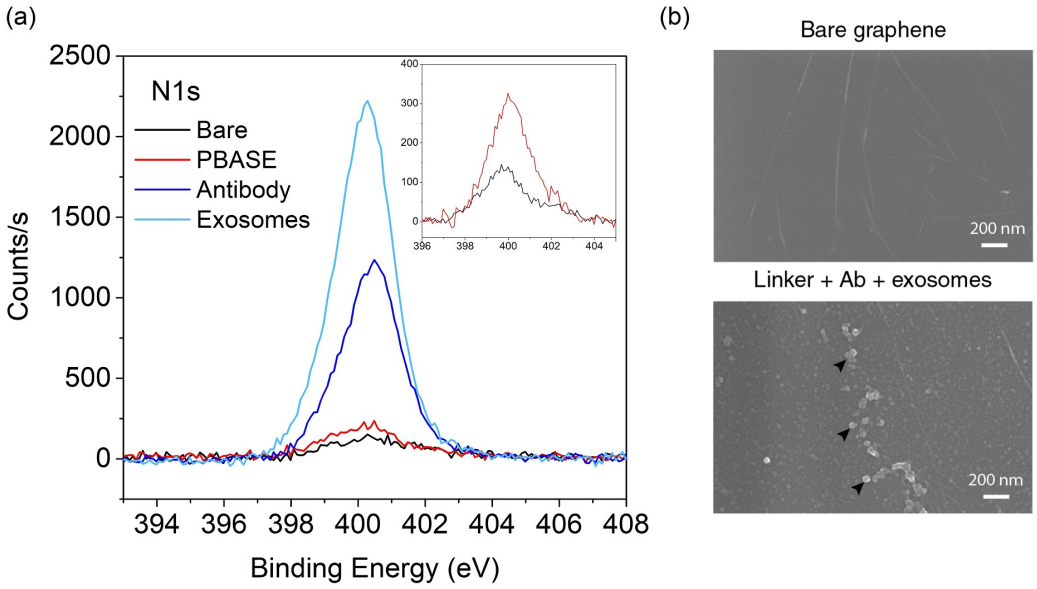

Figure 7.46: N1s XPS spectrum of graphene with different levels of functionalisation and after incubation with a 25 µL droplet of 10 µg/mL exosomes for 30 minutes. Inset: N1s XPS spectrum of bare and PBASE functionalised graphene (b) SEM images of bare and CD63 Ab conjugated graphene with adherent exosomes (arrowheads).

7.4.2 Dependence on Exosome Concentration

Lower concentrations of exosomes were investigated to test the limit of detection of the gFET sensor at this stage. Figure 7.47 shows the sensor response to exosome concentrations of 0.1 µg/mL and 1 µg/mL, which can be directly compared to the initial highest concentration of 10 µg/mL. For each, a similar trend in the additional conductance minimum was observed when compared to the preliminary results in figure 7.45(a) - (c). In each case an additional conductance minimum appears and generally shifts to higher V_g with time due to exosome binding.

In some cases, the additional minimum is not as distinct as in figure 7.45(a) and appears as a shoulder. This makes it difficult to fit this position with a parabola and as a result the exact value of the additional minimum was difficult to determine. The trend of $V_t - V_{PBS}$ against time also showed more variation due to the uncertainty of the minimum position and

did not show clear saturation regions after the 30 minutes. However, the general increase at least indicated that the mechanism of how the exosomes contribute to the graphene's electrical properties was the same: as the exosomes carry negative charge, the positive shift in V_t supports the accumulation of positive charge within the graphene film.

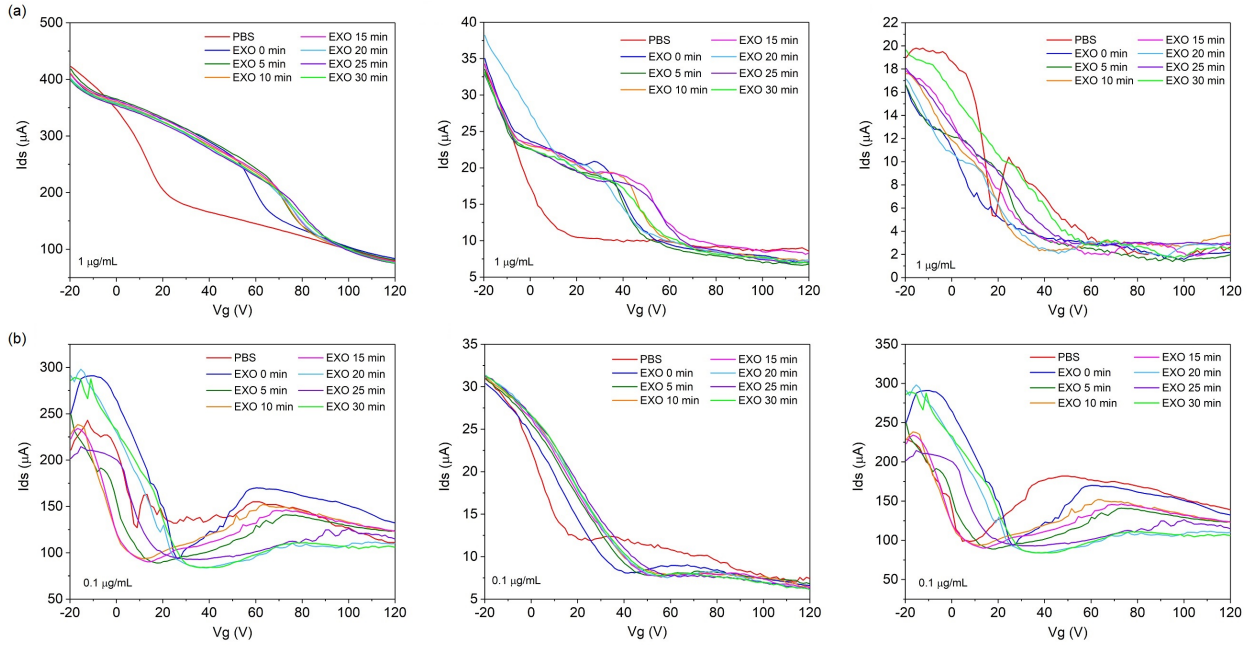

Figure 7.47: I_{ds} - V_g transfer characteristic for 6 fully functionalised gFET sensors and their individual responses to air, PBS and (a) 1 µg/mL and (b) 0.1 µg/mL exosomes over 30 minutes.

When PBS is added to the microfluidic channel, the graphene exposed to the solution becomes significantly n-doped with respect to the original Dirac point as discussed in section 7.3.3.1. For all samples the hole mobility is severely affected by the presence of PBS in the channel. This is due to the increase in resistance as charge carriers move between the different doping regions when V_g is in the hole conduction regime, similar to the effect of contact resistance in section 7.1.2.1. With air, the whole graphene film is p-doped and when PBS is present, regions of P-N-P arise which inhibit hole conduction through the area exposed to PBS and therefore lower conductance is observed compared to air. However, with the presence of exosomes, their negative charge causes the weakening of this n-doping effect as they induce positive charge in the graphene. This instead results in a graphene film with P-n-P doping regions, as seen in figure 7.48.

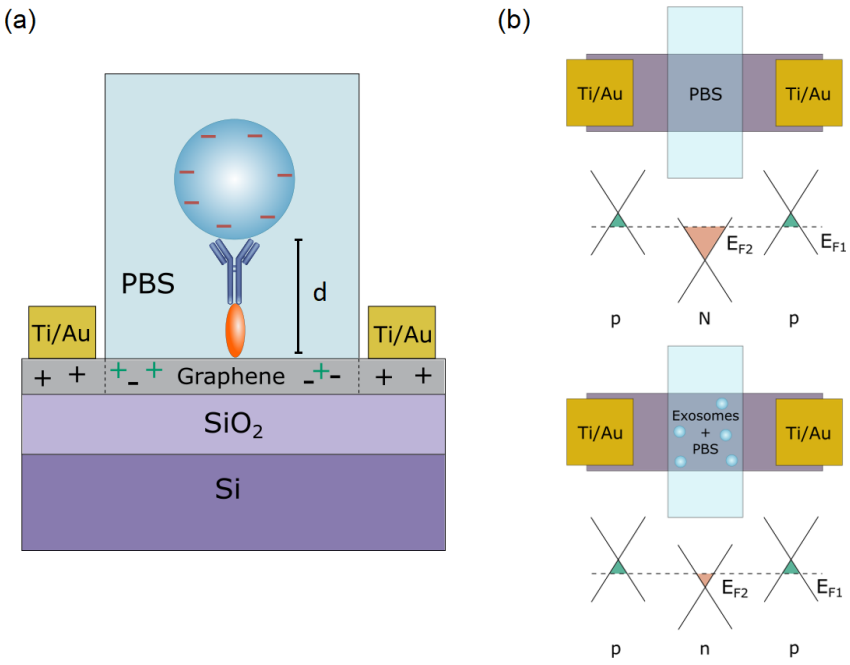

Figure 7.48: Schematic representation of (a) the negatively charge exosomes binding to the functionalised gFET where d is the total length of the PBASE linker and anti-CD63 Ab and (b) regional doping effect as a result of PBS and exosomes where E_{f1} and E_{f2} represent the Fermi levels of the uncovered graphene and graphene exposed to solution, respectively.

Figure 7.49(a) compares all measurements of different exosome concentrations averaged over 3 samples for each concentration. The measurements of the highest exosome concentration are displayed in black, which gave rise to the largest shift in V_t from PBS. For all concentrations, the immediate shift of the additional minimum from V_{PBS} at 0 minutes supports that this initial change is due to the introduction of negatively charged particles close to the graphene surface that exist in a homogeneous distribution. The dependency of V_t - V_{PBS} at 0 minutes on the exosome concentration confirms that a lower concentration of exosomes results in less negative charge existing in solution and a smaller shift in additional minimum as a result. The increase in V_t - V_{PBS} with time for all exosome concentrations and concentration dependency of V_t - V_{PBS} at 30 minutes also shows that a higher exosome concentration results in more negative charge accumulation close to the sensor surface from increased exosome binding.

For each concentration, there are several factors that cause variation in the measured minimum shift for each time point. This may be caused by the influence of the original Dirac point of the

graphene, which is likely to be present at different V_g for each sample. Consider figure 7.47(a) where the Dirac point in air is close to 120 V; as the additional minimum approaches this Dirac point, the superposition of both points causes the minima to overlap. This adds further uncertainty to the position of the additional minimum point. Hence, this can make it difficult to compare the measurements over different samples. In addition, the total area of the graphene film with respect to the area under the microfluidic channel may cause discrepancies between repeat concentration measurements. The size of the graphene film between samples differs whilst the area of the microfluidic channel remains constant. This alters the ratio between the graphene not exposed to the solution and that exposed, between samples, hence introducing another source of uncertainty between repeat experiments. However, these problems are taken into account by averaging the sensor response over 3 samples for each concentration.

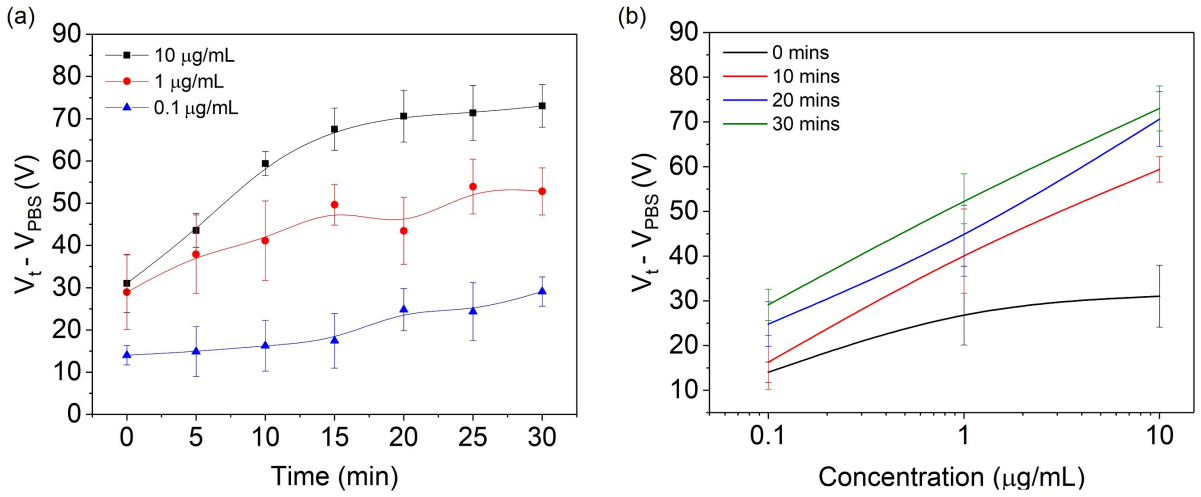

Figure 7.49: (a) Shift in the additional minimum relative to the PBS reference value with time for 3 different exosome concentrations performed over 3 samples each, where $V_t - V_{PBS}$ values were averaged for each time point. (b) Shift in the additional minimum relative to the PBS reference value plotted against exosome concentration for different time points. Error bars denote the standard deviation V_t values obtained for 3 samples for each concentration.

Results from 1 µg/mL exosomes appear similar between repeat results where figure 7.47 shows the similarity between the original Dirac points for all 3 samples ($\approx$ 100 V). This leads to similar shifts in additional conductance minimum after 30 minutes and extracted V_t - V_{PBS} values are lower than that for 10 µg/mL. As the concentration differs by an order of magnitude, the lower

number of exosomes introduced on the sensor surface results in a lower negative charge being imparted on the graphene and therefore, less positive charge accumulates, and the graphene is p-doped (with respect to the PBS blank) to a lower extent. The same is seen for the lowest exosome concentration (figure 7.47(b)), hence this shows the graphene sensor is indeed sensitive to the exosome concentration to some degree. Additionally, V_t - V_{PBS} values for all concentrations appear to be dependent on time, which was not observed for BSA measurements in figure 7.40. This suggests some specificity of the anti-CD63 Ab conjugated sensor, which is more thoroughly investigated in later sections.

Figure 7.49(a) shows sensitivity of the gFET to exosome concentration down to 0.1 µg/mL. The lowest concentration of exosomes detected corresponds approximately to 5000 exosomes/µL based on the number of particles in the stock solution as provided by the supplier. It is not possible that the maximum shift in additional minimum after 30 minutes seen is due to close packing of the exosomes on the sensor surface or binding of all available antibody sites as the close packing of exosomes would result in approximately 4×10^9 captured on the surface, whereas all concentrations used introduce significantly less exosomes (approximately 5×10^4 exosomes for a concentration of 10 µg/mL) into the microfluidic channel. The increase in shift in additional minimum is also consistent for each different exosome concentration and the V_t - V_{PBS} value at which maximum shift occurs is dependent on exosome concentration. Therefore this saturation is most likely due to the reaching of an equilibrium in the binding of exosomes to the surface. The lowest concentration of exosomes measured for this sensor also correlates to realistic concentrations in liquid biopsies and are comparable to concentrations measured by other exosome biosensors [133].

The highest exosomes concentration of 10 µg/mL shows a saturation in the shift in additional minimum after 10 minutes due to the establishment of a binding equilibrium between the exosomes and anti-CD63 antibodies as seen in figure 7.49(a). However for both sets of lower concentration, this saturation is less apparent and may only happen after longer times. In this case, it is difficult to compare the shift in additional minimum after 30 minutes as the binding equilibrium may not yet be reached for every exosome concentration. Instead, figure

7.49(b) shows the direct shift in additional minimum with exosome concentration at each time point. For 0 minutes (black line), the relationship between V_t - V_{PBS} and concentration is highly non-linear, which confirms some instability at this time point due to the Brownian motion of the exosomes when first introduced to the sensor surface. After 10 minutes (red line), this relationship becomes more linear and hence it is more suitable to compare the sensor response at this time point. At 10 minutes, V_t - V_{PBS} linearly increases for increasing exosome concentration as a higher concentration of negative charge coming close to the sensor surface causes increased p-doping of the graphene relative to when only PBS is present.

7.4.3 Isotype Control Measurements

A major part of a biosensor's design is the guarantee that it is specific to the target molecule. The overall aim is to achieve a sensor capable of distinguishing a clear signal from exosomes without detecting other charged biomolecules that may be present in the liquid biopsy. From section 7.3.5, the gFET sensor does indeed show an electrical response to BSA when used as a non-specific target protein but does not exhibit any time-dependent response because BSA does not bind to anti-CD63 Abs. To further confirm the specificity, functionalisation of the sensor surface using a negative control is often employed [217]. The isotype in this case was a purified mouse IgG1κ isotype control and was conjugated onto PBASE functionalised surfaces using the method described in 6.4.3.

Figure 7.50 shows all electrical characteristics measured over 3 samples functionalised with PBASE and conjugated with the isotype control. For all samples the original Dirac point was not visible within the chosen V_g range. Nonetheless with PBS, the additional minimum in the I_{ds} - V_g transfer characteristic was present for all samples between 10 - 20 V. The V_t - V_{PBS} value with exosomes was monitored over 30 minutes and the value after 10 minutes displayed in figure 7.51, which is significantly lower compared to the gFET sensors with anti-CD63 Ab conjugation for all exosome concentrations (figure 7.49(a)). The value of V_t - V_{PBS} after 10 minutes for the isotype control was also comparable to the low value obtained for a PBS control

where there are no exosomes present in solution.

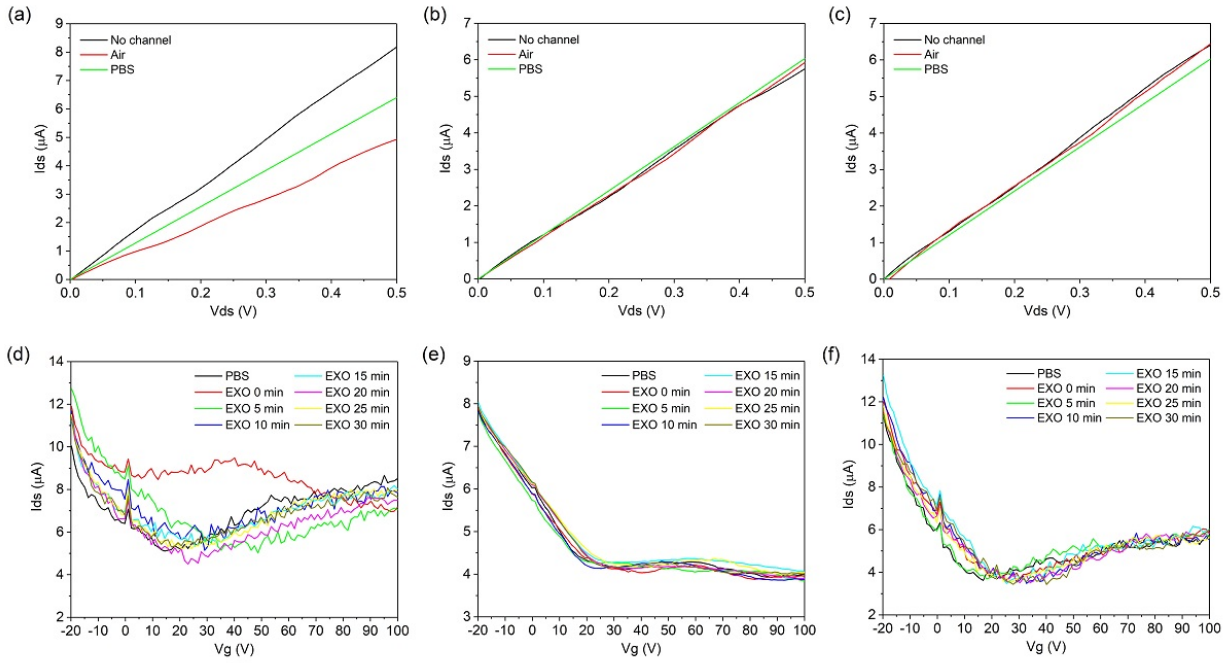

Figure 7.50: I_{ds} - V_{ds} output characteristics at $V_g = 0$ V of sample (a) 1, (b) 2 and (c) 3 and I_{ds} - V_g transfer characteristic for sample (d) 1, (e) 2 and (f) 3 over 30 minutes with introduction of 10 µg/mL exosomes in 0.001× PBS pH 7. All 3 gFET sensors were identically fabricated and functionalised with the isotype control antibody.

As exosomes are introduced into the channel, they still exist as homogeneously distributed negative charges and were still expected to contribute some effect on graphene, similar to the effect of the non-specific target BSA in section 7.3.5. After 10 minutes, V_t - V_{PBS} was 8.9 ± 3.3 V; this small shift in V_t - V_{PBS} can be attributed to the negative charge of the exosomes in solution that are present within the Debye length. Although they are both negative controls, BSA contributes a higher V_t - V_{PBS} shift compared to the exosomes on the isotype control sensor because of the high BSA concentration used. Despite a measured V_t - V_{PBS} value with the isotype control, the difference in magnitude between isotype control and anti-CD63 Ab sensor response to exosomes is large, which suggests that when the sensor is conjugated with non-specific antibodies, the exosomes do not contribute charge modulation to the extent of when specific antibody conjugation is employed. Additionally, the lack of obvious time-dependent shift also supports that the exosomes do not bind, which indicates some degree of specificity.

It is difficult to quote the actual limit-of-detection of the gFET sensor because concentrations lower than 0.1 µg/mL were not studied (as seen in section 7.4.2). However, from figure 7.51, the highest concentration of exosomes still gives a V_t - V_{PBS} value $\sim$ 10 V on the isotype control sensor. This corresponds to the V_t - V_{PBS} value that arises from the non-specific binding of exosomes to the surface. From figure 7.49(a), the magnitude of the V_t - V_{PBS} value from exosome concentrations lower than 0.1 µg/mL is also expected to be $\sim$ 10 V. Hence, the overlap between the expected response of the sensor to the specific detection of $<$ 0.1 µg/mL and response to non-specific binding would make the detection of lower exosome concentrations difficult. This means that for our sensor, the preliminary limit-of-detection is 0.1 µg/mL and this corresponds to 5000 exosomes/µL. With reference to the review of exosome sensing devices in table 5.1, as a proof-of-concept device, this graphene-based sensor compares well to the SPR non-labelling sensors, which detect down to $\sim$ 1000 exosomes/µL. Therefore with some further optimisation and investigation into surface passivation, the graphene-based sensor as a non-labelling device for the detection of exosomes has potential.

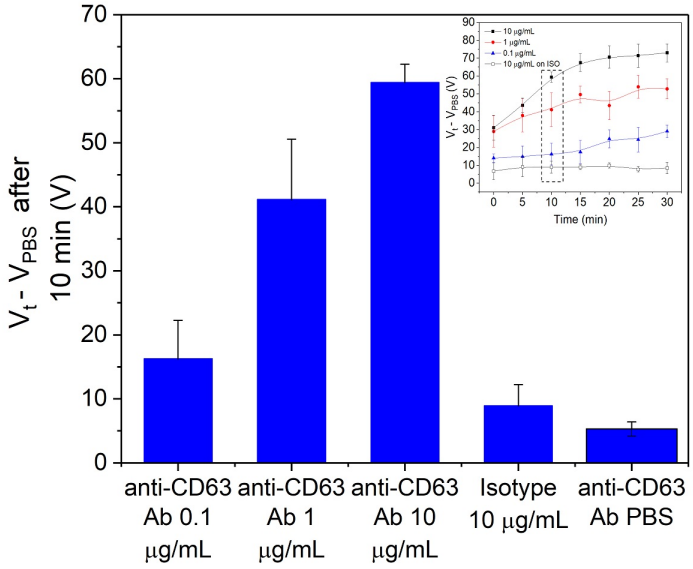

Figure 7.51: Shift in the additional minimum relative to the PBS reference after 30 minutes for anti-CD63 Ab-conjugated samples with exosomes of various concentrations alongside the shifts for the isotype-control conjugated samples with the maximum exosome concentration used (10 µg/mL exosomes) and PBS control (no exosomes). All 4 cases were performed over 3 samples with error bars denoting ± one standard deviation. Inset: V_t - V_{PBS} plot over time reproduced from figure 7.49 with additional curve for the isotype control with 10 µg/mL exosomes. The dashed box shows the chosen V_t - V_{PBS} values after 10 minutes.

As well as choosing the appropriate linkers and antibodies for the functionalisation of the graphene surface, any material used in biosensor applications must employ a form of surface passivation. This couples with the functionalisation procedure to ensure any response coming from undesired, non-specific biological species is prevented or at least minimized and the device limit-of-detection is optimised. For PBASE functionalised surfaces, the NHS ester, if left unreacted will also react with amines present on target species, since much like antibodies, most biological molecules (such as proteins and cells) will be abundant in amines on their surfaces. Section 6.4.4 describes using glycine to terminate unreacted NHS esters. This was chosen because it has the advantage of being a small, simple primary amine, which would not interfere with active antibody sites as large proteins might. Of course, this molecule reacts only with the NHS ester and does not effectively passivate areas of bare graphene, which highlights the importance of establishing the PBASE surface coverage in section 7.2.1.3. However, the surface passivation was not extensively studied in this thesis therefore, the possibility of there being some degree of non-specific adsorption of exosomes onto unfunctionalised areas of the sensor can't be ruled out and must be subject to future study.

7.4.4 Comparison to the Solution Top-Gated gFET

To compare to back-gated measurements with exosomes, a PBASE + anti-CD63 Ab conjugated gFET was fabricated to investigate the solution top-gated response. Figure 7.52 shows the response of the sensor to exosomes over 30 minutes. Here, the Dirac point shows an obvious shift to higher V_g, which is indicative of p-doping and supports the back-gated results in section 7.4.

For the solution top-gated structure, the shift is Dirac point is obvious and clearly observed and shows a similar response with time to figures 7.45 and 7.49(d). The functionalisation with specific antibodies causes the exosomes to bind to the sensor surface and an inhomogeneous charge distribution in the solution as more negative charge accumulates close to the graphene surface. By the electrostatic field-effect, the accumulation of negative charge as a distance away

from the graphene surface results in more positive charge accumulation in the graphene. For back-gated measurements, often the additional minimum would be obscured by not having a well-defined minimum or by its overlapping with the original Dirac point. In figure 7.52(a), the Dirac point remains as a well-defined minimum for every time point, which could make smaller shifts in V_g easier to measure when lower exosome concentrations are involved. With time, there is a shift to higher V_g due to the negatively charged exosomes binding to the sensor surface, which is consistent with results in section 7.4.

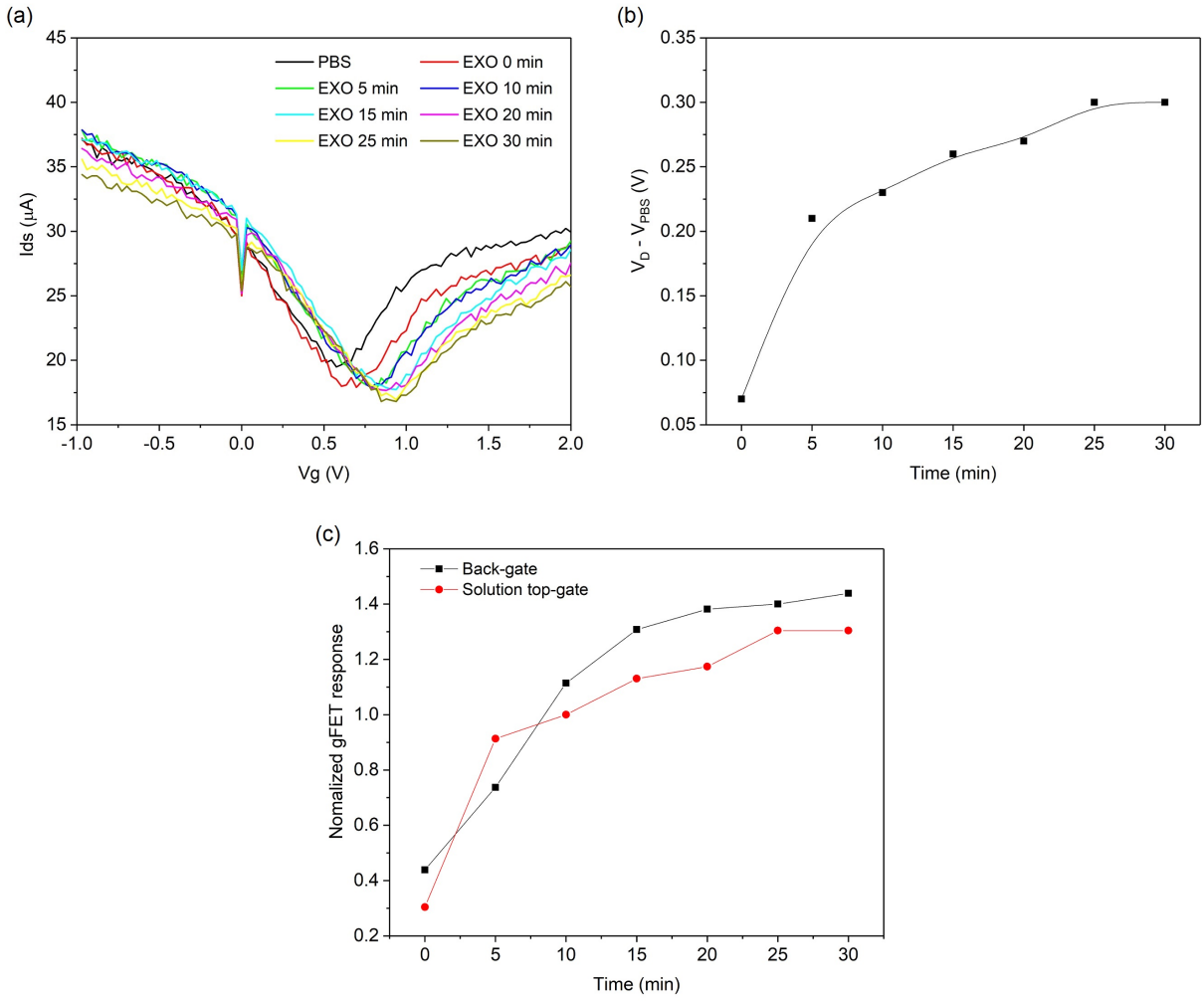

Figure 7.52: (a)I_{ds} - V_g transfer characteristic for a solution top-gated PBASE and anti-CD63 Ab functionalised gFET sensor showing its response to 10 µg/mL exosomes in 0.001× PBS over 30 minutes and (b) Shift in the Dirac point with time from the PBS reference position. (c) Normalized sensor responses of both back and solution top-gated PBASE and anti-CD63 Ab functionalised gFET sensors to 10 µg/mL exosomes in 0.001× PBS over 30 minutes.

In this case, only the highest concentration of exosomes (10 µg/mL exosomes) was measured for the solution top-gate gFET hence figure 7.52(c) compares the solution top-gate response to the back-gated response in figure 7.49(d). For back-gated measurements, the sensing mechanism was dominated by the shift in additional minimum to higher V_g from V_{PBS} due to the electrostatic effects of the negatively charged exosomes binding to the graphene surface. The same mechanism was expected for electrolyte top-gated measurements however, in figure 7.52(c) the normalized relative shift in Dirac point from V_{PBS} is slightly smaller compared to the back-gated measurements with the same exosome concentration in section 7.4. This may be due to capacitative effects, described in section 4.3.3, that may also play a part in exosome detection in electrolyte gated measurements. Here, as exosomes bind to the conjugated anti-CD63 Abs, the difference in ϵ_r between exosomes and PBS causes the capacitance of the EDL to change. As the EDL acts as the dielectric layer in the electrolyte top-gated structure, a change in capacitance can have a greater effect than in back-gated measurements where the dielectric is SiO_2, and its ϵ_r is unaffected by exosome binding. If exosomes had higher ϵ_r than 0.001× PBS, by using equation 3.5 in section 3.2.1, this would cause a higher capacitance, which in turn results in smaller ΔV_D. This would oppose the shift in Dirac point to higher V_g as expected from electrostatic effects. These competing effects could hence explain the smaller positive shift in Dirac point from exosomes in electrolyte top-gate measurements. Therefore by knowing the sensing mechanisms relevant for both back-gate and electrolyte top-gate measurements, changes in the gFET I_{ds} - V_g transfer characteristic can indicate the binding of exosomes to the PBASE and anti-CD63 Ab functionalised surface.

7.4.5 Multiple Exosome Measurements with One Sensor

In the previous cases, different sensors were used to investigate the response to exosome concentration. However, due to each graphene sample having different Dirac points before being measured in solution, this can sometimes make it difficult to compare results between them. A possible way to avoid this is to do measurements of exosomes on the same sample to make measurements directly comparable.

0.1 µg/mL exosomes in PBS were introduced to a single PBASE and anti-CD63 Ab functionalised sensor 4 times, each time being left for 30 minutes to allow for exosome binding to the surface. Figure 7.53 shows the first I_{ds} - V_g transfer characteristic recorded, where the sample was first measured with air in the microfluidic channel with the original Dirac point appearing near 110 V. The response to the PBS blank reference was recorded first as with previous experiments and it is possible to see a clear influence of the superposition on the resulting curve. At 110 V where the original Dirac point was present, there is a significant increase in I_{ds} due to the superimposed curve.

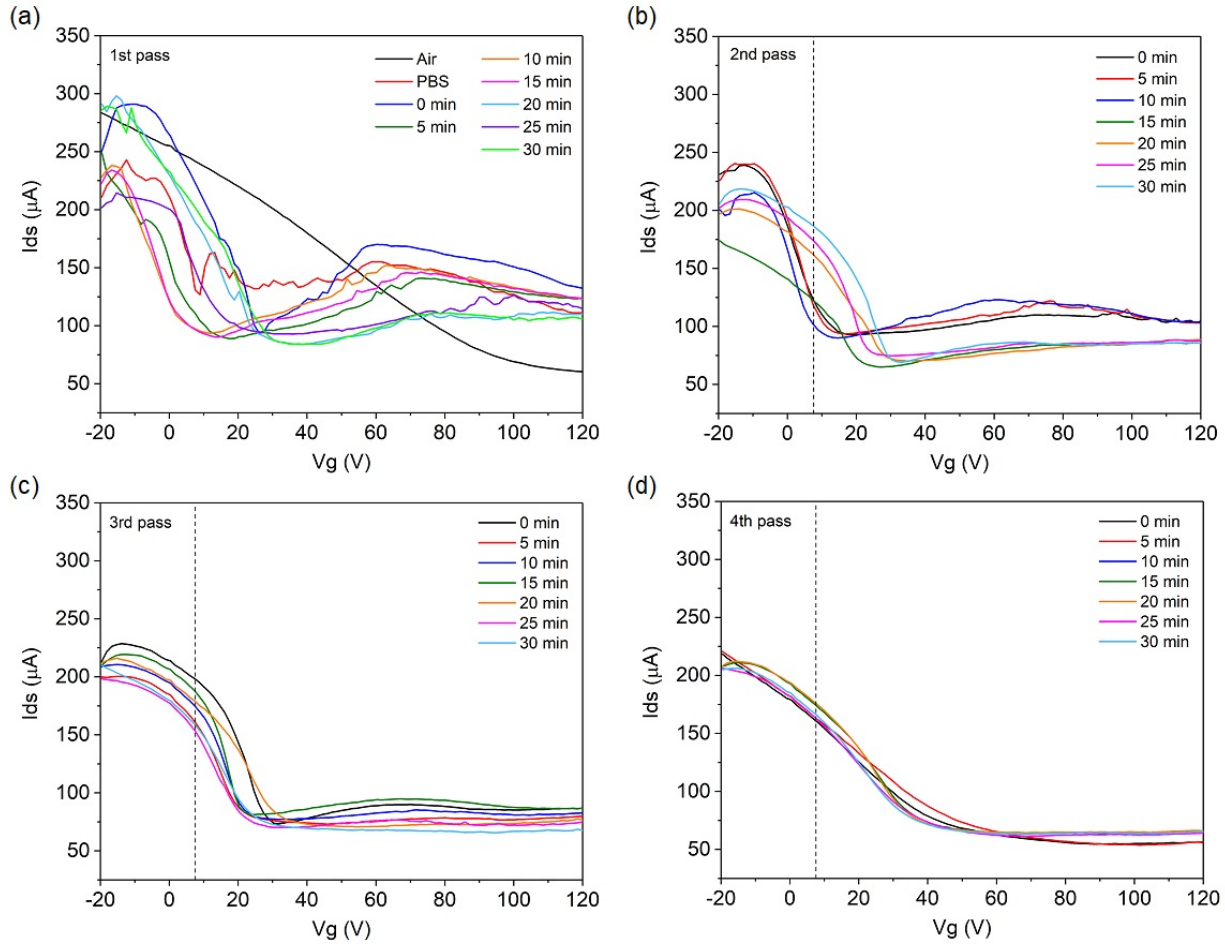

Figure 7.53: I_{ds} - V_g transfer characteristics of the same PBASE and anti-CD63 Ab functionalised gFET sensor measured 4 times with 0.1 µg/mL exosomes through the microfluidic channel: (a) 1st, (b) 2nd, (c) 3rd and (d) 4th exosome pass. The dashed line corresponds to the original position of the PBS reference without exosomes.

Compared to the reference PBS position (figure 7.53 dashed line), with increasing exosomes introduced, there appears to be a slight increase in the additional minimum shift. However, the tracking of V_t shift in figure 7.54 shows an inconsistent increase and each time a new solution is passed through, V_t first decreases before gradually increasing. This suggests that upon passing solutions through, it is possible that some disturbance is caused, possibly due to few unbound exosomes or to functionalised groups, before the solution is able to settle in the microfluidic channel. This reiterates why the experiments were performed over 30 minutes to ensure the initial shift in the additional minimum is not read as a false positive shift from exosome binding.

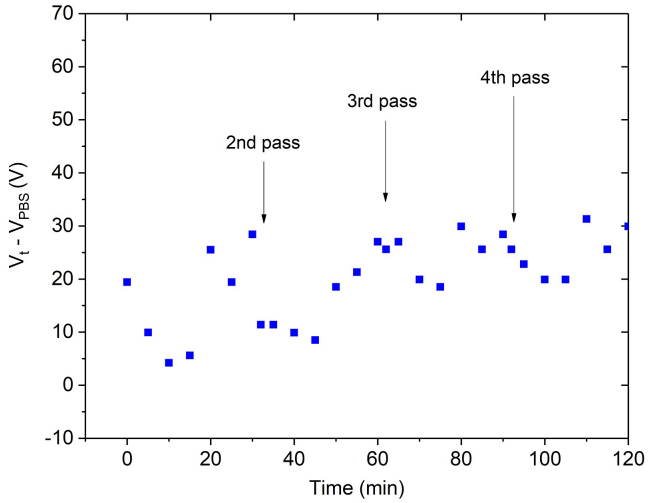

Figure 7.54: Shift in the additional conductance minimum from V_{PBS} with time over a total of 4 passes of 0.1 µg/mL exosomes in 0.001× PBS over a single gFET sensor.

With the first pass, the maximum shift after 30 minutes is 28.4 V as seen in figure 7.54. This is similar to the value obtained for 0.1 µg/mL exosomes in PBS in figure 7.49. However, even after the fourth pass, this does not exceed 29.9 V. As a result, there is no clear step-wise increase in the shift, which is believed to be due to the receptor-ligand reaction kinetics. As with chemical reactions, exosome binding has an associated equilibrium at a certain concentration. Here, it is believed that an equilibrium is already reached after 30 minutes, hence with subsequent passes of the same exosome concentration, minimal additional binding occurs and so the graphene does not experience significant changes to its electrical properties.

To further study the response to exosomes using the sample graphene sensor, another gFET sen-

sor was fabricated and subjected to two different exosome concentrations: 0.1 µg/mL followed by 1 µg/mL and its response seen in figure 7.55. Since it was expected that an equilibrium is reached limiting the shift of the additional conductance minimum using the same exosome concentration, it was assumed that a higher concentration may result in a more obvious step-wise change.

As seen in figure 7.55, the initial I_{ds} - V_g response is similar to that in figure 7.49 as the original Dirac point, when measured with air in the microfluidic channel, is seen near 110 V, however upon introduction of PBS through the channel it seems this point is greatly influenced by the superposition of the additional characteristic. The superposition of curves in figure 7.27 shows the case where the additional minimum does not affect the original Dirac point. However, in some cases, the effect of the additional curve may cause changes in the original curve such that the original Dirac point is obscured. In figure 7.55, the additional conductance minimum is more obvious and shows a sharper dip, making the V_g value easier to determine. Despite this, the response of the sensor did not show as clear trend as with previous measurements but nonetheless the value did shift from the PBS reference. Subsequently, 1 µg/mL exosomes in PBS was passed through the channel and left for 30 minutes. There was a clear, both immediate and overall shift in V_t and the range of $V_t - V_{PBS}$ resembles that in figure 7.47.

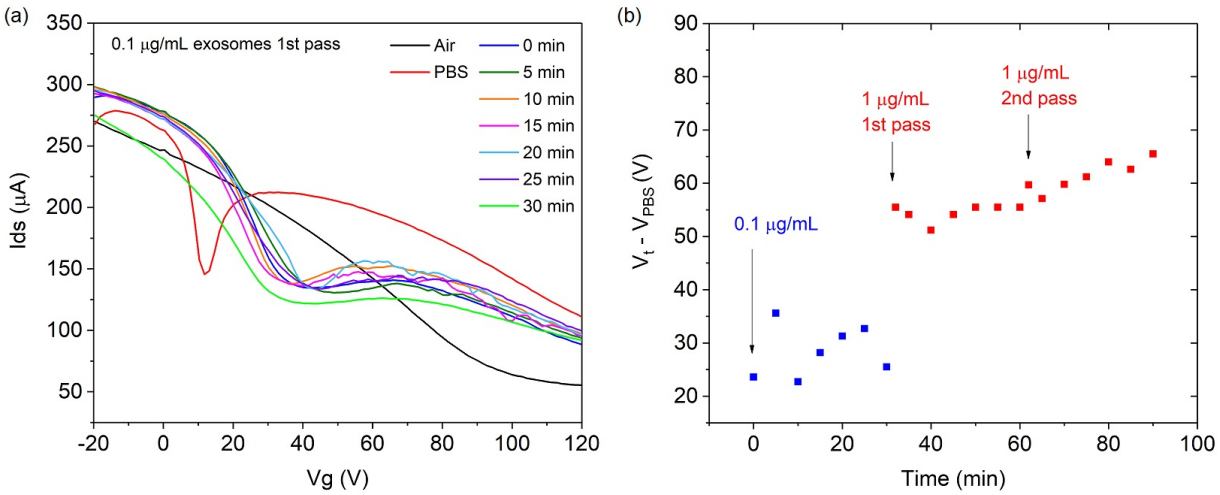

Figure 7.55: (a) I_{ds} - V_g transfer characteristic of the functionalised gFET sensor for air, PBS and the first pass of 0.1 µg/mL exosomes over 30 minutes. (b) The shift in the additional conductance minimum from V_{PBS} with time for 0.1 µg/mL and subsequent 1 µg/mL exosomes in 0.001× PBS.

The result shows that the gFET sensor is responsive to changes in exosome concentration as there is a clear step-wise increase in $V_t - V_{PBS}$ with a concentration change. As the shift is believed to be due to the establishment of an equilibrium between the attachment and detachment of exosomes to the sensor surface after 30 minutes at a specific concentration, it is reasonable to assume that with a concentration change, a re-establishment of this equilibrium must be achieved, hence this then affects $V_t - V_{PBS}$. However, there appears to be a small linear shift upon the second pass of the same concentration is introduced to the sensor surface similar to the shift seen from passes of the same exosome concentration seen in figure 7.55. Although there is a small increase, it is not nearly as significant as that achieved by a change in exosome concentration.

To assess the sensor's sensitivity to changes in exosome concentrations, exosome concentrations between 0.1 µg/mL - 1 µg/mL were prepared in increments of 0.5 µg/mL. The same sensor was then subjected to these sequentially and their individual transfer characteristics recorded. Figure 7.56 shows tracks $V_t - V_{PBS}$ for this sensor and shows a response between 0.1 µg/mL and 1 µg/mL consistent with that in figures 7.49 and 7.55. By introducing an intermediate concentration of 0.5 µg/mL, the change in $V_t - V_{PBS}$ per 0.5 µg/mL exosomes appears to be

8.7 V then 7.1 V, which is roughly consistent with previous measurements.

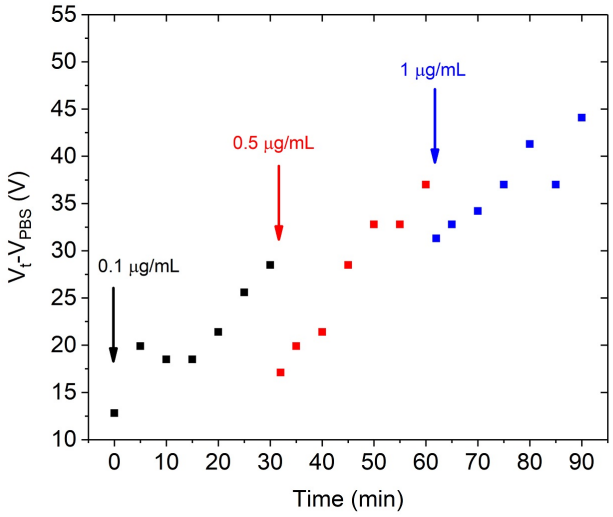

Figure 7.56: The shift in additional conductance minimum from V_{PBS} with time for 0.1 µg/mL, 0.5 µg/mL and 1 µg/mL exosomes in 0.001× PBS.

Overall, this shows that the sensor is responsive to small changes in exosome concentration. In figure 7.56 the increase in $V_t - V_{PBS}$ between different exosome concentrations is again due to the re-establishment of the binding equilibrium between the exosomes and anti-CD63 antibodies. This indicates that the same gFET sensor can detect changes in exosome concentration down to 0.5 µg/mL.

7.4.6 Summary of Exosome Measurements

By using a PBASE and anti-CD63 Ab functionalised graphene gFET sensor in both the back-gated and solution top-gated set-up, exosomes derived from the plasma of healthy patients were sensed with a current limit-of-detection of 0.1 µg/mL exosomes in 0.001× PBS. For the back-gated set-up, the mechanism of sensing was established to be through the tracking of the additional minimum in the I_{ds} - V_g transfer characteristic with time after introduction of exosomes. Like BSA, exosomes exhibit negative surface charge and as a result cause the accumulation of positive charge and p-doping in graphene (relative to when there are no exosomes and only PBS present) through the electrostatic effect. However unlike BSA, the gFET

response changes with time for all exosome concentrations due to the specific binding of exosomes to the anti-CD63 antibodies on the sensor surface. At time = 0 minutes, a homogeneous distribution of negative charge in solution exists but becomes inhomogeneous as exosomes bind to the surface. Hence, when the I_{ds} - V_g transfer characteristic was monitored over 30 minutes, the binding of exosomes results in the shift of the additional minimum (V_t – V_{PBS}), which increases with time. For the highest concentration of exosomes, a saturation in V_t – V_{PBS} is observed at the end of the 30 minutes due to the establishment of a binding equilibrium but is not apparent for lower exosome concentrations as the equilibrium takes longer to reach. The solution top-gated gFET was also identically fabricated and tested against the highest exosome concentration whereby a similar trend with time was observed, which proves both set-ups are effective in exosomes sensing.

In addition to using BSA as non-specific target negative control, the sensor was fabricated with an isotype control antibody (IgG1 κ antibody). Exosomes were not expected to bind and the gFET showed much lower response, which was comparable to a PBS-only control, than when conjugated with the specific anti-CD63 antibodies. In conclusion, the sensor has been shown to detect exosomes down to 0.1 µg/mL (5000 exosomes/µL) with one sensor being shown to detect incremental changes in concentration down to 0.5 µg/mL. This compares well to other non-labelling sensor such as those based on SPR, which have detected down to 1000 exosomes/µL. From a device perspective, once ligand-receptor binding occurs, the exosomes are then effectively permanently bound to the sensor surface, which makes them difficult to remove and makes reusability unrealistic. At this stage, the sensor is functional as a disposable tool for isolated exosome solutions. As the solution top-gated sensor was also shown to be effective in section 7.4.4, multiple measurements using the same sensor could also be implemented in that set-up.

Chapter 8

Conclusion

8.1 Summary of Thesis Achievements

In this thesis, a gFET structure was fabricated using functionalised CVD graphene for the label-free detection of exosomes. Firstly, the graphene after transfer onto SiO_2/Si substrates was characterised to ensure an appropriate surface for modification. As large-area CVD graphene was used, it was crucial to maintain a homogeneous, defect-free film as the presence of defects and holes or tears in the film would certainly affect the final biosensor. By identifying features in the film that could lead to non-ideal electrical and chemical properties, appropriate steps can be taken during the graphene transfer process to ensure these are minimised. It was concluded that despite careful transfer onto substrates, each independently fabricated sample could differ in terms of electrical properties. This would obviously affect the sensing mechanism as each sample could give a different response to exosomes and these implications had to be considered in later electrical measurements.

Several different layers of functionalisation were used to tailor the graphene surface for exosome capture, the first of which was a PBASE linker. This non-covalently bonded to the graphene surface through π - π stacking and did not disrupt graphene's sp^2-hybridised structure such that graphene's electronic properties were preserved. A comparison between a covalent linker

and PBASE was performed using Raman spectroscopy, which indeed confirmed that covalently-bonded linkers introduced a higher density of defects than non-covalent functionalisation, as quantified by the I(D)/I(G) peak ratio. Furthermore, electrical measurements of PBASE functionalised graphene showed that despite non-covalent functionalisation, the presence of the molecule modulates graphene's electrical properties by p-doping the film with respect to DMF. Although the presence of the molecule is confirmed using XPS and UV-Vis spectroscopy, further investigation in addition to the DC measurement results is necessary to determine the homogeneity of functionalisation and surface coverage. Following PBASE functionalisation, anti-CD63 antibody conjugation was also investigated through similar characterisation techniques. XPS was used to confirm the presence of the anti-CD63 antibody and Raman spectroscopy showed that its attachment did not introduce defects as the disorder-induced D peak did not show significant change between samples functionalised with only PBASE and PBASE + anti-CD63 antibody functionalised samples.

Having established the functionalisation procedure, the gFET device was integrated with a microfluidic channel for the introduction of liquids to the sensor surface. By using low flow rates as not to disturb the graphene upon introduction of liquids, the graphene's electrical properties were affected when charged species were introduced into the channel. The use of the microfluidic channel meant that only a certain area of the whole graphene film was exposed to liquid. The modulation of the graphene under the channel by charged species in solution led to different regions of doping within the same graphene film between the exposed and unexposed graphene. The exposed graphene would therefore have a different Dirac point to the unexposed graphene and the superposition of these on the measured I_{ds} - V_g transfer characteristic manifested as double conductance minima. As PBS is introduced to the channel, the shift of the additional minimum to lower V_g was attributed to the screening of positive trapped charges between the graphene/SiO_2 interface, and as this additional minimum was present at similar V_g for the same PBS concentrations between all samples, this acted as a sensing reference point, V_{PBS}. The shift in this additional minimum with exosomes from V_{PBS}, hence provided the primary sensing metric and this relative measurement removed the effect of variability between independently

fabricated samples.

Due to the binding of exosomes to the gFET sensor surface, the accumulation of negative charge would cause the additional minimum to shift to higher V_g, which saturated over time. This effect was found to be dependent on exosome concentration and showed that the gFET sensor was indeed sensitive to the concentration of exosomes bound to anti-CD63 antibodies down to 100 µg/mL. The binding therefore was found to establish an equilibrium, which could then only be affected by a further change in exosome concentration. The time dependency was attributed to the time taken to ensure binding of the maximum number of exosomes. This time-dependency was not observed BSA was used as a non-specific target or when the surface was conjugated with an isotype control antibody, which suggests specificity of the anti-CD63 antibody sensor to exosomes.

Finally, a solution top-gate gFET biosensor was optimised for exosome detection and was also found to be sensitive to exosomes. It was originally believed that this geometry would give higher sensitivity due to the smaller V_g ranges used as a result of the EDL. In this case, the shift in Dirac point was directly monitored rather than an additional minimum as only the graphene exposed to the solution was gated. The sensor again showed sensitivity to BSA and exosomes similar to the back-gated gFET and capacitative effects as well as electrostatic effects contributed to the sensing mechanism.

Overall the results presented in the thesis prove the proof-of-principle concept of using a gFET biosensor for the label-free detection of exosomes, which has not been studied before. The sensitivity of the device to exosome concentration implies that this could be the starting point for a low-cost, disposable sensor for the quantification of exosomes. Various characteristics of exosomes may indicate the presence of cancer such as higher concentrations in serum, expression of different transmembrane proteins and of different protein cargo. By having the potential to isolate and detect these from a liquid biopsy, the gFET biosensor could be implemented as a powerful diagnostic tool.

8.2 Future Work

8.2.1 Surface Passivation

This thesis presents the basic proof-of-principle of the gFET sensor for exosomes, hence there are many areas in which the device can be improved and optimised. Namely, a thorough investigation into the effectiveness of the surface passivation employed in this thesis is necessary. Although, the functionalisation used showed specificity to exosomes to some extent for multiple concentrations, the surface passivation employed does not prevent adsorption of exosomes to unfunctionalised areas of the graphene. This also ties into the need to determine the surface coverage of PBASE molecules, if this can be guaranteed to be near 100 %, surface passivation using molecules that only terminate unreacted NHS esters may suffice.

8.2.2 Device Miniaturisation and Patterning

The main difference between the work presented here and for other gFET biosensors in literature is the size of the device. All measurements performed were on large-area graphene, however device sensitivity can be immediately improved by using miniturised devices that can be patterned using conventional photolithographic techniques. An obvious next step for future measurements would be fabricating graphene microarrays on a single wafer as illustrated in figure 8.1. Hence, after a single transfer of graphene to the substrate, the whole film can be patterned to produce multiple gFETs with µm length scales. Figure 8.1(a) shows how a microfluidic channel could then be placed on top such that the whole graphene area is exposed to solution, which may improve device sensitivity. Isolation of the metal contacts from the solution can be done using an SU-8 (epoxy-based) photoresist, which then allows more flexibility for the microfluidic channel dimensions.

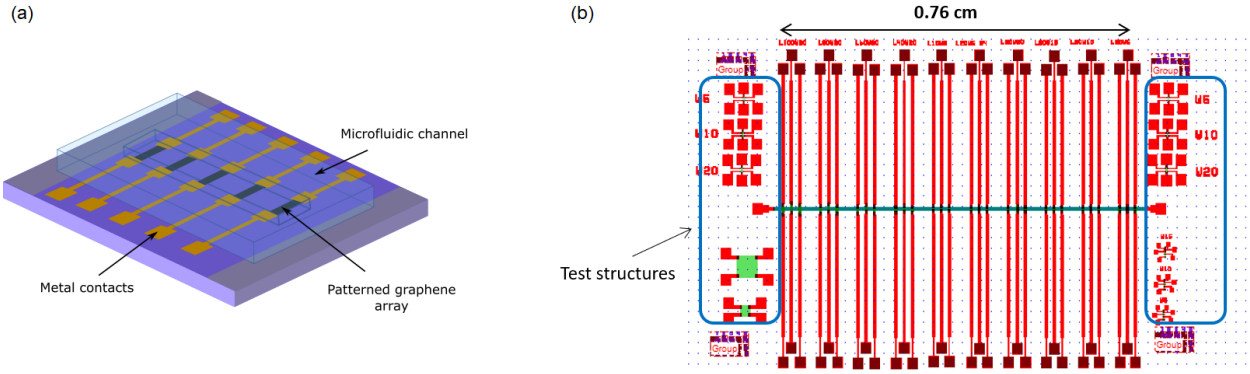

Figure 8.1: (a) Schematic representation of a patterned gFET microarray on a single substrate with patterned metal contacts and microfluidic integration. (b) Design of the mask used for fabrication of the gFET array and metal contacts. Test structures have also been designed on the outer edges for Hall measurements and measurements of contact resistance.

Figure 8.1(b) shows the design of a mask that is currently being tested for exosome sensing. In this design, the graphene is patterned to various widths and lengths (width = 5 - 20 µm and length = 20 - 100 µm) for investigations into which gives better device performance for the sensor. Additionally, test structures are present on the outer edges of the substrate such as Hall bar and Van der Pauw structures for mobility measurements and structures for measurements of contact resistance. If the graphene is transferred onto a SiO_2/Si substrate, this provides the opportunity to perform both back and solution top-gate measurements.

8.2.3 Tumour-Cell Derived Exosomes

The overall aim for the gFET sensor was to provide a point-of-care diagnostic tool for the label-free sensing of exosomes for early-stage cancer detection. Obvious improvements include further sensitivity optimisation and further investigation into the correlation of the response to exosome concentration. Additionally, this thesis has focused only on healthy exosomes and the next logical step would be to perform similar measurements using tumour cell-derived exosomes. As discussed in chapter 5, how exosomes can be used as biomarkers is not entirely straightforward as those from tumour cells may express different transmembrane proteins, carry

different protein cargo or be present in serum in higher concentrations [218]. Although it may be possible to quantify the concentration of exosomes in the liquid biopsy using the gFET sensor, this value may vary from patient to patient and would not entirely signify the presence of cancer. More realistically, the presence of surface proteins present on tumour cell-derived exosomes may be more viable.

Recently, Q. Li et al. [219] showed that K562 leukemia cells and their derived exosomes carry similar proteins on their surface such as interleukin-15 (IL-15). The quantification and specific capture of these exosomes would be possible using the gFET sensor if the graphene surface was conjugated with anti-IL-15 antibodies. Upon introducing a solution of healthy exosomes spiked with IL-15 carrying exosomes, the response of the sensor would be attributed to the binding of IL-15 carrying exosomes only. This would be a potential implication of the gFET sensor for the diagnosis of leukemia, however it is acknowledged that one of the biggest challenges facing cancer diagnosis using liquid biopsies is the number of different disease types. The biomarkers for each type of disease must be known and therefore implies that the potential of all exosome biosensors partially lies with the overall advance in the field of exosomes as biomarkers in itself.

8.2.4 Surface Acoustic Wave gFET Biosensor

The proposed gFET sensor's working principle is fundamentally based on the detection of charged species. Most gFET-based biosensors also detect biomolecules using sensing mechanisms based on charge or a change in the dielectric properties of the gate as discussed in section 4.3. Alternatively, some sensors based on graphene mechanical resonators detect the mass of adsorbed particles, which has been implemented for graphene gas sensors [220]. However, less commonly discussed are opportunities for using graphene for a combination of mass and charge detection. A device that would allow for such measurements is a graphene-based surface acoustic wave (SAW) device, which is illustrated in figure 8.2.

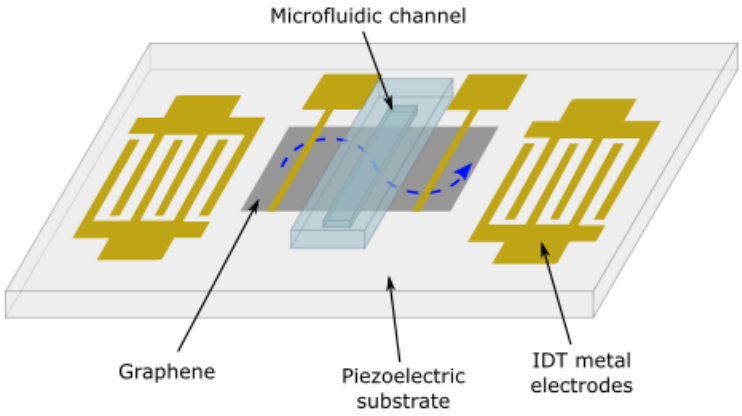

Figure 8.2: Schematic representation of the design of a graphene SAW device with interdigitated tranducers (IDTs) for the generation of the SAW, piezoelectric substrate, graphene film and integrated microfluidic channel. The blue dashed line shows the propagation of the SAW.

A benefit of graphene is its easy transfer onto a range of different substrates, which includes piezoelectric materials. Upon application of a signal between the IDTs, the SAW is generated through the piezoelectric material, with certain resonant frequency. When exosomes are introduced through the microfluidic channel they specifically bind to the surface of the functionalised graphene and as a result, the resonant frequency shift gives an indication of the amount of mass attached to the surface. Additionally, the fabrication of additional metal contacts allows for a solution top-gated gFET, which can simultaneously detect exosomes based on the effect of their charge on the graphene's electronic properties.

Bibliography

[1] Y. Wang, Z. Li, J. Wang, J. Li, and Y. Lin, "Graphene and graphene oxide: Biofunctionalization and applications in biotechnology," *Trends in Biotechnology*, vol. 29, no. 5, pp. 205–212, 2011.

[2] L. Tang, Y. Wang, Y. Li, H. Feng, J. Lu, and J. Li, "Preparation, structure, and electrochemical properties of reduced graphene sheet films," *Advanced Functional Materials*, vol. 19, no. 17, pp. 2782–2789, 2009.

[3] Y. Lu, M. B. Lerner, Z. John Qi, J. J. Mitala, J. Hsien Lim, B. M. Discher, and A. T. Charlie Johnson, "Graphene-protein bioelectronic devices with wavelength-dependent photoresponse," *Applied Physics Letters*, vol. 100, no. 3, 2012.

[4] R. D. Munje, S. Muthukumar, A. Panneer Selvam, and S. Prasad, "Flexible nanoporous tunable electrical double layer biosensors for sweat diagnostics," *Scientific Reports*, vol. 5, p. 14586, 11 2015.

[5] S. Bae, H. Kim, Y. Lee, X. Xu, J.-S. Park, Y. Zheng, J. Balakrishnan, T. Lei, H. Ri Kim, Y. I. Song, Y.-J. Kim, K. S. Kim, B. Özyilmaz, J.-H. Ahn, B. H. Hong, and S. Iijima, "Roll-to-roll production of 30-inch graphene films for transparent electrodes," *Nature Nanotechnology*, vol. 5, no. 8, pp. 574–578, 2010.

[6] S. Pang, Y. Hernandez, X. Feng, and K. Müllen, "Graphene as Transparent Electrode Material for Organic Electronics," *Advanced Materials*, vol. 23, pp. 2779–2795, 7 2011.

[7] Q. He, S. Wu, Z. Yin, and H. Zhang, "Graphene-based electronic sensors," *Chemical Science*, vol. 3, p. 1764, 5 2012.

[8] M. Choudhary, "Graphene Oxide based Label Free Ultrasensitive Immunosensor for Lung Cancer Biomarker, hTERT," *Journal of Biosensors & Bioelectronics*, vol. 04, no. 04, pp. 1–9, 2013.

[9] L. Zhou, H. Mao, C. Wu, L. Tang, Z. Wu, H. Sun, H. Zhang, H. Zhou, C. Jia, Q. Jin, X. Chen, and J. Zhao, "Label-free graphene biosensor targeting cancer molecules based on non-covalent modification," *Biosensors and Bioelectronics*, vol. 87, pp. 701–707, 2017.

[10] M. Yang, A. Javadi, H. Li, and S. Gong, "Ultrasensitive immunosensor for the detection of cancer biomarker based on graphene sheet," *Biosensors and Bioelectronics*, vol. 26, no. 2, pp. 560–565, 2010.

[11] A. V. Vlassov, S. Magdaleno, R. Setterquist, and R. Conrad, "Exosomes: Current knowledge of their composition, biological functions, and diagnostic and therapeutic potentials," *Biochimica et Biophysica Acta (BBA) - General Subjects*, vol. 1820, pp. 940–948, 7 2012.

[12] L. Grasso, R. Wyss, L. Weidenauer, A. Thampi, D. Demurtas, M. Prudent, N. Lion, and H. Vogel, "Molecular screening of cancer-derived exosomes by surface plasmon resonance spectroscopy.," *Analytical and bioanalytical chemistry*, vol. 407, pp. 5425–32, 7 2015.

[13] Cancer Research UK, "Lifetime risk of cancer."

[14] B. Bohunicky and S. A. Mousa, "Biosensors: the new wave in cancer diagnosis.," *Nanotechnology, science and applications*, vol. 4, pp. 1–10, 12 2010.

[15] K. S. Novoselov, A. K. Geim, S. V. Morozov, D. Jiang, Y. Zhang, S. V. Dubonos, I. V. Grigorieva, and A. A. Firsov, "Electric field effect in atomically thin carbon films.," *Science (New York, N.Y.)*, vol. 306, pp. 666–9, 10 2004.

[16] K. S. Novoselov, S. V. Morozov, T. M. G. Mohinddin, L. A. Ponomarenko, D. C. Elias, R. Yang, I. I. Barbolina, P. Blake, T. J. Booth, D. Jiang, J. Giesbers, E. W. Hill, and A. K.

Geim, "Electronic properties of graphene," *Physica Status Solidi (B) Basic Research*, vol. 244, no. 11, pp. 4106–4111, 2007.

[17] X. Du, I. Skachko, A. Barker, and E. Y. Andrei, "Approaching ballistic transport in suspended graphene," *Nature Nanotechnology*, vol. 3, pp. 491–495, 8 2008.

[18] T. Susi, T. Pichler, and P. Ayala, "X-ray photoelectron spectroscopy of graphitic carbon nanomaterials doped with heteroatoms," *Beilstein Journal of Nanotechnology*, vol. 6, pp. 177–192, 1 2015.

[19] R. Garg, N. Dutta, and N. Choudhury, "Work Function Engineering of Graphene," *Nanomaterials*, vol. 4, no. 2, pp. 267–300, 2014.

[20] L. Hao, J. Gallop, J. Chen, M. Adabi, N. Klein, A. Sierakowski, S. Goniszewski, K. Gajewski, Y. Chen, O. Shaforost, and T. Gotszalk, "Self-supporting graphene films and their applications," *IET Circuits, Devices & Systems*, vol. 9, no. 6, pp. 420–427, 2015.

[21] C. F. Matos, F. Galembeck, and A. J. Zarbin, "Multifunctional and environmentally friendly nanocomposites between natural rubber and graphene or graphene oxide," *Carbon*, vol. 78, pp. 469–479, 11 2014.

[22] B. J. Schultz, R. V. Dennis, V. Lee, and S. Banerjee, "An electronic structure perspective of graphene interfaces," *Nanoscale*, vol. 6, p. 3444, 3 2014.

[23] M. Orlita and M. Potemski, "Dirac electronic states in graphene systems: optical spectroscopy studies," *Semiconductor Science and Technology*, vol. 25, p. 063001, 6 2010.

[24] H. Pfleiderer and W. Kusian, "Ambipolar field-effect transistor," *Solid-State Electronics*, vol. 29, pp. 317–319, 3 1986.

[25] A. Geim and K. Novoselov, "The rise of graphene.," *Nat. Mater.*, pp. 183–191, 2007.

[26] B. Deng, Z. Liu, and H. Peng, "Toward Mass Production of CVD Graphene Films," *Advanced Materials*, pp. 1–25, 9 2018.

[27] X. Li, Y. Zhu, W. Cai, M. Borysiak, B. Han, D. Chen, R. D. Piner, L. Colomba, and R. S. Ruoff, "Transfer of large-area graphene films for high-performance transparent conductive electrodes," *Nano Letters*, vol. 9, no. 12, pp. 4359–4363, 2009.

[28] Z.-Y. Juang, C.-Y. Wu, A.-Y. Lu, C.-Y. Su, K.-C. Leou, F.-R. Chen, and C.-H. Tsai, "Graphene synthesis by chemical vapor deposition and transfer by a roll-to-roll process," *Carbon*, vol. 48, pp. 3169–3174, 9 2010.

[29] X. Chen, L. Zhang, and S. Chen, "Large area CVD growth of graphene," *Synthetic Metals*, vol. 210, pp. 95–108, 12 2015.

[30] J. Chen, Q. Liu, J. Gallop, and L. Hao, "Microwave method for high-frequency properties of graphene," *IET Circuits, Devices & Systems*, vol. 9, no. 6, pp. 397–402, 2015.

[31] S. Bhaviripudi, X. Jia, M. S. Dresselhaus, and J. Kong, "Role of Kinetic Factors in Chemical Vapor Deposition Synthesis of Uniform Large Area Graphene Using Copper Catalyst," *Nano Letters*, vol. 10, pp. 4128–4133, 10 2010.

[32] M. Adabi, *Comprehensive Study of Large-Area CVD Graphene Field Effect Structures at DC and Microwave Frequencies*. PhD thesis, Imperial College London, 2016.

[33] B. J. Kang, J. H. Mun, C. Y. Hwang, and B. J. Cho, "Monolayer graphene growth on sputtered thin film platinum," *Journal of Applied Physics*, vol. 106, p. 104309, 11 2009.

[34] L. Gao, W. Ren, H. Xu, L. Jin, Z. Wang, T. Ma, L.-P. Ma, Z. Zhang, Q. Fu, L.-M. Peng, X. Bao, and H.-M. Cheng, "Repeated growth and bubbling transfer of graphene with millimetre-size single-crystal grains using platinum," *Nature Communications*, vol. 3, p. 699, 1 2012.

[35] Y.-C. Lai, S.-C. Yu, P. M. Rafailov, E. Vlaikova, S. Valkov, S. Petrov, J. Koprinarova, P. Terziyska, V. Marinova, S. H. Lin, P. Yu, G. C. Chi, D. Dimitrov, and M. M. Gospodinov, "Chemical vapour deposition growth of graphene layers on metal substrates," *Journal of Physics: Conference Series*, vol. 558, p. 012059, 12 2014.

[36] Y. Zhang, L. Gomez, F. N. Ishikawa, A. Madaria, K. Ryu, C. Wang, A. Badmaev, and C. Zhou, "Comparison of Graphene Growth on Single-Crystalline and Polycrystalline Ni by Chemical Vapor Deposition," *The Journal of Physical Chemistry Letters*, vol. 1, pp. 3101–3107, 10 2010.

[37] Y. Huang, X. Dong, Y. Shi, C. M. Li, L.-J. Li, and P. Chen, "Nanoelectronic biosensors based on CVD grown graphene.," *Nanoscale*, vol. 2, no. 8, pp. 1485–1488, 2010.

[38] X. Dong, Y. Shi, W. Huang, P. Chen, and L. J. Li, "Electrical detection of DNA hybridization with single-base specificity using transistors based on CVD-grown graphene sheets," *Advanced Materials*, vol. 22, no. 14, pp. 1649–1653, 2010.

[39] P. Huang, H. Zhu, L. Jing, Y. Zhao, and X. Gao, "Graphene covalently binding aryl groups: Conductivity increases rather than decreases," *ACS Nano*, vol. 5, no. 10, pp. 7945–7949, 2011.

[40] S. Xu, J. Zhan, B. Man, S. Jiang, W. Yue, S. Gao, C. Guo, H. Liu, Z. Li, J. Wang, and Y. Zhou, "Real-time reliable determination of binding kinetics of DNA hybridization using a multi-channel graphene biosensor," *Nature Communications*, vol. 8, p. 14902, 2017.

[41] J. Ping, R. Vishnubhotla, A. Vrudhula, and A. T. C. Johnson, "Scalable Production of High-Sensitivity, Label-Free DNA Biosensors Based on Back-Gated Graphene Field Effect Transistors," *ACS Nano*, vol. 10, no. 9, pp. 8700–8704, 2016.

[42] M. Yi and Z. Shen, "A review on mechanical exfoliation for the scalable production of graphene," *Journal of Materials Chemistry A*, vol. 3, pp. 11700–11715, 5 2015.

[43] Y. Ohno, K. Maehashi, and K. Matsumoto, "Label-free biosensors based on aptamer-modified graphene field-effect transistors.," *Journal of the American Chemical Society*, vol. 132, no. 51, pp. 18012–18013, 2010.

[44] K. Bolotin, K. Sikes, Z. Jiang, M. Klima, G. Fudenberg, J. Hone, P. Kim, and H. Stormer, "Ultrahigh electron mobility in suspended graphene," *Solid State Communications*, vol. 146, pp. 351–355, 6 2008.

[45] N. Petrone, C. R. Dean, I. Meric, A. M. Van Der Zande, P. Y. Huang, L. Wang, D. Muller, K. L. Shepard, and J. Hone, "Chemical vapor deposition-derived graphene with electrical performance of exfoliated graphene," *Nano Letters*, vol. 12, no. 6, pp. 2751–2756, 2012.

[46] J. An, E. Voelkl, J. W. Suk, X. Li, C. W. Magnuson, L. Fu, P. Tiemeijer, M. Bischoff, B. Freitag, E. Popova, and R. S. Ruoff, "Domain (Grain) Boundaries and Evidence of "Twinlike" Structures in Chemically Vapor Deposited Grown Graphene," *ACS Nano*, vol. 5, pp. 2433–2439, 4 2011.

[47] L. G. Guex, B. Sacchi, K. F. Peuvot, R. L. Andersson, A. M. Pourrahimi, V. Ström, S. Farris, and R. T. Olsson, "Experimental review: chemical reduction of graphene oxide (GO) to reduced graphene oxide (rGO) by aqueous chemistry," *Nanoscale*, vol. 9, pp. 9562–9571, 7 2017.

[48] M. Zhou, Y. Zhai, and S. Dong, "Electrochemical Sensing and Biosensing Platform Based on Chemically Reduced Graphene Oxide," *Analytical Chemistry*, vol. 81, pp. 5603–5613, 7 2009.

[49] S. V. Tkachev, E. Y. Buslaeva, A. V. Naumkin, S. L. Kotova, I. V. Laure, and S. P. Gubin, "Reduced graphene oxide," *Inorganic Materials*, vol. 48, pp. 796–802, 8 2012.

[50] S. Mao, G. Lu, K. Yu, Z. Bo, and J. Chen, "Specific protein detection using thermally reduced graphene oxide sheet decorated with gold nanoparticle-antibody conjugates," *Advanced Materials*, vol. 22, no. 32, pp. 3521–3526, 2010.

[51] C. Berger, Z. Song, X. Li, X. Wu, N. Brown, C. Naud, D. Mayou, T. Li, J. Hass, A. N. Marchenkov, E. H. Conrad, P. N. First, and W. A. de Heer, "Electronic confinement and coherence in patterned epitaxial graphene.," *Science (New York, N.Y.)*, vol. 312, pp. 1191–6, 5 2006.

[52] W. A. de Heer and C. Berger, "Epitaxial graphene," *Journal of Physics D: Applied Physics*, vol. 45, p. 150301, 4 2012.

[53] C. Coletti, C. Riedl, D. S. Lee, B. Krauss, L. Patthey, K. Von Klitzing, J. H. Smet, and U. Starke, "Charge neutrality and band-gap tuning of epitaxial graphene on SiC by molecular doping," *Physical Review B - Condensed Matter and Materials Physics*, vol. 81, no. 23, pp. 1–8, 2010.

[54] C. Riedl, U. Starke, J. Bernhardt, M. Franke, and K. Heinz, "Structural properties of the graphene-SiC(0001) interface as a key for the preparation of homogeneous large-terrace graphene surfaces," *Physical Review B*, vol. 76, p. 245406, 12 2007.

[55] Z. Tehrani, G. Burwell, M. a. M. Azmi, A. Castaing, R. Rickman, J. Almarashi, P. Dunstan, a. M. Beigi, S. H. Doak, and O. J. Guy, "Generic epitaxial graphene biosensors for ultrasensitive detection of cancer risk biomarker," *2D Materials*, vol. 1, no. 2, p. 025004, 2014.

[56] L. Liao, Y.-C. Lin, M. Bao, R. Cheng, J. Bai, Y. Liu, Y. Qu, K. L. Wang, Y. Huang, and X. Duan, "High-speed graphene transistors with a self-aligned nanowire gate," *Nature*, vol. 467, pp. 305–308, 9 2010.

[57] M. Bigas, E. Cabruja, J. Forest, and J. Salvi, "Review of CMOS image sensors," *Microelectronics Journal*, vol. 37, pp. 433–451, 5 2006.

[58] R. J. Baker, "MOSFET Operation," in *CMOS*, pp. 131–160, Hoboken, NJ, USA: John Wiley & Sons, Inc., 5 2011.

[59] M. C. Lemme, T. J. Echtermeyer, M. Baus, and H. Kurz, "A Graphene Field-Effect Device," *IEEE Electron Device Letters*, vol. 28, pp. 282–284, 4 2007.

[60] Y. Liu, X. Dong, and P. Chen, "Biological and chemical sensors based on graphene materials," *Chem. Soc. Rev.*, vol. 41, pp. 2283–2307, 2 2012.

[61] E. H. Nicollian and J. R. Brews, *MOS (metal oxide semiconductor) physics and technology*. Wiley-Interscience, 2003.

[62] F. Schwierz, "Graphene transistors," *Nature Nanotechnology*, vol. 5, no. 7, pp. 487–496, 2010.

[63] G. Gui, J. Li, and J. Zhong, "Band structure engineering of graphene by strain: First-principles calculations," *Physical Review B*, vol. 78, p. 075435, 8 2008.

[64] M. Y. Han, B. Özyilmaz, Y. Zhang, and P. Kim, "Energy Band-Gap Engineering of Graphene Nanoribbons," *Physical Review Letters*, vol. 98, p. 206805, 5 2007.

[65] R. Balog, B. Jørgensen, L. Nilsson, M. Andersen, E. Rienks, M. Bianchi, M. Fanetti, E. Lægsgaard, A. Baraldi, S. Lizzit, Z. Sljivancanin, F. Besenbacher, B. Hammer, T. G. Pedersen, P. Hofmann, and L. Hornekær, "Bandgap opening in graphene induced by patterned hydrogen adsorption," *Nature Materials*, vol. 9, pp. 315–319, 4 2010.

[66] P. A. Denis, "Band gap opening of monolayer and bilayer graphene doped with aluminium, silicon, phosphorus, and sulfur," *Chemical Physics Letters*, vol. 492, pp. 251–257, 6 2010.

[67] S. Kim, J. Nah, I. Jo, D. Shahrjerdi, L. Colombo, Z. Yao, E. Tutuc, and S. K. Banerjee, "Realization of a high mobility dual-gated graphene field-effect transistor with Al2O3 dielectric," *Applied Physics Letters*, vol. 94, p. 062107, 2 2009.

[68] C.-C. Lu, Y.-C. Lin, C.-H. Yeh, J.-C. Huang, and P.-W. Chiu, "High Mobility Flexible Graphene Field-Effect Transistors with Self-Healing Gate Dielectrics," *ACS Nano*, vol. 6, pp. 4469–4474, 5 2012.

[69] B. J. Kim, H. Jang, S.-K. Lee, B. H. Hong, J.-H. Ahn, and J. H. Cho, "High-Performance Flexible Graphene Field Effect Transistors with Ion Gel Gate Dielectrics," *Nano Letters*, vol. 10, pp. 3464–3466, 9 2010.

[70] A. Facchetti, M.-H. Yoon, and T. J. Marks, "Gate Dielectrics for Organic Field-Effect Transistors: New Opportunities for Organic Electronics," *Advanced Materials*, vol. 17, pp. 1705–1725, 7 2005.

[71] S. J. Park, O. S. Kwon, S. H. Lee, H. S. Song, T. H. Park, and J. Jang, "Ultrasensitive Flexible Graphene Based Field-Effect Transistor (FET)-Type Bioelectronic Nose," *Nano Letters*, vol. 12, pp. 5082–5090, 10 2012.

[72] D.-M. Sun, C. Liu, W.-C. Ren, and H.-M. Cheng, "A Review of Carbon Nanotube- and Graphene-Based Flexible Thin-Film Transistors," *Small*, vol. 9, pp. 1188–1205, 4 2013.

[73] Kenry, J. C. Yeo, and C. T. Lim, "Emerging flexible and wearable physical sensing platforms for healthcare and biomedical applications," *Microsystems & Nanoengineering*, vol. 2, p. 16043, 12 2016.

[74] Y. H. Kwak, D. S. Choi, Y. N. Kim, H. Kim, D. H. Yoon, S. S. Ahn, J. W. Yang, W. S. Yang, and S. Seo, "Flexible glucose sensor using CVD-grown graphene-based field effect transistor," *Biosensors and Bioelectronics*, vol. 37, no. 1, pp. 82–87, 2012.

[75] M. Lemme, T. Echtermeyer, M. Baus, B. Szafranek, J. Bolten, M. Schmidt, T. Wahlbrink, and H. Kurz, "Mobility in graphene double gate field effect transistors," *Solid-State Electronics*, vol. 52, pp. 514–518, 4 2008.

[76] B.-W. Hwang, H.-I. Yeom, D. Kim, C.-K. Kim, D. Lee, and Y.-K. Choi, "Enhanced transconductance in a double-gate graphene field-effect transistor," *Solid-State Electronics*, vol. 141, pp. 65–68, 3 2018.

[77] P. K. Ang, W. Chen, A. T. S. Wee, and K. P. Loh, "Solution-Gated Epitaxial Graphene as pH Sensor," *Journal of the American Chemical Society*, vol. 130, pp. 14392–14393, 11 2008.

[78] J. L. Xia, F. Chen, P. Wiktor, D. K. Ferry, and N. J. Tao, "Effect of top dielectric medium on gate capacitance of graphene field effect transistors: implications in mobility measurements and sensor applications," *Nano Letters*, vol. 10, no. 12, pp. 5060–5064, 2010.

[79] A. Di Bartolomeo, F. Giubileo, F. Romeo, P. Sabatino, G. Carapella, L. Iemmo, T. Schroeder, and G. Lupina, "Graphene field effect transistors with niobium contacts and asymmetric transfer characteristics," *Nanotechnology*, vol. 26, p. 475202, 12 2015.

[80] Mika M. Kohonen, M. E. Karaman, , and R. M. Pashley, "Debye length in multivalent electrolyte solutions," *Langmuir*, vol. 16, no. 13, p. 5749–5753, 2000.

[81] K. Maehashi, T. Katsura, K. Kerman, Y. Takamura, K. Matsumoto, and E. Tamiya, "Label-Free Protein Biosensor Based on Aptamer-Modified Carbon Nanotube Field-Effect Transistors," *Analytical Chemistry*, vol. 79, no. 2, p. 782–787, 2007.

[82] S. Song, L. Wang, J. Li, C. Fan, and J. Zhao, "Aptamer-based biosensors," *TrAC Trends in Analytical Chemistry*, vol. 27, pp. 108–117, 2 2008.

[83] H.-M. So, K. Won, Y. Hwan Kim, B.-K. Kim, B. Hwan Ryu, P. Sun Na, H. Kim, and J.-O. Lee, "Single-Walled Carbon Nanotube Biosensors Using Aptamers as Molecular Recognition Elements Scheme 1. Binding of Thrombin on a SWNT-FET-Based Aptamer Sensor," *J. AM. CHEM. SOC*, vol. 127, p. 44, 2005.

[84] J. Kim, A. Babajanyan, A. Hovsepyan, K. Lee, and B. Friedman, "Microwave dielectric resonator biosensor for aqueous glucose solution," *Review of Scientific Instruments*, vol. 79, no. 8, 2008.

[85] S. Cheng, K. Hotani, S. Hideshima, S. Kuroiwa, T. Nakanishi, M. Hashimoto, Y. Mori, and T. Osaka, "Field effect transistor biosensor using antigen binding fragment for detecting tumor marker in human serum," *Materials*, vol. 7, no. 4, pp. 2490–2500, 2014.

[86] E. Stern, R. Wagner, F. J. Sigworth, R. Breaker, T. M. Fahmy, and M. A. Reed, "Importance of the debye screening length on nanowire field effect transistor sensors," *Nano Letters*, vol. 7, no. 11, pp. 3405–3409, 2007.

[87] C.-H. Chu, I. Sarangadharan, A. Regmi, Y.-W. Chen, C.-P. Hsu, W.-H. Chang, G.-Y. Lee, J.-I. Chyi, C.-C. Chen, S.-C. Shiesh, G.-B. Lee, and Y.-L. Wang, "Beyond the Debye

length in high ionic strength solution: direct protein detection with field-effect transistors (FETs) in human serum," *Scientific Reports*, vol. 7, p. 5256, 12 2017.

[88] S. Park, H. C. Kim, and T. D. Chung, "Electrochemical analysis based on nanoporous structures," *The Analyst*, vol. 137, p. 3891, 7 2012.

[89] F. Liu, Y. H. Kim, D. S. Cheon, and T. S. Seo, "Micropatterned reduced graphene oxide based field-effect transistor for real-time virus detection," *Sensors and Actuators, B: Chemical*, vol. 186, pp. 252–257, 2013.

[90] R. Stine, J. T. Robinson, P. E. Sheehan, and C. R. Tamanaha, "Real-time DNA detection using reduced graphene oxide field effect transistors," *Advanced Materials*, vol. 22, no. 46, pp. 5297–5300, 2010.

[91] S. C. Tsang, Z. Guo, Y. K. Chen, M. L. H. Green, H. A. O. Hill, T. W. Hambley, and P. J. Sadler, "Immobilisierung von platinierten und iodierten DNA-Oligomeren an Kohlenstoff-Nanoröhren," *Angewandte Chemie*, vol. 109, pp. 2291–2294, 10 1997.

[92] F. Balavoine, P. Schultz, C. Richard, V. Mallouh, T. W. Ebbesen, and C. Mioskowski, "Helical Crystallization of Proteins on Carbon Nanotubes: A First Step towards the Development of New Biosensors," *Angewandte Chemie International Edition*, vol. 38, pp. 1912–1915, 7 1999.

[93] M. Pumera, A. Ambrosi, A. Bonanni, E. L. K. Chng, and H. L. Poh, "Graphene for electrochemical sensing and biosensing," *TrAC - Trends in Analytical Chemistry*, vol. 29, no. 9, pp. 954–965, 2010.

[94] S. Eissa, G. C. Jimenez, F. Mahvash, A. Guermoune, C. Tlili, T. Szkopek, M. Zourob, and M. Siaj, "Functionalized CVD monolayer graphene for label-free impedimetric biosensing," *Nano Research*, vol. 8, no. 5, pp. 1698–1709, 2015.

[95] J. L. Bahr, J. Yang, D. V. Kosynkin, J. Bronikowski, R. E. Smalley, J. M. Tour, and M. J. Bronikowski, "Functionalization of Carbon Nanotubes by Electrochemical Reduction of Aryl Diazonium Salts : A Bucky Paper Electrode Functionalization of Carbon Nanotubes

by Electrochemical Reduction of Aryl Diazonium Salts : A Bucky Paper Electrode," *Journal of the American Chemical Society*, vol. 123, no. 27, pp. 6536–6542, 2001.

[96] G. L. C. Paulus, Q. H. Wang, and M. S. Strano, "Covalent Electron Transfer Chemistry of Graphene with Diazonium Salts," *Accounts of Chemical Research*, vol. 46, pp. 160–170, 1 2013.

[97] P. Allongue, M. Delamar, B. Desbat, O. Fagebaume, R. Hitmi, J. Pinson, and J. M. Saveant, "Covalent Modification of Carbon Surfaces by Aryl Radicals Generated from the Electrochemical Reduction of Diazonium Salts," *J.Am.Chem.Soc.*, vol. 119, no. 8, pp. 201–207, 1997.

[98] A. Chaussé, M. M. Chehimi, N. Karsi, J. Pinson, F. Podvorica, and C. Vautrin-Ul, "The Electrochemical Reduction of Diazonium Salts on Iron Electrodes. The Formation of Covalently Bonded Organic Layers and Their Effect on Corrosion," *Chemistry of Materials*, vol. 14, no. 1, p. 392–400, 2002.

[99] H. Liu, Y. Liu, and D. Zhu, "Chemical doping of graphene," *J. Mater. Chem.*, vol. 21, pp. 3335–3345, 2 2011.

[100] M. Mooste, E. Kibena, J. Kozlova, M. Marandi, L. Matisen, A. Niilisk, V. Sammelselg, and K. Tammeveski, "Electrografting and morphological studies of chemical vapour deposition grown graphene sheets modified by electroreduction of aryldiazonium salts," *Electrochimica Acta*, vol. 161, pp. 195–204, 2015.

[101] Rongjing Cui, Hong-Cheng Pan, Jun-Jie Zhu, and H.-Y. Chen, "Versatile Immunosensor Using CdTe Quantum Dots as Electrochemical and Fluorescent Labels," *Analytical Chemistry*, vol. 79, no. 22, p. 8494–8501, 2007.

[102] V. Georgakilas, J. N. Tiwari, K. C. Kemp, J. A. Perman, A. B. Bourlinos, K. S. Kim, and R. Zboril, "Noncovalent Functionalization of Graphene and Graphene Oxide for Energy Materials, Biosensing, Catalytic, and Biomedical Applications," *Chemical Reviews*, vol. 116, no. 9, pp. 5464–5519, 2016.

[103] J. A. Mann and W. R. Dichtel, "Noncovalent functionalization of graphene by molecular and polymeric adsorbates," *Journal of Physical Chemistry Letters*, vol. 4, no. 16, pp. 2649–2657, 2013.

[104] J. T. Sun, Y. H. Lu, W. Chen, Y. P. Feng, and A. T. S. Wee, "Linear tuning of charge carriers in graphene by organic molecules and charge-transfer complexes," *Physical Review B*, vol. 81, p. 155403, 4 2010.

[105] K. Thodkar, D. Thompson, F. Lüönd, L. Moser, F. Overney, L. Marot, C. Schönenberger, B. Jeanneret, and M. Calame, "Restoring the Electrical Properties of CVD Graphene via Physisorption of Molecular Adsorbates," *ACS Applied Materials & Interfaces*, vol. 9, pp. 25014–25022, 7 2017.

[106] H. C. Cheng, R. J. Shiue, C. C. Tsai, W. H. Wang, and Y. T. Chen, "High-quality graphene p-n junctions via resist-free fabrication and solution-based noncovalent functionalization," *ACS Nano*, vol. 5, no. 3, pp. 2051–2059, 2011.

[107] J. A. Mann, T. Alava, H. G. Craighead, and W. R. Dichtel, "Preservation of Antibody Selectivity on Graphene by Conjugation to a Tripod Monolayer," *Angewandte Chemie International Edition*, vol. 52, pp. 3177–3180, 3 2013.

[108] S. Yoshitake, Y. Yamada, E. Ishikawa, and R. Masseyeff, "Conjugation of Glucose Oxidase from Aspergillus niger and Rabbit Antibodies Using N-Hydroxysuccinimide Ester of N-(4-Carboxycyclohexylmethyl)-Maleimide," *European Journal of Biochemistry*, vol. 101, pp. 395–399, 11 1979.

[109] R. J. Chen, Y. Zhang, D. Wang, and H. Dai, "Noncovalent Sidewall Functionalization of Carbon Nanotubes for Protein Immobilization," *Journal of the American Chemical Society*, vol. 123, no. 16, pp. 3838–3839, 2001.

[110] A. Antonucci, J. Kupis-Rozmysłowicz, and A. A. Boghossian, "Noncovalent Protein and Peptide Functionalization of Single-Walled Carbon Nanotubes for Biodelivery and Optical

Sensing Applications," *ACS Applied Materials & Interfaces*, vol. 9, pp. 11321–11331, 4 2017.

[111] S. R. Guo, J. Lin, M. Penchev, E. Yengel, M. Ghazinejad, C. S. Ozkan, and M. Ozkan, "Label free DNA detection using large area graphene based field effect transistor biosensors," *Journal of Nanoscience and Nanotechnology*, vol. 11, no. 6, pp. 5258–5263, 2011.

[112] X. V. Zhen, E. G. Swanson, J. T. Nelson, Y. Zhang, Q. Su, S. J. Koester, and P. Bühlmann, "Noncovalent monolayer modification of graphene using pyrene and cyclodextrin receptors for chemical sensing," *ACS Applied Nano Materials*, vol. 1, no. 6, pp. 2718–2726, 2018.

[113] P. K. Ang, A. Li, M. Jaiswal, Y. Wang, H. W. Hou, J. T. L. Thong, C. T. Lim, and K. P. Loh, "Flow sensing of single cell by graphene transistor in a microfluidic channel," *Nano Letters*, vol. 11, no. 12, pp. 5240–5246, 2011.

[114] T. Cohen-Karni, Q. Qing, Q. Li, Y. Fang, and C. M. Lieber, "Graphene and Nanowire Transistors for Cellular Interfaces and Electrical Recording," *Nano Letters*, vol. 10, pp. 1098–1102, 3 2010.

[115] S. Sharma, H. Byrne, and R. J. O'Kennedy, "Antibodies and antibody-derived analytical biosensors.," *Essays in biochemistry*, vol. 60, no. 1, pp. 9–18, 2016.

[116] L. M. Weiner, R. Surana, and S. Wang, "Monoclonal antibodies: versatile platforms for cancer immunotherapy," *Nature Reviews Immunology*, vol. 10, pp. 317–327, 5 2010.

[117] C. Janeway, *Immunobiology 5 : the immune system in health and disease*. Garland Pub, 2001.

[118] J. Ping, J. Xi, J. G. Saven, R. Liu, and A. T. C. Johnson, "Quantifying the effect of ionic screening with protein-decorated graphene transistors," *Biosensors and Bioelectronics*, vol. 89, pp. 689–692, 2017.

[119] Y. Y. Wang and P. J. Burke, "Polyelectrolyte multilayer electrostatic gating of graphene field-effect transistors," *Nano Research*, vol. 7, no. 11, pp. 1650–1658, 2014.

[120] D. J. Kim, I. Y. Sohn, J. H. Jung, O. J. Yoon, N. E. Lee, and J. S. Park, "Reduced graphene oxide field-effect transistor for label-free femtomolar protein detection," *Biosensors and Bioelectronics*, vol. 41, no. 1, pp. 621–626, 2013.

[121] K. Bradley, M. Briman, A. Star, and G. Gru, "Charge Transfer from Adsorbed Proteins," *Nano Letters*, vol. 4, no. 2, p. 253–256, 2004.

[122] Z. Hao, Y. Zhu, X. Wang, P. G. Rotti, C. DiMarco, S. R. Tyler, X. Zhao, J. F. Engelhardt, J. Hone, and Q. Lin, "Real-Time Monitoring of Insulin Using a Graphene Field-Effect Transistor Aptameric Nanosensor," *ACS Applied Materials & Interfaces*, vol. 9, pp. 27504–27511, 8 2017.

[123] J. Lin, D. Teweldebrhan, K. Ashraf, G. Liu, X. Jing, Z. Yan, R. Li, M. Ozkan, R. K. Lake, A. A. Balandin, and C. S. Ozkan, "Gating of single-layer graphene with single-stranded deoxyribonucleic acids," *Small*, vol. 6, no. 10, pp. 1150–1155, 2010.

[124] K. Besteman, J. O. Lee, F. G. M. Wiertz, H. A. Heering, and C. Dekker, "Enzyme-coated carbon nanotubes as single-molecule biosensors," *Nano Lett.*, vol. 3, pp. 727–730, 2003.

[125] S. Adam, E. H. Hwang, V. Galitski, and S. D. Sarma, "A self-consistent theory for graphene transport," in *Proceedings of the National Academy of Sciences*, vol. 104, pp. 18392–18397, 2007.

[126] A. Newaz, Y. S. Puzyrev, B. Wang, S. T. Pantelides, and K. I. Bolotin, "Probing charge scattering mechanisms in suspended graphene by varying its dielectric environment," *Nature Communications*, vol. 3, p. 734, 2012.

[127] O. Teschke, G. Ceotto, and E. F. de Souza, "Interfacial water dielectric-permittivity-profile measurements using atomic force microscopy," *Physical Review E*, vol. 64, p. 011605, 6 2001.

[128] A. Chronopoulos, T. J. Lieberthal, and A. E. del Río Hernández, "Exosomes as a platform for 'liquid biopsy' in pancreatic cancer," *Convergent Science Physical Oncology*, vol. 3, p. 013005, 2 2017.

[129] J. Ko, E. Carpenter, and D. Issadore, "Detection and isolation of circulating exosomes and microvesicles for cancer monitoring and diagnostics using micro-/nano-based devices," *The Analyst*, vol. 141, no. 2, pp. 450–460, 2016.

[130] R. Kalluri, "The biology and function of exosomes in cancer.," *The Journal of clinical investigation*, vol. 126, pp. 1208–15, 4 2016.

[131] K. Lee, H. Shao, R. Weissleder, H. Lee, and L. E. E. E. T. Al, "Acoustic purification of extracellular microvesicles," *ACS Nano*, vol. 9, no. 3, pp. 2321–2327, 2015.

[132] S. A. Melo, L. B. Luecke, C. Kahlert, A. F. Fernandez, S. T. Gammon, J. Kaye, V. S. LeBleu, E. A. Mittendorf, J. Weitz, N. Rahbari, C. Reissfelder, C. Pilarsky, M. F. Fraga, D. Piwnica-Worms, and R. Kalluri, "Glypican-1 identifies cancer exosomes and detects early pancreatic cancer," *Nature*, vol. 523, pp. 177–182, 7 2015.

[133] M. He and Y. Zeng, "Microfluidic exosome analysis toward liquid biopsy for cancer," *Journal of laboratory automation*, vol. 21, no. 4, pp. 599–608, 2016.

[134] E. van der Pol, A. N. Boing, P. Harrison, A. Sturk, and R. Nieuwland, "Classification, Functions, and Clinical Relevance of Extracellular Vesicles," *Pharmacological Reviews*, vol. 64, no. 3, pp. 676–705, 2012.

[135] Z. Andreu and M. Yáñez-Mó, "Tetraspanins in extracellular vesicle formation and function.," *Frontiers in immunology*, vol. 5, p. 442, 2014.

[136] T. Akagi, K. Kato, N. Hanamura, M. Kobayashi, and T. Ichiki, "Evaluation of desialylation effect on zeta potential of extracellular vesicles secreted from human prostate cancer cells by on-chip microcapillary electrophoresis," *Japanese Journal of Applied physics*, vol. 01, no. 53, pp. 01–4, 2014.

[137] S. Bosch, L. de Beaurepaire, M. Allard, M. Mosser, C. Heichette, D. Chrétien, D. Jegou, and J.-M. Bach, "Trehalose prevents aggregation of exosomes and cryodamage," *Scientific Reports*, vol. 6, no. 1, p. 36162, 2016.

[138] E. Beit-Yannai, S. Tabak, and W. D. Stamer, "Physical exosome:exosome interactions.," *Journal of cellular and molecular medicine*, vol. 22, pp. 2001–2006, 3 2018.

[139] J. R. Edgar, "Q&A: What are exosomes, exactly?," *BMC Biology*, vol. 14, no. 1, p. 46, 2016.

[140] C. Rajagopal and K. B. Harikumar, "The Origin and Functions of Exosomes in Cancer.," *Frontiers in oncology*, vol. 8, p. 66, 2018.

[141] A. S. Azmi, B. Bao, and F. H. Sarkar, "Exosomes in cancer development, metastasis, and drug resistance: a comprehensive review," *Cancer and Metastasis Reviews*, vol. 32, pp. 623–642, 12 2013.

[142] F. Properzi, M. Logozzi, and S. Fais, "Exosomes: the future of biomarkers in medicine.," *Biomarkers in medicine*, vol. 7, no. 5, pp. 769–78, 2013.

[143] X.-K. Hao, Z. Li, Y.-Y. Ma, J. Wang, X.-F. Zeng, R. Li, and W. Kang, "Exosomal microRNA-141 is upregulated in the serum of prostate cancer patients," *OncoTargets and Therapy*, vol. 9, p. 139, 12 2015.

[144] K. Shimbo, S. Miyaki, H. Ishitobi, Y. Kato, T. Kubo, S. Shimose, and M. Ochi, "Exosome-formed synthetic microRNA-143 is transferred to osteosarcoma cells and inhibits their migration," *Biochemical and Biophysical Research Communications*, vol. 445, pp. 381–387, 3 2014.

[145] S. R. Pfeffer, K. F. Grossmann, P. B. Cassidy, C. H. Yang, M. Fan, L. Kopelovich, S. A. Leachman, and L. M. Pfeffer, "Detection of Exosomal miRNAs in the Plasma of Melanoma Patients.," *Journal of clinical medicine*, vol. 4, pp. 2012–27, 12 2015.

[146] Y.-L. Hsu, J.-Y. Hung, W.-A. Chang, Y.-S. Lin, Y.-C. Pan, P.-H. Tsai, C.-Y. Wu, and P.-L. Kuo, "Hypoxic lung cancer-secreted exosomal miR-23a increased angiogenesis and vascular permeability by targeting prolyl hydroxylase and tight junction protein ZO-1," *Oncogene*, vol. 36, pp. 4929–4942, 8 2017.

[147] J. Baran, M. Baj-Krzyworzeka, K. Weglarczyk, R. Szatanek, M. Zembala, J. Barbasz, A. Czupryna, A. Szczepanik, and M. Zembala, "Circulating tumour-derived microvesicles in plasma of gastric cancer patients," *Cancer Immunology, Immunotherapy*, vol. 59, pp. 841–850, 6 2010.

[148] G. Poste and G. L. Nicolson, "Arrest and metastasis of blood-borne tumor cells are modified by fusion of plasma membrane vesicles from highly metastatic cells.," *Proceedings of the National Academy of Sciences of the United States of America*, vol. 77, pp. 399–403, 1 1980.

[149] W.-x. Chen, X.-m. Liu, M.-m. Lv, L. Chen, J.-h. Zhao, S.-l. Zhong, M.-h. Ji, Q. Hu, Z. Luo, J.-z. Wu, and J.-h. Tang, "Exosomes from Drug-Resistant Breast Cancer Cells Transmit Chemoresistance by a Horizontal Transfer of MicroRNAs," *PLoS ONE*, vol. 9, p. e95240, 4 2014.

[150] F. Haderk, R. Schulz, M. Iskar, L. L. Cid, T. Worst, K. V. Willmund, A. Schulz, U. Warnken, J. Seiler, A. Benner, M. Nessling, T. Zenz, M. Göbel, J. Dürig, S. Diederichs, J. Paggetti, E. Moussay, S. Stilgenbauer, M. Zapatka, P. Lichter, and M. Seiffert, "Tumor-derived exosomes modulate PD-L1 expression in monocytes.," *Science immunology*, vol. 2, p. eaah5509, 7 2017.

[151] P. Li, M. Kaslan, S. H. Lee, J. Yao, and Z. Gao, "Progress in Exosome Isolation Techniques.," *Theranostics*, vol. 7, no. 3, pp. 789–804, 2017.

[152] J. Nilsson, J. Skog, A. Nordstrand, V. Baranov, L. Mincheva-Nilsson, X. Breakefield, and A. Widmark, "Prostate cancer-derived urine exosomes: a novel approach to biomarkers for prostate cancer," *British Journal of Cancer*, vol. 100, pp. 1603–1607, 2009.

[153] C. Chen, J. Skog, C.-H. Hsu, R. T. Lessard, L. Balaj, T. Wurdinger, B. S. Carter, X. O. Breakefield, M. Toner, and D. Irimia, "Microfluidic isolation and transcriptome analysis of serum microvesicles," *Lab Chip*, vol. 10, pp. 505–511, 2 2010.

[154] K. Ueda, N. Ishikawa, A. Tatsuguchi, N. Saichi, R. Fujii, and H. Nakagawa, "Antibody-coupled monolithic silica microtips for highthroughput molecular profiling of circulating exosomes," *Scientific Reports*, vol. 4, p. 6232, 5 2015.

[155] J. Schageman, E. Zeringer, M. Li, T. Barta, K. Lea, J. Gu, S. Magdaleno, R. Setterquist, and A. V. Vlassov, "The complete exosome workflow solution: from isolation to characterization of RNA cargo.," *BioMed research international*, vol. 2013, p. 253957, 9 2013.

[156] M. He and Y. Zeng, "Microfluidic Exosome Analysis toward Liquid Biopsy for Cancer," *Journal of laboratory automation*, vol. 21, no. 4, pp. 599–608, 2016.

[157] L. Zhu, K. Wang, J. Cui, H. Liu, X. Bu, H. Ma, W. Wang, H. Gong, C. Lausted, L. Hood, G. Yang, and Z. Hu, "Label-Free Quantitative Detection of Tumor-Derived Exosomes through Surface Plasmon Resonance Imaging," *Analytical Chemistry*, vol. 86, pp. 8857–8864, 9 2014.

[158] H. Im, H. Shao, Y. I. Park, V. M. Peterson, C. M. Castro, R. Weissleder, and H. Lee, "Label-free detection and molecular profiling of exosomes with a nano-plasmonic sensor," *Nature Biotechnology*, vol. 32, no. 5, pp. 490–495, 2014.

[159] D. L. M. Rupert, C. Lässer, M. Eldh, S. Block, V. P. Zhdanov, J. O. Lotvall, M. Bally, and F. Höök, "Determination of Exosome Concentration in Solution Using Surface Plasmon Resonance Spectroscopy," *Analytical Chemistry*, vol. 86, pp. 5929–5936, 6 2014.

[160] P. Zhang, M. He, and Y. Zeng, "Ultrasensitive microfluidic analysis of circulating exosomes using a nanostructured graphene oxide/polydopamine coating.," *Lab on a chip*, vol. 16, no. 16, pp. 3033–42, 2016.

[161] Z. Zhao, Y. Yang, Y. Zeng, and M. He, "A Microfluidic ExoSearch Chip for Multiplexed Exosome Detection Towards Blood-based Ovarian Cancer Diagnosis," *Lab on a chip*, vol. 16, p. 489, 2 2016.

[162] H. Shao, J. Chung, K. Lee, L. Balaj, C. Min, B. S. Carter, F. H. Hochberg, X. O. Breakefield, H. Lee, and R. Weissleder, "Chip-based analysis of exosomal mRNA mediating drug resistance in glioblastoma," *Nature Communications*, vol. 6, p. 6999, 12 2015.

[163] ThermoFisher, "Overview of Cell Lysis and Protein Extraction."

[164] MicroChem, "PMMA Data Sheet," 2001.

[165] Optimax, "Compound Microscope Basics," 2018.

[166] S. Kasap, H. Khaksaran, S. Çelik, H. Özkaya, C. Yanık, and I. I. Kaya, "Controlled growth of large area multilayer graphene on copper by chemical vapour deposition," *Physical Chemistry Chemical Physics*, vol. 17, pp. 23081–23087, 8 2015.

[167] L. M. Malard, M. A. Pimenta, G. Dresselhaus, and M. S. Dresselhaus, "Raman spectroscopy in graphene," *Physics Reports*, vol. 473, no. 5-6, pp. 51–87, 2009.

[168] D. M. Basko, S. Piscanec, and A. C. Ferrari, "Electron-electron interactions and doping dependence of the two-phonon Raman intensity in graphene," *Physical Review B*, vol. 80, no. 16, p. 165413, 2009.

[169] Horiba Scientific, "Raman Spectroscopy: What is the spatial resolution of a Raman microscope?," 2018.

[170] P. Venezuela, M. Lazzeri, and F. Mauri, "Theory of double-resonant Raman spectra in graphene: Intensity and line shape of defect-induced and two-phonon bands," *Physical Review B*, vol. 84, p. 035433, 7 2011.

[171] J.-J. Chen, J. Meng, D.-P. Yu, and Z.-M. Liao, "Fabrication and Electrical Properties of Stacked Graphene Monolayers," *Scientific Reports*, vol. 4, p. 5065, 5 2015.

[172] C. J. Shearer, A. D. Slattery, A. J. Stapleton, J. G. Shapter, and C. T. Gibson, "Accurate thickness measurement of graphene," *Nanotechnology*, vol. 27, p. 125704, 3 2016.

[173] Royal Society of Chemistry, "U-V Introduction to Ultraviolet-Visible Spectroscopy 1 (UV) Background Theory," 2009.

[174] H. Q. Ta, D. J. Perello, D. L. Duong, G. H. Han, S. Gorantla, V. L. Nguyen, A. Bachmatiuk, S. V. Rotkin, Y. H. Lee, and M. H. Rümmeli, "Stranski–Krastanov and Volmer–Weber CVD Growth Regimes To Control the Stacking Order in Bilayer Graphene," *Nano Letters*, vol. 16, pp. 6403–6410, 10 2016.

[175] M. Kalbac, O. Frank, and L. Kavan, "The control of graphene double-layer formation in copper-catalyzed chemical vapor deposition," *Carbon*, vol. 50, pp. 3682–3687, 8 2012.

[176] W. Zhang, C.-T. Lin, K.-K. Liu, T. Tite, C.-Y. Su, C.-H. Chang, Y.-H. Lee, C.-W. Chu, K.-H. Wei, J.-L. Kuo, and L.-J. Li, "Opening an Electrical Band Gap of Bilayer Graphene with Molecular Doping," *ACS Nano*, vol. 5, pp. 7517–7524, 9 2011.

[177] J.-H. Chen, M. Ishigami, C. Jang, D. Hines, M. Fuhrer, and E. Williams, "Printed Graphene Circuits," *Advanced Materials*, vol. 19, pp. 3623–3627, 11 2007.

[178] W. Choi, M. A. Shehzad, S. Park, and Y. Seo, "Influence of removing PMMA residues on surface of CVD graphene using a contact-mode atomic force microscope," *RSC Advances*, vol. 7, pp. 6943–6949, 1 2017.

[179] S. D. Sarma, S. Adam, E. H. Hwang, and E. Rossi, "Electronic transport in two dimensional graphene," *Reviews of Modern Physics*, vol. 83, pp. 407–470, 5 2010.

[180] W. Liu, S. Kraemer, D. Sarkar, H. Li, P. M. Ajayan, and K. Banerjee, "Controllable and rapid synthesis of high-quality and large-area bernal stacked bilayer graphene using chemical vapor deposition," *Chemistry of Materials*, vol. 26, no. 2, pp. 907–915, 2014.

[181] M. Radosavljević, S. Heinze, J. Tersoff, and P. Avouris, "Drain voltage scaling in carbon nanotube transistors," *Applied Physics Letters*, vol. 83, pp. 2435–2437, 9 2003.

[182] J. Bai, L. Liao, H. Zhou, R. Cheng, L. Liu, Y. Huang, and X. Duan, "Top-Gated Chemical Vapor Deposition Grown Graphene Transistors with Current Saturation," *Nano Letters*, vol. 11, pp. 2555–2559, 6 2011.

[183] H. A. Krebs, "Chemical Composition of Blood Plasma and Serum," *Annual Review of Biochemistry*, vol. 19, no. 1, pp. 409–430, 1950.

[184] H. Medina, Y. C. Lin, D. Obergfell, and P. W. Chiu, "Tuning of charge densities in graphene by molecule doping," *Advanced Functional Materials*, vol. 21, no. 14, pp. 2687–2692, 2011.

[185] M. S. Dresselhaus, A. Jorio, A. G. Souza Filho, and R. Saito, "Defect characterization in graphene and carbon nanotubes using Raman spectroscopy.," *Philosophical transactions. Series A, Mathematical, physical, and engineering sciences*, vol. 368, pp. 5355–77, 12 2010.

[186] M. Kalbac, A. Reina-Cecco, H. Farhat, J. Kong, L. Kavan, and M. S. Dresselhaus, "The influence of strong electron and hole doping on the Raman intensity of chemical vapor-deposition graphene," *ACS Nano*, vol. 4, no. 10, pp. 6055–6063, 2010.

[187] X. Dong, D. Fu, W. Fang, Y. Shi, P. Chen, and L. J. Li, "Doping single-layer graphene with aromatic molecules," *Small*, vol. 5, no. 12, pp. 1422–1426, 2009.

[188] Chemical Book, "CAS Database List: N,N-Dimethylformamide," 2017.

[189] A. Pirkle, J. Chan, A. Venugopal, D. Hinojos, C. W. Magnuson, S. McDonnell, L. Colombo, E. M. Vogel, R. S. Ruoff, and R. M. Wallace, "The effect of chemical residues on the physical and electrical properties of chemical vapor deposited graphene transferred to SiO2," *Applied Physics Letters*, vol. 99, no. 12, pp. 3–5, 2011.

[190] G. Wu, K. Wai Chiu Lai, X. Tang, M. Meyyappan, and K. W. C Lai, "Chemical Functionalization of Graphene with Aromatic Molecule," *2015 IEEE 15th International Conference on Nanotechnology (IEEE-NANO)*, 2015.

[191] Z. Sun, Z. Yan, J. Yao, E. Beitler, Y. Zhu, and J. M. Tour, "Growth of graphene from solid carbon sources," *Nature*, vol. 468, pp. 549–552, 11 2010.

[192] F. T. Johra, J.-W. Lee, and W.-G. Jung, "Facile and safe graphene preparation on solution based platform," *Journal of Industrial and Engineering Chemistry*, vol. 20, pp. 2883–2887, 9 2014.

[193] X. Zhang, F. Gao, X. Cai, M. Zheng, F. Gao, S. Jiang, and Q. Wang, "Application of graphene–pyrenebutyric acid nanocomposite as probe oligonucleotide immobilization platform in a DNA biosensor," *Materials Science and Engineering: C*, vol. 33, pp. 3851–3857, 10 2013.

[194] G. Zhu, L. Zhang, Y. Wang, X. Xu, and X. Peng, "Interactions between pyrene and pyridinium ionic liquids studied by ultraviolet–visible spectroscopy," *Journal of Molecular Liquids*, vol. 213, pp. 289–293, 1 2016.

[195] ThermoFisher, "Amine-Reactive Crosslinker Chemistry," 2018.

[196] V. K. Singh, S. Kumar, S. K. Pandey, S. Srivastava, M. Mishra, G. Gupta, B. Malhotra, R. Tiwari, and A. Srivastava, "Fabrication of sensitive bioelectrode based on atomically thin CVD grown graphene for cancer biomarker detection," *Biosensors and Bioelectronics*, vol. 105, pp. 173–181, 5 2018.

[197] L. Mikoliunaite, R. D. Rodriguez, E. Sheremet, V. Kolchuzhin, J. Mehner, A. Ramanavicius, and D. R. Zahn, "The substrate matters in the Raman spectroscopy analysis of cells," *Scientific Reports*, vol. 5, p. 13150, 10 2015.

[198] A. E. Baker, A. R. Mantz, and M. L. Chiu, "Raman spectroscopy characterization of antibody phases in serum.," *mAbs*, vol. 6, no. 6, pp. 1509–17, 2014.

[199] I. Ettah, L. Ashton, I. Ettah, and L. Ashton, "Engaging with Raman Spectroscopy to Investigate Antibody Aggregation," *Antibodies*, vol. 7, p. 24, 7 2018.

[200] C. Watts, *Electromagnetic Sensing of Cell Suspensions in Microfluidic Systems*. PhD thesis, Imperial College London, 2017.

[201] J. Mystkowska, J. R. DĄBROWSKI, K. Kowal, K. Niemirowicz, and H. Car, "Physical and chemical properties of deionized water and saline treated with low-pressure and low-temperature plasma," *Chemik International*, vol. 67, no. 8, pp. 719–724, 2013.

[202] T. Feng, D. Xie, J. Xu, H. Zhao, G. Li, T. Ren, and H. Zhu, "Back-gate graphene field-effect transistors with double conductance minima," *Carbon*, vol. 79, no. 1, pp. 363–368, 2014.

[203] J. Moser, A. Verdaguer, D. Jiménez, A. Barreiro, and A. Bachtold, "The environment of graphene probed by electrostatic force microscopy," *Applied Physics Letters*, vol. 92, p. 123507, 3 2008.

[204] M. Luna, J. Colchero, and A. M. Baró, "Study of Water Droplets and Films on Graphite by Noncontact Scanning Force Microscopy," *Journal of Physical Chemistry B*, vol. 103, no. 44, p. 9576–9581, 1999.

[205] S. O. Ugwu and S. P. Apte, "The Effect of Buffers on Protein Conformational Stability," tech. rep., 2004.

[206] K. Matsumoto, Y. Ohno, and K. Maehashi, "Utilizing research into electrical double layers as a basis for the development of label-free biosensors based on nanomaterial transistors," *Nanobiosensors in Disease Diagnosis*, vol. 5, p. 1, 12 2015.

[207] J. Baltazar, H. Sojoudi, S. A. Paniagua, J. Kowalik, S. R. Marder, L. M. Tolbert, S. Graham, and C. L. Henderson, "Facile formation of graphene P-N junctions using self-assembled monolayers," *Journal of Physical Chemistry C*, vol. 116, no. 36, pp. 19095–19103, 2012.

[208] Y. Sun, D. Xie, C. Zhang, X. Li, J. Xu, M. Sun, C. Teng, X. Li, and H. Zhu, "Poly (ethylene imine)-modulated transport behaviors of graphene field effect transistors with double Dirac points," *Journal of Applied Physics*, vol. 121, no. 13, p. 134305, 2017.

[209] S. Goniszewski, M. Adabi, O. Shaforost, S. M. Hanham, L. Hao, and N. Klein, "Correlation of p-doping in CVD Graphene with Substrate Surface Charges," *Scientific Reports*, vol. 6, no. 1, p. 22858, 2016.

[210] J.-M. Park, D. Lee, J. Shim, T. Jeon, K. Eom, B.-G. Park, and J.-H. Lee, "Analysis and suppression of drain current drift in graphene FETs," *Semiconductor Science and Technology*, vol. 30, pp. 105013–105019, 10 2015.

[211] Open Stax, "Chapter 17: Electrochemistry," in *Chemistry*, pp. 915–962, 2016.

[212] J.-M. Park, D. Lee, J. Shim, T. Jeon, K. Eom, B.-G. Park, and J.-H. Lee, "Pulsed I-V measurement method to obtain hysteresis-free characteristics of graphene FETs," *Semiconductor Science and Technology*, vol. 29, pp. 095006–095012, 9 2014.

[213] H. Wang, Y. Wu, C. Cong, J. Shang, and T. Yu, "Hysteresis of Electronic Transport in Graphene Transistors," *ACS Nano*, vol. 4, pp. 7221–7228, 12 2010.

[214] T. Feng, D. Xie, G. Li, J. Xu, H. Zhao, T. Ren, and H. Zhu, "Temperature and gate voltage dependent electrical properties of graphene field-effect transistors," *Carbon*, vol. 78, pp. 250–256, 11 2014.

[215] S. Pramanik and R. Chakraborty, "Study of Electrochemical Interaction between Bovine Serum Albumin and Ti-O Based Nanotubes," *International Journal of Biosensors and Bioelectronics*, vol. 2, no. 3, pp. 96–98, 2017.

[216] J. H. Park, T. N. Sut, J. A. Jackman, A. R. Ferhan, B. K. Yoon, and N.-J. Cho, "Controlling adsorption and passivation properties of bovine serum albumin on silica surfaces by ionic strength modulation and cross-linking," *Physical Chemistry Chemical Physics*, vol. 19, pp. 8854–8865, 3 2017.

[217] R. Janissen, P. K. Sahoo, C. A. Santos, A. M. da Silva, A. A. G. von Zuben, D. E. P. Souto, A. D. T. Costa, P. Celedon, N. I. T. Zanchin, D. B. Almeida, D. S. Oliveira, L. T. Kubota, C. L. Cesar, A. P. d. Souza, and M. A. Cotta, "InP Nanowire Biosensor with Tailored Biofunctionalization: Ultrasensitive and Highly Selective Disease Biomarker Detection," *Nano Letters*, vol. 17, pp. 5938–5949, 10 2017.

[218] P. Kharaziha, S. Ceder, Q. Li, and T. Panaretakis, "Tumor cell-derived exosomes: A message in a bottle," *Biochimica et Biophysica Acta (BBA) - Reviews on Cancer*, vol. 1826, pp. 103–111, 8 2012.

[219] Q. Li, Q. Huang, T. Huyan, Y. Wang, Q. Huang, and J. Shi, "Bifacial effects of engineering tumour cell-derived exosomes on human natural killer cells," *Experimental Cell Research*, vol. 363, pp. 141–150, 2 2018.

[220] J. Lloyd-Hughes and T.-I. Jeon, "A Review of the Terahertz Conductivity of Bulk and Nano-Materials," *Journal of Infrared, Millimeter, and Terahertz Waves*, vol. 33, pp. 871–925, 9 2012.

Appendix

Determination of Multilayer Graphene Coverage Using ImageJ

The % coverage of bi- or multilayer islands on the graphene films was determined from optical micrographs. By using ImageJ, the image was greyscaled and contrasted such that an appropriate threshold could be applied to distinguish the islands from the bulk of the monolayer film. This process is described by figure 3. Figures 3(b) and (c) show the application and result of thresholding. This is a technique used to divide the image into two sets of pixels, which is easily done by using a heavily contrasted greyscale image whereby the dark areas and lighter areas can be separated such that a binary image is produced. The result is seen in figure 3(c). The image is made up of two different types of pixels where in this case, the black multilayer islands are the 'foreground' and all other white space is the 'background'.

ImageJ then analyses the particles and identifies all areas marked as the foreground. Each particle is then numbered and their areas automatically calculated. The % coverage of multilayer islands is then calculated from equation 1.

$$\%\, coverage = \frac{Total\ area\ of\ foreground}{Total\ micrograph\ area} \times 100 \tag{1}$$

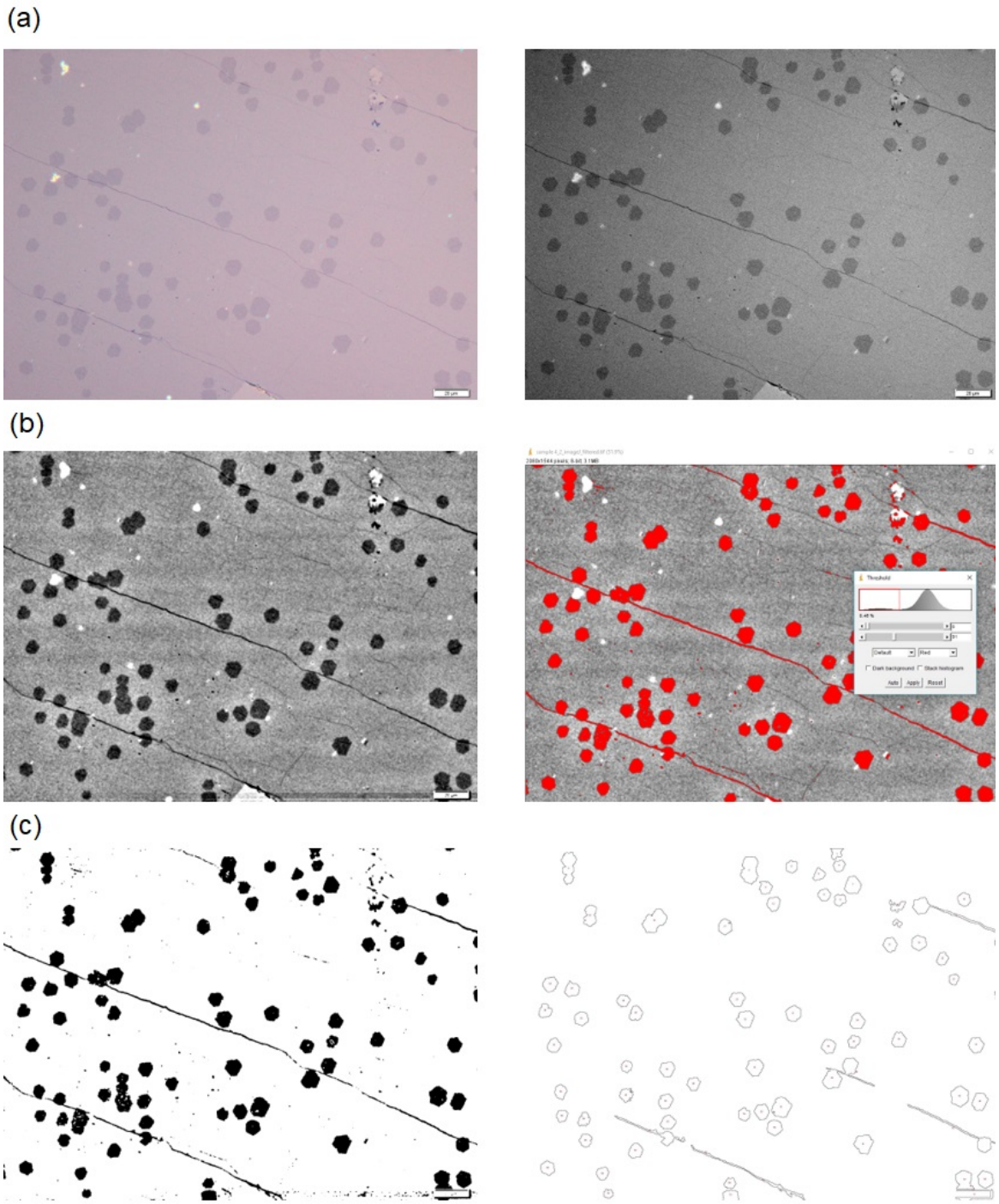

Figure 3: Process of determining the % coverage of multilayer graphene from an optical micrograph using ImageJ analysis. (a) Conversion of the optical micrograph to a greyscale image. (b) Increased image contrast and process of thresholding. (c) Image after applying the threshold and result of particle analysis.

Data Processing of Back-gated Measurements

Where possible, the additional minimum that arises I_{ds} - V_g transfer characteristics in the back-gated measurements with PBS, BSA and exosomes, was fit to a parabola to extract an accurate V_g value at which the minimum occurs. In some cases this was difficult due to the shape of the additional minimum. In these cases, the values were taken directly from the I_{ds} - V_g transfer characteristics and typically averaged over multiple samples. Figure 4 shows the process used to extract an accurate minimum value. Here, the parabolic fit is applied between specified values of V_g and then extracted as a separate plot. The first derivative of this plot then gives the exact point of inflection when $Y = 0$.

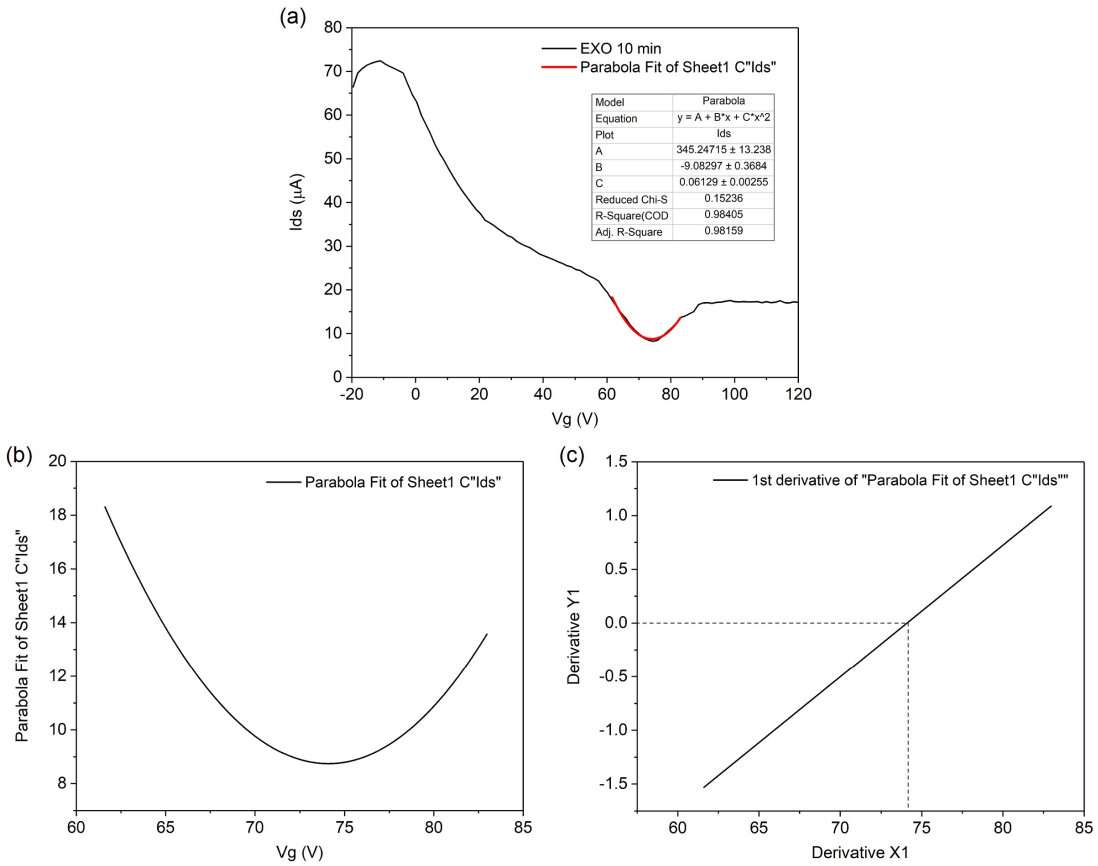

Figure 4: (a) I_{ds} - V_g transfer characteristic from a PBASE and anti-CD63 Ab conjugated gFET sensor with exosomes in 0.001X PBS present in the microfluidic channel for 10 minutes. The red line shows the parabolic fit applied to the additional minimum. (b) Extracted parabola plotted separately and (c) its 1st derivative showing the V_g value of the minimum (dashed line).